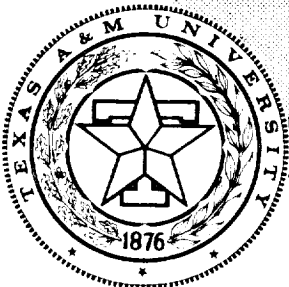


1111 1111 1111
11 39-OR

CENTER for MECHANICS of COMPOSITES

**Texas A&M University
College Station, Texas**

314742 ✓
P340



**EXPERIMENTAL OBSERVATIONS AND FINITE ELEMENT ANALYSIS
OF THE INITIATION OF FIBER MICROBUCKLING
IN NOTCHED COMPOSITE LAMINATES**

A Final Report ✓

prepared by

E. GAIL GUYNN

WALTER L. BRADLEY

OZDEN O. OCHOA

NASA Research Grant NAG-1-659

November 12, 1990

Contract Monitor: Dr. Charles E. Harris

NASA Langley Research Center

Mechanics & Materials Branch

Hampton, Virginia 23665

(NASA-CR-185354) EXPERIMENTAL OBSERVATIONS
AND FINITE ELEMENT ANALYSIS OF THE
INITIATION OF FIBER MICROBUCKLING IN NOTCHED
COMPOSITE LAMINATES Final Report (Texas A&M
Univ.) 340 p

N91-13756

unclass
0314742

CSCL 20K G3/39



ACKNOWLEDGMENTS

The author acknowledges with gratitude the assistance and contributions of the following people:

- NASA Langley Research Center, Hampton, Virginia for their generous financial and mentor-type support of this project under grant number NAG-1-659, and in particular, the many helpful discussions with the project monitors, Dr. John D. Whitcomb and Dr. Charles E. Harris, and his associates;
- Fiberite Corporation — An ICI Company, Tempe, Arizona particularly Mr. David Leach, for their generous financial and material support for this research project;
- Hercules, Inc., Magna, Utah for supplying the non-surface treated AS4 fibers for one phase of this research project;
- Quadrax Corporation, Providence, Rhode Island, particularly Mr. Gary Mull and Mr. Andrew MacGowan, for supplying the Interlaced APC-2 material for one phase of this research project.



TABLE OF CONTENTS

	Page
ABSTRACT	ii
ACKNOWLEDGMENTS	iv
TABLE OF CONTENTS	v
LIST OF TABLES	x
LIST OF FIGURES	xi
NOMENCLATURE	xxi
CHAPTER	
I INTRODUCTION	1
Objectives and Scope	3

TABLE OF CONTENTS (Continued)

CHAPTER	Page
II REVIEW OF LITERATURE	6
Compression Test Methods	6
Compressive Failure Modes	10
Shear and Extension Modes of Fiber Microbuckling	10
Fiber Shear	12
End Crushing	12
Longitudinal Splitting	13
Delamination	13
Euler Buckling	14
Compressive Failure Models	14
Shear and Extension Modes of Fiber Microbuckling	15
Fiber Shear	56
Longitudinal Splitting	58
Micromechanics & Damage Approaches to Compression Strength	65
Euler Buckling	66
Related Studies	69
Microbuckling and Kinking	72
Effects of Resin Properties on Compressive Strength of Composite Materials	86
Effects of Fiber Properties on Compressive Strength of Composite Materials	94
Mechanical Properties of Fibers	94
Fiber Volume Fraction	98
Fiber Waviness	104
Effects of Interfacial Bonding on Compressive Strength of Composite Materials	109
Environmental Effects on Compressive Strength of Composite Materials	114

TABLE OF CONTENTS (Continued)

CHAPTER	Page
III	EXPERIMENTAL PROCEDURES 119
	Materials 119
	Methods 125
	Compression Specimen Geometry 127
	Compression Test Methods 127
	Examination of Fiber Microbuckling Damage . . . 139
	Damage Progression Investigation 139
	X-radiography 140
	Scanning Electron Microscopy 140
	Material Property Characterization 141
IV	FINITE ELEMENT ANALYSIS 153
	Theory 153
	The Straight Fiber Problem 153
	The Wavy Fiber Problem 155
	Model Geometries 155
	The Straight Fiber Problem 156
	The Wavy Fiber Problem 159
	Implementation 160
	ABAQUS Procedures 164
	Constituent Properties 165
	Convergence Studies 171
	Model Details 172
	The Straight Fiber Problem 172
	The Wavy Fiber Problem 173

TABLE OF CONTENTS (Continued)

CHAPTER		Page
V	EXPERIMENTAL RESULTS	176
	Material Property Characterization	176
	Lamina Shear Constitutive Behavior	176
	Initial Fiber Waviness	182
	Fiber/Matrix Interfacial Bond Strength	186
	Delamination Fracture Toughness	189
	Damage Progression Investigation	207
	Effects of Supporting Ply Orientation	215
	Effects of Initial Fiber Waviness	227
	Effects of Interfacial Bond Strength	229
	Effects of Resin-Rich Regions Between Plies	236
	Microbuckling Failures at 132°C	240
	Comments on Fiber Microbuckling Initiation	243
VI	FINITE ELEMENT RESULTS	245
	The Straight Fiber Problem	245
	Case 1S	245
	Case 2S	245
	Case 3S	247
	Case 4S	247
	Case 5S	247
	The Wavy Fiber Problem	247
	Effects of Matrix Constitutive Behavior	248
	Effects of Initial Fiber Curvature	261
	Effects of Interfacial Bond Strength	266
	Effects of Free Surface	272
	Effects of Fiber Constitutive Properties	274

TABLE OF CONTENTS (Continued)

CHAPTER		Page
VII	DISCUSSION	280
	Experimental Results	280
	Material Property Characterization	280
	Initiation of Fiber Microbuckling	282
	Finite Element Results	291
	The Straight Fiber Problem	291
	The Wavy Fiber Problem	292
	A Comparison of Experimental and Finite Element Results	295
VIII	CONCLUSIONS AND RECOMMENDATIONS	298
	Conclusions	298
	Recommendations for Future Work	300
	Experimental	300
	Finite Element Analysis	300
	Future Project	301
	REFERENCES	302
	VITA	317

LIST OF TABLES

Table	Page
I. Composite Laminate Material Test Matrix.	122
II. Effects of Supporting Fiber Orientation.	123
III. Effects of Initial Ply Waviness.	124
IV. Effects of Resin-Rich Regions.	126
V. Mechanical Properties 21°C of Constituent Properties. ¹³⁷	142
VI. Laminate Engineering Constants (21°C).	143
VII. Ramberg-Osgood Parameters for Resin Nonlinear Constitutive Behavior.	169
VIII. Measured and Assumed Mechanical Properties of Constituent Materials.	170
IX. Interfacial Strength and Fracture Toughness Data.	190
X. Strain Concentration Factors (21°C).	218
XI. Critical Buckling Strains for the Straight Fiber Problem.	246
XII. Fiber Microbuckling Initiation Strains for the Wavy Fiber Problem.	249

LIST OF FIGURES

Figure	Page
1. Failure modes and model of a unidirectional composite subjected to a longitudinal compressive load.	
a) Longitudinal splitting due to secondary transverse tensile stresses.	
b) Fiber microbuckling out-of-phase (extension mode).	
c) Fiber microbuckling in-phase (shear mode). ²⁴	
d) In-phase fiber microbuckling, including the localized shearing stresses induced by cutouts or discontinuities. ⁶⁰	11
2. Test-theory correlation by Greszczuk ²⁶ for compressive strength of composites.	
a) Comparison of reinforcement and microbuckling failures.	
b) Effect of resin shear modulus on microbuckling strength.	
c) Comparison of reinforcement and microbuckling failures.	
d) Effect of initial deformations on microbuckling strength.	28
3. Schematical representation of Eqns. 16 and 18, ⁶¹ the relation between the nominal compressive stress of the composite material and the shearing strain of the matrix.	35
4. Kurashige's results for unidirectional composites. ⁶³	
a) Dependence of compressive strength on buckling wavelength.	
b) Dependence of compressive strength on fiber volume fraction for shear mode fiber microbuckling.	39
5. Composite compressive strength as a function of the minimum radius of curvature for glass fibers in a polyester resin. ⁵⁷	42
6. Comparison of measured and predicted values of apparent shear modulus as a function of axial compressive stress for unidirectional boron/epoxy composites. ⁶⁷	44
7. A hypothetical shear stress versus shear strain curve for a graphite/epoxy unidirectional composite, suggested by Wang. ^{68,69}	47
8. A hypothetical compression strength, σ_c , as a function of lateral fiber deflection, $f(\sigma_c)$, suggested by Wang. ^{68,69}	48
9. Compressive strength as a function of ply orientation for $[\pm\theta]_s$ -class AS4/3502 laminates. ⁷³	51

LIST OF FIGURES (Continued)

Figure	Page
10. Typical analytical and experimental results for a graphite/epoxy [(0/90) ₆] _s laminate. ⁷² a) X-radiographs. b) Load-displacement curves. c) Illustration of specimen damage.	53
11. Predicted and experimental values of longitudinal compressive strength, theories of Rosen (Eqns. 1 and 3) and Broutman(Eqn. 4). ²⁴	61
12. Stresses involved in the longitudinal splitting failure of a composite with curved fibers, developed by Piggott. ⁵⁸	63
13. Dimensionless plot, developed by Piggott, ⁵⁸ for composite compressive strength when controlled by transverse splitting and transverse matrix compression failure.	64
14. Schematics describing kink bands. ⁹⁸ a) Simple kink. b) Conjugate kink, type 1. c) Conjugate kink, type 2. d) Notation for a simple kink, in-plane and out-of-plane.	74
15. Kink orientation relationship as a function of post-failure deformation, Δl . ⁹⁸	75
16. Estimated kink-band inclinations. ⁸⁷ a) $\frac{E_T}{G} = 2$. b) $\frac{E_T}{G} = 4$	85
17. Effect of resin tensile modulus on composite tensile and compressive strengths. ²³	87
18. Effect of resin tensile modulus on compressive modulus and strength of T300 and T700 composites. ²³	88

LIST OF FIGURES (Continued)

Figure	Page
19. Compression strength as a function of fiber volume fraction. ⁴⁷ a) Experimental data. b) Comparison of fiber buckling theory and experimental data for two epoxy composites. c) Comparison of fiber buckling and interfacial debonding failure theories.	100
20. The effects of fiber volume fraction on compressive strength and modulus. ⁵⁷ a) Compressive strength as a function of fiber volume fraction for various fibers embedded in a polyester resin. b) Compressive modulus as a function of fiber volume fraction for various fibers embedded in a polyester resin.	102
21. Variation of compression strength as a function of fiber volume fraction. ⁸²	103
22. Compressive strength of composites obtained from IITRI and RAE test fixtures. ⁸⁸	105
23. Test-theory comparison of compressive microbuckling strength of circular fiber-reinforced composites having various fiber volume fractions. ⁵³	106
24. Variation of composite compressive strength with fiber volume fraction for good interfacial bonding ($k = 1$) and for poor interfacial bonding ($k = 0$). ⁴⁸	111
25. Effect of interfacial bonding on the compressive strength of glass/polyester composites. ⁵⁷	113
26. Environmental effects on the unidirectional compressive strength of CFRP. ¹³³ a) Experimentally determined variation of compressive strength with temperature. b) Expected variation of compressive strength with temperature-humidity exposure.	116

LIST OF FIGURES (Continued)

Figure	Page
27. Schematic of compression specimen.	128
28. Compression test facilities.	
a) Overview of MTS test stand, controller, and data acquisition.	
b) Close-up showing gripped specimen, stereomicroscope in the background, and video image of notch edge.	
c) Surface view of edge-notched specimen with strain gages, gripped in MTS test stand.	
d) Edge view of specimen with strain gages.	131
29. High temperature compression test facilities.	
a) Overview of MTS test stand, controller, and data acquisition.	
b) Close-up showing gripped specimen, stereomicroscope in the background, video image of notch edge, and the heat gun.	
c) Surface view of edge-notched specimen with strain gages, gripped in MTS test stand.	
d) Edge view of specimen with strain gages.	134
30. Resin shim casting fixture.	137
31. Fracture toughness test configurations.	
a) Mode I.	
b) Mode II.	150
32. Models for straight fiber problem.	
a) Infinite model.	
b) Semi-infinite model.	
c) Finite, ten fiber/matrix model.	157
33. Unit cell used for infinite array of fibers and matrix, for straight and wavy fiber models. Geometry shown with initial curvature, $\frac{a_0}{L}$	158
34. Flow chart of PATRAN and ABAQUS processes.	161
35. Nodes, integrations points, and local coordinates for S8R5 ¹⁶⁴ and CPS8R ¹⁶⁴ elements.	162
36. Equivalent stress-strain behaviors (used in FEA) of the PEEK resin.	166
37. Shear constitutive behaviors of APC-2 as a function of temperature.	177

LIST OF FIGURES (Continued)

Figure	Page
38. Dye-penetrant enhanced radiographs of a tension-loaded $[\pm 45]_{2s}$ specimen. a) Virgin specimen, prior to loading. b) Applied axial strain level is 2%. c) Applied axial strain level is 8%.	179
39. Dye-penetrant enhanced radiograph of a compression-loaded $[\pm 45]_{8s}$ specimen. Applied axial strain level is 9.7%.	181
40. Shear constitutive behaviors of PEEK resin as a function of temperature.	183
41. Cross-sections of laminates for initial fiber waviness studies. a) APC-2 tape laminates, $[\pm 45/0/90]_{3s}$. b) Quadrax 8-harness, $[\pm 45/\langle 0/90 \rangle]_{3s}$. c) Quadrax 1-harness, $[\pm 45/\langle 0/90 \rangle]_{3s}$	185
42. Representative in-plane fiber waviness in $[0_{24}]$ APC-2 laminates.	188
43. Resin deformation near fracture crack tips. a) Mode I, APC-2. b) Mode I, AU4U/PEEK. c) Mode II, APC-2. d) Mode II, AU4U/PEEK.	192
44. Mode I load-displacement data for $[0_{24}]$ laminates.	194
45. G_I versus crack length for $[0_{24}]$ DCB specimens.	195
46. Micrographs of Mode I DCB fracture surfaces. a) Overview of APC-2 fracture surface. b) APC-2 fiber/matrix interface. c) Overview of AU4U/PEEK fracture surface. d) AU4U/PEEK fiber/matrix interface.	197

LIST OF FIGURES (Continued)

Figure	Page
47. Cross-sections perpendicular to DCB specimen length to show crack fracture path. a) Specimen OG5, APC-2. b) Specimen OG5, APC-2. c) Specimen OG3, APC-2. d) Specimen OP4, AU4U/PEEK.	200
48. Mode II load-displacement data for $[0_{24}]$ laminates.	202
49. G_{II} versus normalized crack length for $[0_{24}]$ ELS specimens.	204
50. Micrographs of Mode II ELS fracture surfaces. a) Overview of APC-2 fracture surface. b) APC-2 fiber/matrix interface. c) Overview of AU4U/PEEK fracture surface. d) AU4U/PEEK fiber/matrix interface.	206
51. Cross-sections perpendicular to ELS specimen length to show crack fracture path. a) APC-2. b) AU4U/PEEK.	209
52. Damage progression in a 0° ply. a) Initial state. b) Increment 3, 2.0% local strain. c) Increment 4, 2.5% local strain.	212
53. Damage progression for an initially damaged 0° fiber. a) Initial state. b) Increment 1, 1.0% local strain. c) Increment 2, 1.5% local strain. d) Increment 4, 2.5% local strain.	214
54. Bar chart showing the effects of supporting ply orientation on fiber microbuckling initiation strains in laminates <i>A</i> , <i>B</i> , <i>C</i> , <i>D</i> , and <i>E</i> , tested at 21°C and 77°C	216



LIST OF FIGURES (Continued)

Figure	Page
55. Bar chart showing the effects of supporting ply orientation on local fiber microbuckling initiation strains in laminates <i>A</i> , <i>B</i> , <i>C</i> , <i>D</i> , and <i>E</i> , tested at 21°C and 77°C.	219
56. Bar chart showing the free surface effects on fiber microbuckling initiation strains in laminates <i>A</i> and <i>B</i> , tested at 21°C and 77°C.	221
57. Representative in- and out-of-plane fiber microbuckling damage in APC-2 laminates. a) $[(\pm 45/0_2)_3/\pm 45/0]_s$, 21°C, notch view. b) $[(0_2/\pm 45)_3/0/\pm 45]_s$, 21°C, notch view. c) $[(0_2/\pm 45)_3/0/\pm 45]_s$, 77°C, surface view. d) $[(0_2/\pm 45)_3/0/\pm 45]_s$, 77°C, notch view.	224
58. Representative in-plane fiber microbuckling damage in APC-2 laminates. a) Shearing deformation in matrix, 21°C. b) In-plane fiber microbuckling in interior 0° ply, 77°C. c) Matrix drawing between fibers, 77°C. d) Matrix drawing between fibers, 77°C.	226
59. Bar chart showing the effects of ply waviness on fiber microbuckling initiation strains in laminates <i>K</i> , <i>KQ8</i> , and <i>KQ1</i> , tested at 21°C and 77°C.	228
60. Representative in-plane fiber microbuckling damage at 21°C, notch view. a) APC-2 tape laminate, $[\pm 45/0/90]_{3s}$. b) Quadrax laminate, 1-harness, $[\pm 45/(0/90)]_{3s}$. c) Quadrax laminate, 8-harness, $[\pm 45/(0/90)]_{3s}$. d) Quadrax laminate, 8-harness, $[\pm 45/(0/90)]_{3s}$	231
61. Bar chart showing the effects of the interfacial bond on fiber microbuckling initiation strains.	233

LIST OF FIGURES (Continued)

Figure	Page
62. Fiber microbuckling in the experimental AU4U/PEEK material, $[(\pm 45/0_2)_3/\pm 45/0]_s$. All views are from the notch center. a) 21°C. b) 21°C. c) 77°C. d) 77°C.	235
63. Bar chart showing the effect of resin-rich regions on fiber microbuckling initiation strains in laminates <i>A</i> , <i>G</i> , and <i>H</i> , tested at 21°C, 77°C, and 132°C.	237
64. Notch view of in-plane fiber microbuckling in APC-2 laminates with resin-rich regions. a) Specimen cross-section, $[(\pm 45/f/0_2/f)_3/\pm 45/f/0]_s$, 77°C. b) Detail from a. c) Out-of-plane fiber microbuckling into resin-rich region, $[(\pm 45/f_3/0_2/f_3)_3/\pm 45/f_3/0]_s$, 21°C.	239
65. Failures in APC-2 laminates tested at 132°C, $[(\pm 45/0_2)_3/\pm 45/0]_s$. a) Overview. b) Detail from a. c) Fiber/matrix interfacial bond and matrix deformation. d) Fiber/matrix interfacial bond and matrix deformation.	242
66. Global stress-strain response of infinite series for four matrix constitutive behaviors with $\frac{a_o}{L} = 0.0050$	250
67. Local shear strain versus global applied strain of infinite series for four matrix constitutive behaviors with $\frac{a_o}{L} = 0.0050$	252
68. Fringe plot of axial strain, ϵ_{xx} , distribution. Global applied strain is 2692 $\mu\epsilon$. Nonlinear matrix, 21°C; $\frac{a_o}{L} = 0.0050$	254
69. Fringe plot of transverse strain, ϵ_{yy} , distribution. Global applied strain is 2692 $\mu\epsilon$. Nonlinear matrix, 21°C; $\frac{a_o}{L} = 0.0050$	255
70. Fringe plot of engineering shear strain, γ_{xy} , distribution. Global applied strain is 2692 $\mu\epsilon$. Nonlinear matrix, 21°C; $\frac{a_o}{L} = 0.0050$	256

LIST OF FIGURES (Continued)

Figure	Page
71. Distribution of strain energy along the matrix. Global applied strain is 2692 $\mu\epsilon$. Nonlinear matrix, 21°C; $\frac{a_o}{L} = 0.0050$	258
72. Distribution of strain energy along the fiber. Same for all levels of applied strain. Nonlinear matrix, 21°C; $\frac{a_o}{L} = 0.0050$	259
73. Distribution of strain energy along the matrix. Global applied strain is 16392 $\mu\epsilon$. Nonlinear matrix, 21°C; $\frac{a_o}{L} = 0.0050$	260
74. Global stress-strain response of semi-infinite plate. Nonlinear matrix, 21°C; $\frac{a_o}{L} = 0.0050$	262
75. Global stress-strain response of infinite series for four initial fiber curvatures. Nonlinear matrix, 21°C.	264
76. Local shear strain versus global applied strain of infinite series for four initial fiber curvatures. Nonlinear matrix, 21°C.	265
77. Global stress-strain response of infinite series for 2 locations debonded 10.7%. Nonlinear matrix, 21°C; $\frac{a_o}{L} = 0.0050$	267
78. Fringe plot of engineering shear strain, γ_{xy} , distribution with 10.7% debond at symmetry line (Case D1). Global applied strain is 2692 $\mu\epsilon$. Nonlinear matrix, 21°C; $\frac{a_o}{L} = 0.0050$	268
79. Fringe plot of engineering shear strain, γ_{xy} , distribution with 10.7% debond in region of maximum shear (Case D2). Global applied strain is 2662 $\mu\epsilon$. Nonlinear matrix, 21°C; $\frac{a_o}{L} = 0.0050$	269
80. Global stress-strain response for infinite series for 3 debond lengths along the region of maximum shear. Nonlinear matrix, 21°C; $\frac{a_o}{L} = 0.0050$	271
81. Local shear strain versus global applied strain for infinite series (Case 2C) and semi-infinite plate. Nonlinear matrix, 21°C; $\frac{a_o}{L} = 0.0050$	273
82. Deformed shape of semi-infinite model. Applied strain is 16715 $\mu\epsilon$, prior to fiber microbuckling initiation. Nonlinear matrix, 21°C; $\frac{a_o}{L} = 0.0050$	275

LIST OF FIGURES (Continued)

Figure	Page
83. Deformed shape of semi-infinite model. Applied strain is $39462 \mu\epsilon$, at fiber microbuckling initiation. Nonlinear matrix, 21°C ; $\frac{a_0}{L} = 0.0050$	276
84. Global stress-strain response of infinite series for two isotropic fiber constitutive behaviors. Nonlinear matrix, 21°C ; $\frac{a_0}{L} = 0.0050$	277
85. Local shear strain versus global applied strain of infinite series for two isotropic fiber constitutive behaviors. Nonlinear matrix, 21°C ; $\frac{a_0}{L} = 0.0050$	279
86. Schematic of variation in ϵ_I as a function of temperature for failure by exceeding the matrix yield strain or the fiber/matrix interfacial bond strength.	286
87. Schematic of ϵ_I as a function of temperature for laminates with built-in resin-rich regions.	288
88. Failure strain of T300/5208 [$\pm 45/0_2 / \pm 45/0_2 / \pm 45/0/90$] $_2$, laminates as a function of hole size. ¹¹² Laminates contain center holes.	290

NOMENCLATURE

a	Hole diameter, mm
a_o	Initial amplitude of fiber waviness
$\frac{a_o}{L}$	Waviness ratio
DCB	Double Cantilever Beam
d_f	Fiber diameter, $\mu\epsilon$
ELS	End-Loaded Split Laminate
E_k	Young's modulus: $k = 1, 2$ for lamina properties; $k = x, y$ for laminate properties; $k = cy$ for measured compression modulus
G_k	Shear modulus: $k = 12$ for lamina properties; $k = xy$ for laminate properties
G_I	Mode I steady-state strain energy release rate, J/m^2
G_{II}	Mode II steady-state strain energy release rate, J/m^2
IFSS	Interfacial Shear Strength, MPa
ITS	Interfacial Testing System
L	Wavelength of initial fiber waviness
LID	Laminate Identification letters
MTS	Material Test System
NDE	Nondestructive Examination
S	Sample standard deviation
s	Axis following the wavy fiber contour
SCF	Stress Concentration Factor
SEM	Scanning Electron Microscope

w	Specimen width, mm
x, y, z	Global coordinate axes
ϵ_{xx}	Applied strain, $\mu\epsilon$
ϵ_{cr}	Critical buckling strain for straight fiber, $\mu\epsilon$
ϵ_I	Global or remote fiber microbuckling initiation strain, $\mu\epsilon$
γ_k	Shear strain: $k = m$ for matrix; $k = 1, 2$ for composite lamina
γ_{ym}	Matrix shear yield strain, associated with the yield point on the τ_m - γ_m curve, $\mu\epsilon$
σ_{xx}	Applied stress, MPa
τ_k	Shear stress: $k = m$ for matrix; $k = 1, 2$ for composite lamina
ν_k	Poisson's ratio: $k = 12$ for lamina properties; $k = xy$ for laminate properties; $k = cxy$ for compression loading

CHAPTER I

INTRODUCTION

The high strength-to-weight ratio of composite materials is ideally suited for aerospace applications where they are already used in commercial and military aircraft secondary structures and will soon be used for heavily loaded primary structures. One problem impeding the widespread application of composites, particularly thermoplastic composites, is their inherent weakness in compressive strength when compared to the tensile properties of the same material. This result is not surprising, given that the composite's tensile and compression strength comes primarily from long narrow fibers. The effective strength of these fibers in compression is generally much lower than their strength in tension due to fiber microbuckling which leads to additional local fiber buckling and/or shear crippling, delamination, loss of structural stiffness, and macroscopic compressive failure. Nevertheless, it is desirable to develop composite systems with the smallest penalty in compressive strength possible.

Previous work¹⁻⁴ on tough matrix composite laminates containing center holes indicates that the compressive failure of these composites initiates with microbuckling of the 0° fibers toward an unsupported surface in 0° plies either in-plane for interior 0° plies or out-of-plane for surface 0° plies. Compressive failure in the laminates which did not contain surface 0° s initiated with in-plane fiber microbuckling into the center hole. Growth of this initial damage to a critical size at which catastrophic failure occurs required little additional load. This result suggests that the compression strength is controlled by initiation of fiber microbuckling, particularly for the PEEK system of that investigation. The in-

Journal model is *AIAA Journal of Aircraft*.

and out-of-plane fiber microbuckling appears to precede shear crippling damage in the systems studied in Refs. 1-4. Furthermore, the fiber microbuckling and shear crippling often lead to local delamination when the local strain necessary to accommodate the large localized interlaminar shear strains exceeds the resin ductility of the matrix. These local delaminations apparently do not propagate (to become macroscopic delaminations) immediately in composites made with tougher resins. Eventually, final compressive failure occurs when large scale brooming and/or generalized delamination.

The significant role of local constraints on the initiation of fiber microbuckling was also indicated in Refs. 1-4. For example, when $\pm 45^\circ$ fibers were used as surface plies, in-plane fiber microbuckling appeared to initiate at a strain level which is much higher than the initiation strain when the 0° fibers were the surface plies and the microbuckling was out-of-plane. These results indicate that one reason most compression strength models overpredict the actual compression strengths observed in experiments is that they make no allowance for free surface effects, i.e. these models implicitly assume infinitely large laminates. It should be noted that the term "fiber microbuckling" used in the literature and throughout this dissertation, refers to large lateral deflections of initially wavy fibers leading to fiber breakage, rather than a bifurcation instability.

Many theories have been proposed and developed to predict the compressive strength of unidirectional composite laminates. However, few similar investigations have been conducted for multidirectional composite laminates, even though these laminates are more widely used than unidirectional laminates in composite structural components. Furthermore, an uncertainty in the modes and mechanisms of compression failures in composites remains because of the lack of a clear under-

standing of all possible modes of failure. In order to more accurately predict the compressive strength of composite laminates, the strain level at which fiber microbuckling initiates must be determined. Additionally, the factors that affect this strain level must be studied systematically. Accurate evaluation of this strain level is important because this process appears to control the strength of ductile composite systems.

Objectives and Scope

The primary objectives of this dissertation research have been to develop a better understanding of the factors that affect the semi-circular edge-notched compressive strength and to identify the associated failure mode(s) of thermoplastic composite laminates with multidirectional stacking sequences.

The experimental observations¹⁻⁴ and the detailed literature review (presented in Chapter II of this dissertation) suggest at least four factors that affect the determination of the strain levels at which fiber microbuckling initiates and thus, partially control the composite's compression strength. These factors are listed as follows:

- (i) the degree of initial fiber waviness,
- (ii) the fiber/matrix interfacial bond strength,
- (iii) the effects of the free surfaces, and
- (iv) the nonlinear shear constitutive behavior for the composite laminate.

Throughout this dissertation, waviness and curvature are used interchangeably when discussing the fiber shape.

Two additional independent variables that are also important in the determination of the strain level at which either in- and/or out-of-plane fiber microbuckling

initiates are listed below:

- (v) the orientation of the supporting plies adjacent to the 0° plies through the thickness of a laminate and
- (vi) the thickness of the resin-rich region between plies.

In this dissertation research, specimens containing two semi-circular edge notches (on opposite free edges) are loaded in compression at a relatively slow rate to provide more stable development of fiber microbuckling damage. During loading, the initiation of in- and out-of-plane fiber microbuckling is monitored. Most specimens are interrupted at the first indication of fiber microbuckling and subsequently examined in the scanning electron microscope (SEM). The nominal strain associated with the initiation of fiber microbuckling is measured. Then, the measured nominal initiation strain is used in conjunction with two-dimensional finite element analysis (ABAQUS) to determine the local strain at the notch. This experimental program is used to provide a systematic understanding of the relative significance of the six variables (previously mentioned) on the initiation of fiber microbuckling, the compression strength limiting step of thermoplastic composites. Additionally, it provided valuable details about the fiber microbuckling process and associated damage development.

Geometric and material nonlinear two-dimensional finite element analysis (implementing ABAQUS) is used to model the initiation of fiber microbuckling of both the ideal straight fiber and the more realistic initially wavy fiber. The models with the straight fibers consider the effects of finite size, free surface, fiber constitutive properties, and provide an upper limit for the fiber microbuckling initiation strain levels. Wavy fiber models are used to investigate the effects of matrix constitutive behavior, initial fiber curvature, fiber/matrix interfacial bond

strength, free surface, and fiber constitutive properties on fiber microbuckling initiation strain levels.

Following this brief introduction, this dissertation contains an extensive review of the relevant literature in Chapter II. Details of the materials used and the experimental procedures are presented in Chapter III. The finite element analysis models and procedures are detailed in Chapter IV. Chapters V and VI contain summaries of the experimental and finite element results, respectively. A discussion of the experimental and finite element results is presented in Chapter VII. Finally, the conclusions from this investigation and recommendations for future work are summarized in Chapter VIII.

CHAPTER II

REVIEW OF LITERATURE

This chapter reviews the literature pertaining to the compression strength of composite materials. This review covers compression test methods, failure modes, existing failure models, and microbuckling and kinking. Additionally, the effects of each of the resin, fiber, interfacial bond, environment and initial fiber curvature on compressive strength of composite materials are reviewed. Papers encompassing the areas of delamination/inherent flaws and damage tolerance (compression after impact studies) are omitted from this review since they are not directly related to the research herein. For simplicity, the equations and figures cited in this chapter follow the nomenclature and units used in the corresponding reference. Additionally, the nomenclature used is explained with each reference and is considered independent of the list of nomenclature in this dissertation. This nomenclature list pertains only to the research herein.

Compression Test Methods

Because of the inhomogeneity of graphite/polymeric composites, the mechanical properties measured are more sensitive to testing equipment and procedures than are those properties for isotropic, homogeneous materials. A brief overview of compression test methods, fixtures, and specimens is given in Ref. 5. Leonard⁵ summarized results indicating that more than one test method may be valid, depending on the type of failure being tested. Reliable compressive properties are the most difficult of all mechanical properties to acquire because of the sensitivity of compression tests to a range of factors, including test methods, quality of material, and uneven loading of specimens.⁶ However, accurate prediction of the compression

strength is important because this mechanical property is typically the most critical and most susceptible to cyclic loading and environmental degradation.⁶ The most common compressive test methods are reviewed within this section.

Three American Society for Testing and Materials (ASTM) approved standard test procedures for compression tests of composite materials include Test for Compressive Properties of Rigid Plastics (D695 – 85),⁷ Test for Compressive Properties of Oriented Fiber Composites (D3410 – 75),⁸ and Flexure Test of Flat Sandwich Constructions (C393 – 62).⁹ Recently, these standard test methods have been combined into one standard, Test Method for Compressive Properties of Unidirectional or Crossply Fiber-Resin Composites (D3410 – 87).¹⁰

Compression test methods currently in use are generally of three types: the sandwich beam compression test method, the unsupported compression coupon test methods, and the supported compression coupon test methods. The sandwich beam compression test method was evaluated by Shuart.¹¹ The ASTM approved sandwich beam test method is C393 – 62.⁹ The sandwich construction used in this test method is typical of many composite applications, but the beam is criticized because of its fabrication cost and the undetermined influence of the honeycomb core on the mechanical properties of the composite. Shuart's results indicate that the sandwich beam in four-point bending is a viable compression test method. However, laminate orientation, test temperature, and type of honeycomb core material were shown to affect the type of beam failure.

Many fixtures have been developed and employed to test specimens with an unsupported gage length. The standard tests are ASTM D3410-87, Procedures A and B.¹⁰ The most widely used fixture of this type is the Illinois Institute of Technology Research Institute (IITRI) wedge-grip compression test fixture. This

fixture was developed by Hofer and Rao¹² to incorporate the better features of earlier fixtures and also eliminate many of their problems. This fixture incorporates trapezoidal wedge grips which eliminate the problems of slippage and wall friction in the Celanese test methods (ASTM D3410-87, Procedure A). The upper and lower grips are linked together with precision shafts and linear bearings to insure alignment. Additionally, the fixture is adaptable to elevated temperature tests.¹³ The major disadvantage of this test fixture is that the specimen gage length (12.7 mm) is very short and the failure mechanisms are thus difficult to observe. Woolstencroft, Curtis, and Haresceugh¹⁴ compared test techniques to evaluate the unidirectional compression strength of carbon fiber-reinforced plastic (CFRP). They compared five test techniques, all of which had an unsupported gage length. Their results indicate that the Royal Aircraft Establishment (RAE) specimen was the optimum configuration. This specimen has a tapered gage thickness with the specimen ends mounted in relatively large blocks of aluminum alloy. This specimen gives a failure level indicative of the unidirectional compressive strength (based on results from finite element analysis) and does not have an induced secondary stress state through the thickness of the gage section.

Gurdal and Starbuck¹⁵ developed a new compression test fixture to incorporate the useful features of existing fixtures. The new fixture uses an end-loaded coupon supported by four circular support pins, rather than plates, to prevent out-of-plane displacement of the specimen. Additional benefits include a reduction of the stress concentration due to Poisson's contraction at the grips and better defined boundary conditions. A combination of experimental data and finite element analysis indicates that the fixture and test coupons are adequate for the determination of Young's moduli in the principal material directions by using specimens with 0° and 90° fiber

orientations. However, the determination of Poisson's ratio requires the analysis of the specimen to include the effects of the end constraints.

Adsit¹⁶ evaluated four techniques, an effort undertaken by the ASTM Committee D-30 on High-Modulus Fibers and Their Composites. The test methods were the ASTM D695-85, the Celanese (D3410-75), the IITRI, and the sandwich beam. The first of these techniques introduces load into the specimen by end-loading while in the other techniques, the specimens are shear-action loaded. His results indicate that end-loading (D695-85) unidirectional specimens leads to lower compressive strengths than the other methods. This result occurs because the fibers are not exactly the same length, a consequence of machining the specimen ends. It should also be noted that the Celanese, IITRI, and sandwich beam methods all gave similar results and that the modulus of elasticity was not a function of the loading method.

The supported compression test methods include those procedures in which the coupon specimen is fully supported in the gage section to prevent Euler buckling, end brooming, and splitting during loading. Typically, the gage section for these tests is ten to twenty times the length of the unsupported gage sections. Ryder and Black¹⁷ present a good description of these test fixtures. A more recently developed design used in the aircraft industry is the Boeing fixture.¹⁸ In Ref. 17 the specimens were gripped on one end and pressed against a bearing plate on the other, but they can be gripped on both ends. This test procedure follows the ASTM Standard D695-85 in Ref. 7.

Compression test methods have been reviewed by many investigators (Refs. 5, 6, 11, 12, 14, 16, 19, 20). This brief review in addition to a more detailed survey of compression techniques^{5,6,14,20} indicates that one specific technique is not sufficient

to determine compression strength; each of the methods described have certain advantages and other disadvantages. However, each of the three basic techniques provide consistent results for specific cases. The results presented in Refs. 6, 16, and 21 indicate the specimens should be end-loaded with some shear loading induced through the gripped specimen ends. Additionally, the specimen ends should be tabbed. Tabs help prevent longitudinal splitting and crushing of the specimen ends.²¹ However, the tab surfaces must be carefully machined flat and parallel, relative to each other, to achieve the best possible specimen alignment and thus, strain uniformity across the specimen, as shown in Ref. 6.

Rehfield et al²² developed a closed-form solution to predict the stress field at the laminate-tab interface in unidirectional composite specimens. Reasonable results (compared to finite element analysis) were presented for two end-loaded unidirectional composite material systems.

Compressive Failure Modes

The common failure modes observed in composite materials loaded in compression are reviewed in this section. These failure modes include shear and extension modes of fiber microbuckling, fiber shear, end crushing, longitudinal splitting, delamination, and Euler buckling. It should be noted that several of these failure modes may occur in the same specimen or component during compressive failure. Additionally, Ref. 23 summarizes the failure modes of the constituent materials.

Shear and Extension Modes of Fiber Microbuckling

Compressive strength may be controlled by fiber microbuckling, as shown in Fig. 1. Such fiber microbuckling will occur either in-phase (shear mode) or out-of-phase (extension mode). In the shear mode, the matrix material is shear deformed;

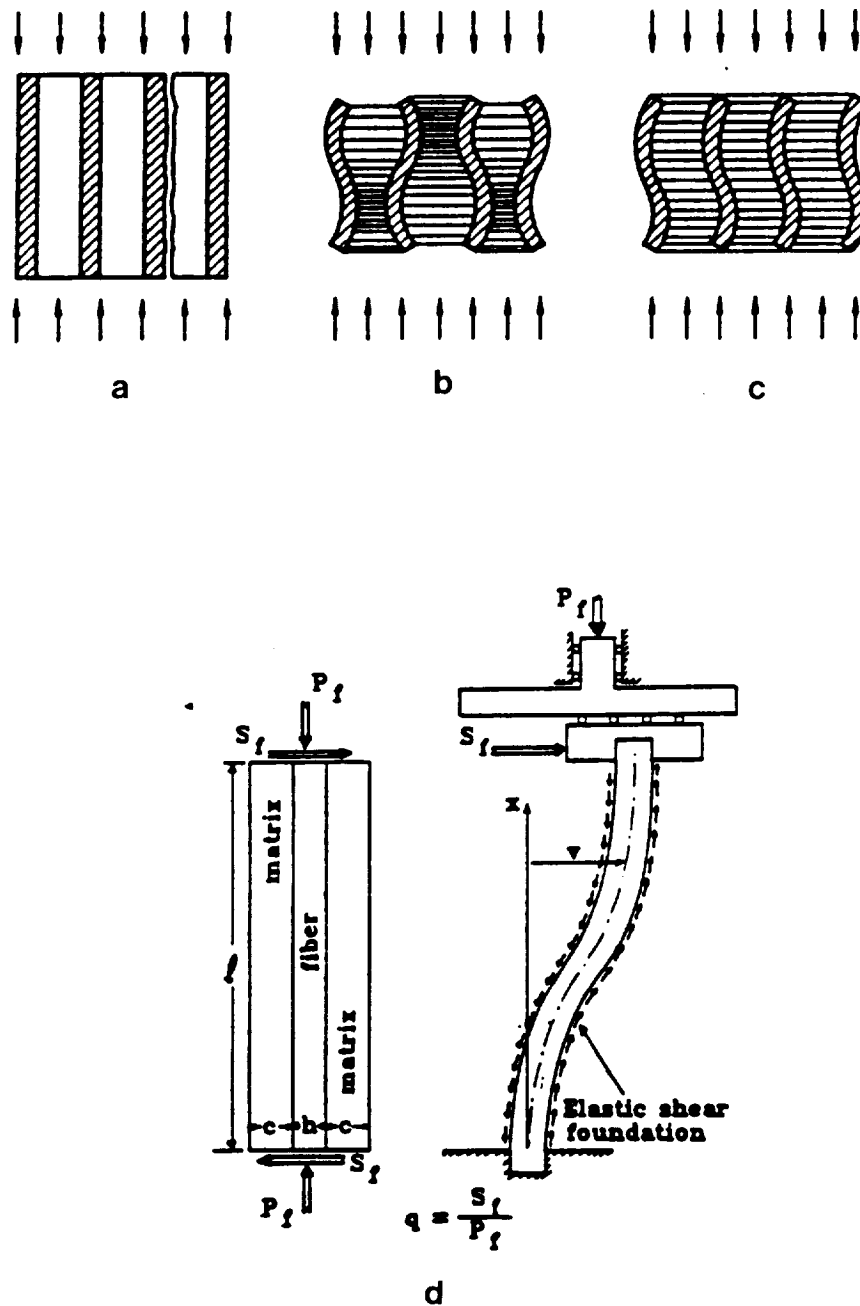


Fig. 1 Failure modes and model of a unidirectional composite subjected to a longitudinal compressive load.

- a) Longitudinal splitting due to secondary transverse tensile stresses.
- b) Fiber microbuckling out-of-phase (extension mode).
- c) Fiber microbuckling in-phase (shear mode).²⁴
- d) In-phase fiber microbuckling, including the localized shearing stresses induced by cutouts or discontinuities.⁶⁰

in the extension mode, the matrix material between the fibers is stretched in the direction perpendicular to the fibers. Fiber microbuckling may be assisted by fiber/matrix debonding due to transverse tensile stresses, a process that leaves the fibers with less support. Furthermore, in-plane microbuckling (contained within a given ply) may lead to delamination between plies. Generally, extension mode microbuckling is observed in composites with a lower fiber volume fraction ($< 20\%$) while shear mode microbuckling is observed in composites with a higher fiber volume fraction.²⁴

Factors that may influence the initiation of fiber microbuckling are the initial fiber curvature, fiber defects, fiber misalignment, yarn twist, voids, and poor fiber/matrix adhesion. It is suspected that fiber microbuckling leads to fiber kinking followed by shear crippling of the composite.

Fiber Shear

A second mechanism of failure observed during compression testing is fiber shear. In this failure mode a sufficiently high compressive stress is applied to the specimen (or component), without inducing macroscopic or microscopic buckling, to induce failure in the fibers by shear deformation. This failure mechanism is usually observed in composites which have a compressive strength similar to their tensile strength. It has been suggested, as reported for example in Ref. 25, that this failure mode constitutes an upper bound in compressive strength.

End Crushing

This compressive failure mode is common in composite specimens, particularly unidirectional composites, that are end-loaded but have insufficient transverse support within the grips. The result is crushing damage at or near the point of

end loading. These failures are a result of local stress concentrations due to end effects and are a function of the compressive test fixture, as reported in Ref. 16. This type of failure was observed in some of the ultimate compression strength tests for multiaxial lay-ups in Ref. 1. The use of tabs^{6,19} and/or greater surface support in the gripped area will help prevent this type of failure during testing.

Longitudinal Splitting

The difference in the Poisson's ratio between the matrix and the fibers leads to differential dilatation (being stretched beyond normal dimensions) during compressive loading. Because the matrix expands more than the fiber when loaded in compression, a tensile stress develops at the interface between the matrix and the fibers. If this stress is sufficiently large, fiber/matrix debonding occurs, leading to failure by longitudinal splitting, a so-called interaction failure. As will be presented in detail later in this review, this failure is more likely to occur in composites made with anisotropic fibers (e.g., graphite or Kevlar) rather than isotropic fibers (e.g., stainless steel or E - glass).²⁶ Longitudinal splitting may also result from the constraint imposed by the grips which prevents the material contained in the grips from the same Poisson expansion (due to compressive loading) as the material in the gage section. This Poisson difference results in transverse tensile stresses in the gage section, adjacent to the grips, and it leads to failure by longitudinal splitting. This failure is most typically observed in unidirectional composites.

Delamination

Compressive loading may lead to a delamination failure mode in multiaxial lay-up composite laminates. Although the failure may initiate by either transverse tension induced longitudinal splitting or fiber microbuckling, these damage modes

can cause local delamination. If the delamination propagates to a critical size, a global failure (by buckling of the sublaminates) occurs. Furthermore, out-of-plane microbuckling causes mode I loading between adjacent plies while in-plane microbuckling causes mode II loading between adjacent plies. In either case, if a critical local strain level is achieved, delamination is initiated. Localized delaminations were observed in Ref. 4. If the applied compression load is sufficiently large, the delamination propagates immediately, resulting in laminate failure by buckling of the sublaminates (formed by the delaminations).

Euler Buckling

Euler buckling is the only mechanism of compressive failure attributed to a macroscopic, elastic instability during compression loading. This type of failure was first analyzed for isotropic materials by Leonhard Euler as a function of the material elastic properties and the specimen geometry, ignoring microstructural details. A large thickness to length ratio in the gage section of test specimens is necessary to avoid this geometrically induced instability and thus measure the actual compressive strength of the material. Otherwise, the measured "compressive strength" is geometry dependent and not a true material property.

Compressive Failure Models

Summary papers describing the numerous compressive failure models appear to be limited. However, a few authors^{23,24,26,27-30} have included detailed reviews of the existing models. Reference 29 is specifically a review of recent (1980 through August 1987) compression research on composite materials including test methods, failure theories and mechanisms, and experimental investigations. Stuart²⁸ includes an

historical and chronological review of proposed compression failure theories applying to the short-wavelength buckling (microbuckling) phenomenon.

In this section, mathematical theories pertaining to the failure modes described in the previous section will be thoroughly reviewed.

Shear and Extension Modes of Fiber Microbuckling

According to many researchers (in particular, Ref. 28), Dow and Gruntfest³¹ first postulated that the compressive failure of unidirectional composites was a result of one of two phenomena: (i) high tensile stresses perpendicular to the loading direction, located at the fiber/matrix interface (so-called transverse tension failure) or (ii) buckling of the fibers within the matrix (so-called microbuckling). An equation to predict the laminate compressive strength at microbuckling was derived using Timoshenko and Gere.³² This equation is based on a model consisting of columns supported by an elastic foundation. An empirical constant was included in this equation. Reference 31 was the first to associate fiber instability with the compressive strength of unidirectional laminates.

Rosen's classic study,³³ also referencing results from Timoshenko and Gere,³² of the compressive failure of unidirectional composite materials focused on fiber instability in glass/epoxy laminates using a two-dimensional model. The fibers were modelled as columns supported by an elastic matrix foundation. This model assumed that the fibers were stiff relative to the matrix and that shear deformations in the fiber could be neglected relative to those in the matrix. Rosen first suggested that compressive failure of a unidirectional composite occurred when the fibers buckled in either of two possible modes, the extension mode (Fig. 1b) or the shear

mode (Fig. 1c). Using an energy formulation, Rosen obtained

$$\sigma_c = 2V_f \left[\frac{V_f E_m E_f}{3(1 - V_f)} \right]^{\frac{1}{2}} \quad (1)$$

for the extension mode and

$$\sigma_c = \frac{G_m}{1 - V_f} + \frac{\pi^2 V_f E_f h^2}{12\lambda^2} \quad (2)$$

for the shear mode where

σ_c = compression strength of the unidirectional composite,

V_f = fiber volume fraction,

E_m = Young's modulus of the matrix,

E_f = Young's modulus of the fiber,

G_m = shear modulus of the matrix

h = fiber diameter, and

λ = half-wavelength of the buckling mode shape.

Since the half-wavelength is much larger than the fiber diameter, i.e. $\lambda \gg h$, the magnitude of the second term in Eqn. 2 is much smaller than the magnitude of the first term. Neglecting the second term, Rosen wrote the approximate, but more familiar, relationship for the shear mode fiber microbuckling as

$$\sigma_c = \frac{G_m}{1 - V_f}. \quad (3)$$

Compressive strength was predicted using the lower value from Eqns. 1 and 3. Equation 3 usually yields the more conservative compressive strength prediction for composite materials. Rosen's results for glass/epoxy showed that for low fiber volume fractions ($\leq 20\%$) the extension mode is the lower stress, while for high volume fractions ($> 20\%$) of fibers the shear mode predominates.



Rosen recognized that Eqn. 3 gave predicted strengths that were two to three times greater than the experimental strengths when the elastic shear modulus of the matrix was used. More realistic strength predictions were obtained when the matrix shear modulus was assumed to vary inelastically as a function of the applied load, from its elastic value at 1% strain to a zero value at 5% strain. It should be noted from Eqn. 3 that fiber microbuckling initiated failures are a function of the matrix shear modulus, the material property which appears to have the most significant effect on composite compressive strength.

Hayashi³⁴ postulated and confirmed the "shear instability mode" of compression buckling. He suggested that this type of failure occurred when the material's flexural rigidity was much larger than its shear rigidity. This concept of shear instability type failure for orthotropic materials is the same that described by Rosen³³ for composite materials. Using minimization of potential energy, Hayashi concluded that shear instability occurs for an arbitrary shear deformation when

$$\sigma_c = G \quad (4)$$

where

σ_c = compressive strength of the material and

G = shear modulus of the material.

Here, the shear modulus is a function of the applied load, and the shear tangent modulus usually decreases with the increase of compressive stress beyond the load level required to give matrix yielding. According to Jones,³⁵ the shear modulus for a unidirectional composite material is calculated as a function of its constituent properties from

$$G_{12} = \frac{G_m}{V_f \frac{G_m}{G_f} + (1 - V_f)} \quad (5)$$



where

G_{12} = in-plane shear modulus of the unidirectional lamina,
also referred to as G_{LT} ,

G_f = shear modulus of the fiber, and

all other variables were defined with Eqn. 2.

Since $G_m \ll G_f$ typically, the first term in the denominator may be neglected. Equation 5 is then approximated by

$$G_{12} = \frac{G_m}{1 - V_f}. \quad (6)$$

Substitution of Eqn. 6 into Eqn. 4 ($G = G_{12}$ for composite materials) yields Eqn. 3, Rosen's approximate equation for shear mode fiber microbuckling.

In a parallel study, Schuerch³⁶ used minimization of potential energy with assumptions similar to Rosen's³³ to also derive Eqns. 1 and 3, independent of Rosen. This analysis does assume that the shear modulus is a function of the applied strain. Schuerch showed good correlation between experiments and theory for boron/magnesium unidirectional composites. He considered these results remarkable, perhaps even fortuitous, considering the relatively crude analysis and limited experimental data.

For the extension mode of microbuckling against a plastic foundation (i.e., elastic-perfectly plastic matrix), Dow, Rosen, and Hashin³⁷ proposed the equation of inelastic buckling to be given by

$$\sigma_c = \left[\frac{V_f E_f \sigma_{ym}}{3(1 - V_f)} \right]^{\frac{1}{2}} \quad (7)$$

where

σ_c = compressive strength of the material,

- E_f = Young's modulus of the fibers,
 V_f = fiber volume fraction, and
 σ_{ym} = yield stress of the matrix.

Foye³⁸ concluded that the instability mode of fiber microbuckling failure appeared to be the most prevalent in compression failures. Foye also proposed a macrostability model that makes no reference to the reinforcement details and, in theory, applies to all orthotropic materials. The model produced the following modified stress-strain law:

$$\tau = (G + \sigma) \gamma \quad (8)$$

where

- τ = shear stress component,
 σ = normal stress component,
 γ = shearing strain, and
 G = minimum longitudinal-transverse shear modulus.

When the direction of the tensile stress is reversed, i.e. compressive, and this stress becomes sufficiently large, the unit element would experience a complete loss of effective shear stiffness at the point where $\sigma_c = G$. Consequently, the element would be susceptible to crippling in a shearing mode as described by Eqn. 4, providing an upper bound for compression strength. Additionally, he uses the Reuss estimate or "stiffness in series" model (equivalent to Eqn. 5, Jones³⁵) to show the upper bound to be the same as Eqn. 3, reported by Rosen. Foye postulated that the measured compression strengths are lower than analytical predictions due to premature failures caused by local imperfections (e.g., variations in fiber volume fraction, fiber waviness, void concentrations, and unbonded areas). Strength predictions were also modified to include void and filler contents.

Sadowski, Pu, and Hussain³⁹ assumed a small volume fraction of fibers so that the mutual interference of fibers is negligible. Consequently, their mathematical model is an infinitely long single wavy fiber surrounded by an infinite matrix. The purpose of this analysis is to model the fiber instability caused by processing-induced thermal stresses. Additionally, they assumed that the fiber is subjected only to compression, but not twisting caused by the surrounding matrix. Their results predict high critical strain levels ($\approx 15\%$ for $\frac{E_f}{E_m} = 5000$) and show that the same graphs are applicable for practically all values of ν , Poisson's ratio of the matrix. Additionally, the graphs indicate that including the effect of shear deformation of the fiber has a negligible effect on compressive failure strains for large values of $\frac{E_f}{E_m}$. However, for low values of $\frac{E_f}{E_m}$ ($< 20\%$), including the effect of shearing deformation of the fiber increases the critical buckling strains by $\approx 20\%$.

Lager and June⁴⁰ used boron/epoxy (2 different matrices) to evaluate the trends of the microstability failure theory suggested in Refs. 33, 36, and 39. Their unidirectional composites were fabricated with excellent control on fiber location and volume fraction. These authors measured compression strength values approximately 63% of those predicted by Eqns. 1 and 3 using initial moduli, independent of the axial strain level. However, excellent correlations between the trends of the data and the theoretical predictions were observed. Their justification for 0.63 as an influence coefficient is that the idealized model assumes that all of the matrix material is effective in resisting buckling of the fibers. Their influence coefficient presumes the matrix material is only 63% effective.

Chung and Testa⁴¹ applied Biot's⁴² mathematical incremental deformation analysis to investigate the elastic stability of unidirectional fibers in a composite plate. Biot's analysis is modified by the following assumptions:

- (i) the plate is infinitely large,
- (ii) $L \gg 2h_2$,
- (iii) $2h_2 \gg t$,
- (iv) $\frac{E_1}{E_2} > 1$, and
- (v) $\lambda \gg h_1$,

where

L = fiber length,

h_1 = fiber diameter,

$2h_2$ = fiber spacing,

t = plate thickness,

ν_2 = Poisson's ratio for the matrix,

E_1, E_2 = Young's modulus of the fiber and matrix, respectively, and

λ = fiber buckling wavelength.

The formal analysis states that the stability of an equilibrium state predicted by the equations of the classical theory of an elastic medium may be determined by considering perturbations about the equilibrium state. The equations governing the perturbations (Biot's incremental deformations) are superimposed on the initial equilibrium state deformation). The solutions for sinusoidal modes of buckling are then found in the form of transcendental equations for the critical values of load and corresponding wavelengths, which can be solved numerically for fixed values of three parameters ($\frac{E_1}{E_2}, \frac{h_2}{h_1}, \nu_2$) appearing in these equations.

Simpler expressions are obtained by introducing several approximations in the analysis. One simplification was to ignore the incremental deformation in the matrix. This formulation reduced to Rosen's³³ column on an elastic foundation analysis, Figs. 1b and 1c. Comparison of these results with the formal solution



indicated that the compressive stress in the matrix has little effect on the stability of the fibers even as you go above the shear stress required for matrix yielding. Additionally, approximations reduced the solution to those frequently derived by energy methods (long-wavelength solution) and by considering a fiber in an infinite medium (short-wavelength solution), e.g. Ref. 39. Experimental results for low fiber volume fraction laminates show good agreement with analytical results and show evidence of the buckling modes described in the analysis.

Guz⁴³ also confirmed the “shear instability mode” of failure, Eqn. 4, as the limiting value of compression. Reference 43 did not contain any experimental results or significant new ideas.

Hayashi⁴⁴ modified his previous analyses³⁴ for orthotropic bulk materials to unidirectional fiber-reinforced composite materials. This author proposed that failure occurs when the compressive stress in the matrix, σ_m , reaches its shear instability limit, σ_m^* , equivalent to matrix yield strength. At this point shear deformation takes place in the matrix, and the matrix loses the supporting action for the fibers. The matrix shear instability limit, rather than the fiber instability limit as described in previous analyses, is defined as

$$\sigma_m^* = G_m(\sigma_m^*) \quad (9)$$

where

$$\begin{aligned} \sigma_m^* &= \text{shear instability limit of the matrix and} \\ G_m(\sigma_m^*) &= \text{tangent shear modulus of the matrix when the stress is } \sigma_m^*. \end{aligned}$$

Using the rule of mixtures, the compressive strength of the composite is given by

$$\sigma_c = \sigma_f^* V_f + \sigma_m^* (1 - V_f) \quad (10)$$

where

- σ_m^* = the stress on the matrix at which instability or yielding first occurs, Eqn. 9,
 V_f = fiber volume fraction, and
 σ_f^* = fiber stress corresponding to σ_m^* , the point where matrix instability first occurs.

This analysis assumes that the strain in the fiber and the matrix are the same. The analysis is different from Schuerch³⁶ and Rosen,³³ Eqn. 3, by the fact that Eqn. 3 is singular for $V_f = 1$ and is different from the result in Eqn. 10. Experimental results from Lager and June⁴⁰ were compared with this analysis. Some agreement between data and analysis existed, but no explanation was suggested for irregularities between data and analysis.

Lanir and Fung⁴⁵ based their model for unidirectional composite compression strength on the assumptions that the fiber buckles inside the matrix and that both the fiber and matrix remain in the linear elastic range. These authors modelled cylindrical columns of matrix, each reinforced with a parallel, straight fiber. They consider pre-, in-situ, and postbuckling failures. In their analysis for the postbuckling range, the number of modes of buckling increases with increasing loads. They also concluded, that in common composites, the buckling of the fiber has no significant effect on the overall behavior of the composite in the linear elastic range. However, they predicted that fiber microbuckling significantly affects the behavior of the composite in the plastic range, particularly for high values of $\frac{E_f}{E_m}$.

Suarez, Whiteside, and Hadcock⁴⁶ appear to be the first researchers to investigate compressive failures in multidirectional laminates. They investigated the compressive strengths of multidirectional boron/epoxy laminates both theoretically and experimentally. Test specimens included coupons, honeycomb sandwich columns,



and honeycomb sandwich beams. These authors modelled the composites using a beam on elastic foundation approach. They assumed that the outer ply (always 0° orientation) failed by out-of-plane fiber microbuckling, and then they treated the remainder of the laminate as an elastic foundation with both extensional and shearing stiffness. They concluded that laminate initial waviness has a considerable effect on predicted compression strengths. Consistent assumptions of initial waviness (0.002–0.004, the ratio of waviness amplitude to lamina thickness) provided good correlation with some tests. Filament fracture and global instability were also discussed.

Hayashi and Fujikake⁴⁷ attempted to predict the ultimate compressive strength of unidirectional fiber-reinforced composites, assuming that general failure occurs by fiber buckling or fiber/matrix debonding. The critical loads were computed considering the nonlinear behavior of the matrix. The fiber microbuckling analysis presented in Ref. 47 is similar to previous analyses in that the energy method is applied. However, the analysis is unique because it is the first to consider a composite of finite size, rather than the infinite plates previously reviewed. This model is a two-dimensional, semi-infinite plate with the fiber ends simply-supported. The first fiber is considered to have a free edge, deflecting the most, and the deflections become exponentially smaller as fibers are considered from outer to inner locations. The failure strength is theoretically selected as the lower value between the fiber buckling load and the interfacial failure load. The finite size of the model leads to lower fiber buckling loads and more continuous behaviors than observed in previous analyses.

Kulkarni, Rice, and Rosen⁴⁸ investigated the compressive strength of unidirectional Kevlar 49/epoxy composites. These composites were selected because

quite often their measured compressive strengths are only 20% of their tensile strengths. A unique feature that distinguishes Kevlar 49 fibers from other fibers is their anisotropy. The shear modulus is less than 2% of the axial tensile modulus of the fiber. Consequently, the fiber axial shear modulus is of the same order of magnitude as the matrix shear modulus. Kulkarni et al,⁴⁸ using an energy approach and assuming that the buckling wavelength is much larger than the fiber diameter, derived the critical composite buckling stress for the shear mode as

$$\sigma_c = G_{12} = \frac{G_m}{1 - V_f + V_f \frac{G_m}{G_f}} \quad (11)$$

where

$$\begin{aligned} V_f &= \text{fiber volume fraction,} \\ G_m &= \text{shear modulus of the matrix, and} \\ G_f &= \text{shear modulus of the fiber.} \end{aligned}$$

For $\frac{G_m}{G_f} \ll 1$, Eqn. 11 reduces to Rosen's approximation in Eqn. 3. However, the expression for σ_c in Eqn. 11 is bounded for all values of V_f .

Equation 11 is identical to Eqn. 5 with $\sigma_c = G_c$, which is also the Reuss estimate of the longitudinal-transverse shear modulus, G_{LT} , of a unidirectional composite. This estimate is a "stiffness in series" model derived using rule of mixtures.

Kulkarni et al⁴⁸ modified their analysis to include the effect of an imperfect fiber/matrix bond. Equation 11 becomes

$$\sigma_c = G_m \left[\frac{1 - (1 - k) V_f}{1 - \left(1 - \frac{G_m}{G_f} k\right) V_f} \right]^2 \left[1 - \left(1 - \frac{G_m}{G_f}\right) V_f \right] \quad (12)$$

where k is a bonding parameter. The bonding parameter is restricted such that

$$-\left(\frac{1 - V_f}{V_f}\right) \leq k \leq 1$$

where the limits represent no bonding and perfect bonding, respectively. Graphs presented in Ref. 48 show no quantitative conclusions but do indicate lower strengths predicted by Eqn. 12.

The most thorough investigation of the compressive strength of unidirectional composites conducted by one researcher was completed by Greszczuk in Refs. 26, 49–53. In these references, he accomplished a very systematic, but idealistic, investigation of the variables that influence the compressive strength of unidirectional composites. These studies are considered idealistic because nearly perfect model composites (straight metal rods surrounded by resin) are tested. The variables studied include specimen geometry, constituent (fiber and matrix) properties, fiber volume fraction, reinforcement shape (flat laminae or circular fibers), reinforcement size, fiber array (square, hexagonal, and arbitrary), internal imperfections (unbonded fibers, bowed fibers, misaligned fibers), and fiber end configuration.

In addition to failure by microbuckling, the following types of failure were observed: (i) compression yielding of the reinforcement, (ii) compression failure of the reinforcement (45° shear), (iii) transverse splitting of the fibers, (iv) transverse cracking of the composites, and (v) inelastic microbuckling.

An approximate micromechanics solution for interfiber stresses in unidirectional composites subjected to in-plane shear and transverse normal loadings is presented in Ref. 49. Although this investigation is not directly related to microbuckling of unidirectional composites, it does provide a foundation for other Greszczuk studies. Greszczuk's solution was shown to be sufficiently accurate for application-oriented composites (fiber volume fraction ranging between 40% and 75%). The level of accuracy is established by comparison of the results with a rigorous elasticity solution and with experimental results. The transverse and shear

moduli predicted by the approximate theory also show good agreement with the values predicted by the rigorous elasticity theory.

In Ref. 26, Greszczuk compared many of the existing fiber microbuckling analyses and showed that Rosen's³³ was the most conservative, predicting the lowest failure stress, although still high. Greszczuk's nearly perfect composite specimens were designed such that they would not fail by Euler column buckling. Greszczuk compared Rosen's shear mode microbuckling equation (Eqn. 2) with the Euler equation to derive the general relationship between σ_{Euler} and $\sigma_{microbuckling}$ as

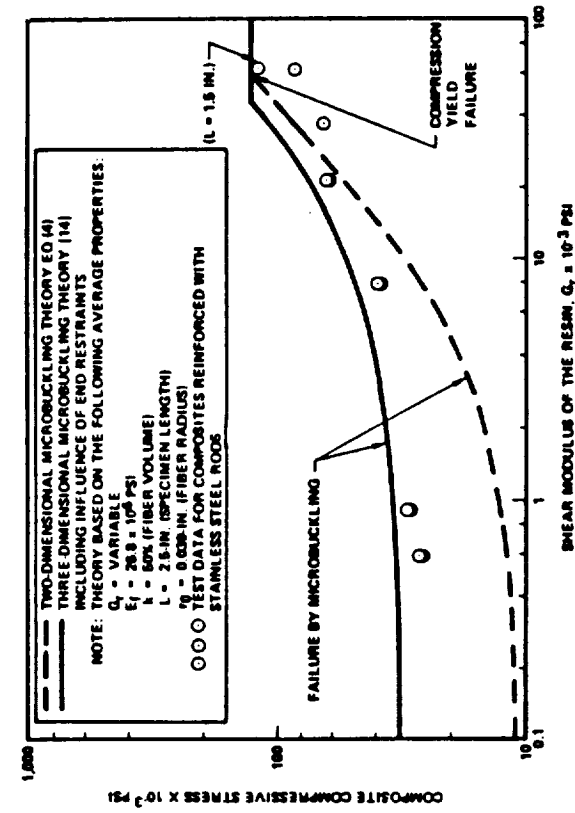
$$\sigma_{Euler} = \left[\frac{(w/h)^2}{\frac{12G_r}{k(1-k)\pi^2 E_f} \left(\frac{L}{h}\right)^2 + 1} \right] \sigma_{microbuckling} \quad (13)$$

where

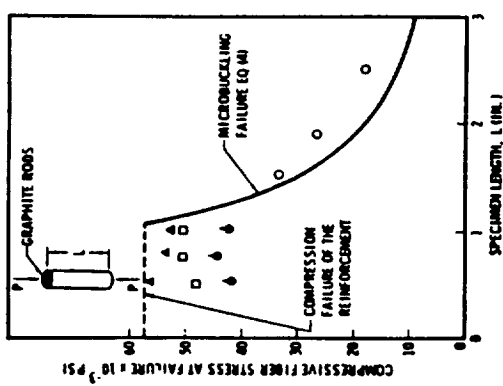
- w = width of the composite specimen,
- h = fiber diameter,
- G_r = shear modulus of the resin,
- k = fiber volume fraction,
- E_f = Young's modulus of the fiber, and
- L = length of the composite specimen.

Typical test-theory comparisons by Greszczuk are shown in Fig. 2. The results in Figs. 2a and 2c show that for composites reinforced with low-modulus resin, tests and theory show the same trend indicating that microbuckling is a valid failure mode. Moreover, as Young's modulus of the resin is increased significantly (from ≈ 2 ksi, resin A, to ≈ 457 ksi, resin H), the failure is independent of the length of the composite specimen and is governed by the compressive strength of the reinforcement.

Figure 2b shows very clearly that the compressive strength of the composites



a



b

Fig. 2 Test-theory correlation by Greszczuk²⁶ for compressive strength of composites.

- a) Comparison of reinforcement and microbuckling failures.
- b) Effect of resin shear modulus on microbuckling strength.

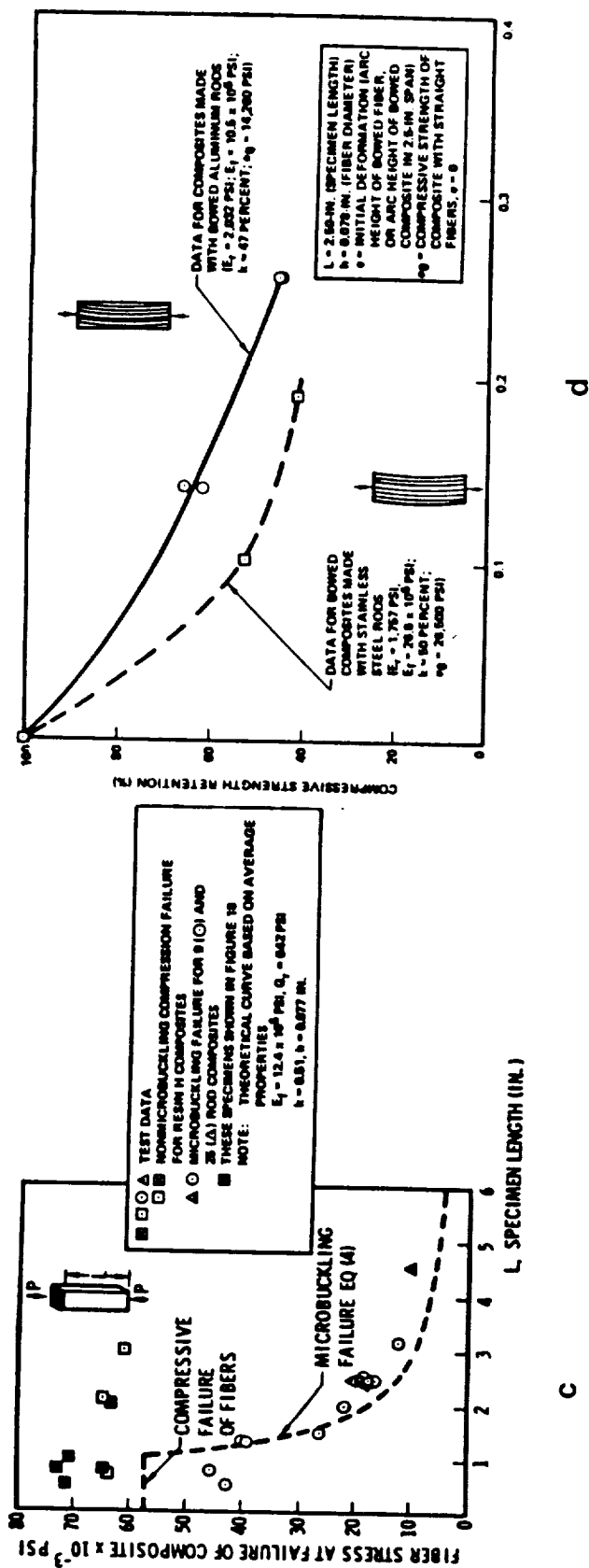


Fig. 2 Continued
 c) Comparison of reinforcement and microbuckling failures.
 d) Effect of initial deformations on microbuckling strength.

was found to increase with increasing resin shear modulus. Below a critical resin shear modulus, the failure was by microbuckling, and above this level, failure occurred by compression yielding of the reinforcement.

The results in Fig. 2d show that initial imperfections in the form of bowed fibers significantly reduce the microbuckling strength of composites. The author reported that other factors (misaligned fibers and unbonded fibers) were found to reduce the compressive strength of composites. For example in a composite made with a low modulus resin (≈ 2.0 ksi) and aluminum rods ($k \approx 50\%$), a 5° fiber misalignment decreases the compressive microbuckling strength by 25%.

Greszczuk⁵⁰ did not observe numerous buckle waves; he stated that numerous buckle waves form in the specimen if microbuckling is in the extension mode, which, according to Ref. 50, requires that the reinforcement volume fraction be less than $\approx 5\%$. Additionally, Greszczuk pointed out that Rosen's³³ analysis assumes that the lamina ends are simply-supported. However, if the laminae are not simply-supported, then Eqn. 2 becomes

$$\sigma_c = \frac{G_m}{1 - V_f} + e \frac{\pi^2 E_f V_f}{12} \left(\frac{h}{\lambda} \right)^2 \quad (14)$$

where e depends on the end-fixity of the individual laminae and the variables are described with Eqn. 2. This analysis is based on Ref. 32. Consequently, when end-fixity is considered, the second term in Eqn. 14 may not be negligible, especially for nearly perfect composites. However, for graphite fibers, $\frac{h}{\lambda} \ll 1$, and the second term in Eqn. 15 will be negligible. Similar results were also presented in Refs. 52 and 53.

The authors of Refs. 30 and 54–58 also completed a very thorough investigation of the factors that affect the unidirectional compression strength and failure modes

of carbon-, glass-, and Kevlar-reinforced polyester resins. The details of these results will be presented in each of the appropriate sections within this chapter.

Guz⁵⁹ considered a continuum and a piecewise-homogeneous medium approach to describe compressive failures in unidirectional composite materials. Both analyses yielded Eqn. 4, the same result as obtained by Hayashi³⁴ and Guz.⁴³

Gurdal and Haftka⁶⁰ recently modified Rosen's³³ beam on elastic foundation microbuckling model to include the localized shearing stresses that are either induced by the presence of a discontinuity or as a result of the externally applied loads, both for anisotropic plates with a cutout. These authors, like Rosen, also neglected the shearing deformation of the fibers and the extensional deformation of the matrix. The model is shown, for comparison, in Fig. 1d. Using an energy approach, the resulting equation for the fiber microbuckling load is

$$P_{f,c} = 2cG_m \left(1 + \frac{h}{2c}\right)^2 + \frac{\pi^2}{l^2} E_f I_f \quad (15)$$

where

- $P_{f,c}$ = critical fiber force,
- $2c$ = matrix (foundation) width
- h = fiber (beam) width
- l = column length
- G_m = matrix elastic shear modulus
- E_f = fiber elastic Young's modulus, and
- I_f = fiber first moment of inertia.

Equation 15 is similar to Rosen's (Eqn. 2); however, Rosen assumed $l \gg h$ and neglected the second term in Eqn. 2 to obtain Eqn. 3. In Ref. 60, it is assumed that the wavelengths that lead to failure are small so that the second term in

Eqn. 15 significantly contributes to the critical load and may not be neglected. Additionally, this analysis allows lateral displacement of the column end, caused by the shearing stresses induced at the local discontinuity or cutout, prior to fiber microbuckling. While Rosen's analysis assumes the fibers are straight until the critical microbuckling load is achieved. Gurdal and Haftka assume the strength failure criteria, rather than microbuckling instability, for the fibers of the principal load-carrying laminae. High bending stresses developed at the restrained ends (see Fig. 1d) are believed to cause the fiber breakage that leads to shear crippling. The analysis is essentially a point stress criterion, applied on a ply-by-ply basis around the cutout, that compares the resulting shear-compression coupling stresses with the fiber strength. One problem with the analysis is that the distance from the cutout or boundary to the failure point needs to be a material constant, considered to be independent of the ply combinations and laminate stacking sequence. The fiber-kinking model predicts significant reductions in the load-carrying capacity for laminates where the 0° plies are critical. Additionally, the model predicted that rotation of the principal axis of anisotropy of the plate with respect to the loading direction caused a strength reduction under pure compression, while rotation in a direction opposite the shearing stresses (in shear compression coupling) improved the load-carrying capacity of the plate. However, these predictions were not verified with experimental data.

Most of the fiber microbuckling models, Refs. 31-60, proposed to date are two-dimensional models in which neither initial fiber waviness, fiber/matrix debonding, nor matrix nonlinearity were considered. These idealizations have resulted in models that consistently overpredict the actual compressive strengths observed in composite materials testing. However, in Refs. 49-53, Greszczuk illustrated

that these analyses were valid for ideally straight fibers with good fiber/matrix bonding. His success with the idealized composites indicates that these equations fail to predict compressive strength because they do not include the three previously mentioned.

Effects of Matrix Nonlinearity — Hayashi's and Fujikake's⁴⁷ analytical work indicates that the compressive strength of unidirectional composite materials may be reduced as much as 50% due to the nonlinear, rather than linear, behavior of the resin.

Effects of Fiber Waviness — In earlier studies, authors^{38,46} suggested that both laminate and initial fiber waviness have a considerable effect on predicted compression strengths. Hanasaki and Hasegawa⁶¹ suggested in 1974 that the compression strength of unidirectional composites is lowered if the fibers are not straight due to their initial curvature. These authors used a moment equilibrium approach (the free body diagram contained two fibers, separated by one layer of matrix) assuming that (i) the deformation is two-dimensional, (ii) the influence of the normal strain in the matrix parallel to the fiber axis and that of Poisson's ratio may be neglected, and (iii) neither deflections nor moments exist at each end of the finite length of fibers.

From the general solution, satisfying the boundary conditions, the buckling load, and thus, compressive strength (for a straight fiber), of the composite material becomes

$$\sigma_c = \left[\frac{G_m}{(1-V)V} + \frac{\pi^2 E_f w^2}{12l_o^2} \right] \left[V + (1-V) \frac{E_m}{E_f} \right] \quad (16)$$

where

G_m = shear modulus of the matrix,

w = width of the fibers,

W = width of the matrix,

$V = \frac{w}{W+w}$ = fiber volume fraction,

E_m, E_f = Young's modulus of the matrix and fiber, respectively, and

l_o = half-wavelength of the buckling mode.

As $\frac{l_o}{w}$ is considered to be large and $\frac{E_m}{E_f}$ small, the approximate solution obtained is the same as that of Rosen's analysis,³³ namely Eqn. 3, for shear mode fiber microbuckling. At loads below this buckling load, assuming the initial curvature may be approximated by a sine wave, the nominal compressive stress becomes as follows:

$$\sigma' = \left[1 - \frac{a\pi}{\gamma_{max}(1-V)l + a\pi} \right] \left[\frac{G_m}{(1-V)V} + \frac{\pi^2 E_f w^2}{12l^2} \right] \left[V + (1-V) \frac{E_m}{E_f} \right] \quad (17)$$

or more simply, assuming $\frac{E_m}{E_f} \ll 1$,

$$\sigma' = \left[\frac{1}{1 + \frac{a\pi}{\gamma_{max}(1-V)l}} \right] \left[\frac{G_m}{(1-V)} \right] \quad (18)$$

where

a = amplitude of the initial curvature,

l = half-wavelength of the initial curvature, and

γ_{max} = maximum shearing strain in the matrix, and

the other variables are defined with Eqn. 16.

It should be noted that G_m is a function of γ_{max} in these equations. Additionally, when $\gamma_{max} = 0$, $\sigma' = 0$, and when γ_{max} is large, σ' (Eqn. 18) = σ_c (Eqn. 16). The compressive strength of the composite material is the maximum value of σ' . At this stress level, the composite material becomes unstable elastically. Figure 3 (Ref. 61) shows this relationship schematically. The decrease in the compressive stress at higher values of matrix shear strain is attributed to the decreasing value of



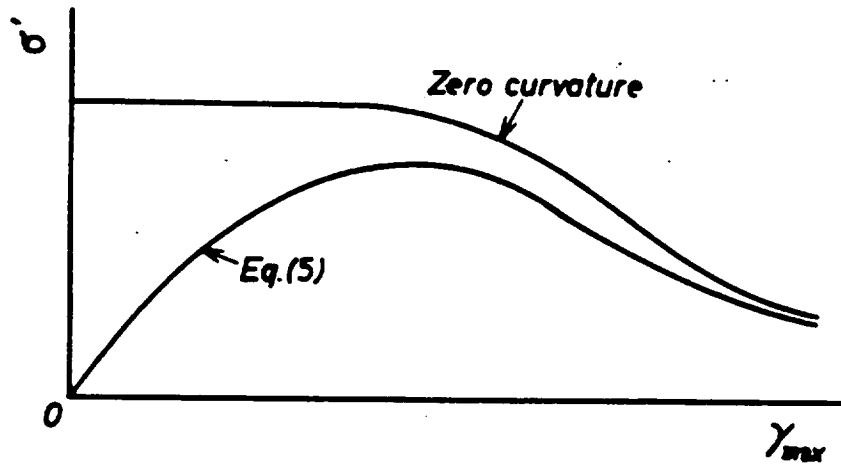


Fig. 3 Schematical representation of Eqns. 16 and 18,⁶¹ the relation between the nominal compressive stress of the composite material and the shearing strain of the matrix.

G_m at higher shear strain values. Consequently, the compressive strength becomes lower than the buckling stress represented by Eqn. 16. From Eqn. 17, it may be seen that the strength depends on V , $\frac{a}{l}$, G_m , and E_m , and that the strength decrease becomes large with the increase of V and $\frac{a}{l}$.

Maewal⁶² developed an analysis of the shear mode buckling as well as the initial postbuckling behavior of unidirectional composites loaded in compression. He considered a periodically laminated medium and assumed that the constitutive equations of the two isotropic constituents are linear relationships between the Piola-Kirchoff stress of the second kind (refer to undeformed state) and the Lagrangian finite strain tensor, or equivalently, that the respective strain energy functionals are quadratic in the strain components. This theory considers only geometric nonlinearity. Maewal's analysis is different from most of the other models described in this dissertation because it considers the instability phenomenon on the basis of continuum theory (macroscopic behavior explained disregarding molecular considerations) that includes the composite microstructure rather than a column on elastic foundation analysis. His results indicate that compressive microbuckling of the composite can occur at small strain only for those laminates where $\frac{E_f}{E_m}$ is relatively large. Additionally, his analysis of the initial postbuckling behavior suggests that the composite is not imperfection sensitive; in other words, the initial waviness of the fibers is not expected to reduce the microbuckling stress significantly. It should be noted that this result contradicts other results presented in this literature review.

Kurashige⁶³ also used a continuum approach, but included internal kinematical constraints of inextensibility (continuity conditions at the fiber/matrix boundary). By nature of continuum theory, a distinction between fibers and matrix does not

exist. Fibers are introduced into this analysis by considering that only portions of the ends of the continuum are loaded, and thus, these portions represent the load-bearing fibers. The matrix is assumed only to transfer load to the fibers by shear at the fiber/matrix interface. Kurashige modelled the dependence of the compressive strength on fiber buckling wavelength as well as fiber volume fraction. He developed the buckling conditions as

$$\tan\left(\frac{V_f \chi}{\zeta}\right) - \frac{(1/\chi)}{\tanh\left(\frac{1-V_f}{\zeta}\right)} = 0 \quad (19)$$

for the extension mode and

$$\tan\left(\frac{V_f \chi}{\zeta}\right) - \left(\frac{1}{\chi}\right) \tanh\left(\frac{1-V_f}{\zeta}\right) = 0 \quad (20)$$

for the shear mode where

$$\begin{aligned} V_f &= \frac{h}{H} = \text{fiber volume fraction,} \\ \zeta &= \frac{1}{\pi k_o} \left(\frac{l}{H}\right) = \text{nondimensional buckling half-wavelength,} \\ \chi &= \frac{k}{k_o}, \\ k &= \left(\frac{p_o - \mu}{2\mu + \lambda}\right)^{\frac{1}{2}}, \\ k_o &= \left(\frac{\mu}{2\mu + \lambda}\right)^{\frac{1}{2}}, \\ \mu, \lambda &= \text{Lamé's constants,} \\ h &= \text{fiber radius,} \\ H &= \text{matrix half-width, and} \\ l &= \text{buckling half-wavelength.} \end{aligned}$$

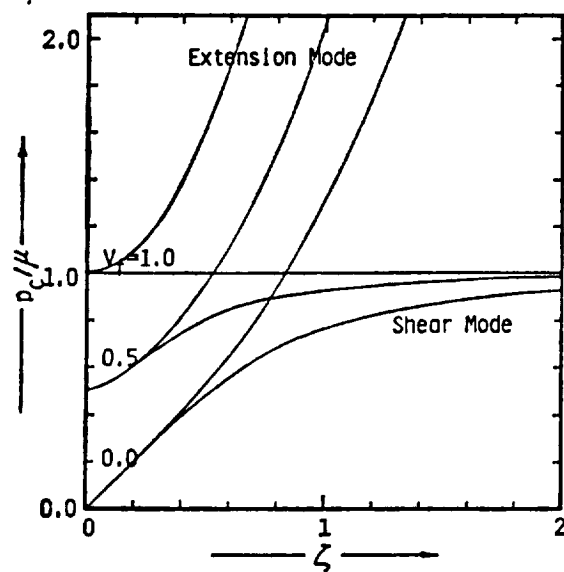
From the root of either Eqn. 19 or 20, the compressive strength, p_c is determined by

$$\frac{p_c}{\mu} = \frac{V_f}{(1 + \chi^2)}. \quad (21)$$

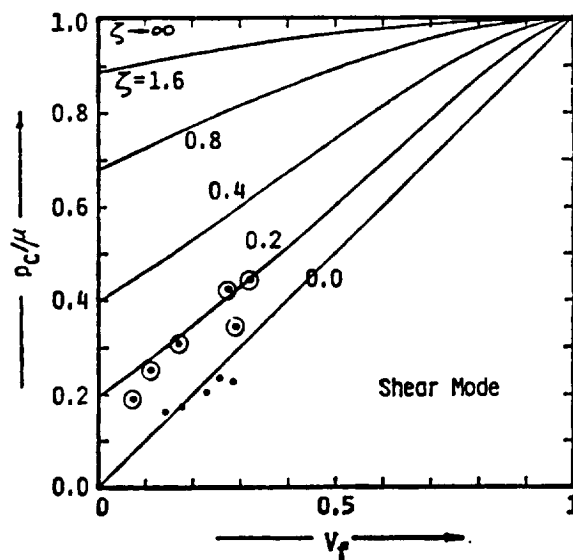
His results are shown in Fig. 4. Additionally, Kurashige included experimental results of DeFerran and Harris⁶⁴ in Fig. 4b. The solid circles are the results for the polyester resin reinforced with hard-drawn steel wires, while the open circles for that reinforced with fully softened wires of the same steel. However, DeFerran and Harris did not include a description of the buckling wavelength in their experiment so the theory and results cannot be compared. Figure 4a indicates that the compressive strength of unidirectional composites is an increasing function of the nondimensionalized buckling wavelength, ζ . In all cases, the shear mode appears to be more critical. However, this model predicts infinite compressive strength for the extension mode microbuckling which is not realistic. The results in Fig. 4b indicate that the compressive strength increases with increasing fiber volume fraction, but in this case, the strengths are bounded.

Kurashige⁶⁵ also analyzed the compressive strength of cross-ply composite laminates consisting of fiber-reinforced elastic layers. He assumed that the composite consisted of three types of layers: (i) axial layers that are load-bearing, incompressible, and inextensible (good approximation for $E_f \gg E_m$, (ii) cross layers that are incompressible and isotropic, and (iii) thin bonding layers made of incompressible elastic materials that connect the axial and cross layers.

Rather than using the conventional traction continuity conditions, step conditions at the layer interfaces involving singular stresses due to fiber-inextensibility were applied. The predictions indicate a sharp increase in compressive strength as the nondimensional buckling wavelength is increased from 0 to approximately 0.3, at which the compressive strength reaches a plateau. The level of this plateau was shown to decrease as the resin shear modulus decreased and/or the thickness of the resin-rich layer between the axial and cross layers increased.



a



b

Fig. 4 Kurashige's results for unidirectional composites.⁶³
 a) Dependence of compressive strength on buckling wavelength.
 b) Dependence of compressive strength on fiber volume fraction for shear mode fiber microbuckling.

Chang and Lessard⁶⁶ used energy principles to develop an analytical model to predict the fiber buckling strength of unidirectional composites. In particular, these authors wanted to understand the effect of fiber-matrix interaction due to nonuniform loading on the fiber buckling strength of these composites. The model included fiber bending energy, matrix shearing energy, and matrix extension energy which is attributed to the interaction of the fibers and the matrix. These authors assumed that (i) the matrix does not support compressive loads, (ii) the material behaves linear elastically. Under a uniform load distribution with straight fibers, this analysis yielded Eqn. 2, Rosen's well-known buckling equation. Of particular interest, these authors considered a $[(0/90)_6]_s$ composite laminate with a center hole loaded in compression. Nonlinear finite element analysis was used to determine the normal stress distribution adjacent to the hole in the 0° plies. This distribution is applied to their infinite array of fibers and matrix. This analysis showed that the multidirectional fiber microbuckling strength can be 1.79 (lay-up dependent) times the uniaxial compressive strength. However, this analysis considers only linear material behavior. It is possible that the stress concentration may be considerably larger (or smaller) when the nonlinear material behavior is considered. The purpose of the analysis is to show that the effects of load distribution have a significant influence on the local fiber buckling strengths.

Piggott⁵⁸ developed rule of mixtures analyses to model the factors (fiber strength, matrix yield strength, degree of fiber/matrix adhesion, and degree of fiber waviness) believed to have an important influence on compression strength. Six governing equations were developed, and the actual failure stress for a given situation was determined by the failure process that operated at the lowest stress.

In Ref. 57, Martinez et al showed that the compression strength was approxi-



mately given by the expression

$$\sigma_{1cu} = \sigma_o + bR \quad (22)$$

where σ_o and b are constants and R is the minimum radius of curvature of the fibers in the region where they are kinked. These results are shown in Fig. 5.

Piggott⁵⁸ predicted the stress in a sinusoidal shaped fiber as

$$\sigma_f = \frac{2\lambda^2}{\pi^3 a} \sigma_{2m} = \frac{8R\sigma_{2m}}{\pi d} \quad (23)$$

where

- d = the fiber diameter,
- λ = wavelength per unit fiber length,
- a = amplitude per unit fiber length,
- σ_{2m} = transverse stress exerted by the fiber on the matrix,
- σ_f = longitudinal stress in the fiber, and
- R = minimum radius of curvature of the fiber.

Equation 23 indicates that as the composite stress is increased, σ_f will increase, and thus, σ_{2m} will increase. Unless some other failure process intervenes (e.g. fiber yielding and failure), σ_{2m} will eventually become so large that the fiber separates from the matrix on the inside of the curve, or the matrix yields, so that the fiber can push it aside. In either case, σ_f reaches some maximum value, σ_{fmax} , and the composite fails by

$$\sigma_{1cu} = \sigma_{fmax} \left(V_f + \frac{V_m E_m}{E_f} \right). \quad (24)$$

For soft matrices with perfect fiber/matrix adhesion, σ_f reaches σ_{fmax} when $\sigma_{2m} = \sigma_{my}$, the yield stress of the matrix. In this case, the compressive strength becomes

$$\sigma_{1cu} = \frac{2\lambda^2}{\pi^3 a} \left[V_f + \frac{V_m E_m}{E_f} \right] \sigma_{my}. \quad (25)$$

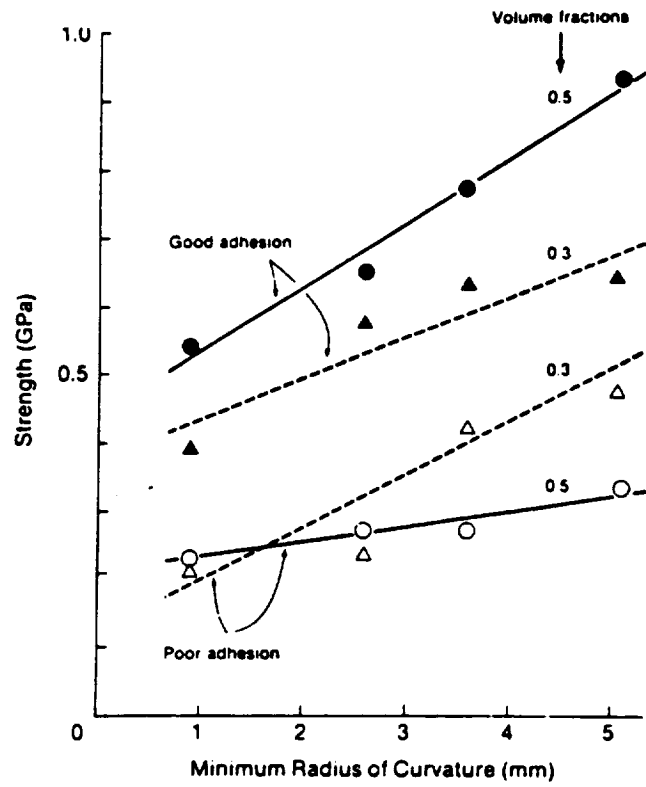


Fig. 5 Composite compressive strength as a function of the minimum radius of curvature for glass fibers in a polyester resin.⁵⁷

If $\frac{E_m}{E_f}$ is negligible, then $\sigma_{1cu} \propto \sigma_{my}$ for geometrically similar composites.

The effects of matrix nonlinearity were modelled in the analysis in Ref. 47 while the effects of fiber waviness were described in Refs. 58 and 61-66. Although including each of these effects made more realistic compression strength predictions, these analyses are still insufficient since at the limits of 0-1 for V_f they predict infinite strengths and no optimum fiber volume fraction. Consequently, both variables must be considered in one analysis.

Effects of Matrix Nonlinearity & Fiber Waviness — Davis⁶⁷ refined the previously mentioned fiber microbuckling models to include both initial fiber curvature and matrix nonlinearity. His model consisted of one fiber layer and two half-layers of matrix analyzed as a multilayered Timoshenko column in axial compression, permitting both bending and shearing deformations in each layer. He measured the initial fiber curvature in a boron/epoxy composite. The ratio of the initial amplitude of the waviness to the length of the wave, $\frac{a_0}{L}$, was measured to range from 0.001875 to 0.003750. Additionally, using compression/torsion tests, Davis observed that the apparent shear modulus ($G - \sigma$) decreases as the axial compressive stress σ increases. However, it should be noted that no analytical effort was made to explicitly establish this relationship. Using an energy methods approach, Davis predicted interlaminar shear stresses and the onset of shear instability, which compares with Eqn. 4. These experimental and analytical results are summarized in Fig. 6. These results clearly indicate that fiber waviness causes the composite to behave like it has a reduced shear modulus. Consequently, neglecting fiber waviness effects causes much larger compressive strength predictions than observed experimentally.

From his energy analysis, Davis showed that small initial deflections, on the order of those measured experimentally, reduce the axial compressive stress at which

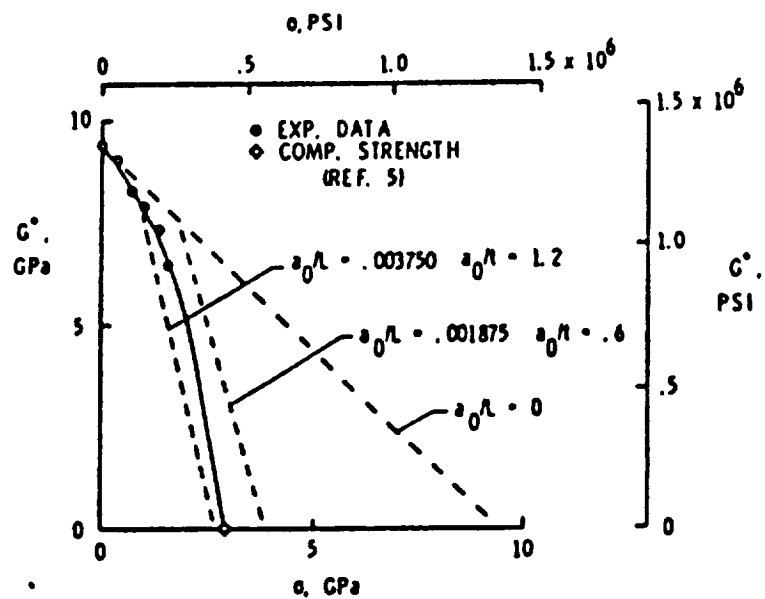


Fig. 6 Comparison of measured and predicted values of apparent shear modulus as a function of axial compressive stress for unidirectional boron/epoxy composites.⁶⁷

shear instability is expected to occur from approximately 9.308 GPa to approximately 3.275 GPa. Within the region bounded by $0.001875 \leq \frac{a_0}{L} \leq 0.003750$, the maximum computed interlaminar shear stress was approximately 75,842 MPa, which is less than the interlaminar strength of the boron-epoxy composite and indicates that failure was due to shear instability and not delamination. Neglecting the initial curvature of the fibers (assuming $\frac{a_0}{L} = 0$ in Fig. 6), as assumed in Refs. 33 and 38 leads to significantly higher compression strength predictions than measured experimentally.

It should be noted that graphite fibers have a lower modulus and are more slender than boron fibers; thus, graphite fibers have a lower stiffness. The consequence of this comparison is that graphite fibers will have larger initial fiber curvature, and thus, greater strength reductions than that measured by Davis⁶⁷ for boron.

Wang^{68,69} used a moment equilibrium approach, assuming an initial fiber curvature and a nonlinear in-plane shear stress-strain relationship, to predict the compressive strength of graphite/epoxy unidirectional composites. Two additional assumptions in his analysis are quoted as follows:

- (i) that an application of an incremental compressive load amplifies the deflection of the fibers which causes a rise in the in-plane shear stress; due to the nonlinear shear behavior, a rise of the shear stress decreases the shear stiffness, which in turn induces additional fiber deflection under the same compressive load; and
- (ii) that compression failure of the composite occurs at the applied load which causes an unstable increase in the fiber deflection, or an excessive increase in the in-plane shear stress.

His analysis yielded

$$\tau_{LT} \approx \left[\frac{\pi G_{LT} \sigma_c}{G_{LT} - \sigma_c} \right] \frac{f_o}{l} \quad (26)$$

where

- τ_{LT} = in-plane shear stress of the composite,
- G_{LT} = in-plane shear modulus of the composite,
- σ_c = applied uniform compressive stress,
- f_o = amplitude of the initial fiber deflection (not infinitesimal in this analysis), and
- l = half-wavelength of the deflection.

The incremental increase in composite shear stress, $\Delta\tau_{LT}$, with increasing applied compressive stress, $\Delta\sigma_c$, is determined by differentiating Eqn. 26 to obtain

$$\Delta\tau_{LT} \approx \left[\frac{\pi \bar{G}_{LT}^2}{(\bar{G}_{LT} - \sigma_c)^2} \right] \frac{f_o}{l} \Delta\sigma_c \quad (27)$$

where

\bar{G}_{LT} = tangential shear modulus (local slope) of the composite.

Equation 27 is an approximation for the composite shear stress-strain curve using piece-wise linear segments. As shown in Fig. 7, successive increases in the composite compressive stress causes increases in the calculated shear stress. The composite shear stress-strain relationship was approximated using the method proposed by Petit,⁷⁰ utilized by Rosen,⁷¹ and compared by Hahn.⁷² In the limit, the shear stiffness of the composite approaches zero resulting in shear mode microbuckling. Figure 8 is a hypothetical graph of σ_c versus $\frac{f(\sigma_c)}{F_o}$ where $f(\sigma_c)$ is the amplitude of fiber deflection at the applied stress. Figure 8 schematically shows this increase in compressive stress (modelled by Eqn. 27) approaching an

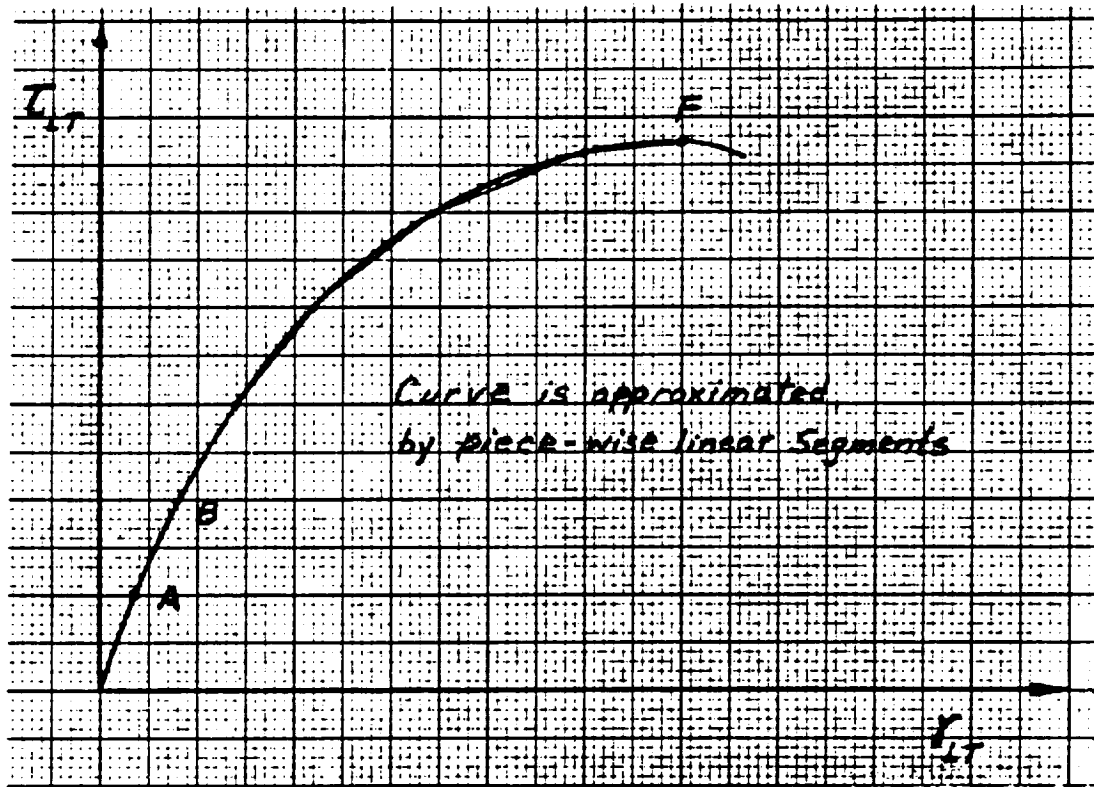


Fig. 7 A hypothetical shear stress versus shear strain curve for a graphite/epoxy unidirectional composite, suggested by Wang.^{68,69}

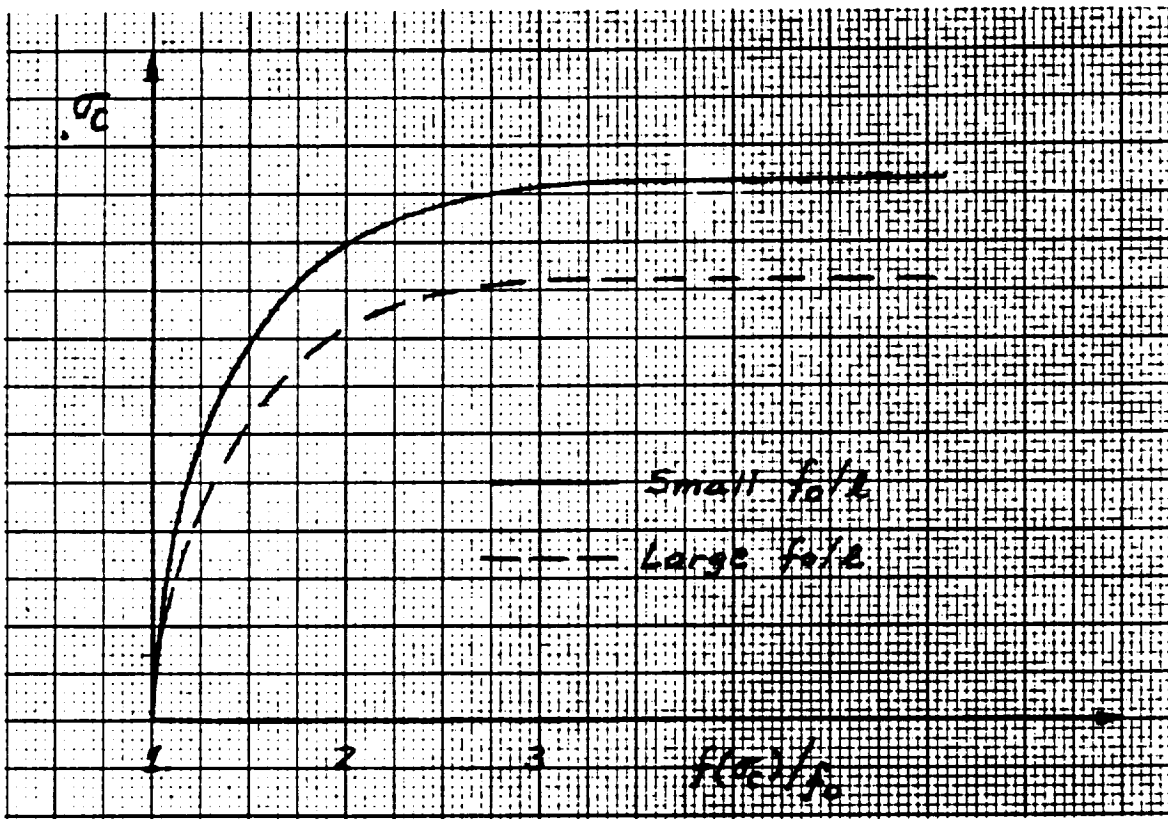


Fig. 8 A hypothetical compression strength, σ_c , as a function of lateral fiber deflection, $f(\sigma_c)$, suggested by Wang.^{68,69}

asymptotic limiting value, which is the compressive strength of the composite for failure by shear microbuckling.

In order to determine $\frac{f_o}{t}$ for the composite, the ultimate σ_c for the unidirectional composite was measured experimentally. Next, a value for $\frac{f_o}{t}$ was selected by trial-and-error such that the predicted σ_c agreed with the experimental σ_c . This value of $\frac{f_o}{t}$ then became a material property of the composite system, regardless of the test conditions. Wang determined $\frac{f_o}{t}$ to be 0.0108 for these carbon fibers. As expected, this value is larger than that for boron since the carbon fibers are more compliant. This pseudo-empirical parameter, which should be independent of temperature, was used to predict the compressive strength over a range of temperatures. The changes in the predicted compressive strength at higher temperatures were then attributed to the shear stress-strain behavior of the composite. His analytical results were in good agreement with the experimentally measured strengths.

Shuart^{28,73} investigated compressive failures in multidirectional composite laminates. In Ref. 28 Shuart studied the short-wavelength buckling of multidirectional composite laminates. In this analysis, the fibers are modelled as an infinite plate supported by matrix material which is treated as an elastic foundation. A laminate then consists of a series of plates and elastic foundations. A linear analysis is derived to determine the short-wavelength buckling response of composite laminates. This analysis was then generalized to a nonlinear analysis to include laminate short-wavelength initial imperfections. Two shearing mechanisms expected to initiate failure were analyzed. These mechanisms were interlaminar shearing caused by initial waviness of the plies (geometrically nonlinear behavior) and in-plane matrix shearing. The in-plane matrix shearing failure mode occurs in angle plies at the fiber/matrix interface and/or in the epoxy matrix between the fibers.⁷⁴ In-plane



shear stresses parallel to the fiber/matrix interface cause this failure mode. These shear stresses may be a function of both fiber waviness and fiber scissoring. However, this analysis was not verified experimentally.

In Ref. 73, Shuart improved the analysis of Ref. 28 by adding the matrix compression failure mode and allowing the in-plane matrix shearing mechanism to include effects from in-plane fiber waviness and fiber scissoring. Matrix nonlinearity is introduced into the analysis in the fiber scissoring analysis. Fiber scissoring is idealized as a simply supported beam on a nonlinear foundation. Because it possesses only shear stiffness, the foundation is modelled as a nonlinear shear spring. This stiffness is obtained from the material's shear stress-strain behavior using the method described in Ref. 71. The laminate compressive strength as a function of ply orientation is shown in Fig. 9 for $[\pm\theta]_s$ -class AS4/3502 laminates. The analysis results predict that interlaminar shearing initiates laminate failure for $0^\circ \leq \theta \leq 15^\circ$, that in-plane matrix shearing (longitudinal splitting) initiates laminate failure for $15^\circ \leq \theta \leq 50^\circ$, and that matrix compression initiates laminate failure for $50^\circ \leq \theta \leq 90^\circ$. Experimental results are also included in Fig. 9. Comparison of the analytical and experimental results show reasonable agreement for $\theta < 45^\circ$ and show excellent agreement for $\theta \geq 45^\circ$.

Chang, Lessard, and Tang⁷⁵ performed an analytical and experimental investigation to study the in-plane failure of laminated multidirectional composites containing an open hole and subjected to compressive loadings. The progressive damage model consists of a stress analysis and a failure analysis. Stresses and strains in the plates were calculated by a nonlinear finite element analysis, which is based on finite deformation theory with consideration of both material and geometric (fiber waviness) nonlinearities. A plane stress condition was assumed for the analysis.

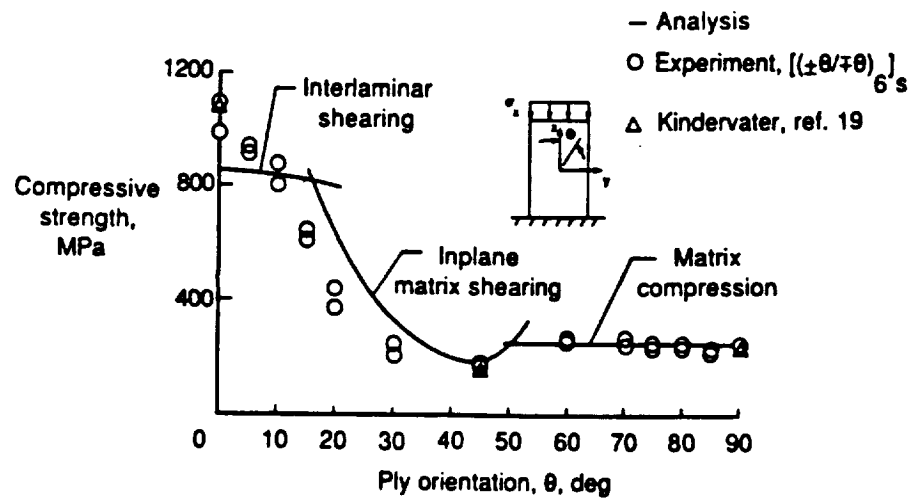


Fig. 9 Compressive strength as a function of ply orientation for $[\pm\theta]_s$ -class AS4/3502 laminates.⁷³

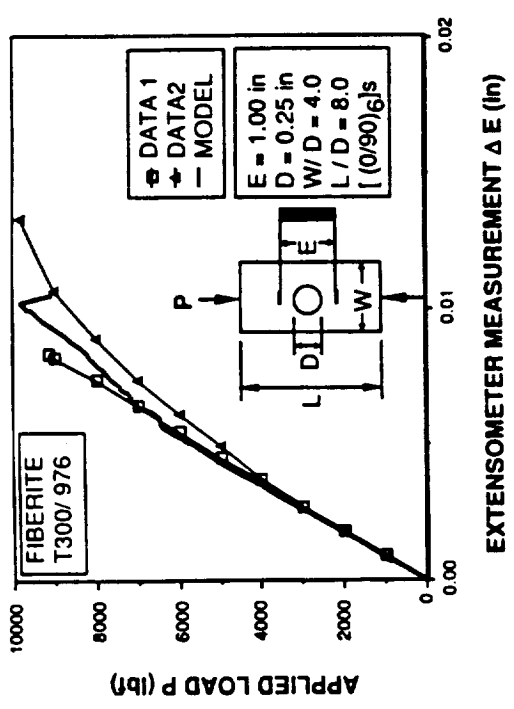


The types and size of damage were predicted by a proposed failure analysis which includes a set of proposed failure criteria and property degradation models for each mode of failure. Matrix cracking, fiber-matrix shearing, and fiber buckling (kinking) were the three basic failure modes considered in this investigation.

Basically, stresses and strains are calculated at each incremental displacement step, and these stresses are evaluated by the failure criteria to determine the occurrence and mode of failure. Mechanical properties in the damaged area are reduced appropriately according to the property degradation models. Stresses and strains are then recalculated to determine any additional damage as a result of stress redistributions at the same load. This procedure continues until no additional damage is found, and the next displacement increment is then pursued. The final collapse load is determined when the plate cannot sustain any additional load. Details of the failure analysis and experiments are given in Refs. 76 and 77, respectively.

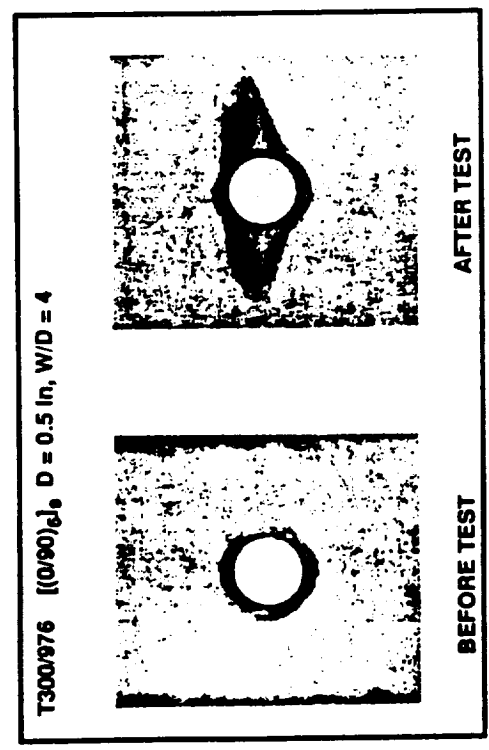
Typical results from this analysis are shown in Fig. 10. Figure 10a shows an enhanced X-radiograph of a $[(0/90)_6]_s$ specimen before and after a test to 90% of failure. From this figure, it is clear that initial damage existed inside the specimen near the hole boundary before the test. The authors suspect this damage was an artifact of the drilling methods. The load-displacement data for two $[(0/90)_6]_s$ specimens are shown in Fig. 10b in addition to the analytical prediction. An excellent agreement was found between the calculations and the data.

Typical model predictions of damage types and sizes are presented in Fig. 10c at different load levels. The model predicted fiber/matrix shearing initiated from the hole boundary near the stress concentration, and then propagated along the loading direction (parallel to the 0° fibers). Fiber buckling (kinking) was predicted

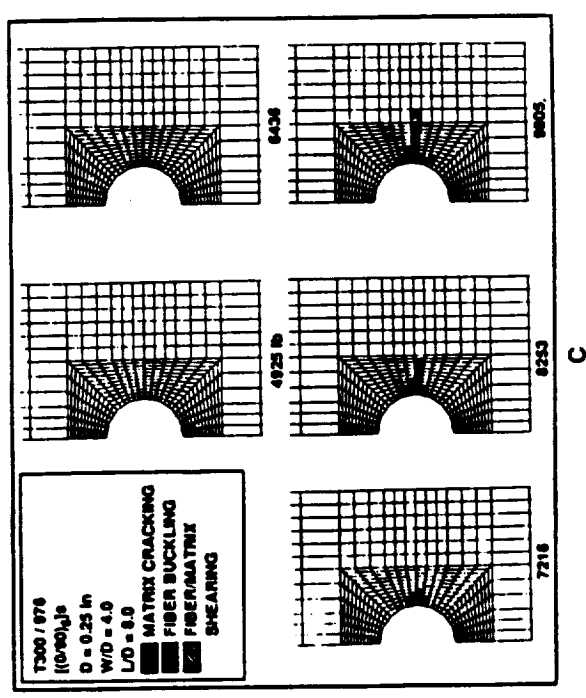


b

Fig. 10 Typical analytical and experimental results for a graphite/epoxy [(0/90)₆]_s laminate.⁷²
 a) X-radiographs.
 b) Load-displacement curves.
 c) Illustration of specimen damage.



a



at a load of about 50000 psi in the 0° plies and grew in the direction normal to its fiber direction.

Davis and Highsmith^{78,79} extended Lee⁸⁰ to incorporate material nonlinearity and compression loading. Lee⁸⁰ modelled fiber curvature with an infinite array of columns on elastic foundations under tensile loading. The analysis in Refs. 78 and 79 incorporates a closed-form solution for G_{12} , obtained from a curve fit through the shear stress-strain data.

Hahn and Williams²³ developed a nonlinear model including fiber curvature and matrix material nonlinearity to predict the compression strength of unidirectional composites. This analysis used a free body diagram of only one fiber and assumed that the local shear stress-strain behavior was linear. In reality, this linear behavior is not expected. The compressive strength is predicted by

$$\sigma_c = V_f G_{LT} \frac{1}{1 + \frac{\pi f_o}{l \gamma_{LT}}} \quad (28)$$

where

- V_f = fiber volume fraction,
- γ_{LT} = composite shear strain,
- G_{LT} = composite shear modulus, approximated as the secant modulus at a given γ_{LT} ,
- f_o = amplitude of the initial fiber curvature, and
- l = buckle half-wavelength.

If no initial curvature is assumed (i.e., $\frac{f_o}{l} = 0$) then

$$\sigma_c = V_f G_{LT}. \quad (29)$$

When G_{LT} is approximated by $\frac{G_m}{1-V_f}$ (Eqn. 6), Eqn. 29 is different from Eqn. 3 by the factor V_f . The difference derives from the selection of the free body. Rosen³³

used a fiber surrounded by matrix in his free body diagram. Since Eqn. 3 is known to overpredict the strength and because applying the equilibrium forces and moments to the fiber is a reasonable model, Hahn and Williams prefer Eqn. 29 over Eqn. 3.

If a bilinear shear stress-strain relation showing elastic-perfectly plastic behavior is assumed, then the compression strength becomes

$$\sigma_c^* = V_f G_{LT} \frac{1}{1 + \frac{\pi f_o}{l \gamma_y}} \quad (30)$$

where

γ_y = shear yield strain of the composite and the other variables are defined with Eqn. 28. Equation 30 assumes that the matrix yields at γ_y and no additional shear stress may be supported. Consequently, yielding spreads over the entire length of the buckled fiber, changing the deformed configuration to the form of kinking. This change from microbuckling to kinking occurs with very little increase in the applied load.

Equation 30 indicates that the higher G_{LT} and γ_y , the stronger the composite in compression. However, a weak fiber/matrix interface will reduce γ_y , and possibly G_{LT} , and cause a reduced compressive strength.

It should be noted that this result is very similar to that obtained by Hanasaki and Hasegawa.⁶¹ The results of Ref. 61 are given in Eqns. 16-18. To show that these results are similar, refer to Eqn. 30 and let

$$V_f = V,$$

$$\gamma_y = \gamma_{max} (1 - V),$$

$$G_{LT} = \frac{G_m}{1 - V},$$

and

$$f_o = a.$$

Thus, the result of Hanasaki and Hasegawa (Eqn. 18), except for the V_f in the numerator of Eqn. 30 is obtained. Again, the factor of V_f appears because of the selection of the free body diagram.

The effect of fiber waviness is to give significantly larger shear stresses (and thus, shear strains) for a given axial compressive stress level. Consequently, the composite reaches its shear instability limit at a lower applied stress level. Unfortunately, the incremental nature of the calculations used to determine this stress level does not allow the compressive strength to be expressed as a simple function of the initial fiber curvature. It is clear that the stress level at which nonlinear shear stress-strain behavior begins directly influences the compressive strength of the composite. Finally, fiber/matrix debonding causes this nonlinear behavior to initiate at an even lower applied stress level, resulting in a further reduced compressive strength.

Fiber Shear

Collings⁸¹ investigated the transverse compressive behavior of unidirectional carbon/epoxy composites. In these tests, failure occurred by interlaminar shear and was limited by the strength of the fiber/matrix interfacial bond. However, when the specimen was constrained laterally (to prevent interlaminar shear), failure was by fiber shear, and the failure stresses were very close (within 8%) to longitudinal compressive strengths for the same material. Based on these results, Collings concluded that the shear strength of the fiber is much less than that of the resin and the fiber/matrix interfacial bond.

Hancox⁸² suggested that since the buckling and instability models developed to date (1975) did not accurately predict the compression strength of unidirectional composites and similarities were observed between compression and tensile strengths, the compression strength of a composite must be governed by the same mechanism as the tensile strength, an inherent property of the fiber. It has been suggested in Ref. 25 that this failure mode constitutes an upper bound for compression strength.

Greszczuk⁵³ suggested that when a unidirectional composite specimen is loaded to a stress level where fiber failure occurs by shear (rather than microbuckling) of the fiber, the compressive strength may be predicted by the following rule of mixtures relationship,

$$\sigma_c = F_f k + \sigma_r^* (1 - k) \quad (31)$$

where

- F_f = compressive strength of the fiber,
- k = fiber volume fraction, and
- σ_r^* = compressive stress in the resin at failure, computed as the product of the resin modulus and the fiber failure strain, $E_m \epsilon_f$.

This type of compressive strength is only realized in practice when the composite has a relatively stiff matrix and a good interfacial bond to prevent premature failure by fiber microbuckling or longitudinal splitting.

Ewins and Ham²⁵ investigated the longitudinal and constrained transverse compression strengths of unidirectional graphite/epoxy composites. They proposed, based on their results, that if no other potential failure mode occurs at a lower stress, failure will occur by shear across the fibers and the matrix on a plane of near

maximum shear stress. Assuming that the matrix carries only a small portion of shear load, the composite compressive strength will be limited primarily by the shear strength of the fibers. However, at approximately 100°C the failure mode changed from fiber shear to fiber microbuckling, probably due to the reduced matrix shear modulus and the change in the constitutive behavior of the resin.

Longitudinal Splitting

Even though the induced tensile stresses at the fiber/matrix boundary are small compared to the applied axial compressive stresses, the transverse tensile strength is also small compared to the axial compressive strength. Thus, it is possible for the induced transverse tensile stresses to cause fiber/matrix debonding leading to longitudinal splitting (an interaction failure) and a reduction in the ultimate compression strength.

Kim⁸³ investigated the static strength of graphite/epoxy off-axis and angle-ply laminates under uniaxial tension and compression. Experimental data were compared with the Tsai-Wu tensor polynomial failure criterion. Both theory and experiment show greater strength in compression than in tension for these laminates. This phenomenon is explained by considering that the transverse strength in compression is four times greater than that in tension for this material system. The agreement between theory and experiment is very good except for angles smaller than $\pm 15^\circ$. To understand this behavior, the state of stress within the angle-ply laminate was examined. When uniaxial compression is applied to the specimen, σ_1 is compressive for all angles while σ_2 changes from tension to compression at approximately 40° . Whole fiber tow breaks, sheared matrix, and cleavage indicate that all three stress components appear to play a significant role in the failure (longitudinal splitting) of these specimens.

Greszczuk⁵¹ predicted the transverse tensile strength of glass/epoxy, graphite/epoxy, and graphite/phenolic composites using constituent properties and microstructure of the composite. The important aspect of this work is that the analysis accounts for the internal triaxial stress concentrations caused by fibers and voids individually, the interaction of stress concentrations from fibers and voids, and the volume fraction of ineffective or unbonded fibers. Good correlation between predicted and measured compressive strengths were observed.

Greszczuk⁵³ estimated the compressive strength of interaction failures by

$$F_{LC}^* \approx \frac{F_{LC} F_{Tt}}{F_{Tt} - K F_{LC}} \quad (32)$$

where

$$K \approx - \left(k - \sqrt{\frac{4k}{\pi}} \right) (\nu_f - \nu_r) \frac{E_T}{E_L} \quad (33)$$

and

ν_f, ν_r = Poisson's ratios of the fibers and matrix, respectively,

E_L, E_T = Young's moduli of the composite in the longitudinal
and transverse directions,

F_{Tt} = transverse tensile strength of the composite, and

F_{LC} = longitudinal compressive strength of the composite,
calculated according to the rule of mixtures,

Eqn. 31.

It should be noted that a weak transverse tensile strength (e.g., a poor fiber/matrix interface) yields a compressive failure strength that is much lower than that for fiber shear controlled failure. On the other hand, a very strong transverse tensile strength causes Eqn. 32 to give a result identical to Eqn. 31 in the limit.

Broutman²⁴ developed an alternative expression for the compression strength

of a composite that fails by longitudinal splitting. He concluded that

$$\sigma_c = \frac{(E_f V_f + E_m V_m) \left(1 - V_f^{\frac{1}{3}}\right)}{\nu_f V_f + \nu_m V_m} \epsilon_{mu} \quad (34)$$

where

- E_f, E_m = Young's moduli of the fibers and the matrix, respectively,
- ν_f, ν_m = Poisson's ratios of the fibers and the matrix, respectively,
- V_f, V_m = fiber and matrix volume fractions, respectively, and
- ϵ_{mu} = ultimate strain of the matrix, measured from a tensile test of the neat resin.

In Eqn. 34, compressive failure is assumed to occur when the transverse strain reaches the level required for failure in a transverse tensile test.

Broutman's²⁴ analysis implies that compression failure occurs by longitudinal splitting resulting from the Poisson's expansion in the transverse direction. However, when the specimen is rigidly supported by the grips, each end of the specimen is constrained. Consequently, the transverse tensile stresses leading to failure may be induced by constraint rather than by the Poisson's contraction difference, as assumed by Greszczuk.⁵³ A comparison of Broutman's predictions (Eqn. 34) against Rosen's³³ (Eqns. 1,3) predictions is shown in Fig. 11.

Piggott's⁵⁸ results showed that for stiff matrices failure occurred by splitting, rather than the controlled fiber kinking, though some kinking accompanied the splitting.⁵⁴ Even when the fibers are straight, transverse tensile stresses are present. An estimate of the stress at the fiber/matrix interface is given as

$$\sigma_r = \sigma_{1m} (\nu_m - \nu_f) (0.48 + 0.52V_f - 12V_f^2) \quad (35)$$

where ν_m and ν_f are the Poisson's ratios of the matrix and the fibers.

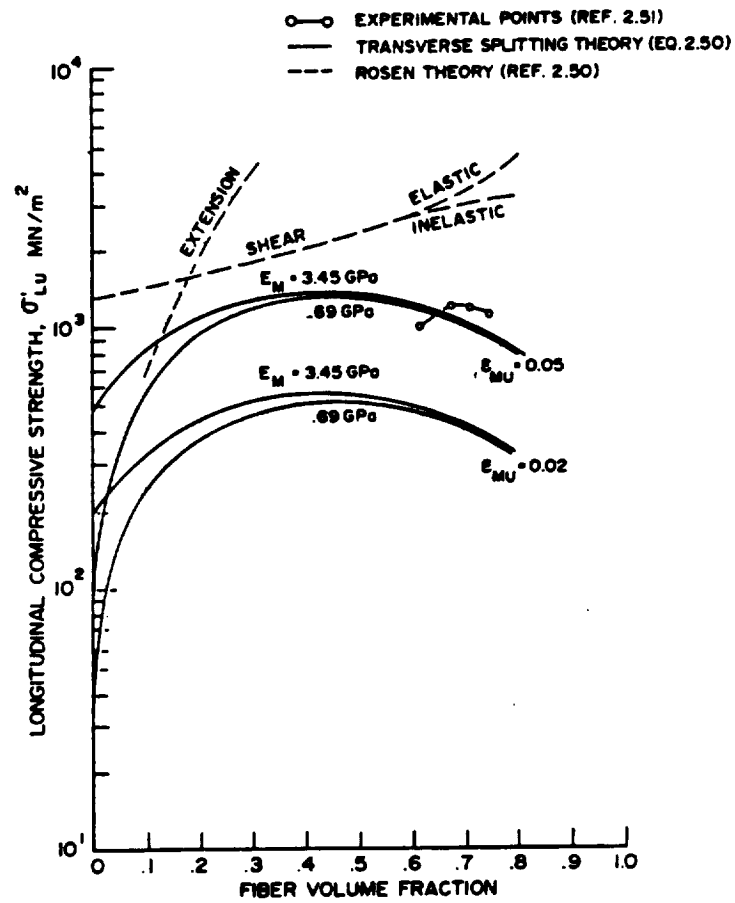


Fig. 11 Predicted and experimental values of longitudinal compressive strength, theories of Rosen (Eqns. 1 and 3) and Broutman (Eqn. 4).²⁴

However, large tensile stresses can be introduced by curved fibers, and these stresses can lead to failure of the bond, especially when the fiber/matrix adhesion is poor. Piggott suggested that three distinct strengths are involved in splitting behavior, as shown in Fig. 12. In addition to the adhesive strength, σ_a , the cohesive strength of the matrix, σ_{mtu} , and the compressive strength of the matrix, σ_{mcu} (or the yield strength, σ_{my}) are involved. The ultimate compression strength for composites made with hard matrices is given by

$$\sigma_{1cu} = \frac{8R}{\pi d} \left(V_f + \frac{V_m E_m}{E_f} \right) \sigma_{mcu} \quad (36)$$

where

- R = fiber radius of curvature,
- d = fiber diameter,
- V_m, V_f = matrix and fiber volume fractions, respectively, and
- E_m, E_f = Young's moduli of the matrix and fibers respectively.

The lines for transverse compression failure, shown in Fig. 13, were plotted using Eqn. 36.

Piggott⁵⁸ predicted that for debonding to occur, the stress must overcome the matrix cohesive strength, σ_{mtu} , in the webs of the fibers (see Fig. 12). In this case the composite strength is predicted by

$$\sigma_{1cu} = \frac{4R}{\pi d} \left\{ \pi \sigma_a + \left[\left(\frac{P_f}{V_f} \right)^{\frac{1}{4}} - 2 \right] \sigma_{mtu} \right\} \left\{ V_f + \frac{V_m E_m}{E_f} \right\} \quad (37)$$

where P_f is the packing factor, equal to $\frac{2\pi}{\sqrt{3}}$ for hexagonal packing and π for square packing and the other variables are defined with Eqn. 36. The curves for splitting failure in Fig. 13 were plotted using Eqn. 37. Figure 13 shows the combined effects of adhesion and fiber volume fraction. Strong nonlinear V_f effects are predicted in

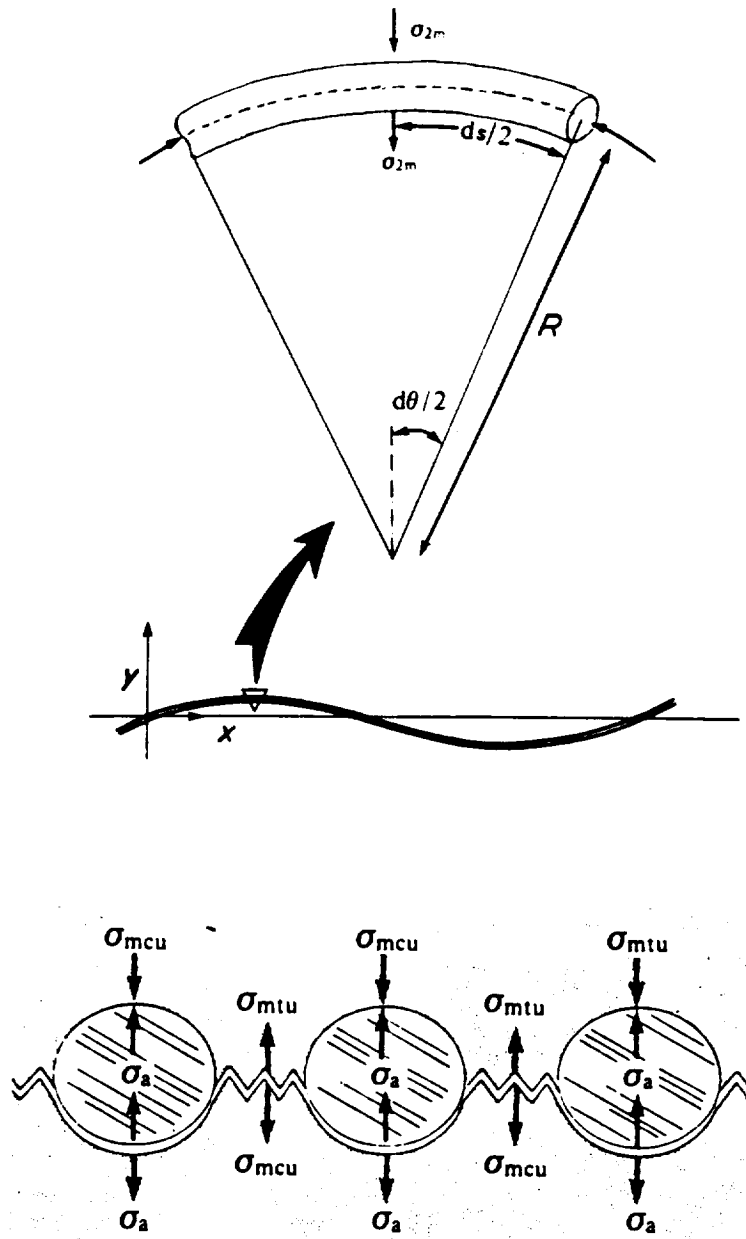


Fig. 12 Stresses involved in the longitudinal splitting failure of a composite with curved fibers, developed by Piggott.⁵⁸



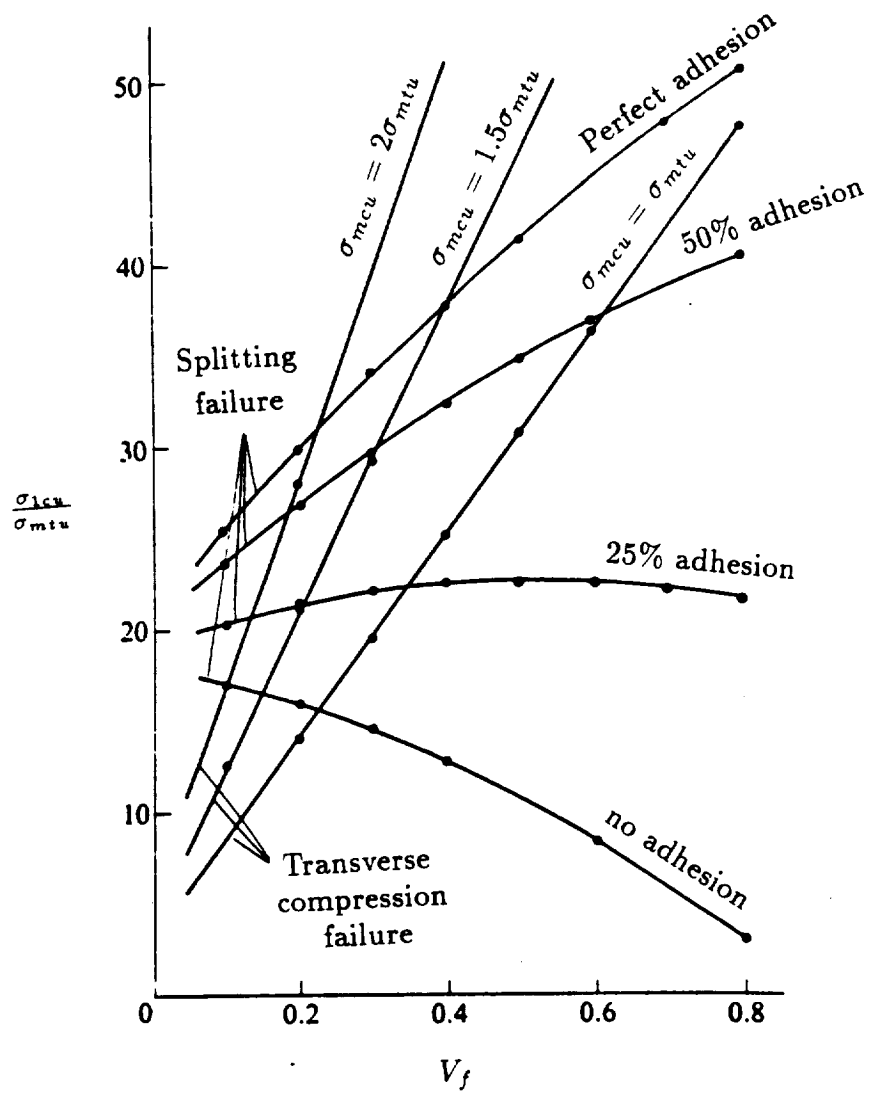


Fig. 13 Dimensionless plot, developed by Piggott,⁵⁸ for composite compressive strength when controlled by transverse splitting and transverse matrix compression failure.

this plot. This figure indicates that transverse compression failure (i.e. the sideways push of the fibers will exceed σ_{mcs}) controls the strength over a range of V_f until this line intersects the appropriate adhesion line and then fiber/matrix debonding controls failure.

In summary, a weak interface, attributed to poor fiber/matrix adhesion may result in a low transverse tensile strength.^{24,51,58} This strength reduction, in turn, may give a lower compressive strength if failure is due to longitudinal splitting caused by interaction effects resulting from secondary transverse tensile stresses. A weak interface combined with secondary transverse tensile stresses may also yield a local interfacial failure which may eventually precipitate other types of failure such as fiber microbuckling or delamination.

Micromechanics & Damage Approaches to Compression Strength

Fried,⁸⁴ Fried and Kaminetsky,⁸⁵ and Fried⁸⁶ studied the influence of the matrix, the reinforcement, and matrix/reinforcement interface on compressive failure. Experimental results for unidirectional laminates (steel, glass, and glass roving fibers embedded in a polyester resin) led Fried to suggest the following failure sequence. The reinforcement phase in a composite material carries the compressive load until the rigid matrix phase yields; upon yielding, the matrix flows and no longer provides support for the reinforcement. Consequently, the reinforcement buckles and the composite laminate fails catastrophically. From a micromechanics (rule of mixtures) type approach, the ultimate strength of the composite was expressed as the following linear function of the matrix yield stress

$$S_{cu} = S_{ry} \left(R + G \frac{E_g}{E_r} \right) \quad (38)$$

where

- S_{cu} = ultimate strength of the composite,
 S_{ry} = resin axial stress at yield,
 R = volume fraction of resin,
 G = volume fraction of glass,
 E_g = Young's modulus for the glass fiber, and
 E_r = Young's modulus for the resin.

This model assumes that (i) the maximum stress in the matrix is its yield stress and that (ii) the strain in the matrix is the same as the strain in the reinforcement. Equation 38 was not valid for the steel reinforcement, probably due to high ductility of steel compared to glass.

Budiansky⁸⁷ completed a brief survey of the current theoretical studies in the area of micromechanics — the mechanics of very small things. Topics discussed include void collapse in metals, transformation toughening in ceramics, fiber kinking in composite materials, and thermoelastic dissipation in rocks. Of particular interest to this review is fiber kinking in composite materials, which will be discussed in the appropriate section in this chapter.

Euler Buckling

Chou and Kelly⁸⁸ used results from Timoshenko and Gere³² with corrections for shear deformation to predict the compressive stress required to give macroscopic buckling.

The Euler buckling equation without shear deformation corrections is

$$P_e = \frac{cE_c I}{l^2} \quad (39)$$

where

$$P_e = \text{critical Euler buckling load,}$$

- E_c = Young's modulus for compression,
 I = moment of inertia,
 l = column length, and
 c = a constant determined by the end constraints of the specimen.

For the idealized end conditions,

- c = 2.47 for clamped-free,
 c = 9.87 for hinged-hinged, and
 c = 20.2 for clamped-hinged.

In highly anisotropic materials such as unidirectional composites, the Euler buckling predictions without shear deformation corrections (Eqn. 39) overestimate the critical Euler buckling load. The additional deflections occur because of the relatively low ratio of shear to axial modulus (≈ 0.04 for composites compared to ≈ 0.31 for metals). This effect may cause another significant reduction in the Euler buckling load (typically by a factor of 4). A suitable correction factor for the low shear stiffness must be applied. The corrected critical load including shear deformation is given by

$$P_{cr} = \frac{P_e}{\left(1 + \frac{nP_e}{AG_c}\right)} \quad (40)$$

where

- n = a numerical factor:
 1.2 for rectangular cross-sections and
 1.11 for circular cross-sections,
 A = cross-sectional area,
 G = composite shear modulus, and
 P_e = Euler buckling load, Eqn. 39.

The critical compressive stress of the column is then given by

$$\sigma_{cr} = \frac{\frac{cE_c}{(l/r)^2}}{1 + \left[\frac{cnE_c}{(l/r)^2 G_c} \right]} \quad (41)$$

where

$$r = \sqrt{\frac{I}{A}} = \text{radius of gyration}$$

and the other variables were defined with Eqns. 39 and 40.

Equation 41 can be simplified by considering the limiting case where

$$\frac{cnE_c}{\left(\frac{l}{r}\right)^2 G_c} \gg 1. \quad (42)$$

This condition is achieved in highly anisotropic composites where $\frac{E_c}{G_c} \gg 1$. Additionally, the condition in Eqn. 42 is obtained for relatively short specimens where $\frac{l}{r}$ is small so that the tendency for Euler buckling is also small. Under the condition of Eqn. 42,

$$\sigma_{cr} = \frac{G_c}{n}. \quad (43)$$

Equation 43, apart from the factor $\frac{1}{n}$, is the same as Eqn. 4, which assumes the composite fails in the shear instability mode.

Additionally, Chou and Kelly⁸⁸ used Eqn. 39 to determine c values of 3.34 and 16.14 for the IITRI and RAE specimens, respectively, both of which are described in the Compression Test Methods section within this chapter.

Wilkinson, Parry, and Wronski⁸⁹ investigated the mechanical properties of fiber-harness sateen (weft- or transverse-faced) and plain weave graphite/epoxy cloths over a range of gage lengths. Euler buckling analysis was found to be applicable for gage lengths in excess of ≈ 15 mm. The column was the specimen in the case of the sateen weave laminates and the longitudinal (warp) bundles

in the plain weave laminates. The failure process involved bundle detachment and kinking, similar to the mechanism operating in nominally uniaxially aligned fibrous composites. Their observations indicate that the surface bundles detach and delaminate.

Lee⁹⁰ presented an equation similar to Chou and Kelly.⁸⁸ Additionally, he stresses the importance of axial alignment; misalignment introduces a bending moment causing strain divergence on either face. He reported results that an eccentricity of 2.5% of the laminate thickness (0.095 mm for a 30-ply, 3.81 mm, laminate) reduces the apparent strength to 87% of the ultimate value.

To summarize, the strength predicted by Euler buckling corrected for shear deformation should be considered an upper limit for the compressive strength that can be experimentally measured for a given specimen of thickness, t , and column or gage length, l . In practice, one would expect to see compressive failures at lower stress levels than those predicted for Euler buckling unless specimens with long thin gage sections are used.

Related Studies

Whitney and Nuismer⁹¹ developed two stress fracture criteria for tensile loaded composite laminates containing stress concentrations (circular holes and straight center cracks). These criteria⁹¹ are based on two parameters (unnotched tensile strength, σ_o and a characteristic dimension), but do not require Linear Elastic Fracture Mechanics (LEFM). One criterion (Point Stress Criterion) assumes that failure occurs when the stress at a characteristic distance, d_o , from the discontinuity reaches the tensile strength σ_o of the unnotched material, while the other criterion (Average Stress Criterion) assumes that failure occurs when the average stress over some characteristic distance, a_o , reaches the unnotched tensile strength. These

criteria were subjected to further experimental scrutiny by Nuismer and Whitney.⁹² However, due to large scatter in the data, no conclusive statement concerning the accuracy of the models was presented. Although Whitney and Nuismer assumed the characteristic distances to be a material property independent of laminate geometry and stress distribution, it should be noted that these adjustable parameters have not yet been related to microstructural features and do not result from a mechanics analysis. In 1979, Nuismer⁹³ extended the average stress failure criterion to compression applications for countersunk fastener holes (both loaded and unloaded), with acceptable agreement between experimental data and theoretical predictions. However, again, no conclusive statements about the accuracy of the models were made.

Reifsnider, Stinchcomb, Bakis, and Yih⁹⁴ investigated the mechanics of the damage development process of notched composite laminates. The three aspects addressed include the local mechanics associated with the damage development sequence, global changes in the stress state near the notch that relax the stress concentration, and the mechanics associated with the residual strength after damage has occurred.

Two multidirectional graphite/epoxy laminates were used to investigate the fatigue response of notched composite laminates under fully reversed ($R = -1$) cyclic loads. The earliest damage detected in the specimens was matrix cracking parallel to the fibers in the vicinity of the stress concentration. In regions with dense matrix cracks in two adjoining plies, small delaminations initiated, grew, and coalesced along the matrix cracks, particularly where two cracks of different orientation cross. These authors observed that delaminations generally initiate the earliest and propagate the fastest at interfaces nearest to the surface of the laminate,

although they eventually appear in a similar fashion at all like interfaces through the laminate thickness. Additionally, they observed that laminate failure in all graphite/epoxy, low-amplitude cycled specimens was by compressive failure of the interior 0° plies after delaminations reduced the support provided by adjacent plies. Finally, they concluded that the residual compressive strength appears to be much more sensitive to damage development around a hole (or notch) than the residual tensile strength.

Renault, Valentin, Perez⁹⁵ investigated multidirectional notched graphite/epoxy laminates loaded in tension. Many of the results in this study are similar to those reported in Ref. 94. Macroscopic damage observed prior to final failure included matrix cracks parallel to the fibers and delaminations near the stress concentrator. A reduction of failure stress, described by Whitney and Nuismer^{91,92} for some lay-ups, was observed when the damage extended from the hole. A similar result was observed by Guynn¹ for compressive loading. Additionally, like Guynn¹ and Reifsnider et al,⁹⁴ these authors observed that the presence of significant damage, in the vicinity of the hole, contributed to modify the stress distributions and diminishes the stress concentrations near the hole. They propose that including these stress reductions in failure prediction models should improve the accuracy of these models.

Guz and Lapusta⁹⁶ assumed three-dimensional linearized theory for a piecewise-homogeneous medium to investigate the stability of a fiber in an elastic compressible matrix near a free cylindrical surface under small precritical deformations. The authors reference other uses of this method for similar stability problems: one fiber, two fibers, an infinite series, a double-periodic system of fibers in an infinite matrix, a fiber near a free plane surface, and also a fiber near a free cylindrical surface under finite deformations. However these references are not readily obtainable

in the United States. Their results indicate that as the fiber gets farther from the free surface, the critical buckling strain approaches that for a fiber in an infinite matrix. Although the fiber in a semi-infinite matrix followed the same trend, the critical strains were as much as 20% lower than those for this cylindrical model.

Burns, Herakovich, and Williams⁹⁷ used linear three-dimensional finite element analysis and the tensor polynomial failure criterion (Tsai-Wu) to predict that failure always initiates at the $[\pm\theta]$ interface at the hole edge for notched angle-ply laminates loaded in compression. The angular location, around the hole edge, of initial failure was shown to be a function of θ , the fiber orientation of the lamina. The dominating stress components initiating failure are the shear stresses τ_{12} and τ_{23} .

Lee⁸⁰ used Euler-Bernoulli beam theory to develop an analysis for predicting the influence of wavy patterns in the main load-carrying layers or wrinkled fibers on the laminate behavior under tensile loading. This analysis assumed linear material behavior. The main load-carrying layers or wrinkled fibers were assumed to be corrugated beams embedded in elastic foundations of various spring constants. Young's moduli for the different laminate configurations were determined experimentally and compared to the model predictions. The model predictions were in close agreement with the present experimental results including both extensometer measurements and moiré interferometry fringe pattern analysis. Furthermore, experimental results reported by other researchers were compared with this analysis showed reasonable agreement.

Microbuckling and Kinking

Pattnaik, Koczak, and Rogers⁹⁸ studied the failure mechanisms of unidirectional metal matrix composite (MMC) cylinders loaded in compression. The normal

mode of compression failure of these composites appeared to be kinking or multiple kinking, both in-plane and out-of-plane. The formation of kink bands are shown schematically in Fig. 14. Figure 14d shows the kink inclination, α , and boundary orientation, β , for both an in-plane and an out-of-plane simple kink. These authors postulate that the range of values for α and β will be a function of the post-failure deformation of the kink band, as shown in the graph in Fig. 15. Unlike graphite/epoxy composites, very few voids or delaminations were observed in these composites because the matrix is a ductile aluminum alloy. The voids created by fiber cracking are filled by metal flow under the high compressive stresses. However, the presence of voids, fiber waviness, and possible fiber/matrix debonding yielded compressive strength values much lower than those predicted by the existing theories of compression failure.

Chaplin⁹⁹ observed and characterized the shear deformation in unidirectional glass-reinforced composites as an "elastic instability." It is therefore not determined by strength considerations, but involves shear instability in a volume of material, not failure on a plane due to a resolved stress. The author's argument is dependent on the assumption that as the shear deformation increases, the angle of the band and the length of the fibers in the band do not change. Chaplin showed that the angle $\alpha = 2\beta$ if no volume change was assumed within the kink band. Experimental results for notched compression specimens showed some difficulty was experienced in controlling the fracture to give stable damage propagation. A strong tendency existed for interlaminar shear failures to propagate from the tip of the notch. Chaplin concluded that the mechanisms of energy absorption are readily identifiable as matrix shear and interfacial failure. The difficulty lies in making allowance for load carried by the shear band after failure. Additionally, Chaplin argued that in

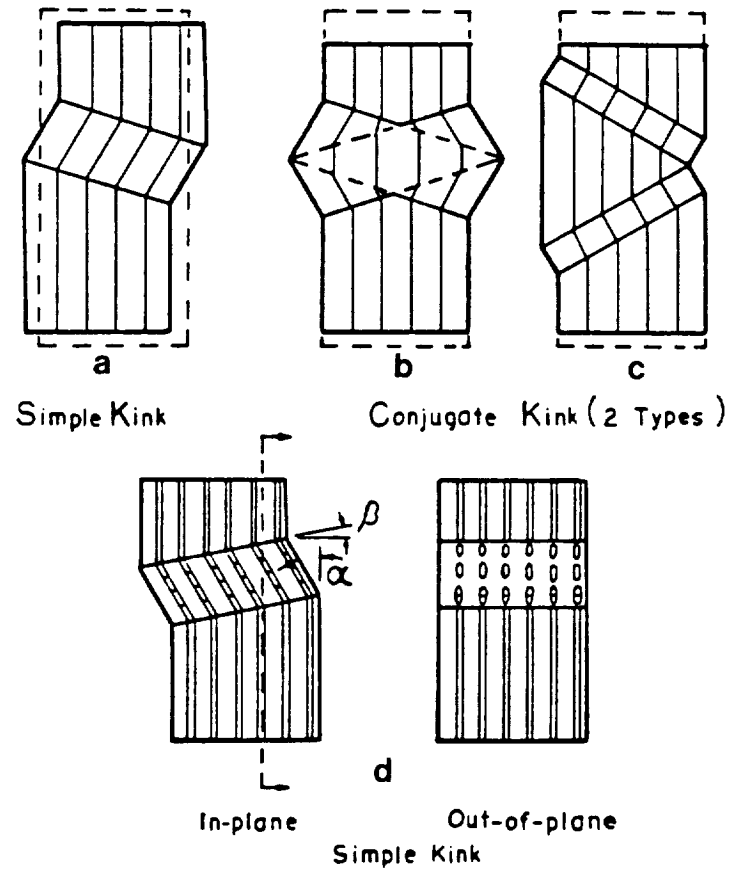


Fig. 14 Schematics describing kink bands.⁹⁸
 a) Simple kink.
 b) Conjugate kink, type 1.
 c) Conjugate kink, type 2.
 d) Notation for a simple kink, in-plane and out-of-plane.

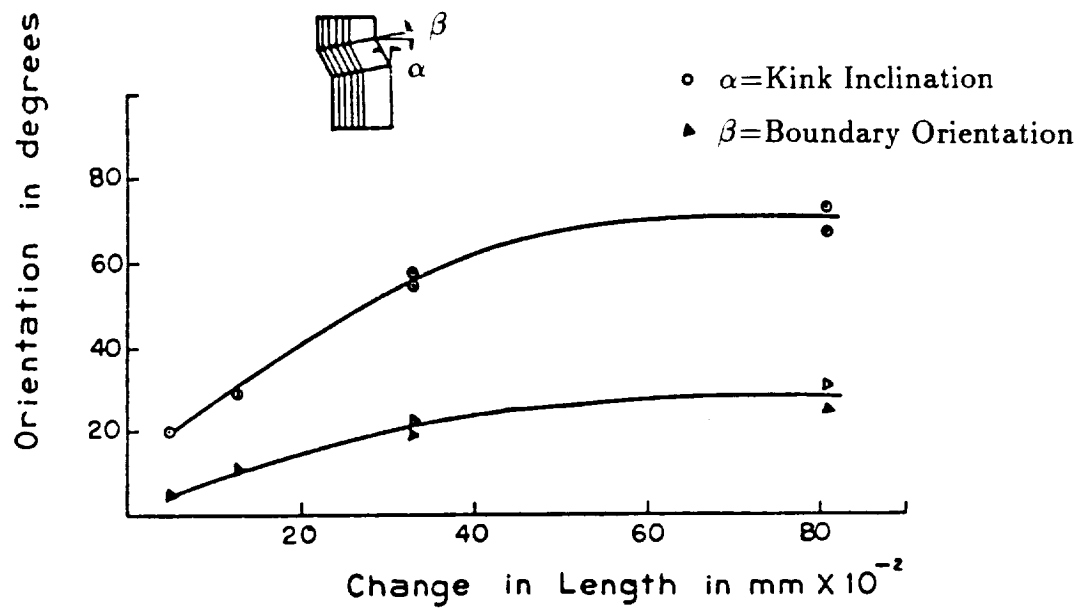


Fig. 15 Kink orientation relationship as a function of post-failure deformation, Δl .⁹⁸

the presence of a hydrostatic stress component, the expected effect would be an increase in compressive strength.

Parry and Wronski¹⁰⁰ studied the mechanisms of deformation and failure of carbon fiber-reinforced composites tested in three-point flexure. They observed a significant increase in acoustic output at the onset of nonlinear behavior on the load-deflection plot. Subsequent microscopic observations showed that the failure was initiated by fiber kinking near the compression roller. Kink growth with decreasing load, increasing deflection, and accompanying stress redistribution led to either flexural or interlaminar failure. In the latter, the growing kink initiated interlaminar cracks in resin-rich zones. These delaminations were not confined to the neutral plane. Finally, they suggested that kink initiation, involving microbuckling of fibers and shear of the matrix, should be associated with the onset of nonlinear deformation.

Parry and Wronski¹⁰¹ investigated kinking and compressive failure in unidirectional carbon fiber-reinforced composites. Based on their results, they suggested that a local surface condition initiates the first buckling and breakage of a group of fibers, which acts as the kink band. This kink band propagates by the buckling and failure of fiber groups ahead of it. Additionally, they concluded that the compressive strength properties are related to the strength, ductility, and toughness of the resin rather than its modulus.

Wronski and Parry¹⁰² evaluated the compressive failure and kinking in unidirectional glass-reinforced composites (GRC). Because the failures were catastrophic, it was difficult to estimate the size of the microstructural unit (bundle of fibers) which initially kinked. They postulated that even for straight fibers the role of the matrix and its effect on fiber microbuckling must be considered. According to these

authors, the buckling causes lateral displacement of the fiber bundles and causes pushing against the support of the matrix. If failure is initiated when the matrix support is lost locally (i.e. matrix yielding), continued loading causes localized gross deformation leading to longitudinal splitting along the bundle boundary. Based on this observation, Wronski and Parry believed that d (Eqn. 23) should be the bundle rather than fiber diameter. Additionally, they concluded that bundle buckling controlled the compressive strength of GRP unless the matrix yield strength was very high.

In Refs. 100–102, Parry and Wronski observed that in the presence of a superposed hydrostatic pressure, the compressive strength of unidirectional composites is increased. Parry and Wronski¹⁰⁰ observed that the hydrostatic pressure suppressed interlaminar cracking (delaminations) in three- and four-point bending tests, but fiber kinking still preceded failure. Additionally, in Ref. 101 they again reported that in the presence of hydrostatic stress, longitudinal splitting and “shear” failures (using in-plane shear specimens) were suppressed, and the effect was to increase the compressive strength. It should be noted that all failures were associated with the propagation of kink bands. These results agree with Chaplin’s⁹⁹ postulate.

Evans and Adler¹⁰³ used observations of carbon/carbon composites to identify the modes and morphology of kinking. Kinking has been attributed to three principle modes: (i) longitudinal compression, (ii) lateral compression, and (iii) lateral displacement or “shear.” The kink morphologies for longitudinal compression and lateral displacement (or shear) are very similar.

A thermodynamic analysis of kinking has accounted for the observed kink morphologies in terms of the strain energy and plastic work associated with the matrix phase. Specifically, minimization of the plastic work dictates the kink



inclination, α , while the minimization of the elastic strain energy determines the kink boundary orientation, β .

The mechanics of kinking were explored using a model for statistical fiber fracture and matrix stress enhancement. The appropriate fracture and deformation parameters were determined in-situ, and these parameters were used to obtain the critical kink formation stress. This expression confirmed that composites should be designed with a maximum resistance to shear kink formation by increasing the fiber fracture strength level and enhancing the matrix yield strength.

Potter and Purslow^{104,105} investigated the compressive failures of multidirectional composite laminates containing center holes. They reported that the first sign of damage (at 60%–70% of failure load, depending on lay-up) was protrusion of the discontinuous 0° plies into the hole. This damage gradually became more pronounced as the loading was increased. Additional associated and necessary damage included in-plane cracks running parallel to the 0° fibers and an area of interlaminar shear failure (localized delamination) at the ply interfaces. Further loading yielded in-plane and out-of-plane fiber microbuckling in the 0° plies. This microbuckling appeared to initiate at locations where splits or cracks, parallel to the fibers, existed in the adjacent 45° plies.

Marom, Davidovitz, Mittelman, and Roman¹⁰⁶ and Davidovitz, Mittelman, Roman, and Marom¹⁰⁷ investigated fracture mechanisms and failure modes of unidirectional Kevlar-reinforced epoxy composites, loaded in three-point bending. They reported the development of diagonal kink (shear) bands in the vicinity of the loading roller. The source of the kink bands is the compressive stress in that side of the specimen near the loading roller. The mechanism for their formation in Kevlar fibers is different than for graphite fibers. In graphite fiber composites,

the kink bands consist of broken pieces of fibers, and in Kevlar fiber composites, they consist of an assembly of kink bands in the individual filaments caused by the unique compression behavior of Kevlar fibers.⁵⁴

Rajendran, Rogers, and Koczak¹⁰⁸ studied the failure mode of alumina/aluminum composites under two loading conditions, an Instron testing machine (displacement-control) and dead-weight loading (load control). Both solid and hollow cylindrical specimens were tested. The typical failure mode, when tested in displacement-control, was kink band formation. These authors proposed that local fiber buckling, initiating at a local stress concentration (e.g. inclusions, voids, and resin-rich areas), and consequent shear deformation of the matrix leads to kinking. As expected, the specimens were crushed catastrophically when loaded in load-control. The experimental compressive strength was compared with theoretical predictions, all of which overpredicted by at least a factor of 2. The largest overprediction was by a factor of 22.

Waas and Babcock¹⁰⁹ completed a detailed experimental investigation to understand the initiation and propagation of failure in laminates in the presence of a stress raiser. They studied damage initiation and propagation throughout the entire load history via real time holographic interferometry and photomicrography of the hole surface. Post-failure examination of the damaged specimens was accomplished using ultrasonic inspection and an optical microscope. From this study, they concluded that the damage was found to initiate by a combination of fiber microbuckling and kinking, and delamination buckling was determined to be the mechanism by which damage propagates to catastrophic failure.

It should be noted that these authors observed much more out-of-plane buckling and delamination formation than reported in in Ref. 1. However, G_{Ic} for the

materials tested in Ref. 1 is much higher than that for the BP907 system in Ref. 109. This greater resistance to delamination may explain why local instability was more in-plane in Ref. 1 and more out-of-plane for Ref. 109. In the absence of delamination, in-plane fiber microbuckling requires only resin shear while out-of-plane fiber microbuckling requires out-of-plane displacement of the adjacent ply, which may be simpler or more difficult depending on the ply orientation and depth.

A very detailed study of the effects of fiber microbuckling and shear crippling on the compressive strength of composite materials has been completed in Refs. 110-114.

Starnes and Williams¹¹⁰ studied the failure characteristics of compression loaded graphite/epoxy structural components. Their results indicate that the strain concentrations near a circular hole in a graphite/epoxy laminate can cause the highly strained fibers near the hole to buckle locally. The paper does not state whether the buckling is in-plane or out-of-plane. However, from his micrographs, it appears to be in-plane. These buckled fibers can fail, and the resulting local damage propagates by a combination of shear crippling and delamination to fail the laminate. Good failure predictions were obtained when the Whitney-Nuismer⁹¹ approach was applied to their data.

Williams¹¹¹ summarized results similar to Ref. 110. He concluded that fiber microbuckling is governed by the stiffness properties of the matrix, the fibers, and the fiber/matrix interfacial bond.

Rhodes, Mikulas, and McGowan¹¹² observed a sequence of failure events for multidirectional laminates slightly different from that previously described in Ref. 110. To determine the sequence of failure events, these authors microscopically examined plies in several panels loaded to different percentages of the estimated

failure load. The first failure was observed in panels loaded to $\approx 85\%$ of the ultimate compressive load and was an interfiber matrix failure in the 0° plies (similar to longitudinal splitting in unidirectional laminates), an addition to the sequence of failure events in Ref. 110. It is anticipated that this failure is a shear failure of the matrix due to the high stress gradient in the vicinity of the hole. Specimens loaded to a higher percentage of the predicted failure load had regions of shear crippling in the 0° plies near where the interfiber matrix failure terminated. An estimate was made of the distance from the edge of the hole to the point where the shear crippling failure was initiated. This distance was approximately equal to d_o used in the Point-Stress Failure Prediction technique for the laminates. However, no attempt was made to accurately determine and correlate this distance with d_o .

Sohi, Hahn, and Williams¹¹³ investigated the compressive failure mechanisms of quasi-isotropic graphite/epoxy composites, and their results are very similar to those reported in Ref. 1 from a parallel study. They concluded that these failures were triggered by the kinking of fibers in the 0° plies. The kinking was followed by delamination and subsequent sublaminates buckling. Additionally, they reported that the kinking usually initiated at the specimen free edge and quite often in the vicinity of the tab ends. They proposed that kinking initiation at the free edge may be a result of the free edge effect or less lateral support provided for the 0° plies at the edge or a combination of these two effects.

Quasi-isotropic laminates were shown to have considerably higher failure strains than the corresponding unidirectional laminates. This improvement was attributed to the better lateral support provided for the 0° plies by the adjacent off-axis plies in quasi-isotropic laminates. Additionally, they observed that the in-plane kinking in the quasi-isotropic laminate was influenced by the stiffness of the off-axis plies

normal to the loading while the out-of-plane kinking was retarded by these off-axis fibers bridging over the kink band.

Hahn and Sohi¹¹⁴ investigated the buckling of a fiber bundle embedded in an epoxy resin to gain insight into compressive failure mechanisms in unidirectional composites. The fibers were embedded in two different resins, one relatively compliant and one relatively stiff. In both resins, the failure mode was found to be microbuckling of the fibers for the E-glass, T300 graphite, and T700 graphite fibers; however, the high-modulus P75 fibers failed in shear without any microbuckling. Buckling induced failure was most evident for the E-glass fibers, while the kinking type of failure (fibers are broken in only 2 locations) was most common for the T300 and T700 graphite fibers. Additionally, Hahn and Sohi observed that fiber fracture occurred immediately after fracture and that fiber/matrix debonding follows fiber buckling. Their observed failure strains and segment lengths of the bundle specimens followed the trends predicted by Lanir and Fung⁴⁵ for a single fiber embedded in an infinite matrix.

Hahn¹¹⁵ improved and combined previous models describing fiber microbuckling²¹ and kinking into one unified model for the compressive strength of unidirectional composites. He suggested that failure is the result of a sequential occurrence of fiber microbuckling, kinking, and fracture. Consequently, kink bands are frequently observed on failure surfaces.

Hahn suggested that when a fiber microbuckles, it pushes or pulls the neighboring fibers, and hence, a group of fibers will likely microbuckle in-phase with one another. As a result of in-phase or shear mode microbuckling, the matrix between fibers experiences shear deformation which provides resistance to further microbuckling. Eventually, with additional loading, the matrix yields, and the microbuckling

changes to kinking. When the matrix cannot support any additional shear, the fibers collapse, and the composite fails, usually catastrophically.

Hahn notes that this process is very localized, and quite often, initiation occurs at a free edge where the support of neighboring fibers is reduced. Once initiated, it then propagates inward. This result is consistent with the results of Guynn and Bradley in Refs. 1, 3, and 4.

The compressive strength for fiber microbuckling predicted in Ref. 21 was given in Eqn. 30. The assumption of fiber kinking at σ_c^* leads to

$$\alpha = \frac{2\tau_y}{\sigma_f^*} \quad (44)$$

where

$$\begin{aligned} \sigma_f^* &= \frac{\sigma_c^*}{V_f} = \text{fiber stress and} \\ \tau_y &= \text{shear stress level corresponding to } \gamma_y. \end{aligned}$$

Additionally, the shear strain in the kink band is given by

$$\gamma^* = \sin \alpha - (1 - \cos \alpha) \tan \beta. \quad (45)$$

It should be noted that any kink band formation caused by fiber failure rather than matrix yielding cannot be described by this analysis. He applied this analysis to data in Ref. 116 with reasonable results, although they could not be verified experimentally because of measurement difficulties. Hahn's analysis qualitatively predicts the effects of constituent phases, including interface and defects on the compressive failure of unidirectional composites.

Kulkarni et al⁴⁹ also observed kink-band formation in the longitudinal and transverse planes, inclined at 55°–60° to the horizontal axis. Lateral restraint provided by the addition of glass fibers in the 90° direction prevented the longitudinal slip plane, but involved a slip in the transverse plane.

Budianski⁸⁷ reviewed the application of kink band theories to the compression failure of composite materials. Three of the theories presented yielded $\beta = 0$ as the critical kink angle (see Fig. 16). He concluded from the results of these theories that the most important factors affecting the kink strength of composites are high composite stiffness in strength and shear. The sensitivity to fiber misalignment is large. One problem concerning Budianski was that experimental observations by different researchers have shown that the kink angle, β , varies from $\approx 10^\circ$ to $\approx 40^\circ$. Budianski showed that localized deviations from the ideal fiber alignment having no particular geometrical bias induce patterns of angular misalignment due to elastic distortion that arrange themselves into inclined domains. These rotations then induce plastic kinking into similarly inclined kink bands.

Failure follows rapidly after plastic deformation begins, so that it is reasonable to identify the failure stress, σ , with the kinking failure stress, σ_s . The consequent correlations between σ_s and the kink angle, β , are

$$\tan \beta = \pm \left[\frac{1 - \sigma_s/G}{E_T/G} \right]^{\frac{1}{2}} \quad (46)$$

for long wave imperfections and

$$\tan \beta = \pm (\sqrt{2} - 1) \left[\frac{1 - \sigma_s/G}{E_T/G} \right]^{\frac{1}{2}} \quad (47)$$

for short wave imperfections where

- σ_s = stress perpendicular to the fiber direction,
- G = elastic shear modulus of the composite, and
- E_T = transverse modulus of the composite.

Equations 46 and 47 predict kink angles between 10° and 35° as shown in Fig. 16.

From the literature on compression failures, it is easy to get the impression that fiber microbuckling and kinking are competing mechanisms. However, recent

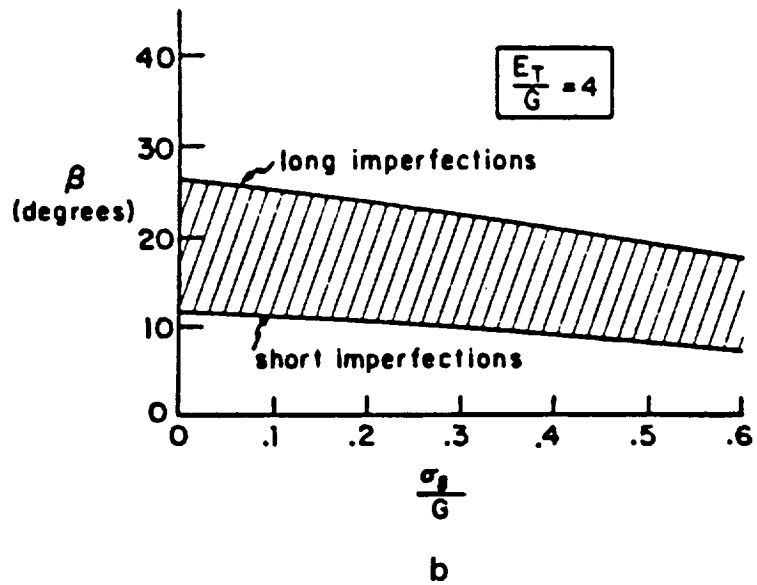
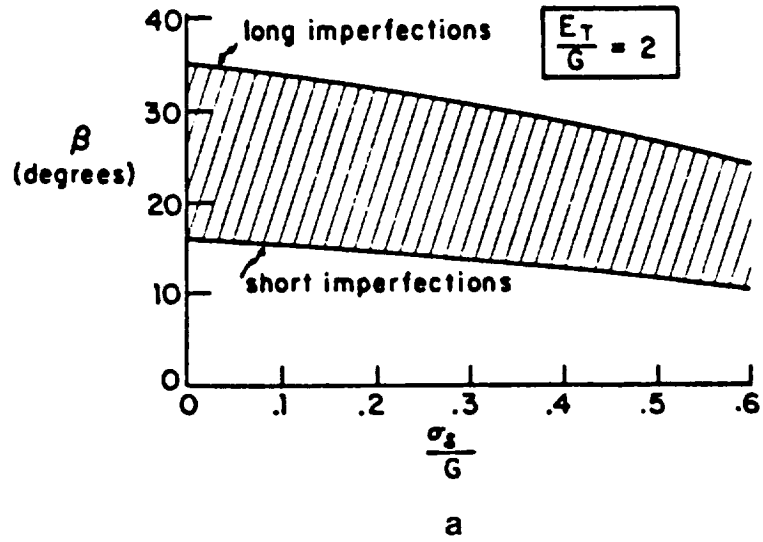


Fig. 16 Estimated kink-band inclinations.⁸⁷
 a) $\frac{E_T}{G} = 2$.
 b) $\frac{E_T}{G} = 4$.

work has indicated that fiber microbuckling occurs first, followed by propagation of this local damage to form kinking.^{1,109,115} Fiber microbuckling and the resultant kinking may form in-plane or out-of-plane. It typically initiates at free edges at the perimeter of the laminate or at an internal hole where local support to resist fiber microbuckling is reduced.

In summary, it has been shown that fiber waviness, fiber/matrix interfacial bonding, and the composite shear yield strength are all important parameters in determining the stress level at which fiber microbuckling initiates. The shear modulus of the matrix, which essentially controls the shear modulus of the composite, was also shown to be an important factor in the determination of the compressive strength of composite materials.

Effects of Matrix Resin Properties on Compressive Strength of Composite Materials

The shear modulus and the nonlinear constitutive behavior are both important in determining the compressive strength of a composite material when the failure mode is fiber microbuckling or macrobuckling, as indicated by Eqns. 1-18, 24-30, and 39-43. Hahn and Williams²¹ illustrated the increase in compressive strength that accompanies an increase in resin modulus (see Figs. 17 and 18). Although the compressive strength in Figs. 17 and 18 is presented as a function of the resin tensile modulus, the shear modulus would show the same trend since it is proportional to the tensile modulus. Similarly, a high resin modulus usually correlates with a high resin yield strength. In contrast, the tensile strength is relatively insensitive to the resin modulus. The consequence of the sensitivity of the compression strength to resin modulus and the insensitivity of the tensile strength to resin modulus is that the ratio of compressive strength to tensile strength increases as the resin modulus

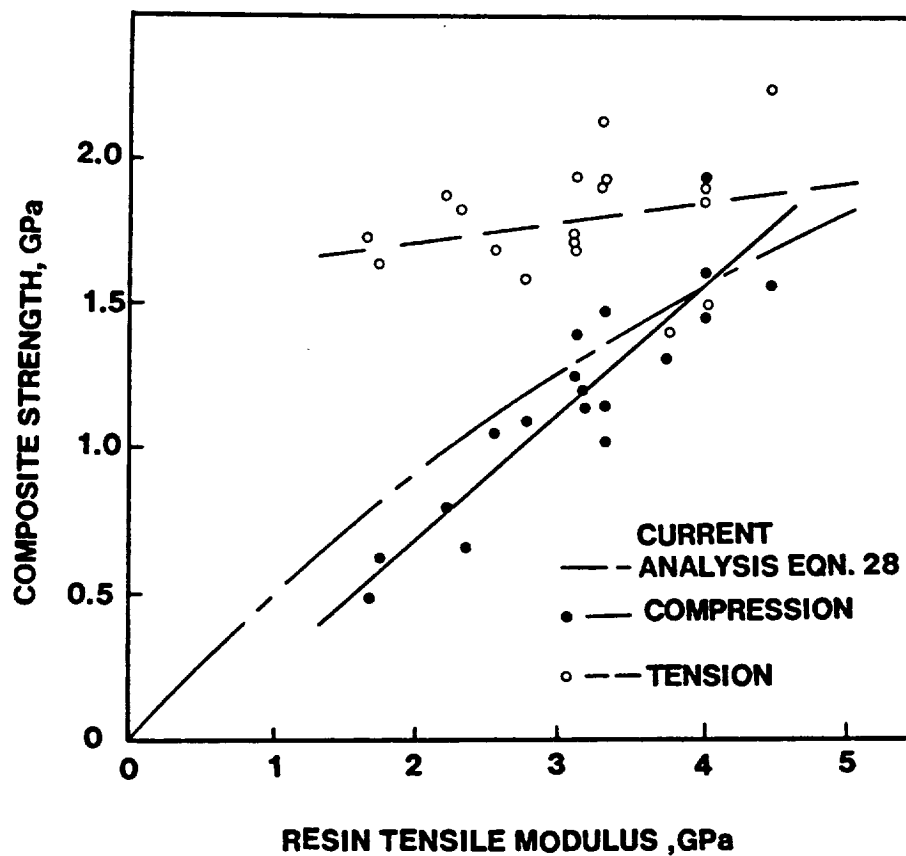


Fig. 17 Effect of resin tensile modulus on composite tensile and compressive strengths.²³

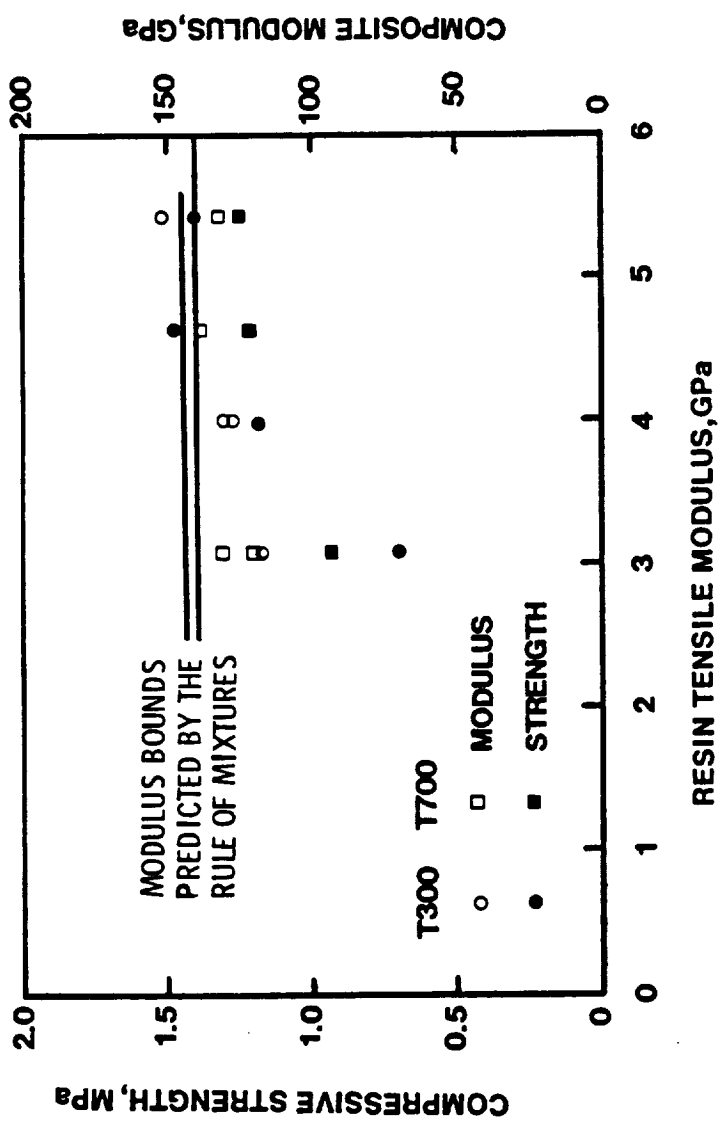


Fig. 18 Effect of resin tensile modulus on compressive modulus and strength of T300 and T700 composites.²³



increases.

Although the unidirectional compressive strength of graphite/epoxy and metal matrix composites has been shown to correlate with the matrix modulus,⁴⁰ the results by Chang^{117,118} for thermoplastic matrix composites show no such correlation. Chang states that the matrix modulus is not the key determinant for compressive strength of unidirectional carbon/thermoplastic matrix composites. He suggests that other factors such as fiber/matrix adhesion, matrix penetration, fiber alignment, and shear stability are more important.

Mabson, Wharram, Tennyson, and Hansen¹¹⁹ investigated the effects of moisture content and elevated temperature on the compressive strength of graphite/epoxy composites. The sandwich beam test method yielded compressive stiffness values consistently higher than the "pure" compressive data (IITRI type fixture) for all environmental conditions studied. Elevated temperature ($\approx 100^\circ\text{C}$) combined with high moisture content ($\approx 1.7\%$ H_2O) resulted in no significant change in compressive stiffness but a large reduction in compressive strength (21%–43%), relative to ambient condition strengths. This compressive strength reduction may be attributed to a degradation in the shear modulus and/or shear yield strength of the matrix.

Sternstein, Yurgartis, and Srinivasan¹²⁰ studied the out-of-plane bending failure of thermoplastic matrix composites, including the effects of the graphite fibers on the ability of the matrix to deform and yield. These composites were evaluated using a four-point bending jig that allowed observation of the edge failures in the light microscope.

For these thermoplastic matrices, they observed time dependent fiber fracture which occurs in buckles or kink bands. Additionally, all failures initiated on the

compression side of the bending sample. It appeared that the enhanced ductility of a thermoplastic (relative to a thermoset) composite resulted in ply buckling instability as a dominant failure mode. This result indicates that compressive properties are critical for thermoplastic and thermoset composites. However, thermoplastic matrix composites are more vulnerable due to their lower modulus and/or yield strength of the resin.

Sternstein et al¹²⁰ observed large scale yielding as evidenced by shear bands and crazes or relatively large displacements of fibers only in resin-rich regions of the specimens. Observation of the delaminations indicated that matrix deformation was limited to a small interfacial region and that the crack propagated by shear (mode II) rather than tension (mode I).

Bishop¹²¹ reported slightly different failure modes for carbon fiber/PEEK (APC-1) composites, compared to carbon fiber/epoxy composites. The failure mechanisms are slightly different because of the lower shear modulus, the lower compressive strength, and the greater shear strength of the carbon fiber-reinforced PEEK. Compressive failures of fibers or shear failure across the fibers is likely to occur in PEEK composites, and failure modes due to shear forces parallel to the fibers are less likely to occur.

Miyano, Kanemitsu, Kunio, and Kuhn¹²² investigated the fracture strength of unidirectional CFRP for various directions and modes of loading over wide ranges of temperature and strain rates, in conjunction with similar investigations on the epoxy resin matrix. Additionally, the role of the matrix resin on these fracture strengths, based on SEM observations of the fracture surfaces, was discussed. Time and temperature dependence of tensile, compressive, and flexural strengths in the CFRP for both longitudinal and transverse directions exhibited the same viscoelas-

tic behavior as the matrix epoxy resin. However, the longitudinal compressive and flexural fracture strengths of unidirectional CFRP was dominated by the deformation properties of the matrix, whereas the transverse tensile, transverse compressive, and flexural fracture strength of unidirectional CFRP was strongly affected by the fracture strength of the matrix.

These authors observed that for transverse tension, compression, and bending, the resin adheres to the fracture surfaces at 60°C while much less resin adhered to the fracture surfaces at 180°C. Additionally, they confirmed, using Dow's³¹ equation, that the microscopic mode of failure is fiber microbuckling in both longitudinal compression and flexural in every case.

Greszczuk's²⁶ results presented in Figs. 2a-2c show that increasing Young's modulus or the shear modulus of the resin significantly increases the composite strength, and if increased enough, the failure mode is then governed by the compressive strength of the reinforcement rather than microbuckling of the reinforcement.

Lee⁹⁰ conducted an experimental study of compression properties of a number of reinforced thermoplastic composites to determine the effects of these matrices on compression strength and to provide a direct comparison with carbon reinforced epoxides. His results indicate that unidirectional APC-2 gave similar compression strength to both epoxide (XA-S/Fibredux 914C and XA-S/MY750) systems tested. However, no comparison is given regarding the matrix moduli of these materials.

Hahn and Sohi¹⁰⁹ observed that fiber microbuckling is more uniformly distributed in a very soft resin, but quite localized in stiff resins. The results of Williams¹¹¹ indicate that a higher shear modulus resin should also increase the strain at which microbuckling initiates.

Recall that in 1963, Fried⁸⁴ proposed that in the limit the point at which the

resin "yields," or flows, determines the load carrying capacity of the composite. He also hypothesized that resin physical characteristics (stiffness, shear strength, shear rigidity, and tensile strength) and content affect the stability of the reinforcement. Experimental results in a subsequent study⁸⁵ supported these initial hypotheses. In particular, the compressive strength varied directly with the resin compressive yield strength for unidirectional filament wound materials. Results from an even later study⁸⁶ showed that resin yield will be the failure mode only in laminates with low void contents and good reinforcement/matrix interfaces. Piggott and Harris⁵⁴ showed that the matrix yield stress is an important factor controlling compression properties of fiber-reinforced composites. However, beyond a certain limiting matrix yield stress, the compressive strength remains constant or declines. They postulated that this phenomena may indicate a change from matrix control to interface control of compressive strength.

The results of many researchers (Refs. 26, 33, 54, 65, 84-86, 111, 117-122) have shown that the matrix shear modulus is the matrix property with the most significant effect on compressive strength. However, it is difficult with experimental correlations to determine whether resin initial modulus, tangent modulus, or yield strength controls fiber microbuckling since it is essentially impossible to vary these mechanical properties independently.

The reduction in the compressive strength of a composite material that results from the nonlinear constitutive behavior in the shear stress versus shear strain relationship of the resin has been noted by many investigators (Refs. 26, 67-69, 73-79). Hahn and Williams²⁶ observed that although the elastic moduli of the resin varied significantly, the tangential moduli at failure were relatively consistent. This observation implies that the tangential modulus at failure, rather than the initial

elastic modulus, controls the compressive failures in composite materials. Wang's⁶⁷ results support this argument. The analytical work of Hayashi and Fujikake⁴⁷ indicates that the compressive strength of unidirectional composite materials may be reduced as much as 50% due to the nonlinear behavior of the resin. Kurashige's⁶⁵ analysis predicted a decrease in the ultimate compressive strength as the resin shear modulus decreased and also as the thickness of the resin-rich layer between the axial and cross layers increased.

Shuart and Williams⁷⁴ observed in-plane shearing between the fiber and matrix (i.e., matrix shearing) as the primary compression failure mechanism for an all $\pm 45^\circ$ laminates with a hole. However, the matrix shearing contribution to failure appeared to be reduced and delamination observation increased as the percentage of 90° plies in the laminate thickness was increased.

Sohi et al¹¹³ investigated the effects of resin toughness and modulus on the failure modes of graphite/epoxy composites. They observed that tougher, and thus more ductile, resins resisted delamination following fiber kinking better than the more brittle resins, even though the tougher resins allowed fiber kinking at lower strains. Regardless of the resin, failure initiation in all seven systems studied was believed to be governed by the same mechanism, fiber kinking in the 0° plies. The mode of propagation following the initial fiber kinking changed with resin ductility. For brittle resins, delamination immediately follows fiber kinking initiation. On the other hand, tougher resins allow more stable fiber kinking and resist any delamination growth.

In summary, a high compressive strength in a composite material may only be obtained when microbuckling and macrobuckling are inhibited. Both analytical and experimental results indicate that a large shear modulus and yield strength are

necessary to obtain a high compressive strength.

Effects of Fiber Properties on Compressive Strength of Composite Materials

The tensile strength of the fiber is always the limiting factor when determining the tensile strength of a composite material. However for compressive loading, the compressive strength of the fiber is significant only when fracture is initiated by fiber shear failure. In this section, the effects of the mechanical properties of the fiber, the volume fraction of the fiber, and the waviness of fiber on the compression strength of composite materials is explained.

Mechanical Properties of Fibers

Three investigations,^{25,81,82} cited in this review of the compressive strength of composite materials indicate fiber shear as the failure mode. However, more recent studies^{1,4,68,69,115} indicate that fiber microbuckling is the limiting factor in compression strength, even when a relatively stiff epoxy matrix is used.

Van Dreumel¹²³ indicated that aramid fibers, compared to carbon fibers, may be very attractive, especially for compression loaded structures. He noted that the Young's modulus, E_f , for a unidirectional carbon fiber laminate is a linear function of the applied stress while it is constant for aramid fiber laminates. The data presented, considering specific stiffnesses and strengths, showed that carbon fibers are favorable for stiffness critical designs while aramid fibers are preferred for strength critical designs. However, when considering buckling behavior, structural stability is governed by stiffness. In particular, \sqrt{E} is the important parameter. Although the compressive strength ratio of carbon to aramid fiber unidirectional laminates is 6, the Euler buckling strength ratio is only 1.3.

Turner and Cogswell¹²⁴ reviewed the mechanical property data base for a range of continuous fiber/PEEK composites to demonstrate the diversity of thermoplastic composite materials that may be produced. It is important to note that with most of the fibers, high efficiencies (80–90%) of fiber property utilization are observed. Experimental results indicate that the on-fiber nucleation of crystallization explains the very close physical proximity of the resin molecules to the fiber surface. Although this is a necessary condition for good adhesion, it is not a sufficient guarantee of good bonding.

Piggott and Harris⁵⁶ measured the unidirectional compression strength of hybrid composites reinforced with carbon, Kevlar, and/or glass fibers. All of the hybrid composites showed interactions, deviating from rule of mixtures behavior. The observed interactions were beneficial for the case of strength and detrimental for the case of stiffness. Microscopic examination of compression tested specimens showed highly localized transverse failure surfaces for carbon/carbon hybrids. Kevlar composites failed by a highly localized shear kinking band with no longitudinal splitting. In carbon-glass hybrids, the kinking in the adjacent glass-rich regions appears to inhibit the progress of cracks that have initiated in the carbon.

Williams,¹¹¹ based on his results, hypothesized that the higher bending strains in a buckled fiber initiate local failure. His results showed that composites made with higher tensile strain fibers exhibited higher laminate strengths.

Hahn and Sohi¹¹⁴ observed that low-modulus fibers (e.g. E-glass) are more susceptible to fiber microbuckling (probably due to greater fiber waviness), while intermediate-modulus graphite fibers are more likely to fail by fiber kinking. High-modulus fibers (P75) failed by fiber shear.

DeTeresa et al¹¹⁶ studied the mechanical anisotropy of an aramid polyamide

fiber, Kevlar 49, in tension, compression, and torsion. Ratios of tensile-to-compressive strength, tensile-to-shear strength, and tensile-to-shear modulus of 5:1, 17:1, and 70:1, respectively, were measured for Kevlar 49. The high anisotropy of mechanical behavior for Kevlar 49 is illustrated by the measured 70:1 ratio of tensile-to-shear modulus. After compression loading, they observed lateral shifts of fiber segments, similar to slip bands in metals, called fiber kinking. No sinusoidal microbuckling instabilities were observed for these fibers. This observation implies that the microbuckling theories of unidirectional composites which satisfactorily predict the compressive strengths of composites based on isotropic glass fibers may have no bearing on the compressive strength of Kevlar composites.

The relatively low values of shear strength and modulus for Kevlar 49 may account for the relatively low in-plane shear modulus, strength, and interlaminar shear strength of Kevlar composites. For composites having a strong fiber/matrix interfacial bond, failure may occur within the Kevlar fiber, rather than in the matrix or at the interface. Therefore, any analysis of mechanical performance for Kevlar composites should consider that the fiber shear modulus and strength are in the range of matrix shear properties.

In Refs. 126, 127, and 128, DeTeresa et al modelled straight, highly oriented polymer fibers as a collection of chains that interact laterally. The critical stresses to buckle this fiber or collection of chains are calculated using a shear instability analysis (similar to those in Refs. 33, 34, and 36) developed to predict the compressive strengths of fiber-reinforced composites. This buckling stress is predicted to be equal to the shear modulus of the fibers, similar to Eqn. 4 for composites, and is the limiting value of fiber compressive strength. It should be noted that stresses to initiate shear instability are dominated by properties of the elastic foundation and

not the column. As with composites, the theory overestimates the fiber compressive strength, but a correlation of shear modulus with axial compressive strength is predicted. The authors consider it remarkable that this simple analysis, disregarding defects and inhomogeneities, predicts within an order of magnitude of the measured compressive strengths.

Based on their results, DeTeresa et al¹²⁸ suggest a possible hierarchy for compressive failure of composite materials. On a macroscopic scale, failure may occur by a global elastic instability first analyzed by Leonard Euler. At a smaller scale, namely the lamina, failure may occur by fiber microbuckling, modelled with an elastic instability analysis in Refs. 33, 34, and 36. Finally, the authors have shown that the microstructure of polymer fibers undergoes an elastic instability that manifests itself as kink banding.

Hahn and Williams²³ summarized the reported compressive fiber failure modes as shear, kinking, and bending. High modulus graphite fibers fracture in shear along a maximum shear plane. These shear failures are typically observed only in a composite with a very stiff resin and minimum fiber waviness, two factors that inhibit fiber microbuckling. When these fiber shear failures occur, the composite compressive strength is very nearly equal to its tensile strength. Fiber strength dominates compressive strength in both of these cases. In this particular case, the compressive strength is predicted using Eqn. 31, and a linear relationship between compressive strength and fiber volume fraction should be observed. Kevlar fibers, on the other hand, fail in a kink mode because of Kevlar's characteristic weak bond in the radial direction that permits individual fibers to split into fibrils. Both shear failure and fiber kinking are characteristic failure modes for fibers with well-aligned fibrillar structure. However, the low ductility for graphite fibers leads to shear

fracture or microbuckling while the development of fibrils for Kevlar fibers results in kinking. These kinking failures are indicative of a low compressive strength fiber and thus, a low compressive strength composite. Brittle fibers with amorphous structure (e.g., glass) usually fail in bending, starting from the tension side. Medium to high-strength fibers can also fail in bending. Bending failures occur after fiber microbuckling in which case the fiber strength does not play an important factor in determining the compressive strength.

It has been established from this review that fiber tensile modulus is not a particularly significant variable in the determination of the compressive strength of composite laminates. The fiber tensile modulus appears explicitly in Eqns. 1, 2, 7, 13–17, 24, and 25, which give the compressive strength for fiber microbuckling failures. The fiber shear modulus is explicit in Eqns. 5, 11, and 12 which also predict the compressive strength for fiber microbuckling failures. However, the contribution of the fiber modulus to the calculated compressive strength in each case is small, unless the fiber shear modulus is the same order of magnitude as the matrix shear modulus and/or the microbuckling wavelength is less than or equal to ten times the fiber diameter.

Indirectly, the fiber modulus may be more important in the determination of the composite's compressive strength if it reduces the fiber waviness, which would increase the compressive strength (see Eqns. 16–30). However, fiber waviness ultimately depends on fiber stiffness which is more sensitive to fiber diameter than fiber modulus.

Fiber Volume Fraction

All of the models for compressive strength described previously in this review indicate that the fiber volume fraction, V_f , is an important variable in determining



compression strength. When V_f does not appear explicitly in the equations, it is present implicitly through the composite shear modulus G , as shown in Eqn. 5. The monotonic increase in compressive strength with increasing fiber volume fraction has been observed by a number of investigators (see Refs. 47, 51, 54, 55, 23, 63, 81, 84, 85, and 88).

The results from Hayashi and Fujikake,⁴⁷ showing the variation in compression strength as a function of fiber volume fraction, are given in Fig. 19. The results shown in Figs. 19a and 19c indicate that an optimum fiber volume fraction ($\approx 50\%$ – 60%) yields a maximum compressive strength for polyester composites. The results in Ref. 47 suggest that the fiber distribution is also important. A heterogeneous fiber distribution facilitates interfacial failures at a lower average fiber volume fraction than a homogeneous distribution. The fiber volume fraction results shown in Fig. 19 are more continuous than those presented by Rosen.³³

Piggott and Harris⁵⁴ tested unidirectional Kevlar-, carbon-, and glass-reinforced composites. The results indicate that both strength and modulus are a linear function of volume fractions for moderate volume fractions, $\leq 30\%$ and $\leq 45\%$, respectively. It is interesting to note that beyond these fiber volume fractions, both the strength and modulus appear to decrease and that deviations from the rule of mixtures type behavior increase. At 30% fiber volume fraction, the Kevlar fiber composites behaved as though their compression modulus and strength were significantly smaller than their tensile values, while carbon fiber composites were only slightly more compliant and weaker in compression than tension.

Piggott and Wilde⁵⁵ concluded that the compressive strength of fibers play a very important role in the compressive strength of steel-reinforced composites when failure occurs at strains that are less than the matrix yield strain. They observed

Table 1. Young's Moduli of Fibers.

Fiber	E_f kg./mm ²
For Polyester Specimen	7.28×10^3
For Epoxy Specimen	7.13×10^3

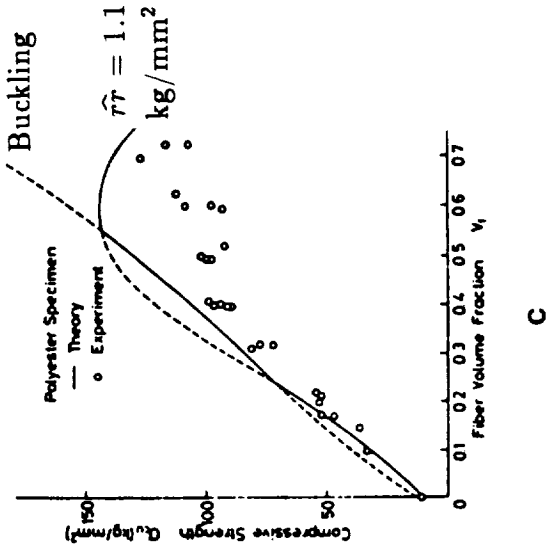
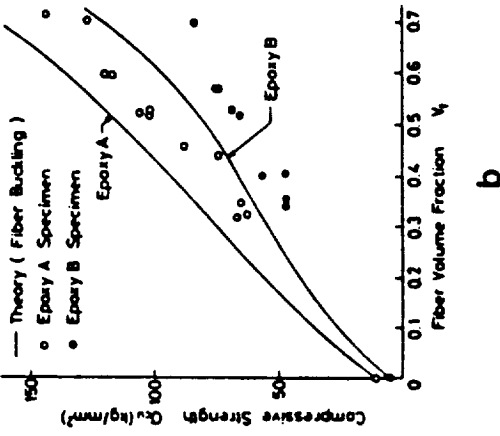
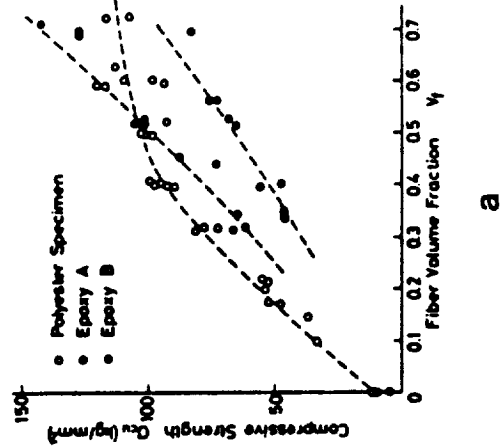


Fig. 19 Compression strength as a function of fiber volume fraction.⁴⁷

- a) Experimental data.
- b) Comparison of fiber buckling theory and experimental data for two epoxy composites.
- c) Comparison of fiber buckling and interfacial debonding failure theories.

a linear relationship, sufficiently predicted using rule of mixtures (Eqn. 31), for the variation of the composite compressive strength as a function of fiber volume fraction.

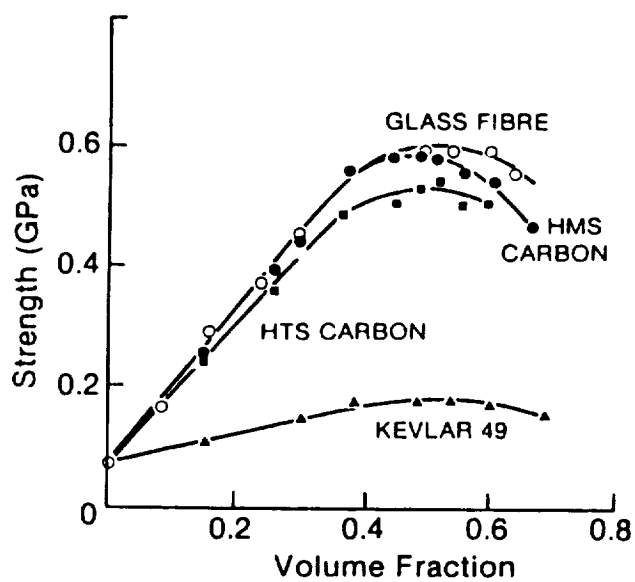
Martinez et al⁵⁷ also showed that both the composite compressive strength and modulus are very linear functions of fiber volume fraction, as shown in Fig. 20, up to a limiting V_f . The limiting fiber volume fractions for strength and modulus are $\approx 40\%$ and $\approx 50\%$, respectively. Beyond these limiting values of V_f , both the strength and modulus decrease. They attributed these maximums in compressive strength at intermediate V_f values to interfacial bond failures (see Eqns. 32–34). This result also suggests (like Ref. 47) that fiber distribution is important. A heterogeneous fiber distribution would facilitate interfacial failures at lower V_f values than a homogeneous fiber distribution.

Kurashige⁶³ predicted increasing compressive strength with increasing fiber volume fraction (see Fig. 4).

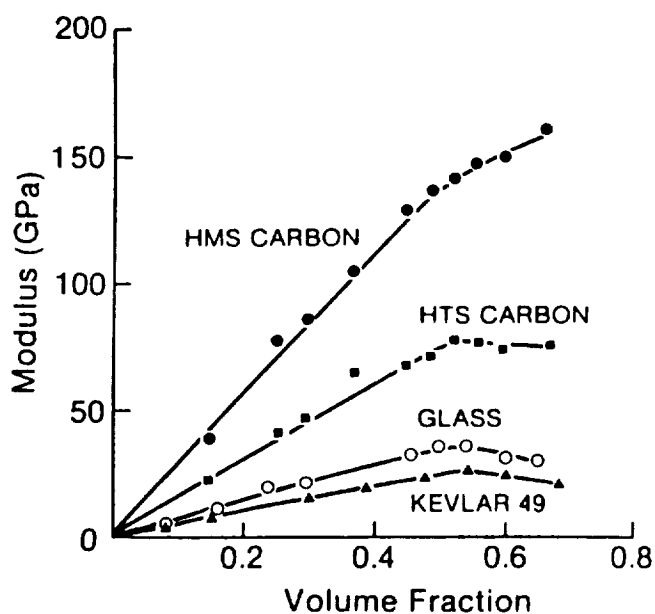
Hancox⁸² observed a very linear increase in unidirectional compression strength as the fiber volume fraction of the carbon/epoxy composites was increased, as shown in Fig. 21. The results shown in Fig. 21 would be predicted by Eqn. 31 for a fiber shear failure mode, which was the fracture mode described by Hancox.

Fried⁸⁴ concluded that the effectiveness of the reinforcement is influenced by the nature and physical characteristics of the basic material (compressive modulus and strength, shear characteristics, and degree of ductility or brittleness) and by geometric factors (straightness, distribution uniformity, and cross-sectional shape). A later study⁸⁵ showed that the compressive strength was maximized when the fiber volume fraction was optimized.

Chou and Kelly⁸⁸ found that compressive strength increased with increasing



a



b

Fig. 20 The effects of fiber volume fraction on compressive strength and modulus.⁵⁷

- a) Compressive strength as a function of fiber volume fraction for various fibers embedded in a polyester resin.
- b) Compressive modulus as a function of fiber volume fraction for various fibers embedded in a polyester resin.

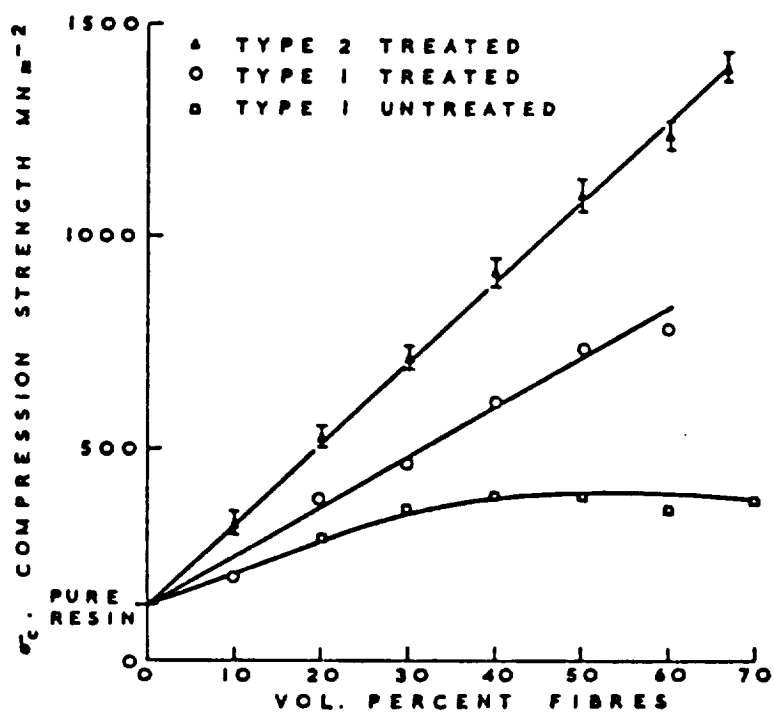


Fig. 21 Variation of compression strength as a function of fiber volume fraction.⁸²

fiber volume fraction in a manner consistent with Eqn. 41 for fiber microbuckling as shown in Fig. 22. The solid lines (IITRI) and broken lines (RAE) are the predictions for the upper and lower limits of the slenderness ratio. Greszczuk⁵³ observed a similar trend, shown in Fig. 23. In both cases, the trend in the experimental data was well described by Eqn. 41, although the absolute values of the experimentally determined strengths were lower than the predictions. The theoretical values probably overpredict because Eqn. 41 neglects the effects of initial fiber waviness and resin nonlinearity at the higher stress levels.

Lager and June⁴⁰ varied the fiber volume fraction from 0.05 through 0.46 for boron/epoxy laminates. They observed excellent correlation between the trends of the data and the theoretical predictions from Eqns. 1 and 3. However, measured compressive strengths were only 63% of those predicted. As postulated by Rosen,³³ the shear mode failure dominated the higher fiber volume fraction composites.

Fiber Waviness

Models that attempt to describe the effect of fiber waviness on compression strength have been reviewed in two sections of this chapter (see Eqns. 16–30, and Refs. 26, 57, 61–66, 67–80).

Woven fabrics are attractive materials for load-bearing structural applications for many reasons. Two-dimensional woven fabrics provide more balanced (compared to unidirectional tape) in-plane material properties, provide excellent impact resistance because of the 2-D reinforcement, handle easily, and have relatively low fabrication costs.¹²⁹ Fabrics may be made using many types of weaves.¹³⁰ Each 2-D weave consists of two sets of yarns. By definition, warp corresponds to the length direction of the fabric, and fill or weft corresponds to the width direction of the fabric.

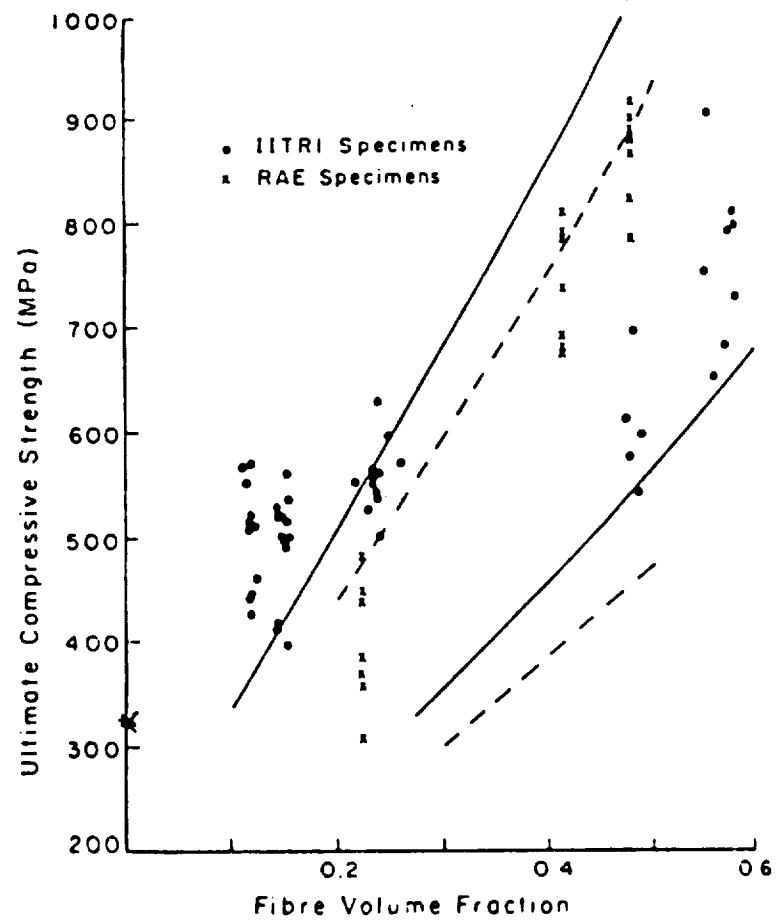


Fig. 22 Compressive strength of composites obtained from IITRI and RAE test fixtures.⁸⁸

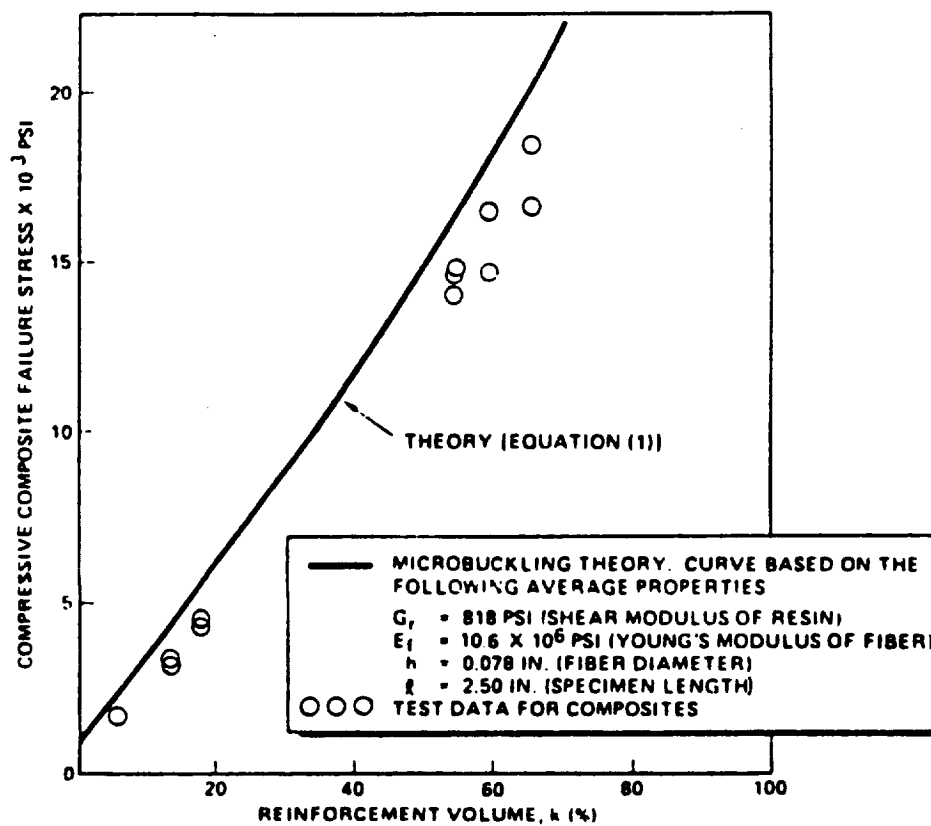


Fig. 23 Test-theory comparison of compressive microbuckling strength of circular fiber-reinforced composites having various fiber volume fractions.⁵³



Yau and Chou¹²⁹ evaluated the open hole strength of carbon/PEEK and carbon/epoxy composites with drilled and molded holes. Molded holes were formed in the prepreg layer-by-layer, prior to curing. These holes were made by allowing the woven fiber bundles to wrap around a steel pin. Different hole diameters were formed by using different diameter steel pins. The authors attribute the strengthening mechanisms in the molded holes to an increase in local fiber volume fraction and the maintaining of fiber continuity. The molding process forces the fibers to have a higher local in-plane fiber waviness. However, this curvature is convex away from the free surface, which should inhibit local in-plane fiber microbuckling into the hole. Their results indicate that the molded hole, compared to the drilled hole, greatly increased (up to 47%) the open hole tensile and compression strengths of woven fabric composites (epoxy and PEEK). Considering the normalized strength ($\sigma_{notch}/\sigma_{unnotched}$), PEEK composites exhibited higher tensile and compressive strengths than epoxy composites.

Schapery¹³¹ attributed a 10% increase in the tensile secant modulus for AS4/3502 composites to the straightening of initially wavy fibers.

Greszczuk's²⁶ results, presented in Fig. 21d showed that wavy fibers significantly reduce the compressive strength of composites.

Martinez et al⁵⁷ used a fixture to deliberately kink fibers (induce fiber waviness) during the processing of the composite. This kinking process increased the fiber curvature, and they expressed the waviness using the radius of curvature. Smaller radii of curvature corresponded to larger amplitude waviness. These results are shown in Fig. 5 and indicate that fiber waviness significantly reduces the compressive strength.

Kurashige⁶³ predicted that increasing fiber waviness caused a reduction in

compressive strength (see Fig. 4). However, his strength results were not bounded for the extension mode of fiber microbuckling.

Kurashige⁶⁵ predicted a sharp increase in compressive strength as the nondimensional buckling wavelength was increased from 0 to approximately 0.3, at which point the compression strength reaches a plateau.

Davis⁶⁷ observed primarily in-plane fiber waviness for boron/epoxy composites. The ratio of the initial amplitude of the waviness to the length, $\frac{a_0}{L}$, was measured to range from 0.001875 to 0.003750. His calculations indicate that this magnitude of fiber waviness caused the compressive strength to be reduced by 65% from the ideal strength expected for a composite with perfectly straight fibers.

Wang^{67,69} back calculated, using an iterative technique, $\frac{a_0}{L}$ to be 0.0108 for AS1/3501-6 graphite/epoxy composites. As expected, this value is larger than that for the boron⁶⁷ fibers since the carbon fibers are more slender and more compliant. Wang's observed compressive strength (1.2 GPa) is less than 20% of the G_{12} value (7.1 GPa),¹²⁵ indicating the significant degradation in compression strength that results from fiber waviness.

It is generally noted that composites made with thermoplastic matrices have a compressive strength that is a smaller fraction of their tensile strengths than composites made with thermoset matrices. This difference is generally attributed to a weaker fiber/matrix interfacial bond in thermoplastic composites. However, it is quite possible that another contributing factor is the greater tendency for fiber waviness in thermoplastic composite materials. These composites are more susceptible, compared to thermosets, to fiber waviness because they are processed at higher temperatures, pressures, and viscosity levels. The results reviewed in this section and compared with the models clearly indicate that fiber waviness leads to

premature fiber microbuckling due to larger matrix shear stresses at a given applied compressive stress.

Effects of Interfacial Bonding on Compressive Strength of Composite Materials

The characteristics between the fiber and the matrix control the properties of the final composite. Thus, the effects of the interfacial bond on compression strength is important and is reviewed in this section.

Landro and Pegoraro¹³² accurately evaluated the shear strength at the fiber/matrix interface for two materials, polyethersulphone (PES) and polyetherimide (ULTEM), using a statistical method based on the measurement of the mean critical fiber length. Postmortem SEM examination showed bare fibers, indicating that the chemical bond between the fiber and matrix was weaker than the matrix strength. However, the experimental data showed that the limiting interfacial shear strength was approximately equal to the matrix shear yield stress. They attributed this interfacial strength to the differential thermal shrinkage of the fiber and matrix which gives rise, at the interface, to a pressure that increases the Van der Waal's forces. Additionally, they concluded that this shrinkage phenomena was most important because of the high transition temperatures (softening) of the thermoplastics investigated.

Lanir and Fung⁴⁵ showed that the prebuckling separation of the fiber and the matrix, debonding, decreases the buckling load and may affect the postbuckling behavior of the fiber.

The interfacial failure analysis by Hayashi and Fujikake⁴⁷ assumed that the composite fails when the maximum tensile stress at the fiber/matrix interface ($\hat{r}r_{cr}$) reaches the interfacial bonding strength. Figure 19c is a comparison of experimental

data with the fiber buckling and interfacial bonding failure theories developed in Ref. 47. These authors have indicated that the flattening of the compressive stress versus fiber volume fraction curve (see Fig. 19c) is a result of poor interfacial bonding.

Additionally, Hayashi and Fujikake⁴⁷ and Greszczuk⁵¹ have indicated that both fiber arrangement and fiber volume fraction are important in the determination of compression strength. Different arrangements result in different nearest neighbor distances between fibers which influences the magnitude of the interfacial stresses. Consequently, fiber arrangement is more critical in composites containing relatively weak fiber/matrix interfaces. This result also suggests that a homogeneous fiber arrangement, which maximizes the distance between fibers (for a given fiber volume fraction), will make composites less susceptible to longitudinal splitting.

Kulkarni et al⁴⁸ developed a fiber microbuckling model that included the effect of an imperfect fiber/matrix interfacial bond (Eqns. 11-12). The results of this analysis are shown in Fig. 24. Although no quantitative conclusions are made, it is clear that the significance of the interfacial strength increases with increasing fiber volume fraction. For the case of poor adhesion, increasing the fiber volume fraction is actually detrimental to the composite compressive strength.

Greszczuk⁵¹ predicted the transverse tensile strength of glass/epoxy, graphite/epoxy, and graphite/phenolic composites using constituent properties and microstructure of the composite (Eqns. 32 and 33). This analysis indicates that a reduction in the transverse tensile strength (e.g., a poor fiber/matrix interfacial bond) causes a reduction in the compressive strength.

In Greszczuk's⁵³ nearly perfect composites, he observed fan-shaped internal helical cracks initiating at the fiber/matrix interface. The failure appeared to



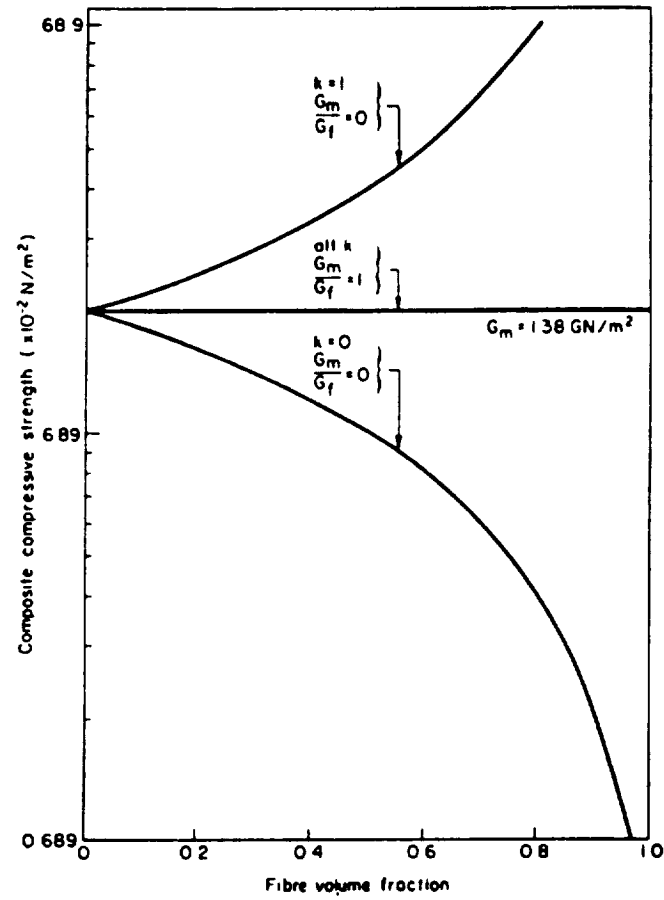


Fig. 24 Variation of composite compressive strength with fiber volume fraction for good interfacial bonding ($k = 1$) and for poor interfacial bonding ($k = 0$).⁴⁸

initiate at the fiber/matrix interface, to propagate along the interface, and then terminate in a helical crack. These experimental observations led to an additional study on the effect of the fiber/matrix interface on compressive strength. As a first approximation, Greszczuk assumed that the shear modulus of a composite with unbonded fibers was equal to the shear modulus of a solid containing cylindrical voids in the amount equal to the amount of unbonded fibers. Experimental data did not correlate well with this analysis. The test/theory ratio of strengths ranged from ≈ 0.84 – 0.92 .

Greszczuk's explanation for the mechanism that causes fiber/matrix debonding is as follows. Because of the differences in Poisson's ratios between the fibers and the matrix, transverse stresses are induced when a composite is subjected to compressive loading in the fiber direction. Even though the induced tensile stresses at the fiber/matrix boundary are small compared to the applied axial compressive stresses, so is the transverse tensile strength compared to the axial compressive strength. Thus, it is possible for the induced transverse tensile stresses to cause fiber/matrix debonding leading to longitudinal splitting (an interaction failure) and a reduction in the ultimate compression strength.

Martinez et al⁵⁷ varied the interfacial bond strength of unidirectional glass-polyester composites by using different fiber surface treatments. These results are shown in Figs. 5 and 25. The results in Fig. 5 show that poor fiber/matrix adhesion has a detrimental effect on the compressive strength of composites. Figure 25 shows the compressive strength as a function of fiber volume fraction for composites with good and poor fiber/matrix adhesion. Again, a significant reduction in compression strength is observed for composites with poor fiber/matrix interfaces. These trends are similar to those reported by Hayashi and Fujikake.⁴⁷

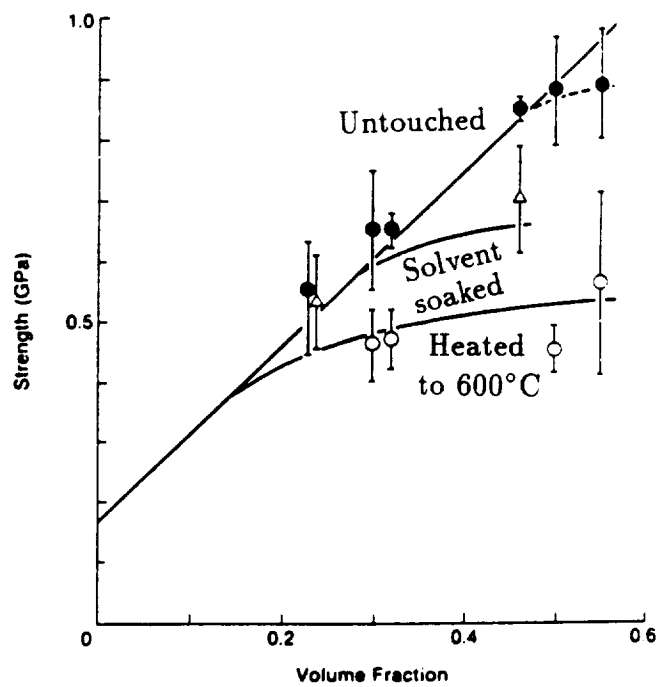


Fig. 25 Effect of interfacial bonding on the compressive strength of glass/polyester composites.⁵⁷

Hancox⁸² also observed a flattening of the compressive stress versus fiber volume fraction curve (see Fig. 21) for composites made with non-surface treated fibers. He reported that the fracture mode for these specimens was usually massive delamination. Poor interfacial bonding, associated with non-surface treated fibers, probably caused the flattening of the data in Fig. 21 which is very similar to that reported by Hayashi and Fujikake⁴⁷ (shown in Fig. 19c). He concluded that poor adhesion between the fibers and the matrix produces composites weaker in compression than those produced with strong fiber/matrix interfaces.

Fried⁸⁶ studied filament wound [0/90], laminates. In this study, he observed that orthogonal materials fail in shear and compression by debonding at the reinforcement/matrix interface. Experimental results showed that the laminate compressive strength was inversely proportional to the void content.

The trends presented in this section indicate that poor interfacial bonding may degrade the compressive strength in two ways. First, it allows failure to occur by longitudinal splitting due to differential Poisson's contraction between the fiber and the matrix.^{24,51,53} Poor interfacial bonding may lead to a reduction in the transverse tensile strength^{53,132} or the matrix ultimate strain²⁴ which results in a reduction in the compressive strength, as calculated in Eqns. 32-34. Second, it can effectively reduce the composite shear modulus, G , and allow fiber microbuckling at a lower compressive stress level, as indicated in Eqns. 4, 5, and 11 (Refs. 24, 51, 68, 69).

Environmental Effects on Compressive Strength of Composite Materials

It has been reported that elevated temperature causes a reduction in compression strength of composites by degrading the shear modulus of the resin¹¹⁹ and the fiber/matrix interfacial bond.¹²² Thus, a brief survey of the literature, describ-

ing the effects of temperature on the compressive strength of composite materials follows.

Ewins and Potter¹³³ illustrated the effects of temperature and humidity (see Fig. 26) on the unidirectional compressive strength of carbon fiber-reinforced plastics (CFRP). They postulated that if the fiber shear failure mode remains dominant, the compressive strength will decrease only slightly with increased temperature, probably due to a decrease in the matrix contribution to strength. However, as temperature increases, the matrix shear modulus and fiber/matrix interfacial bond strength decrease, and at some critical temperature the failure mode changes to one governed primarily by fiber instability (see Fig. 26a.).

The absorption of moisture causes matrix plasticization, a reduction in the matrix modulus, and a reduction in the fiber/matrix interfacial bond strength. Again, following a failure mode change to one of fiber instability, further moisture absorption and a corresponding reduction in shear modulus are likely to result in a rapid reduction in compression strength. The hypothetical combined effect of temperature and moisture absorption is illustrated in Fig. 26b.

Malik, Palazotto, and Whitney¹³⁴ investigated graphite/PEEK (APC-1) quasi-isotropic composites at 21°C, 121°C, and 149°C in tension and compression. These authors reported a rapid reduction in moduli at the glass transition temperature (135°C) of this material and reduced fiber/matrix adhesion at the higher temperatures.

Ramey, Palazotto, and Whitney¹³⁵ continued the test program of Ref. 134 to compare the notched strength (tension and compression) of quasi-isotropic graphite/PEEK (APC-2) and graphite/epoxy composites at 21°C, 121°C, 135°C, and 149°C. This discussion is limited to the results for APC-2 composites. The

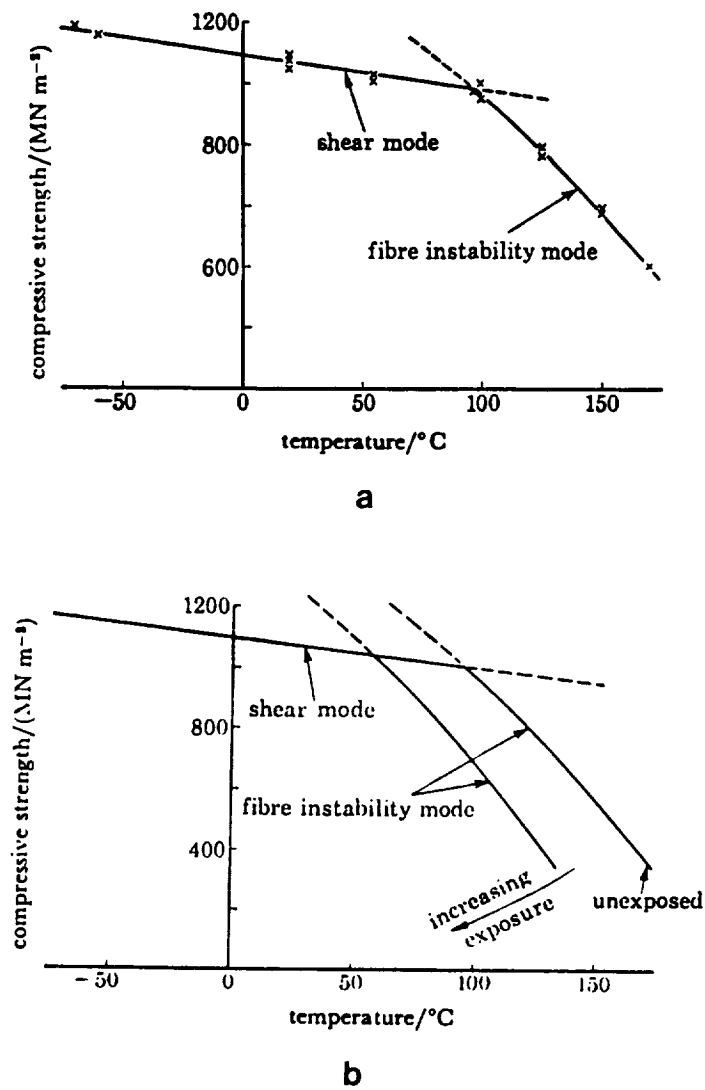


Fig. 26 Environmental effects on the unidirectional compressive strength of CFRP¹³³

a) Experimentally determined variation of compressive strength with temperature.

b) Expected variation of compressive strength with temperature-humidity exposure.

results indicate that APC-2 composites are less resistant to compression loading than tensile loading over the entire range of temperatures. For a given hole diameter, both the tension and compression strengths are reduced as the temperature is increased. However, the tension strength does not illustrate a strength reduction until very near the glass transition temperature, T_g , and this strength reduction is smaller than that for the compression strength. For the graphite/epoxy laminates, the notched tensile strength increases with temperature. This result is attributed to a reduction in the local stress concentrations at the notch, caused by the higher temperatures, that allow the laminate to become tougher than at room temperature where the matrix is brittle.

The compression specimens tested at room temperature broke into two pieces at failure, while those tested at the higher temperatures remained in one solid piece. This failure pattern supports the idea that the room temperature matrix supports the fiber more efficiently than the elevated temperature matrix. The room temperature system stores more energy and thus, releases more energy at failure, large enough to cause catastrophic failure of the specimen.

Postmortem examination of the failure mechanisms indicates that fibers in the 0° surface ply have failed in-plane into the notch and also out-of-plane of the laminate, an intra-laminar failure. Matrix deformation between the 0° crippled fibers and the adjacent 90° ply was attributed to inter-laminar stresses.

Observation shows that the matrix fails in at least a partially cohesive mechanism. Although the fiber/matrix adhesion is reduced at elevated temperatures, the matrix failure was more ductile and also more cohesive than adhesive. Examination of the matrix deformation at the previously mentioned $0/90$ interface indicates that at elevated temperatures, the matrix flows, providing less fiber support and

less load transfer as it becomes more fluid. The consequent inter-lamina strength reduction and reduced fiber support are believed to account for the compression strength reduction for APC-2 composites at elevated temperatures.

Kar, Herfert, and Kessler¹³⁶ investigated AS1/3501-6 multidirectional composites and also found a breakdown of the fiber/matrix bond, leading to reduced compressive strengths, under conditions of elevated temperature and high humidity.

Ewins and Ham²⁵ reported a change in the failure mode from fiber shear to fiber microbuckling at approximately 100°C. They attributed this mode change to a reduced matrix shear modulus and an altered matrix constitutive behavior, thus providing less support for the fibers.

Potter and Purslow^{104,105} observed a reduction in fiber/matrix interfacial bond strength due to hot-wet conditions. In the room temperature-dry specimens, failure occurred within the matrix while in the hot-wet specimens, failure occurred at the fiber/matrix interface. They concluded that hot-wet conditions cause a massive loss of interlaminar shear and axial compressive strengths because of the reduced bond strength and modulus.

In conclusion, the results presented in Refs. 25, 104, 105, and 133–136 indicate that environmental conditions (elevated temperatures and moisture content) cause a reduction in compressive strength of composite materials. This strength reduction has been attributed to degradation of the fiber/matrix interfacial bond¹²² and a reduction in the matrix moduli.¹¹⁹



CHAPTER III

EXPERIMENTAL PROCEDURES

This chapter describes the materials and experimental techniques used in this dissertation research. The materials description also includes the numerous stacking sequences chosen for this investigation. In the methods section, specimen geometries, test methods, damage progression investigation, x-radiography, scanning electron microscopy (SEM), sectioning studies, and material property characterization are described in detail.

Materials

The primary material selected for this investigation is APC-2, an Aromatic Polymer Composite manufactured by Fiberite Corporation — An ICI (Imperial Chemical Industries) Company.¹³⁷⁻¹⁴² APC-2 is an advanced structural composite composed of continuous carbon fibers and “Victrex” PEEK (Polyetheretherketone) semi-crystalline thermoplastic matrix. Compared with other types of thermoplastic resins, PEEK has a potentially higher service temperature, $\approx 121^{\circ}\text{C}$, and is unaffected by solvents.

The glass transition temperature, T_g , for PEEK is 143°C , and the melting temperature, T_m , is 335°C . A compatible high strain carbon fiber (AS4) has been chosen for this composite system. The carbon fibers are well dispersed and thoroughly wetted in the PEEK matrix to give a fiber content of 61% by volume and 68% by weight. APC-2 is recognized for its specially developed interface science to provide effective stress transfer between the fibers and the matrix, and thus, the full properties of the carbon fiber are realized. This thermoplastic system was selected for this investigation because the compression strength of thermoplastics

in general is a primary concern for industry applications. Typically, thermoplastics have compression strength values approximately 50% less than the observed tensile strength, compared to 75–80% for graphite/epoxy systems.

Literature regarding the mechanical property data base for the thermoplastic composites, in particular APC-2, includes mechanical property characterization (Refs. 117, 118, 123, 137, 138, 139), the effects of processing variables on mechanical properties,^{117,137,140,141} the effects of fiber characteristics on mechanical properties,¹²³ and the effects of matrix properties on mechanical properties.^{117,118} The effects of the crystallinity on the mechanical properties is described in Ref. 140. The morphology of the PEEK resin is described in Refs. 137 and 142. A second material, AU4U/PEEK, was designed by Hercules and ICI for this investigation. AU4U/PEEK is an experimental poor interface material. The AU4U/PEEK used the Hercules non-surface treated/unsized fiber batch 707-4D. This fiber is equivalent to AS4 in mechanical properties, but does not have any surface treatment. Although the AU4U fiber did not run as well as the AS4 fiber in the ICI impregnation unit, the prepreg had the standard resin content of $32 \pm 3\%$ by weight.

To evaluate the factors that affect the initiation of fiber microbuckling, the laminate stacking sequence has been varied systematically. A relatively simple baseline stacking sequence, $[(\pm 45/0_2)_3 / \pm 45/0]_s$, has been selected. Two 0° plies were stacked together to facilitate observation of fiber microbuckling initiation. Systematic variations of this stacking sequence allow for a detailed study of the effects of supporting fiber orientation, initial fiber waviness, interfacial bond strength, and resin-rich regions between plies. For consistency, these variations were made through the laminate thickness. Experimental results¹⁴³ indicate that the strength of symmetric composite laminates containing identical ply orientations

may be strongly dependent on the detailed stacking sequence. Consequently, the Pipes and Pagano analysis¹⁴³ was used to verify that the interlaminar peel stresses for each stacking sequence were not unusual values.

The complete test matrix, including all variables (supporting ply orientation, initial fiber waviness, interfacial bond strength, and resin-rich regions) is shown in Table I. The following discussion summarizes the laminates tested to determine the effects of each of the previously mentioned independent variables on fiber microbuckling initiation. The laminate identification letters (LID) are included on each table. These LIDs are used throughout the dissertation for shorthand reference to the various laminates and stacking sequences.

Table II details the laminates used to study the effects of the local constraint (supporting ply orientation) on fiber microbuckling initiation. Five stacking sequences of APC-2 were used to vary the support to the 0° fibers. The $\pm 45^\circ$ plies in the baseline stacking sequence (*A*) were replaced with either $\pm 15^\circ$ (*C*), $\pm 75^\circ$ (*D*) plies, or 90_2° (*E*) plies. Additionally, the 45s and 0s were interchanged in one laminate (*B*) to establish the effect of the free surface (and consequent reduced support) on fiber microbuckling initiation.

Table III lists the three laminates designed to evaluate the effects of initial fiber curvature on fiber microbuckling initiation. Note that the baseline lay-up has been altered slightly for this study. The APC-2 baseline lay-up has become $[\pm 45/0/90]_3$, (*K*) so that the theoretically straight 0/90 tape plies in this stacking sequence may be replaced with Quadrax $\langle 0/90 \rangle$ interlaced plies, where $\langle \rangle$ designates one interlaced ply. Quadrax Unidirectional Interlaced Tapes¹⁴⁴ were formed by interlacing ribbons or strips of APC-2 prepreg. Ribbons may vary from 3.175 mm to 12.7 mm in width. Ribbons for this investigation were 3.175 mm wide. The Quadrax process is different

Table I. Composite Laminate Material Test Matrix.

LID	Stacking Sequence	Variable Investigated
A	$[(\pm 45/0_2)_3/\pm 45/0]_s$	Baseline APC-2
B	$[(0_2/\pm 45)_3/0/\pm 45]_s$	Interchange 0's and 45's to observe surface 0's
K	$[\pm 45/0/90]_{3s}$	Theoretically "straight" fibers
KQ8	$[\pm 45/\langle 0/90 \rangle]_{3s}$	Replace 0/90 with Quadrax $\langle 0/90 \rangle$, 8-harness, compare fiber waviness effects
KQ1	$[\pm 45/\langle 0/90 \rangle]_{3s}$	Replace 0/90 with Quadrax $\langle 0/90 \rangle$, 1-harness, compare fiber waviness effects
F	$[(\pm 45/0_2)_3/\pm 45/0]_s$	Use non-surface treated AS4 fibers in PEEK to provide a poor interface
C	$[(\pm 15/0_2)_3/\pm 15/0]_s$	Vary support to 0's
D	$[(\pm 75/0_2)_3/\pm 75/0]_s$	Vary support to 0's
E	$[(90_2/0_2)_3/90_2/0]_s$	Vary support to 0's
G	$[(\pm 45/f/0_2/f)_3/\pm 45/f/0]_s$	Vary resin rich region: $f = 0.0254$ mm, one layer of PEEK film
H	$[(\pm 45/f_3/0_2/f_3)_3/\pm 45/f_3/0]_s$	Vary resin rich region: $f = 0.0254$ mm, one layer of PEEK film
I	$[\pm 45]_{2s}$	Measure G_{12} , tension tests
J	$[\pm 45]_{8s}$	Measure G_{12} , compression tests
OG	$[0_{24}]$	Measure G_I , G_{II} , and IFSS, commercial APC-2
OP	$[0_{24}]$	Measure G_I , G_{II} , and IFSS, experimental AU4U/PEEK

Table II. Effects of Supporting Ply Orientation.

LID	Stacking Sequence	Variable Investigated
<i>B</i>	$[(0_2 / \pm 45)_3 / 0 / \pm 45]_s$	Vary support to 0's
<i>C</i>	$[(\pm 15 / 0_2)_3 / \pm 15 / 0]_s$	Vary support to 0's
<i>A</i>	$[(\pm 45 / 0_2)_3 / \pm 45 / 0]_s$	Baseline lay-up
<i>D</i>	$[(\pm 75 / 0_2)_3 / \pm 75 / 0]_s$	Vary support to 0's
<i>E</i>	$[(90_2 / 0_2)_3 / 90_2 / 0]_s$	Vary support to 0's

Table III. Effects of Initial Fiber Waviness.

LID	Stacking Sequence	Variable Investigated
<i>K</i>	$[\pm 45/0/90]_{3s}$	Theoretically "straight" fibers
<i>KQ8</i>	$[\pm 45/\langle 0/90 \rangle]_{3s}$	Replace 0/90 with Quadrax $\langle 0/90 \rangle$, 8-harness, compare fiber waviness effects
<i>KQ1</i>	$[\pm 45/\langle 0/90 \rangle]_{3s}$	Replace 0/90 with Quadrax $\langle 0/90 \rangle$, 1-harness, compare fiber waviness effects



from traditional weaving in that the fibers are impregnated first and then interlaced rather than weaving the fiber tows and then impregnating the resin. Consequently, the process is only applicable for thermoplastic composites. Two degrees of waviness and thus, interlacing, were selected: (i) 8-harness Quadrax and (ii) plain weave, 1-harness Quadrax.

The interfacial bond strength was varied by using two different materials, both with the baseline stacking sequence, $[(\pm 45/0_2)_3/\pm 45/0]_s$. One panel was made with APC-2 which has a strong interfacial bond, and the other panel was made with AU4U/PEEK, an experimental poor interface material designed for this investigation. Because the AU4U fibers are equivalent to the AS4 fibers in mechanical properties but do not have any surface treatment, the only difference between the two systems was the level of interfacial adhesion between the fiber and the PEEK matrix.

The effect of the resin-rich regions (Table IV) was evaluated by adding layers of PEEK resin film at each $-45/0$ interface through the thickness of the baseline stacking sequence. Due to cure temperature and pressure, it is difficult to distinguish ply boundaries in unidirectional APC-2; thus, it is assumed that the thickness of the resin-rich regions between plies in the baseline laminate are negligible. In the stacking sequences, the addition of the resin film is denoted by "f." Two different thicknesses, 0.025 mm (f) and 0.075 mm (f_3), of resin film were added to the laminates; these resin-rich regions were the consequence of the addition of one ($i = 1$) and three ($i = 3$) layers of resin respectively.

Methods



Table IV. Effects of Resin-Rich Regions.

LID	Stacking Sequence	Variable Investigated
<i>A</i>	$[(\pm 45/0_2)_3 / \pm 45/0]_s$	Baseline APC-2, no PEEK film added
<i>G</i>	$[(\pm 45/f/0_2/f)_3 / \pm 45/f/0]_s$	Vary resin rich region: $f = 0.0254$ mm, one layer of PEEK film
<i>H</i>	$[(\pm 45/f_3/0_2/f_3)_3 / \pm 45/f_3/0]_s$	Vary resin rich region: $f = 0.0254$ mm, one layer of PEEK film

Compression Specimen Geometry

The compression specimen was 2.54 cm wide by 10.16 cm long with a semi-circular notch (3.175 mm diameter) at each free edge, centered along the gage section. The gage length for this specimen was 2.54 cm. A schematic of the notched compression specimen is shown in Fig. 27. Preliminary experimental results, detailed in Ref. 145, indicate that reducing the gage length from 5.08 cm (used in Refs. 1-4) to 2.54 cm does not introduce significant end effects but does minimize specimen bending and the incidence of Euler buckling. It should be noted that for the end-loading type test methods, the effects on the stress field in the test section are less pronounced than stress concentrations that are a consequence of the shear loading mechanism inherent in the IITRI fixture. The notch was polished with jeweler's files to facilitate the observation of fiber microbuckling initiation. These specimens were strain-gaged front and back (at the specimen's center) with longitudinal strain gages to monitor any specimen bending and to provide accurate measurement of the global or remote strains associated with fiber microbuckling initiation. For the room temperature tests, 21°C, the strain gages were bonded to the specimens using M-Bond 200 adhesive and catalyst, and for the high temperatures tests, 77°C and 132°C, M-Bond 600 adhesive was used. Both adhesives and the catalyst were manufactured by Micromeritics Group, Inc.

Compression Test Methods

Although many compression test methods for composite materials are summarized in Chapter II of this dissertation, the author suspects that a large percentage of these methods inhibit the natural failure mode for a laminate by supporting the specimen's test section in a manner that suppresses or prevents fiber microbuckling.

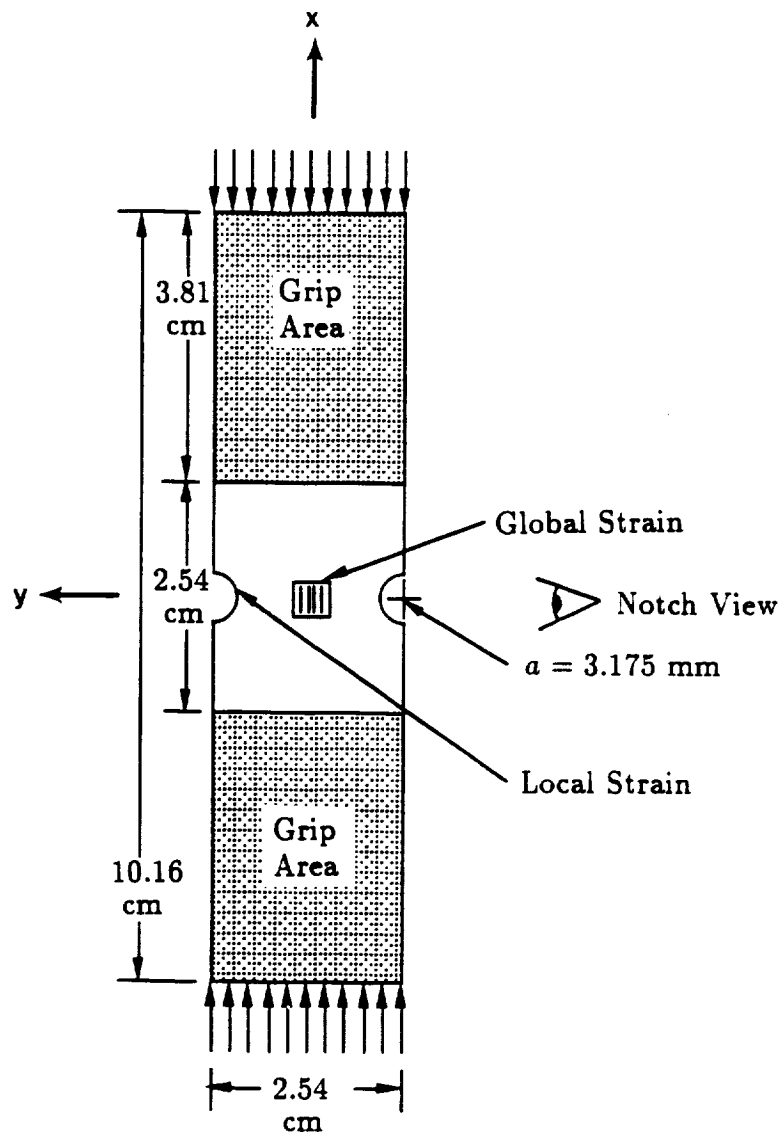


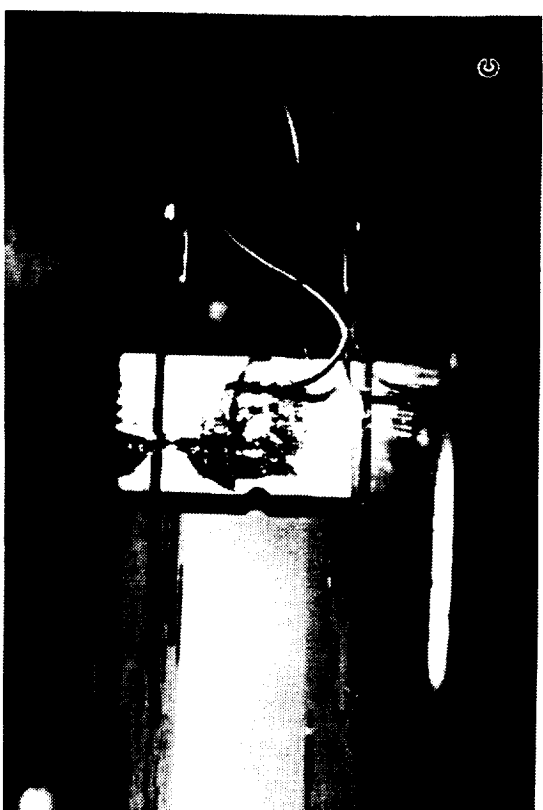
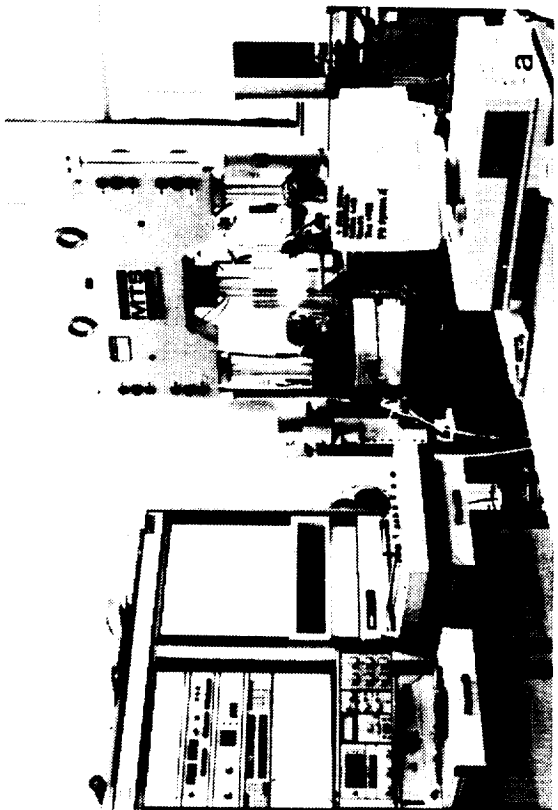
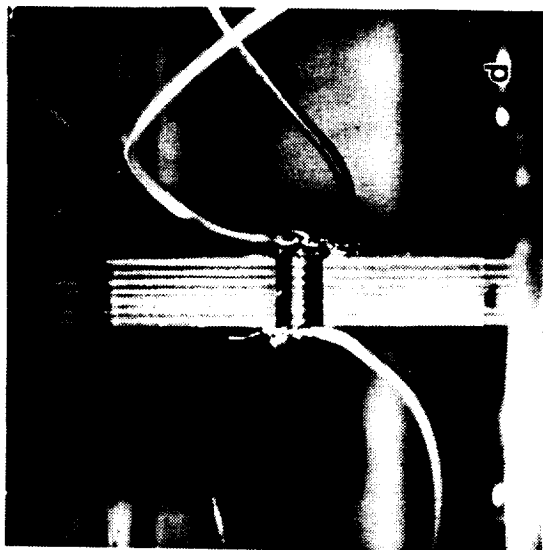
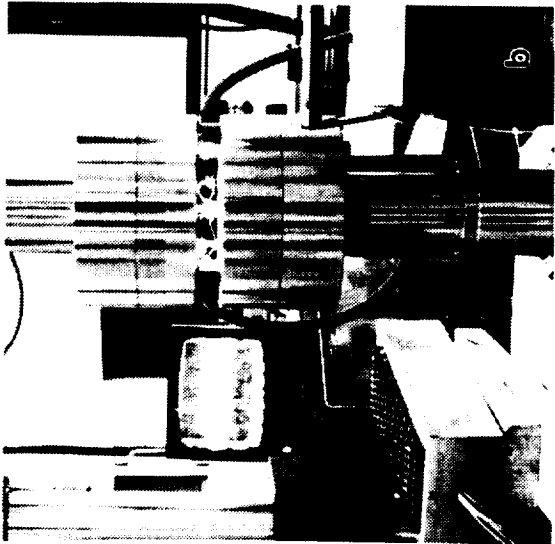
Fig. 27 Schematic of compression specimen.

Ambient Temperature Test Methods — Compression tests were conducted in a specially designed ultra high axial alignment Material Test System (MTS) machine in the Materials and Structures Laboratory of Texas A&M University. The specimens were loaded in compression to fiber microbuckling initiation in the servo-controlled hydraulic test stand at three relatively slow rates in displacement control to provide more stable growth of the damage zone. The displacement rates, based on experience, were 0.127 mm/min for the initial $\approx 50\%$ of the test, 0.074 mm/min for the next $\approx 30\%$ of the test, and 0.018 mm/min for the remainder of the test. The fiber microbuckling process, occurring in the radius of the semi-circular edge notches, was monitored by a colleague, Mr. David L. Crane, using a Wild M8 Zoom Stereomicroscope. Various video cameras and monitors, used in conjunction with the stereomicroscope, were tested as devices for monitoring fiber microbuckling initiation. However, all of these systems were found to be inadequate when compared to the combination of the human eye and the stereomicroscope. Accurate observation of fiber microbuckling requires three-dimensional visualization (some depth of field), which is lost with conventional video and photography. This testing system is shown in Fig. 28. Data from load, displacement, and strain channels were transformed through a 16-channel simultaneous sample and hold analog-to-digital converter with 16-bit resolution. The digital data was then down-loaded from the PDP11/23 to an IBM compatible personal computer. Most tests were interrupted at the first indication of fiber microbuckling and subsequently observed in the SEM. In the other tests, a small fiber microbuckling damage zone was allowed to form before interrupting the tests.

Elevated Temperature Test Methods — High temperature tests were conducted at 77°C and 132°C to provide variation in the constitutive behavior of

- Fig. 28** Compression test facilities.
- a) Overview of MTS test stand, controller, and data acquisition.
 - b) Close-up showing gripped specimen, stereomicroscope in the background, and video image of notch edge.
 - c) Surface view of edge-notched specimen with strain gages, gripped in MTS test stand.
 - d) Edge view of specimen with strain gages.

ORIGINAL PAGE
BLACK AND WHITE PHOTOGRAPH



the PEEK matrix, and thus, additional variation in the support provided to the 0° fibers.

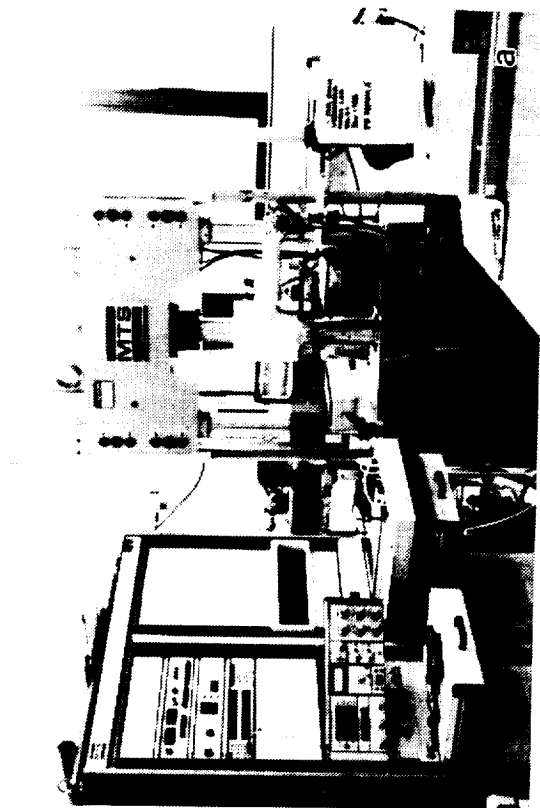
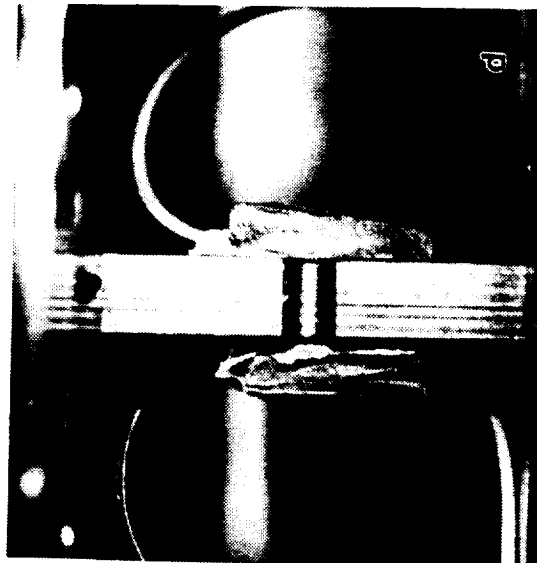
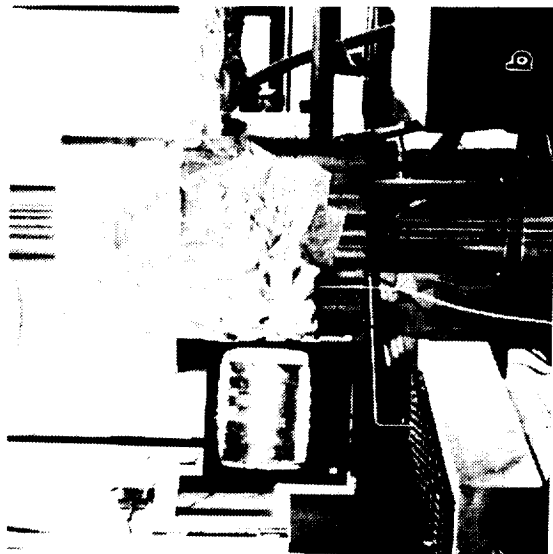
To provide easier observation and access to the specimen, a forced-air heat gun (also used in Ref. 135) with a controller, rather than an environmental chamber, was used to heat the specimen gage section. In addition to easier access, the heat gun heats the specimen to the test temperature much more quickly (20 min. compared to 1 hr) than the traditional environmental chamber which also must heat the massive MTS grips. The high temperature test set-up is shown in Fig. 29. These tests were also conducted in displacement control at the same three rates previously mentioned. Data acquisition and fiber microbuckling initiation observations were accomplished in the same manner as the 21°C tests. It should be noted that General Dynamics in Fort Worth, Texas uses the forced-air heat gun because it more realistically, compared to an environmental chamber, simulates the heat spikes typically experienced by aircrafts.

For these elevated temperature tests, it was necessary to establish an accurate method to control specimen temperature. The small control specimen, shown in Fig. 29c, contains a thermister to provide user-control of the heat gun air temperature. The specimen temperature was monitored with thermocouples on both specimen surfaces. The thermocouple on the specimen surface closer to the heat gun (designated front surface) read $\approx 8^\circ\text{C}$ higher than the thermocouple on the back specimen surface. However, when the heat gun was turned off, the temperature of the front specimen surface rapidly equilibrated with the back surface. Additionally, a thermocouple was embedded in two trial specimens. In both cases, the embedded thermocouple read the same as the thermocouple on the back specimen surface for the range of temperatures in this study. It was concluded

Fig. 29 High temperature compression test facilities.

- a) Overview of MTS test stand, controller, and data acquisition.
- b) Close-up showing gripped specimen, stereomicroscope in the background, video image of notch edge, and the heat gun.
- c) Surface view of edge-notched specimen with strain gages, gripped in MTS test stand.
- d) Edge view of specimen with strain gages.

ORIGINAL PAGE
BLACK AND WHITE PHOTOGRAPH

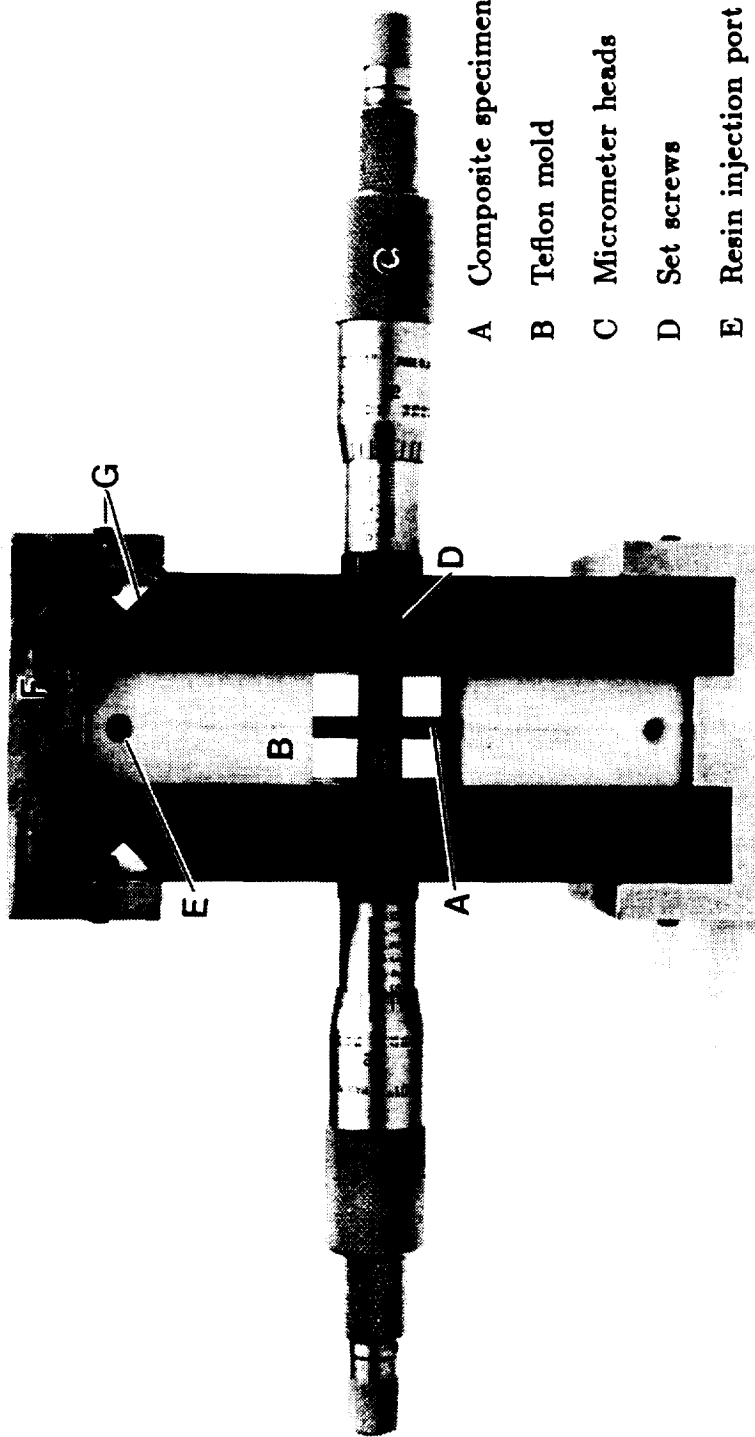


that the heat gun provided constant temperature through the specimen thickness, and thus, the specimen temperature was accurately controlled by monitoring the thermocouple on the back specimen surface.

Specimen Preparation — The specially designed MTS (previously described) contains a collet-type grip arrangement. The collet inserts which grip the specimen are machined for an ideal specimen thickness, e.g. 5.334 ± 0.025 mm. However, due to the nonuniform thickness of laminated composite panels, most specimen ends in previous compression research at Texas A&M University (Refs. 1-4, 145) were shimmed symmetrically with layers of precision brass shims to properly fit into the MTS grips.

To further improve the alignment and gripping support provided during the compression tests, a fixture has been designed to allow homogeneous resin shims to be cast symmetrically onto the specimen ends. The resin shim casting fixture, including appropriate component labels, is shown in Fig. 30. The composite specimen (A) was centered in Teflon (annealed prior to machining) molds (B) using two Mitutoyo micrometer heads (C) with nonrotating spindles. Set screws (D) held the micrometer heads in the fixture. Each Teflon mold contains a 3.175 mm diameter resin injection port (E). Steel end caps (F) are pulled tight against the specimen ends using a set screw and dovetail arrangement (G) to prevent the resin from covering the already machined specimen ends and to prevent leakage. Additionally, Teflon tape was used to seal the interface between the steel end caps (F) and the Teflon molds (B). After the specimen was properly centered in the fixture, resin was injected into the bottom mold until the mold was completely filled. To prevent leakage, a 3.175 mm diameter Teflon rod was inserted into the injection port. After the resin was cured, the fixture was turned upside down and resin shims were

Fig. 30 Resin shim casting fixture.



- A Composite specimen
- B Teflon mold
- C Micrometer heads
- D Set screws
- E Resin injection port
- F Steel end caps
- G Set screw & dovetail

cast, by the same method, onto the other end of the specimen. Consequently, the thickness of the specimen ends with the cast shims was within the thickness tolerances required by the collet inserts, and the shims were uniformly bonded to the specimen ends. This specimen design reduced the global bending significantly when compared to previous test results.^{1-4,145}

The epoxy used as shim material consisted of an all-purpose resin, D.E.R. 31,¹⁴⁶ and a curing agent or hardener, D.E.H. 24,¹⁴⁶ supplied by The Dow Chemical Company,¹⁴⁷ Freeport, Texas. The epoxy was mixed using the recommended ratio of 13 parts by weight (8.22 cc) of hardener per 100 parts by weight (50 cc) of resin. The cure schedule for the epoxy was one hour at 100°C.

Determination of Fiber Microbuckling Initiation Strains — Two types of fiber microbuckling, in- and out-of-plane, were considered in these notched compression tests. In-plane fiber microbuckling occurs in the plane of the laminate ($x-y$ in Fig. 27), and the fibers buckle into the notch radius. Out-of-plane fiber microbuckling is characterized by fibers buckling out of the laminate plane toward the free surface. The nominal strain associated with the initiation of fiber microbuckling was measured with the strain gages at the specimen center, as shown in Fig. 28. It should be noted that this value is the global or remote strain at which either in- or out-of-plane fiber microbuckling is sufficiently general at the notch root radius to be observed with the stereomicroscope. For consistency, fiber microbuckling through the thickness of the 0° ply (or 0₂ plies) is defined as sufficiently general. At the initiation of fiber microbuckling, the specimen was unloaded, manually using the MTS controller, to prevent catastrophic failure. The 0° ply in which fiber microbuckling occurred and the associated global strain levels (gages on both specimen surfaces) were recorded. To include any bending effects, a linear strain distribution was as-

sumed through the specimen thickness. Using this distribution, the actual strain in the 0° ply in which fiber microbuckling initiated was calculated. This strain level was defined as fiber microbuckling initiation, ϵ_I . Two-dimensional finite element analysis was used to convert the measured nominal initiation strain to the local strain at the notch. Within each of the independent variables tested, 2–4 specimens were tested (defined by the scatter) for each variation. The average fiber microbuckling initiation strains are reported in Chapter V (Experimental Results) of this dissertation.

Examination of Fiber Microbuckling Damage

Both in- and out-of-plane fiber microbuckling were examined in the SEM to search for differences between the failures of laminates from the different variables. The damage was examined from one of two viewpoints. Primarily, the viewpoint was from the notch center (into the hole) so that damage in the notch and through the thickness of the laminate may be examined. This viewpoint is designated the “notch view” in Fig. 27. Less often, the specimen surface and near surface damage surrounding the notch were examined. This viewpoint is designated the “surface view.” In this case, the x - y plane in Fig. 27 was examined.

Damage Progression Investigation

An incremental damage study was conducted to evaluate the progression of damage in the notch. The purpose of this investigation was to characterize damage growth observed in-situ in the stereomicroscope. This study was conducted in conjunction with Mr. David L. Crane. The material used was the baseline stacking sequence, $[(\pm 45/0_2)_3 / \pm 45/0]_s$. One notched compression specimen was loaded to five different strain levels. The local incremental strain levels 1 through 5 were, in

percent, 1.0, 1.5, 2.0, 2.5, and 2.54, respectively.

Initially, and on completion of each strain increment, the specimen notches were examined in the SEM. These results were compared with the stereomicroscope observations to "calibrate" the fiber microbuckling observations made in the stereomicroscope. This process insured proper interpretation of these observations made at a magnification ($\approx 20X$) where resolution of individual fibers is barely adequate.

X-radiography

Dye-penetrant enhanced X-radiography was the nondestructive technique used to monitor matrix cracking. A zinc iodide solution was applied to the surface damage to infiltrate to the connected interior damage to act as an enhancing agent. The zinc iodide solution consisted of 60 grams of zinc iodide, 10 ml of water, 10 ml of isopropyl alcohol, and 10 ml of Kodak "Photo-Flo 600" to act as a wetting agent.

Scanning Electron Microscopy

Most nonconductive specimens examined in the scanning electron microscope (SEM) need to be coated with a thin film of conducting material. This coating is necessary to eliminate or reduce the electric charge which builds up rapidly in a nonconducting specimen when scanned by a beam of high-energy electrons. To eliminate any difficulties with charging, each specimen surface for SEM examination was sputter-coated with a thin film of gold palladium approximately 100\AA thick, and then it was examined in a JEOL JSM T330A. Delamination fracture surfaces and unpolished fiber microbuckling zones were examined at a relatively long working distance (48 mm) to provide a greater depth of field, and thus, facilitate the observation of the topography of the fracture surfaces. Polished specimen surfaces,

specimen cross-sections, and sectioning surfaces were examined at a shorter working distance (20 mm) to increase the resolution and contrast highlights of the damage. Additionally, a low accelerating voltage of 5 kV was used to further increase the contrast of the specimen surfaces.

Material Property Characterization

Material Data — The mechanical properties for the constituent materials, PEEK matrix and AS4 fibers, are given in Table V. The fiber diameter was 7 μm . Additionally, the 21°C lamina material properties are summarized in Table V. Note that in Ref. 144, the lamina elastic properties for Quadrax were assumed to be the same for both 8- and 1-harness weaves. Furthermore, no real study has been conducted to determine the mechanical properties of the experimental AU4U/PEEK. However, data from Refs. 149 and 150 indicate that elastic moduli and Poisson's ratio were not significantly affected by the poor interface; the strengths and mode I interlaminar fracture toughness were severely reduced. Thus, the APC-2 elastic properties were assumed to be valid for this material. The 21°C laminate engineering constants, E_x , E_y , G_{xy} , and ν_{xy} for each stacking sequence were computed, using the lamina properties in Table V, with a basic laminate theory program. These constants are summarized in Table VI. Based on the lamina property assumptions, the 8- and 1-harness Quadrax laminates have the same elastic properties. Additionally, the baseline stacking sequence made of the poor interface material was assumed to have the elastic properties as the APC-2 baseline lay-up.

Determination of Lamina Shear Constitutive Behavior — The constitutive behavior for shear loading was determined from tensile and compressive tests of a $[\pm 45]_n$ laminate where n is 2 for tension and n is 8 for compression tests. These tests were conducted at the same temperatures (21°C, 77°C, and 132°C) as the

Table V. Mechanical Properties (21°C) of Constituent Materials.

Material	E_{11} , GPa	E_{22} , GPa	G_{12} , GPa	ν_{12}
PEEK Resin ¹³⁷	3.60	3.60	1.30	0.42
AS4 Fiber ¹³⁷	235	14.0	28.0	0.20
APC-2 Lamina ¹³⁷	134	8.90	5.10	0.30
AU4U/PEEK ^a	134	8.90	5.10	0.30
Quadrax ^b	70.7	70.7	6.10	0.03

^aExperimental poor interface material.^{149,150}

^bAssumed same for both 8- and 1-harness.¹⁴⁴



Table VI. Laminate Engineering Constants (21°C).

LID	Stacking Sequence	E_{xx} , GPa	E_{yy} , GPa	G_{xy} , GPa	ν_{xy}	ν_{yx}
<i>A, F</i>	$[(\pm 45/0_2)_3/\pm 45/0]_s^a$	72.7	22.8	20.8	0.69	0.22
<i>B</i>	$[(0_2/\pm 45)_3/0/\pm 45]_s$	72.7	22.8	20.8	0.69	0.22
<i>K</i>	$[\pm 45/0/90]_{3s}$	51.7	51.7	19.8	0.31	0.31
<i>KQ8,</i> <i>KQ1</i>	$[\pm 45/\langle 0/90 \rangle]_{3s}$ 8-&1-harness	53.6	53.6	19.8	0.27	0.27
<i>C</i>	$[(\pm 15/0_2)_3/\pm 15/0]_s$	121.6	9.2	9.0	0.69	0.05
<i>D</i>	$[(\pm 75/0_2)_3/\pm 75/0]_s$	67.5	66.9	9.0	0.10	0.10
<i>E</i>	$[(90_2/0_2)_3/90_2/0]_s$	67.5	75.8	5.1	0.04	0.04

^aElastic properties assumed same for APC-2 and AU4U/PEEK. ^{149,150}

notched compression tests. The elevated temperature tests give a considerable reduction in the yield point on the τ - γ curve.

The specimens for the tensile tests were 2.54 cm wide by 22.9 cm long with two 2.81 cm long glass/epoxy tabs bonded to each end of the coupon.¹⁴⁸ The specimens for the compression tests were prepared in a manner similar to the notched compression specimens except without the edge notches. High-strain (5%) longitudinal-transverse strain gages were bonded onto both types of specimens using M-Bond AE-15, a high strain (15%) adhesive manufactured by Micromeritics Group, Inc. The tests were conducted in displacement control at a rate of 1 mm/min.

Two specimens, one compression-loaded and one tension-loaded, were monitored for matrix cracking with nondestructive examination, namely dye-penetrant enhanced X-radiography. Each of these tests was paused at every one percent increment of longitudinal strain. The dye-penetrant was applied, allowed to soak, and then the X-ray was taken.

The nonlinear shear stress-strain relationship for these laminates was calculated using the method described by Refs. 70-72, 150. From the remotely applied axial stress (σ_{xx}), longitudinal strain (ϵ_{xx}), and transverse strain (ϵ_{yy}), the in-plane shear stress (τ_{12}) and shear strain (γ_{12}) in each lamina were computed by the following equations:

$$\tau_{12} = \frac{\sigma_x}{2} \quad (48)$$

and

$$\gamma_{12} = \epsilon_x - \epsilon_y = |\epsilon_x| + |\epsilon_y| \quad (49)$$

so that the in-plane shear modulus of a lamina, G_{12} , was computed by

$$G_{12} = \frac{\tau_{12}}{\gamma_{12}} = \frac{\sigma_x}{2(\epsilon_x - \epsilon_y)} \quad (50)$$

from the linear portion of the shear stress-strain data. Using Eqns. 48 and 49, the nonlinear shear stress-strain behavior of the lamina was determined.

Initial Fiber Waviness — A digitizing technique, described in Ref. 152, has been developed for systematic measurement of the amplitude and wavelength of the fiber waviness. This technique employs a Hewlett Packard 7475A plotter equipped with a fiber optic sight, instead of a pen, and a personal computer. Points are digitized along multiple fibers to track the waviness. Based on these measurements, a best-fit sine wave is assumed for the shape of the fiber waviness. This technique is considered for comparison of the degree of fiber waviness of the laminates listed in Table III. The waviness ratio is defined as the initial amplitude of the sine wave (a_o) divided by the wavelength (L), and it is used for comparison of degrees of waviness.

Determination of Fiber/Matrix Interfacial Bond Strength — Numerous experimental techniques, primarily single- or multiple-fiber pull-out tests, to measure the shear strength of the fiber/matrix interfacial bond were summarized in Ref. 153. Mandell, Grande, Tsiang, and McGarry¹⁵⁴ developed the modified microdebonding test for direct in-situ fiber/matrix bond strength determination. In a sequence of steps, a compressive load was applied to individual fibers oriented normal to a polished surface, and the interface was observed microscopically between loading steps, until debonding occurs. The direct result of a test was the force to produce debonding of a particular fiber. The data were reduced to a nominal interfacial shear strength through a two-dimensional finite element analysis using a simplified model of the fiber, surrounding matrix, and homogeneous composite properties

beyond the matrix. The finite element solution incorporated the fiber diameter, spacing to the nearest neighbor fiber, and the elastic (orthotropic) properties of the fiber, matrix, and far-field composite. The finite element analysis indicates that the maximum interfacial shear stress occurs at a distance that is a fraction of a fiber diameter below the free surface. It was assumed that debonding initiates at this point due to the shear stress. However, there is no experimental confirmation of the position where debonding initiates, as it quickly spreads over an area of the circumference of the fiber and up to the surface, and the actual debonding process (during loading) cannot be observed. According to Ref. 147, measurements from the microdebonding test compare (within 5%) with single-fiber pull-out results.

In this investigation, the interfacial shear strength (IFSS) of the fiber/matrix bond was determined in a semi-quantitative way using the Interfacial Testing System (ITS)¹⁵⁵⁻¹⁵⁷ developed at The Dow Chemical Company in Freeport, Texas. The ITS test operates in principle like the previously described microdebonding test. However, the ITS is a totally integrated system that is fully automated to reduce user-induced error and thus, increase repeatability of the results.

To date, only unidirectional laminates have been tested in the ITS to avoid any complications caused by residual cure stresses. However, in this study both unidirectional and multidirectional laminates were tested. Due to different batches of material and residual cure stresses, it is possible that the IFSS will be different for the unidirectional and multidirectional composites. The 24-ply unidirectional laminates of APC-2 (good fiber/matrix interface) and the experimental AU4U/PEEK (poor fiber/matrix interface) were tested as control specimens. Additionally, 0° fibers in the $[(\pm 45/0_2)_3 / \pm 45/0]$, laminates, both APC-2 and AU4U/PEEK, were tested since these plates were used to study the effects of the interfacial bond strength

on fiber microbuckling initiation. In each sample, ten fibers were tested. These interfacial bond strength results were compared qualitatively with the mode I and II fracture toughness results and were used to establish the effects of the interfacial bond on fiber microbuckling initiation.

Delamination Fracture Toughness — Delamination involves the separation of adjacent plies in the thickness direction of the composite for which the material is not reinforced. Delaminations may occur under three primary modes, mode I or opening mode, mode II or shearing mode, and mode III or tearing mode. Any combinations of these modes may also cause delaminations. Delamination initiation and propagation are affected by many factors including the fiber/matrix interfacial strength. Poor fiber/matrix interfaces prohibit full utilization of the matrix toughness, particularly for mode I delamination.¹⁴⁹

The delamination fracture toughness, or the resistance to fracture in the presence of a crack, is typically expressed in terms of the strain energy release rate, G . The analysis assumes that all available energy is used to create a new crack surface; that is, the material is elastic. According to Ref. 158, this assumption is valid, in general, for unidirectional composite laminates. Williams¹⁵⁹ extended linear beam theory analyses (e.g. Refs. 160, 161) to include geometric nonlinearities. Geometric nonlinearities include the large displacements and rotations that develop within thin, highly compliant lay-ups or within tough composites that require large loads to delaminate. In this investigation, data is acquired and reduced following the procedures in Refs. 158 and 159.

Both the mode I and mode II fracture toughnesses of two composite materials, commercial APC-2 and experimental AU4U/PEEK, were evaluated in this portion of the investigation. The purpose was to provide a comparison of the fracture

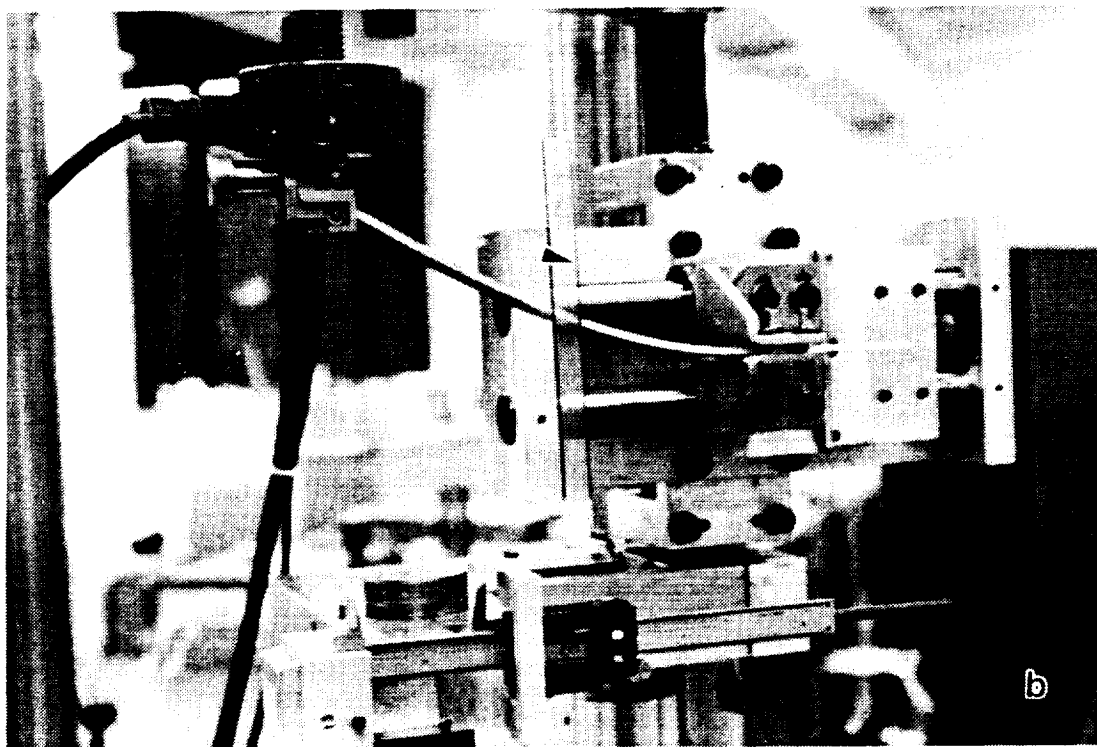
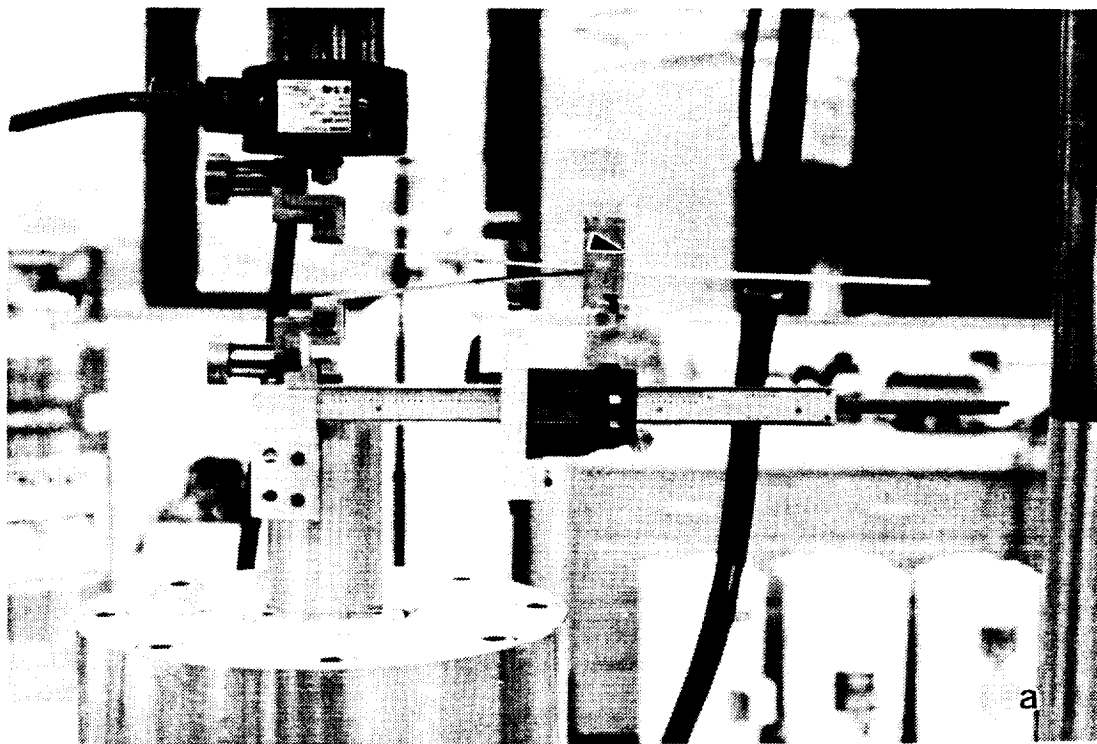
toughness values and fracture mechanisms for the good and poor interface materials. Unidirectional, $[0_{24}]$, laminates were tested. Three specimens from each material were tested in each of the two fracture modes. The specimens were 2.54 cm wide and 25.4 cm long. The delamination starter crack at the midplane of each specimen was a Kapton insert 7.62 cm long and 0.1524 mm thick. The edges of the specimens were painted silver so that the crack tip could be easily detected, and the crack length measured. Magnification of the crack tip also aided this measurement. Aluminum and brass tabs (to introduce loading) were bonded to the cracked end of the specimens using M-Bond 200 adhesive and catalyst, manufactured by Micromeritics Group, Inc.

The experimental set-up used for mode I fracture toughness testing is shown in Fig. 31a. This set-up includes the double cantilever beam (DCB) specimen, a 445 N load cell, and a digital caliper for crack measurements. The crack measurement fixture and procedure are described later. A precrack was introduced with a razor blade (used as a wedge, not a cutting tool) into all DCB specimens to sharpen the initial crack created by the Kapton insert. The DCB specimens were loaded at a relatively slow rate of 1.27 mm/min to provide stable crack growth. Three unload loops at different rates on one specimen were taken to verify that the load-displacement curve returned to zero after each unload. This exercise verified the linear elastic material behavior and the absence of rate effects. Thus, the unload rate was increased to 25.4 mm/min, and the mode I fracture toughness was computed, assuming linear elasticity and geometric nonlinearity,¹⁵⁹ using

$$G_I = \frac{P^2 a_p^2}{BE_b I_m} \quad (51)$$

where

Fig. 31 Fracture toughness test configurations.
a) Mode I.
b) Mode II.



- P = applied load,
 a_p = load-line to crack tip distance or the projected crack length,
 B = specimen width,
 E_b = axial modulus of the beam (E_{11} in this case), and
 I_m = moment of inertia of the cracked leg.

The experimental set-up used for mode II fracture toughness testing is shown in Fig. 31b. This end-loaded split laminate test (ELS) fixture prevents the uncracked beam end from rotation, while allowing free longitudinal movement (through rods and linear bearings) to keep the concentrated load perpendicular at the loaded end. This fixture is noted for its usefulness to study stable crack growth. As with mode I, this set-up includes the 445 N load cell and the digital caliper for crack measurements. Again, the crack measurement fixture and procedure are described later. The ELS specimens were clamped so that the gage length was 20.32 cm. Also, a mode I precrack was introduced with a razor blade (used as a wedge, not a cutting tool) into all the ELS specimens to sharpen the initial crack created by the Kapton insert and to provide an initial crack length to beam length ratio of approximately 0.55. At this ratio and larger ratios, stable crack growth is expected for this test configuration.¹⁵⁸ This crack extension made the initial crack length 11.18 cm long for the ELS specimens. The ELS specimens were loaded at relatively slow rates of 2.54 cm/min for the APC-2 and 0.254 cm/min for the AU4U/PEEK laminates to provide stable crack growth. Multiple unloads at different rates on one specimen again verified the linear elastic material, and the absence of rate effects. Thus, the specimens were unloaded at 25.4 cm/min. Assuming linear elastic material and geometric nonlinearity,¹⁵⁹ the mode II fracture toughness was computed using

$$G_{II} = \frac{6P^2 a_p^2}{BE_b I_m^u} \quad (52)$$

where

I_m^u = moment of inertia of the uncracked leg and

the other variables are explained with Eqn. 51.

Crack length measurements for the DCB and ELS tests were made using the digital caliper fixture (Ref. 158) shown in Fig. 31. First, the crack tip was located visually on the painted specimen edge. The position was then marked with a fine pencil. The load-line to crack tip distance was then measured. The measuring device consists of a digital caliper mounted on the ram below the lower loading grip and a transparent plastic piece scribed with a sighting line (see Fig. 31b). During the test, after the crack tip was marked, the sighting line was moved to the crack tip. The load-line to crack tip distance is directly read from the caliper. To avoid parallax error, the device is adjustable so that the sighting piece may be moved close to the specimen edge. Due to fixture interactions, a razor blade was used for the sighting line in these mode I tests (Fig. 31a).

During the course of the DCB and ELS tests, the load and corresponding projected crack length were measured periodically based on the load-displacement behavior of the specimen. Measurements were made during stable crack advance, except for some instances just after a sudden increment of crack growth followed by arrest. Arrest values are specially noted in the presentation of the results.

Load-displacement data was recorded on an X-Y recorder to provide real-time observation of the load-displacement record. Additionally, load and displacement data were transformed through an analog-to-digital converter. The digital data was then down-loaded from the PDP11/23 to an IBM compatible personal computer.

CHAPTER IV

FINITE ELEMENT ANALYSIS

Geometric and material nonlinear two-dimensional finite element analysis is used to model the initiation of fiber microbuckling of both the ideal straight 0° fiber and the more realistic initially wavy 0° fiber. The models with the straight fibers show the effects of finite size, free surface, fiber constitutive properties, and provide an upper limit for the fiber microbuckling initiation strain levels. Wavy fiber models are used to show the effects of matrix constitutive behavior, initial fiber curvature, fiber/matrix interfacial bond strength, free surface, and fiber constitutive properties on fiber microbuckling initiation strain levels.

This chapter contains a brief review of the theory for both the straight and wavy fiber problems followed by a description of the different model geometries. Model implementation contains a succinct description of the procedures and a summary of the model constituent properties. Finally, the cases, combinations of constituent properties and model geometries, for each of the models are presented.

Theory

The Straight Fiber Problem

The buckling analysis of perfectly straight fibers embedded in matrix (bifurcation instability^{162,163}) is the classical Euler column analysis which has the form of the generalized eigenvalue problem

$$[A]\{v\} = \lambda[B]\{v\} \quad (53)$$

where $[A]$ and $[B]$ are symmetric matrices, λ is a scalar, and $\{v\}$ is a vector. When λ_i and v_i satisfy Eqn. 53, they are called an eigenvalue and eigenvector, respectively. The main objective of an eigenvalue formulation and solution in instability analysis is to predict whether small disturbances, imposed on the equilibrium configuration, increase substantially. The load or strain level at which this situation occurs corresponds to the critical load or strain of the system.

In a stability problem, a load may be reached where deflections increase more rapidly than predicted by linear solution. It is even possible to reach a state where the load carrying capacity decreases with increasing deformation. Consequently, for accurate determination of the displacements, geometric nonlinearity (finite rotations) must be considered. The two-dimensional Lagrangian nonlinear strain-displacement relations (displacements are referred to original configuration) are of the form

$$\begin{aligned}\epsilon_{xx} &= \frac{\partial u}{\partial x} + \frac{1}{2} \left[\left(\frac{\partial u}{\partial x} \right)^2 + \left(\frac{\partial v}{\partial x} \right)^2 \right] \\ \epsilon_{yy} &= \frac{\partial v}{\partial y} + \frac{1}{2} \left[\left(\frac{\partial u}{\partial y} \right)^2 + \left(\frac{\partial v}{\partial y} \right)^2 \right] \\ \epsilon_{xy} &= \frac{1}{2} \left[\frac{\partial u}{\partial y} + \frac{\partial v}{\partial x} + \frac{\partial u}{\partial x} \frac{\partial u}{\partial y} + \frac{\partial v}{\partial x} \frac{\partial v}{\partial y} \right]\end{aligned}\tag{54}$$

The generalized eigenproblem to be solved in the classical Euler problem described is of the form

$$([K_o] + \lambda[K_g])\{u\} = 0\tag{55}$$

where $[K_o]$ represents the usual, small displacements or linear stiffness matrix, $[K_g]$

is the initial stress matrix or geometric matrix, and $\{u\}$ is the displacement vector. The initial stress matrix represents the change in stiffness going from the initial state to the applied load state and is proportional to the change in load. In the solution of this problem, λ denotes the increase factor on applied strains necessary to achieve instability.

The Wavy Fiber Problem

Once the fibers are no longer considered perfectly straight, as typically observed in composites, the problem to be solved is not the classical Euler problem. Recall that the term “fiber microbuckling” has been defined to refer to large lateral deflections of initially wavy fibers leading to fiber breakage, rather than a bifurcation instability. Compared to bifurcation instability, fiber microbuckling is a gradual process. In the wavy fiber case, instability is defined as the point at which additional applied displacement no longer gives an increase in the load carried by the column. This point defines the initiation of fiber microbuckling in the wavy fiber problem. Although geometric nonlinearity (Eqn. 54) is still considered, the problem solution is an incremental inelastic stress-strain analysis.

Model Geometries

Two-dimensional finite element analysis was used to model fiber microbuckling in two different configurations: (i) straight fibers surrounded by matrix and (ii) wavy fibers surrounded by matrix. The straight fiber problem was modelled to illustrate the upper limit in ideal composites, investigating the effects of finite size, free surface, and fiber constitutive properties. The wavy fiber was modelled to show the effects of matrix constitutive behavior, initial fiber curvature, fiber/matrix

interfacial bond strength, free surface, and fiber constitutive properties on fiber microbuckling initiation.

The Straight Fiber Problem

Four types of configurations were modelled for the straight fiber problem. In these models, symmetry was utilized, so that only one-half of the column length was modelled. Nodal displacements were applied at the column symmetry line. The four configurations were the infinite plate, the semi-infinite plate, the finite plate consisting of ten fibers and matrix, and an infinite series of fibers and matrix. Schematics (not to scale) of these geometries are shown in Figs. 32 and 33. It should be noted that the descriptive names for the three plate models (Fig. 32) are meant to imply that the model is sufficiently wide so that the interior fibers are not near a free surface; these names do not imply that the model is infinitely wide, as in Fig. 33.

Infinite Plate — The infinite plate (Fig. 32a) consisted of ten fibers (cross-hatch regions) separated by matrix (white regions) with support provided on each side by an equivalent homogeneous material (dotted regions). The equivalent regions replace the heterogeneous unidirectional lamina and effectively represent a set of smeared elastic properties. Note that since these equivalent properties were from a unidirectional lamina, they include any effects from the initial fiber curvature. The purpose of these regions is to simulate the stiffness of adjacent material in the lamina. Each of these regions are the same width as the ten fibers and matrix. A half-matrix layer exists between the outer fibers and the equivalent regions.

Semi – Infinite Plate — The semi-infinite plate (Fig. 32b) is similar to the infinite plate, but contained only one equivalent region. Consequently, a fiber and a half-matrix are located at the free surface. Additionally, for this plate, a symmetry

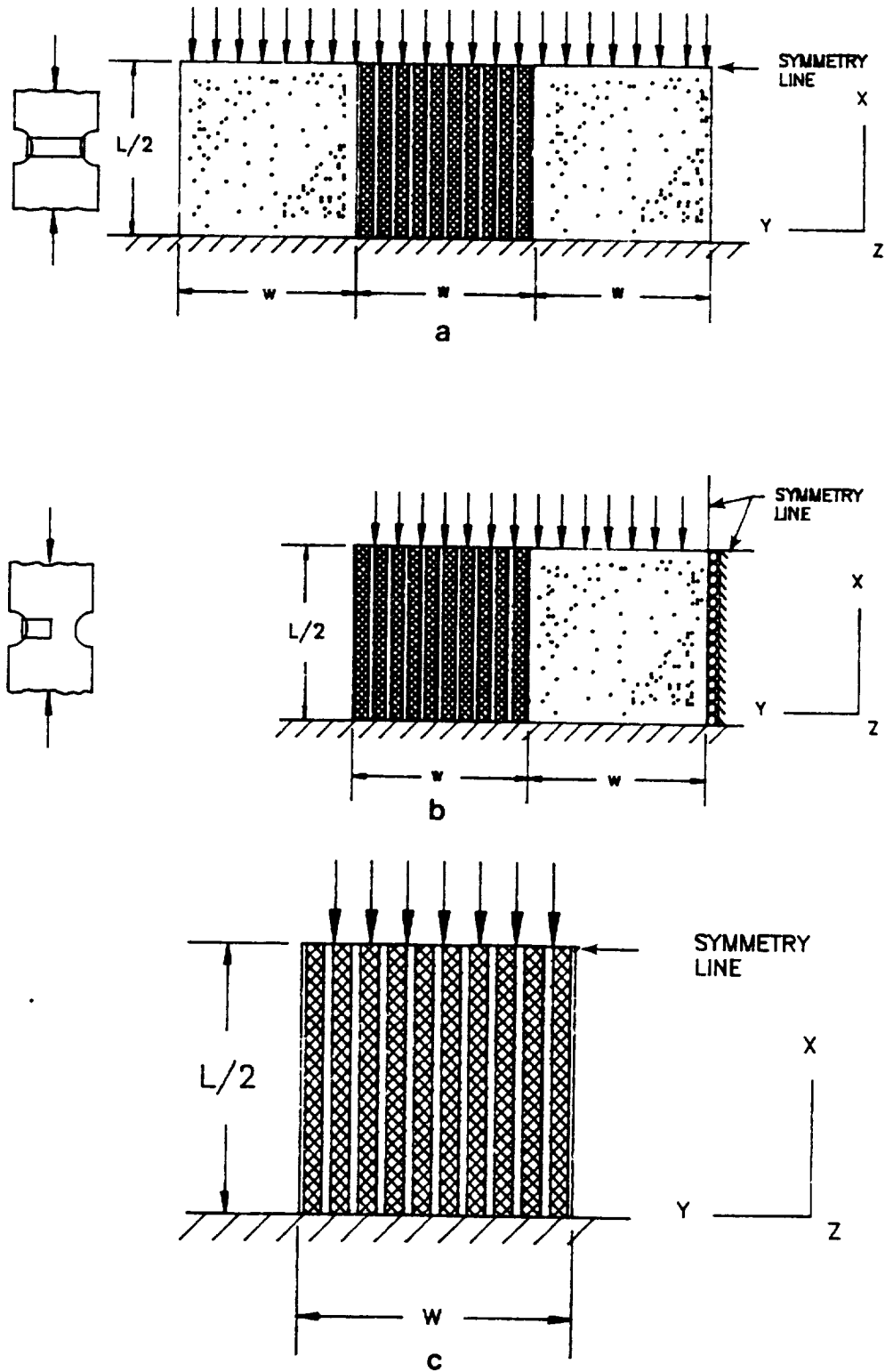


Fig. 32 Models for straight fiber problem.
 a) Infinite model.
 b) Semi-infinite model.
 c) Finite, ten fiber/matrix model.

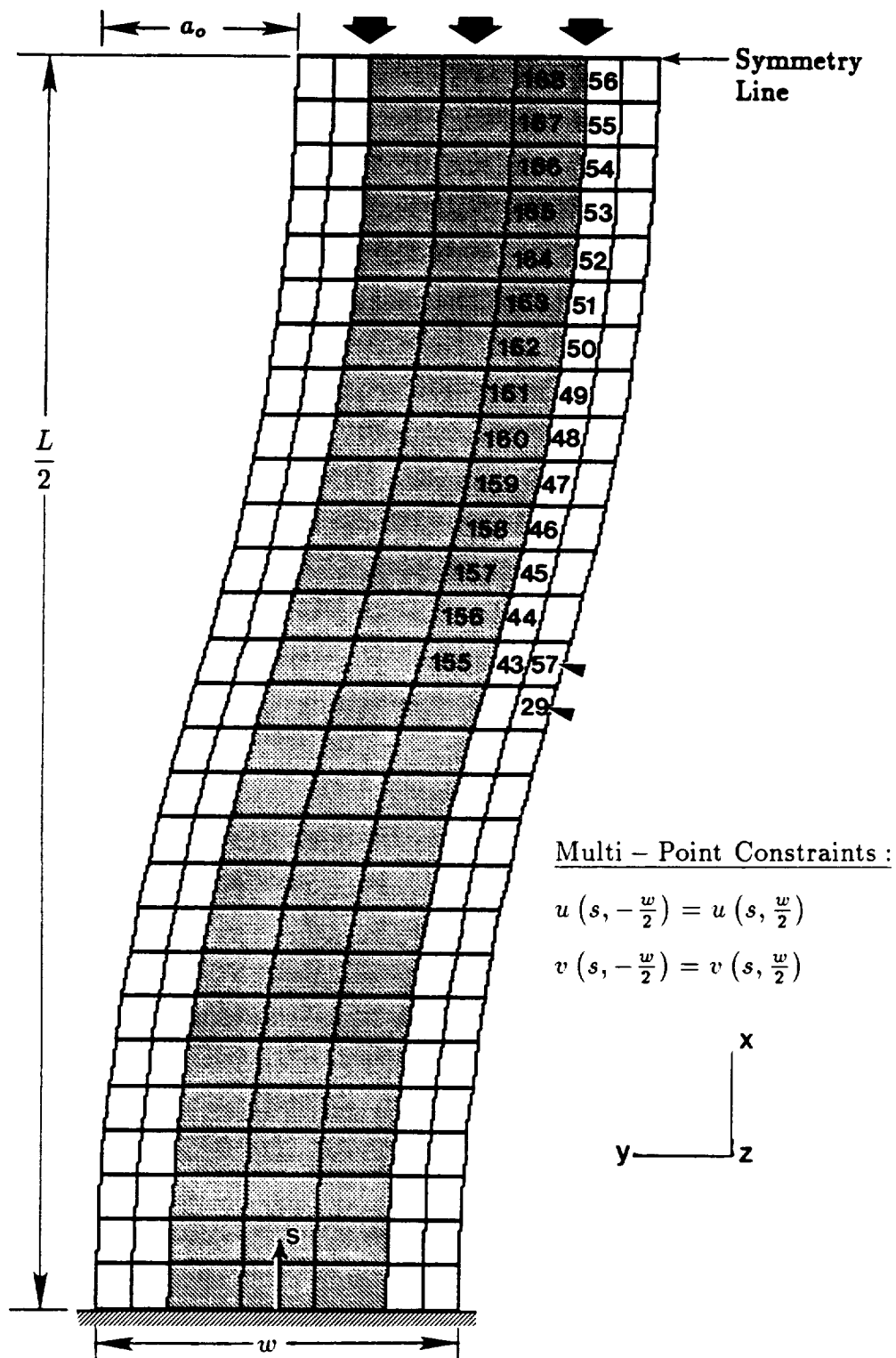


Fig. 33 Unit cell used for infinite array of fibers and matrix, for straight and wavy fiber models. Geometry shown with initial curvature, $\frac{a_0}{L}$.

line is used along the vertical axis at $y = 0$.

Finite Plate — The ten fiber/matrix model (Fig. 32c) consisted of ten fibers separated by nine layers of matrix with half-matrix layers at both outer surfaces. In this case, two free surfaces exist.

Infinite Series — The unit cell, shown with an initial curvature in Fig. 33, is used to represent an infinite array of fibers embedded in matrix. The unit cell consisted of one fiber (shaded region) with half-matrix (white regions) along each side. Multi-point constraint boundary conditions were used to make the unit cell behave as an infinite series of fibers and matrix regions. For clarity, an axis, s , is defined to traverse along the column length, following the contour of the unit cell. The origin of this axis is defined at $x = 0$ and $y = 0$, the base of the column at the center of the fiber width. Using this axis with $u = u(s, y)$ and $v = v(s, y)$, the multi-point constraint boundary conditions are as follows:

$$u\left(s, -\frac{w}{2}\right) = u\left(s, \frac{w}{2}\right) \quad \text{and} \quad v\left(s, -\frac{w}{2}\right) = v\left(s, \frac{w}{2}\right) \quad (56)$$

where w is the width of the unit cell. Because the fiber length, L , is much larger than the initial amplitude of the curvature a_o , the x and s axes are nearly collinear.

The Wavy Fiber Problem

Two types of configurations, semi-infinite plate and infinite fiber/matrix series, were modelled for the wavy fiber problem. As with the straight fiber, symmetry was utilized to reduce computer computations, and nodal displacements were applied at the column symmetry line (see Fig. 33). The fiber waviness was approximated with a sine wave. The initial fiber curvature is defined as the ratio of the initial amplitude of the sine wave to the original length of the sine wave, $\frac{a_o}{L}$, the fiber waviness ratio.

In addition to the straight fiber, three assumed initial fiber waviness ratios were modelled: (i) $\frac{a_0}{L} = 0.0025$, (ii) $\frac{a_0}{L} = 0.0050$, and (iii) $\frac{a_0}{L} = 0.0075$. Arbitrary initial fiber curvatures were assumed because the technique to measure fiber waviness was not fully operational at Texas A&M University at the time of this analysis.

Semi – Infinite Plate — The model for the semi-infinite plate was very similar to that for the straight fiber shown in Fig. 32b. However, this model was generated with an initial waviness ($\frac{a_0}{L} = 0.0050$) buckling toward the free surface, the most critical situation. One edge of the smeared region follows the contour of the half-matrix at the matrix/smear boundary. The other boundary of the smear region is again a vertical symmetry line as shown in Fig. 32b.

Infinite Series — The repeating unit for the infinite series model with an initial curvature is shown in Fig. 33. Except for the initial fiber curvature, the model is identical to the corresponding straight fiber model.

Implementation

The finite element analysis was accomplished using ABAQUS Version 4.7-25.¹⁶⁴ PATRAN, Release 2.3A-1,¹⁶⁵ was used for mesh generation and post-processing. Data were translated between ABAQUS and PATRAN using PATABA: The PAT-ABAQUS Application Interface, Release 3.0A,¹⁶⁶ ABAPAT: The ABAQUS-PAT Application Interface, Release 3.0A,¹⁶⁶ and a translator, written by the author, to extract the global and elemental stress-strain data from the model for x-y plotting. A flow chart summarizing this activity is shown in Fig. 34.

The straight fiber eigenvalue problems were modelled using ABAQUS S8R5 elements, shown in Fig. 35. These elements are doubly-curved shells with eight nodes and 2X2 reduced integration, primarily used for thin shell applications. The

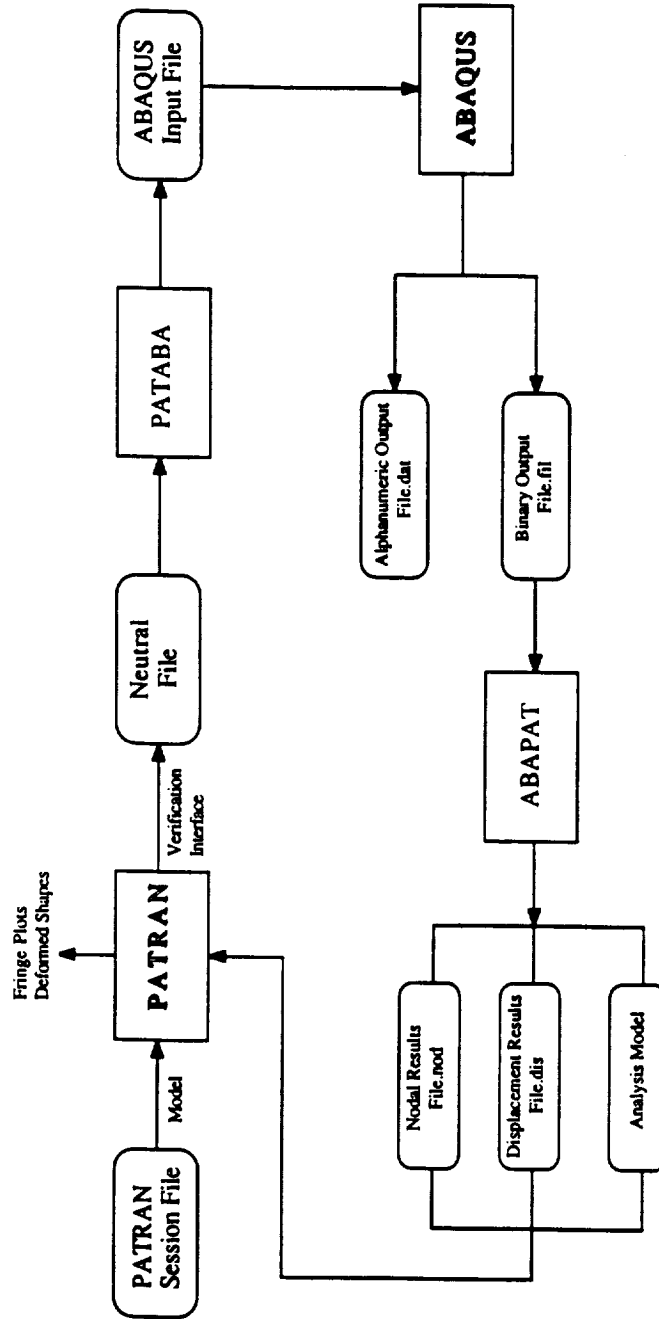


Fig. 34 Flow chart of PATRAN and ABAQUS processes.

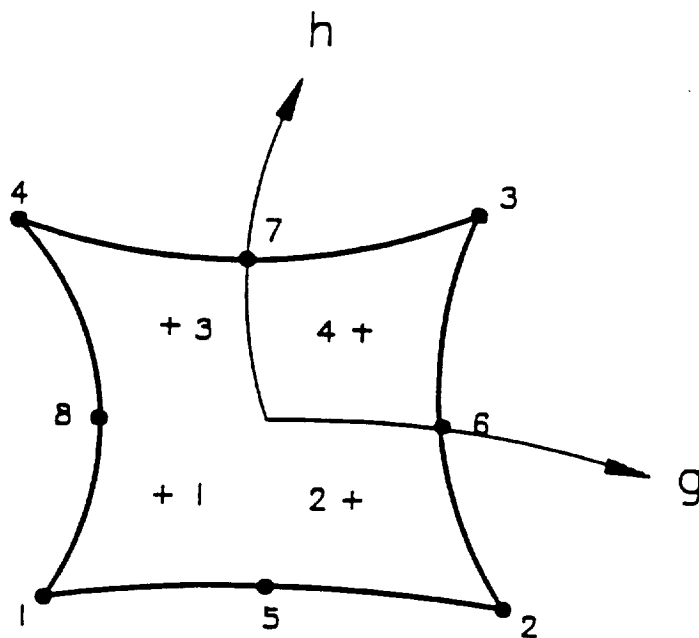


Fig. 35 Nodes, integrations points, and local coordinates for $S8R5^{164}$ and $CPS8R^{164}$ elements.

elements allow five degrees of freedom (three displacements and two in-surface rotations) per node at all nodes except those with specified boundary conditions. At nodes where the boundary conditions are specified, these elements allow six degrees of freedom per node. However, for the incremental inelastic stress-strain analysis, these elements were computationally time consuming. The author realized that u_z , ϕ_x , ϕ_y , and ϕ_z were zero for all elements in these analyses. Consequently, plane stress elements were used for the incremental analysis. These biquadratic elements, designated in ABAQUS as CPS8R (see Fig. 35), are plane stress continuum elements with eight nodes and 2X2 reduced integration. The elements allow two degrees of freedom, u and v , per node. Trial tests with the straight fiber infinite series indicate that these elements predict the critical buckling strain $\approx 10\%$ higher than the S8R5 shell elements. This stiffer solution is a consequence of fewer degrees of freedom. For the purpose of these analyses, 10% difference is acceptable.

Interface elements were used in conjunction with the plane stress continuum elements to model the poor fiber/matrix interfacial bond strength. These elements model the interaction between two deformable structures, along "slide lines," where separation and sliding of finite amplitude, and arbitrary rotation of the surfaces may occur. The surface of interaction was defined by prescribing appropriate interface elements on the surface of one of the bodies (fiber) and associating these elements with a set of nodes on the other surface (matrix), called the "master surface." The slide line elements, ISL22, are three node interface elements that are compatible with second order planar elements and have two degrees of freedom, u and v , at the nodes.

The slide line elements require two parameters: (i) the coefficient of friction, and (ii) the "stiffness in stick." The coefficient of friction is the proportionality

factor in classical Coulomb friction (Amonton's law). This theory assumes that the surfaces do not slip until the shear stress tries to exceed the friction limit, which varies proportionally with the normal compressive stress between the surfaces. Because the theory is implemented by a stiffness method, the "stiffness in stick" is required. This parameter is an elastic stiffness that transmits shear forces across the element as long as these forces are below the friction limit. This stiffness is a "penalty" to simulate zero relative motion between the surfaces prior to slip.

ABAQUS Procedures

ABAQUS contains a capability for estimating elastic buckling by eigenvalue extraction. This estimation is typically useful for "stiff" structures, where the pre-buckling response is almost linear. The buckling load estimate was obtained as a multiplier of the applied loads. The nontrivial solutions to Eqn. 55 provide the estimated buckling strain as $\frac{\lambda \cdot q}{L/2}$ (q is the magnitude of the applied nodal displacements), while the corresponding eigenvector $\{u_i\}_i$ gives the associated buckling mode. ABAQUS only provides an eigensolution for symmetric systems, which means $[K_o]$ and $[K_g]$ must be symmetric, implying that the system has real, positive eigenvalues only. ABAQUS provides the Modified Riks Algorithm for effective solution of nonlinear static equilibrium problems. This algorithm is particularly useful when the load and/or displacement may decrease as the solution evolves, as long as sudden bifurcations do not occur.

The finite element models presented herein do not contain ultimate strength limits to define failure. However, in the incremental analysis of the wavy fiber, the initiation of fiber microbuckling is defined by an instability in the system. The increment following the maximum stress and strain of the system was flagged by a warning that the system matrix contains negative eigenvalues. This warning means

that the system matrix is no longer positive definite; for example, a bifurcation (buckling) load may have been exceeded. The maximum stress and strain, located at the increment prior to this warning, were defined as the initiation of fiber microbuckling in the wavy fiber problem. It was assumed that fiber failure by bending occurred at this point. Additionally, the stress-strain data presented in this dissertation are shown only to the fiber microbuckling strain.

Constituent Properties

For all of these models (both straight and wavy fiber), the fiber volume fraction, V_f , was 60% and the diameter of the fiber, d_f , modelled was $7.6 \mu\text{m}$. The width of the modelled matrix regions were equal and were determined to be $5.1 \mu\text{m}$, based on d_f and V_f . These properties were determined from the material data sheets.¹³⁷ The length of the fiber, L , was selected based on measurements from SEM micrographs. The ratio $\frac{L}{d_f}$ was measured from the micrographs to be ≈ 87 .

Resin — Four different resin constitutive behaviors were used. The behaviors were (i) linear, using given material data,¹³⁷ (ii) 21°C data, (iii) 77°C data, and (iv) 132°C data. The 21°C, 77°C, and 132°C data were measured experimentally.

The equivalent stress-strain behavior of the resin was derived from the lamina τ_{12} - γ_{12} data (Fig. 36). The yield points are indicated with arrows. For the analysis it is assumed that the resin is isotropic, homogeneous, and has constitutive behavior which can be expressed in the form of the Ramberg-Osgood equation. Additionally, it is assumed that $G_f \gg G_m$ ($\frac{G_m}{G_f} = 0.046$), and thus, the shear is primarily transferred by the resin. Using these assumptions, $\tau_{12} = \tau_{12f} = \tau_{12m}$ and $\gamma_{12m} = \frac{\gamma_{12}}{V_m}$. The subscripts f and m correspond to the fiber and matrix, respectively. Once the shear constitutive behavior of the resin was derived, the equivalent stress-strain ($\bar{\sigma}$ - $\bar{\epsilon}$) behavior of the resin was computed using

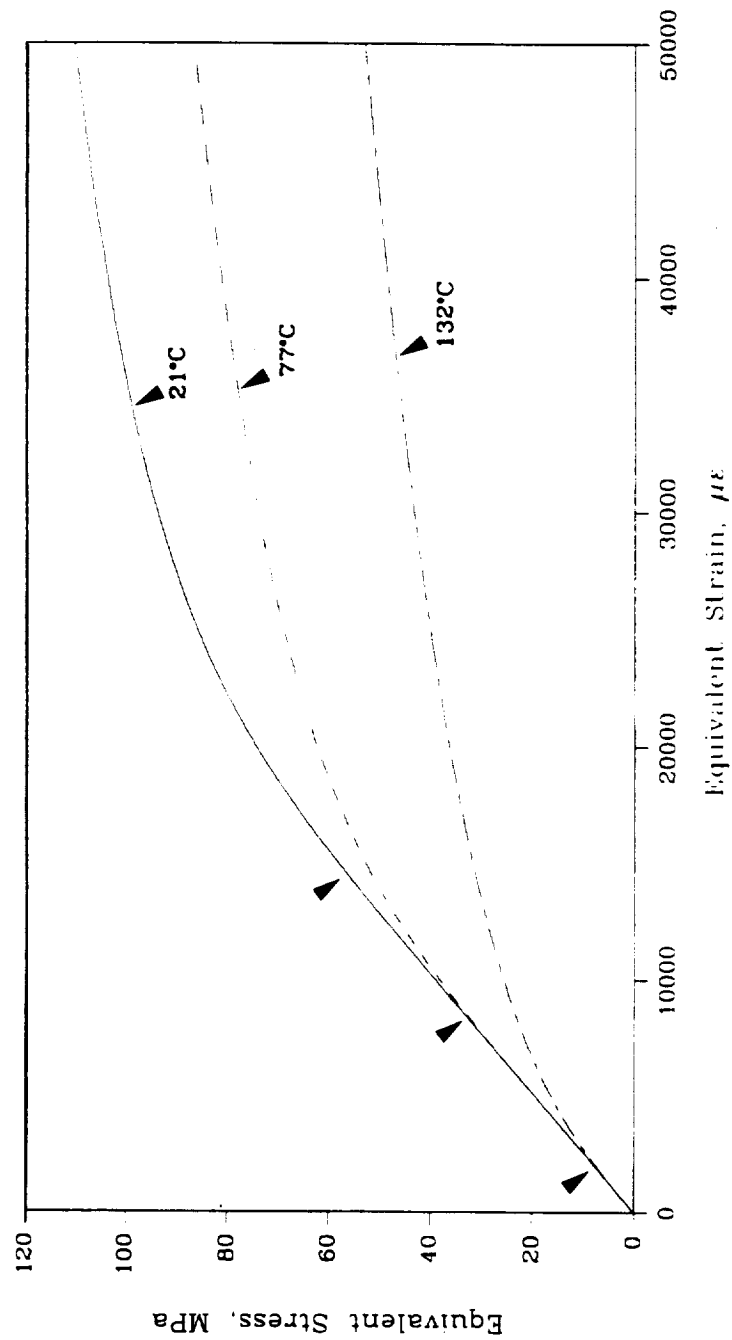


Fig. 36 Equivalent stress-strain behaviors (used in FEA) of the PEEK resin.

$$\bar{\sigma} = \left[\frac{1}{2} [(\sigma_x - \sigma_y)^2 + (\sigma_y - \sigma_z)^2 + (\sigma_z - \sigma_x)^2] + 3 [\tau_{xy}^2 + \tau_{yz}^2 + \tau_{zx}^2] \right]^{\frac{1}{2}}, \quad (57)$$

and for proportional loading (the components of applied stress remain in constant ratio to one another throughout the straining process) only,

$$\bar{\epsilon} = \left[\frac{2}{9} [(\epsilon_x - \epsilon_y)^2 + (\epsilon_y - \epsilon_z)^2 + (\epsilon_z - \epsilon_x)^2] + \frac{1}{3} [\gamma_{xy}^2 + \gamma_{yz}^2 + \gamma_{zx}^2] \right]^{\frac{1}{2}}. \quad (58)$$

Proportional loading may be assumed because these data are derived from tensile tests. For the stress state in the $[\pm 45]_{ns}$ specimens, the equivalent stress-strain behavior is reduced to

$$\bar{\sigma} = \sqrt{3}\tau_{xy} \quad (59)$$

and

$$\bar{\epsilon} = \frac{1}{\sqrt{3}}\gamma_{xy}. \quad (60)$$

The nonlinear constitutive behavior of the resin is fit using the Ramberg-Osgood stress-strain relation

$$\bar{\epsilon} = \frac{\bar{\sigma}}{E} + \frac{\alpha \bar{\sigma}}{E} \left[\frac{|\bar{\sigma}|}{\sigma_o} \right]^{n-1} \quad (61)$$

where

- α = yield offset,
- σ_o = yield stress,
- E = Young's modulus, and

n = the hardening exponent for the plastic term.

Assuming $\alpha = 1$, the values determined for E , σ_o , and n for the best fit through the data are given in Table VII. The equivalent stress-strain data, using the parameters from Table VII, are plotted in Fig. 36. These data (Table VII and Fig. 36) are used to describe the matrix constitutive behavior in these analyses. The axial modulus for the Ramberg-Osgood fit is 8.3% stiffer than the given matrix Young's modulus (Table V). The stiffer modulus is attributed to some fiber contribution in the $[\pm 45]_{ns}$ specimens. Figure 36 shows that as the temperature is increased, the stress and strain corresponding to the yield point on the curve are decreased. This trend is derived from the resin shear constitutive behavior presented in Chapter V.

Fiber — Three types of fibers were used in these analyses. First, the fibers were assumed to be transversely isotropic, having the properties of the AS4 fiber given in Table VIII. For the other two cases, the fiber was assumed to have the isotropic behavior shown in Table VIII. Two types of isotropic fiber properties were assumed for this analysis. In one case (Type A), E_{11} ($E_{22} = E_{11}$) and ν_{12} were the actual values for the AS4 fiber and G_{12} necessary for isotropy was computed. In the other case (Type B), G_{12} and ν_{12} were the actual values for the AS4 fiber and E_{11} ($E_{22} = E_{11}$) necessary for isotropy was computed. However, in shear instability models (Refs. 33, 34, 36, 126–128), the researchers have shown that the resistance to failure is controlled by the shear properties of the foundation and the column. Additionally, the results of Hayashi³⁴ and Kulkarni et al,⁴⁸ analyses that neglect $\frac{G_m}{G_f}$, indicate that as G_f is increased, the compressive strength of the composite is increased. Consequently, the Type B properties were used for the wavy fiber models. For these fibers, $\frac{G_m}{G_f} = 0.046$.

Fiber/Matrix Interface — The models with perfect fiber/matrix interfacial

Table VII. Ramberg-Osgood Parameters for Resin
Nonlinear Constitutive Behavior.

Temperature, °C	E , MPa	σ_o , MPa	n
21	3899	114.2	8.0748
77	3899	82.65	5.8676
132	3899	34.11	3.2625

Table VIII. Measured and Assumed Mechanical Properties of Constituent Materials.

Material	E_{11} , GPa	E_{22} , GPa	G_{12} , GPa	ν_{12}	G_m/E_f
PEEK Resin	3.60	3.60	1.30	0.42	—
AS4 Fiber	235	14.0	28.0	0.20	0.0153
APC-2 Lamina	134	8.90	5.10	0.30	0.0269
Quadrax ^a	70.7	70.7	6.10	0.03	0.0153
Type A Isotropic Fiber	235	235	97.9	0.20	0.0153
Type B Isotropic Fiber	67.2	67.2	28.0	0.20	0.0536
Isotropic Smear Region	13.3	13.3	5.10	0.30	0.2714 ^b

^a Assumed same for both 8- and 1- harness.¹⁴⁴

^b In this case, $\frac{G_m}{E_c}$.

bonds do not require any additional parameters. However, the poor fiber/matrix interfacial bond models require both the coefficient of friction and the “stiffness in stick” for the slide line elements along the interface. In these models, portions of the interface were completely degraded by assuming that both parameters were ideally zero, implying no friction and no shear stress transfer between the fiber and matrix in the debonded region prior to slip.

Unidirectional Lamina — Two types of properties were used for the equivalent homogeneous regions in the analyses. First, the orthotropic unidirectional lamina properties for APC-2, given in Table VIII, were used. Second, a set of isotropic properties, designated isotropic smear, were derived. Since the resistance to failure is controlled by the shear properties of the foundation and the column, G_{12} and ν_{12} were the actual values for the unidirectional lamina and E_{11} ($E_{22} = E_{11}$) necessary for isotropy was computed. These properties are also included in Table VIII. With either set of properties, the equivalent regions were assumed to be linear elastic and in a state of plane stress, consistent with laminate theory.

Convergence Studies

Mesh convergence studies were conducted on the infinite array of fibers and matrix (Fig. 33) for both the straight and wavy fiber problems. The selected mesh, shown in Fig. 33, contains 196 elements. The half-matrix is 2 by 28 elements (aspect ratio is ≈ 9.3) and the fiber is 3 by 28 elements (aspect ratio is ≈ 4.6). In addition to this selected mesh, two other meshes, one coarser and one finer, were attempted. In the coarser mesh, both the half-matrix and the fiber were each 1 by 14 elements. In the finer mesh, the half-matrix was 4 by 56 and the fiber was 3 by 56 elements. Mesh refinement had no effect on the eigenvalues/buckling strains determined for

the straight fiber bifurcation buckling problem because of the global nature of an eigenvalue analysis. To evaluate the effects of mesh refinement on the wavy fiber analysis, the global axial stress and the local elemental shear strains were plotted as a function of the applied axial strain. Also, as expected, the global stress-strain behavior was identical for the three meshes. The average localized shear strains determined with the finest mesh were $\approx 20\%$ different from those computed with the coarser meshes. However, when considering the fringe patterns (color contour plots) for the strain distributions in the model, the coarsest mesh did not provide the same strain distributions as the other two meshes. Consequently, the mesh shown in Fig. 33 was selected as an acceptably refined mesh.

Model Details

Already described within this chapter are the model geometries and constituent properties for the materials in the straight and wavy fiber problems. Within this section, the various combinations of model geometries and constituent properties are summarized.

The Straight Fiber Problem

Five different cases (Cases 1S–5S, S = Straight) were examined for the straight fiber problem. Case 1S is a comparison of the models for the perfect composite with orthotropic properties. Cases 2S and 3S compare the two types of isotropic fibers with orthotropic fibers for the same model in Case 1S. Cases 4S and 5S provide straight fiber models with the same isotropic properties as similar geometries in the wavy fiber analysis. Refer to Tables V and VIII for the constituent properties.

For the straight fiber problem, only linear-elastic constitutive behavior was assumed for the resin. Two reasons, one physical and one mathematical, for this

assumption exist. First, because the fibers were perfectly straight, no shear exists in the resin until after bifurcation buckling, and thus, including nonlinear shear stress-strain behavior would not affect the results. Second, the eigenvalue analysis of all straight fiber problems with nonlinear resin behavior yielded hourglass modes. ABAQUS does not provide automatic hourglass control for nonlinear materials for the elements used in this analysis. Consequently, the author did not show numerically that the finite element analysis would yield the same result for the straight fiber problem, regardless of linear or nonlinear constitutive behavior for the resin.

Case 1S — The infinite, semi-infinite, and finite plates (Fig. 32) and the infinite array of fibers and matrix were each modelled with linear matrix, transversely isotropic fibers, and orthotropic lamina properties for the smear areas.

Case 2S — The finite plate (10 fibers and matrix), Fig. 32c, was modelled with linear matrix and Type *A* isotropic fibers.

Case 3S — The finite plate (10 fibers and matrix), Fig. 32c, was modelled with linear matrix and Type *B* isotropic fibers.

Case 4S — The semi-infinite plate, Fig. 32b, was modelled with linear matrix, Type *B* isotropic fibers, and isotropic smear properties.

Case 5S — The infinite series of fibers separated by matrix was modelled with linear matrix and Type *B* isotropic fibers.

The Wavy Fiber Problem

Fifteen different cases were examined for the wavy fiber problem. The independent variables in these analyses include matrix constitutive behavior (Cases 1C–4C, C = Constitutive), initial fiber curvature (Cases 1W–5W, W = Wavy), interfacial bond strength (Cases 1D–4D, D = Debond), free surface effects (Case 1W), and

fiber constitutive properties (Cases 1F-2F, F = Fiber).

Effects of Matrix Constitutive Behavior — The infinite array of fibers embedded in matrix (Fig. 33) was modelled with Type *B* isotropic fibers. One initial fiber curvature, $\frac{a_0}{L} = 0.0050$, was used. Four different matrix behaviors were modelled: (i) linear, (ii) 21°C, (iii) 77°C, and (iv) 132°C. The models are designated Cases 1C, 2C, 3C, and 4C respectively.

Effects of Initial Fiber Curvature — The semi-infinite plate (Fig. 32b) was modelled with an initial waviness $\frac{a_0}{L} = 0.0050$. The model contained 21°C nonlinear matrix, Type *B* isotropic fibers, and an isotropic smear region. This model (Case 1W) is compared with the straight fiber model in Case 4S.

The infinite series of fibers embedded in matrix (Fig. 33) was modelled with 21°C nonlinear matrix and Type *B* isotropic fibers. Four arbitrary values of initial waviness ($\frac{a_0}{L}$) were modelled: (i) 0.0000, (ii) 0.0025, (iii) 0.0050, and (iv) 0.0075. These models are designated Cases 2W, 3W, 4W, and 5W respectively. Note that Case 4W is the same as Case 2C.

Effects of Interfacial Bond Strength — The infinite series, shown in Fig. 33, was modelled with 21°C nonlinear matrix and Type *B* isotropic fibers. The analysis assumed that at the poor interface, the surfaces were frictionless and zero shear stress was transferred between the matrix and the fiber. Two comparisons, debond location and debond length, are made in these models. For this discussion, refer to Fig. 33 for element numbers and geometry. Note that because the geometry in Fig. 33 is a repeating unit, every fiber in the infinite series is debonded along one edge.

To evaluate the effects of debond location on the initiation of fiber microbuckling, debonds that total 10.7% of the fiber length were placed in two different

locations along the fiber, near the symmetry line (Case 1D) and in the region of the localized maximum shear strains (Case 2D). The debond in Case 1D was placed between the fiber elements 168–166 and the corresponding matrix elements 56–54 respectively. In this case, one continuous debond existed. The debond in Case 2D was placed between the fiber elements 157–155 and the corresponding matrix elements 45–43. Because of the symmetry line, two debonds (each 5.35% of the fiber length) existed in this case. Each debond was along the region of maximum shear.

To evaluate the effects of debond length on fiber microbuckling length, three different debond lengths (10.7%, 25%, and 50% of the fiber length) were modelled. In each of the three cases, one continuous debond existed. The 10.7% debond (Case 1D) was again between the fiber elements 168–166 and the corresponding matrix elements 56–54. The 25.0% debond (Case 3D) was between the fiber elements 168–162 and the corresponding matrix elements 56–50. The 50.0% debond (Case 4D) was between the fiber elements 168–155 and the corresponding matrix elements 56–43.

Effects of Free Surface — The semi-infinite plate (Fig. 32b), described as Case 1W, was used to illustrate the effects of the free surface on fiber microbuckling initiation. Recall that the model had an initial fiber waviness, $\frac{a_0}{L} = 0.0050$, 21°C nonlinear matrix, Type *B* isotropic fibers, and an isotropic smear region.

Effects of Fiber Constitutive Properties — To illustrate the effects of fiber constitutive properties and thus the limitations of this analysis, the infinite series was modelled (Fig. 33) with Type *A* (Case 1F) and Type *B* (Case 2F) isotropic fibers. Note that Case 2F is the same as Cases 2C and 4W. The matrix is 21°C nonlinear and the initial fiber curvature is $\frac{a_0}{L} = 0.0050$.

CHAPTER V

EXPERIMENTAL RESULTS

This chapter contains a complete description of the experimental results of this investigation. As a basis, the material property characterization is presented. These properties include the lamina constitutive behavior, the initial in- and out-of-plane fiber waviness, the fiber/matrix interfacial shear strength, and the modes I and II delamination fracture toughnesses. Next, the results from an incremental damage progression study are presented to establish credibility of the observations of fiber microbuckling initiation. Finally, the effects of supporting ply orientation, initial fiber waviness, interfacial bond strength, resin-rich regions between plies, and resin constitutive behavior on fiber microbuckling initiation are discussed. Note that the absolute values of all fiber microbuckling initiation strains, nominal and local, are used for comparison throughout this chapter. The sample standard deviation (S) of ϵ_I for each of the variables is included in the text for comparison.

Material Property Characterization

Lamina Shear Constitutive Behavior

The shear stress-strain curves obtained from both tension and compression testing of the APC-2 laminates, derived from Eqns. 48 and 49, are shown in Fig. 37. Radiographs, shown in Figs. 38 and 39, indicate that matrix cracking has initiated in the tension-loaded specimens (Fig. 38) by the 2% axial strain level while the radiograph of the compression specimen (Fig. 39) shows no signs of damage at axial strain levels up to 9.7%. At 21°C, the flatter plateau in Fig. 37, obtained from tension testing, is attributed to matrix cracking in the laminate. Consequently,

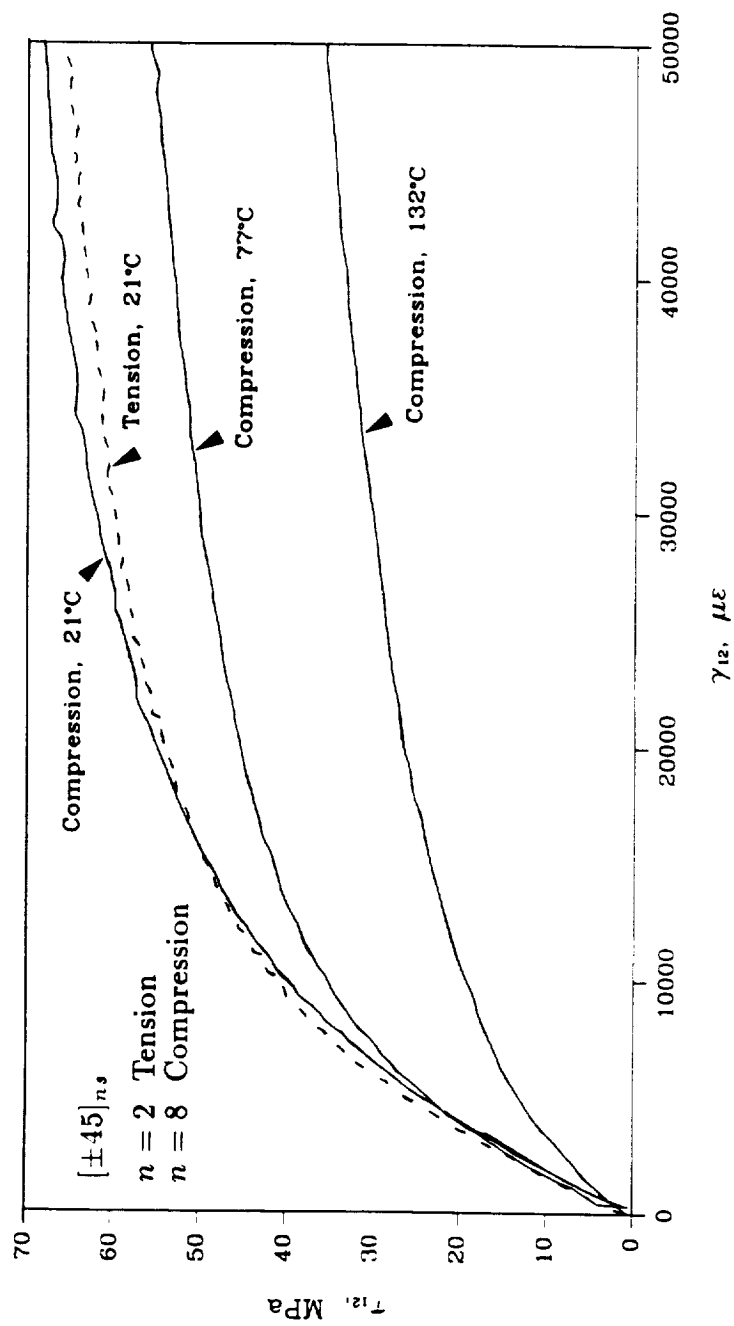


Fig. 37 Shear constitutive behaviors of APC-2 as a function of temperature.

Fig. 38 Dye-penetrant enhanced radiographs of a tension-loaded $[\pm 45]_2$ specimen.
a) Virgin specimen, prior to loading.
b) Applied axial strain level is 2%.
c) Applied axial strain level is 8%.

ORIGINAL PAGE
BLACK AND WHITE PHOTOGRAPH

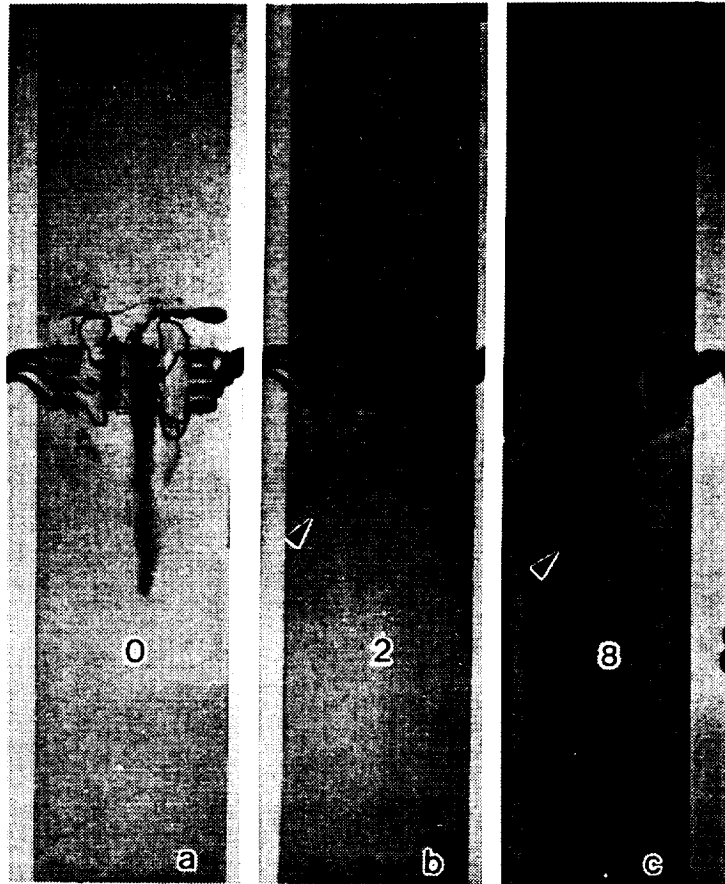
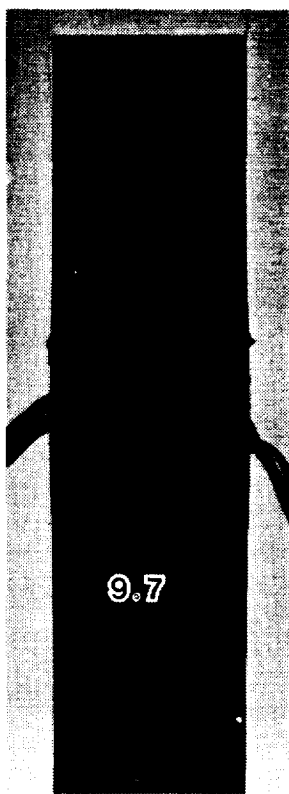




Fig. 39 Dye-penetrant enhanced radiograph of a compression-loaded $[\pm 45]_s$ specimen. Applied axial strain level is 9.7%.

ORIGINAL PAGE
BLACK AND WHITE PHOTOGRAPH



compression testing of $[\pm 45]_8$ specimens was selected for determination of the lamina constitutive behavior. Lamina shear constitutive behaviors obtained from compressive loading, derived using Eqns. 48 and 49, for 21°C, 77°C, and 132°C tests are shown in Fig. 37. The shear stresses and strains associated with the composite yield points in Fig. 37 are approximately 29 MPa and 6300 $\mu\epsilon$ at 21°C, 25 MPa and 5300 $\mu\epsilon$ at 77°C, and 5 MPa and 1200 $\mu\epsilon$ at 132°C. The corresponding resin shear constitutive behaviors (derived in Chapter IV) are shown in Fig. 40. Additionally, an assumed theoretically linear behavior has been added to the figure. From this data the elastic shear modulus of the resin, G_m , was measured to be 2.0 GPa, significantly higher than given in Table V.¹³⁷ The higher PEEK shear modulus is attributed to the fiber contribution and the fiber/matrix interaction. These curves indicate that at 77°C and 132°C, there is a significant reduction in the shear stress and strain associated with the yield point on the $\tau_m-\gamma_m$ curve. The shear stresses and shear strains associated with the resin yield points in Fig. 40 are approximately 18 MPa and 9000 $\mu\epsilon$ at 21°C, 15 MPa and 7700 $\mu\epsilon$ at 77°C, and 2 MPa and 1200 $\mu\epsilon$ at 132°C. It is anticipated that this reduction decreases the amount of support for the fibers and reduces the strain level at which fiber microbuckling initiates.

Initial Fiber Waviness

The laminates designed to evaluate the effects of initial fiber waviness on fiber microbuckling initiation are summarized in Table III, and their cross-sections are shown in Fig. 41. The 0° fiber direction is marked with an arrow on this figure. The purpose of the Quadrax laminates was to build some initial fiber waviness into the laminates. However, comparison of the tape laminate (Fig. 41a) with the Quadrax laminates (Fig. 41b and 41c) shows that interlacing caused a global out-of-plane ply waviness rather than a localized fiber waviness. The out-of-plane waviness ratio,

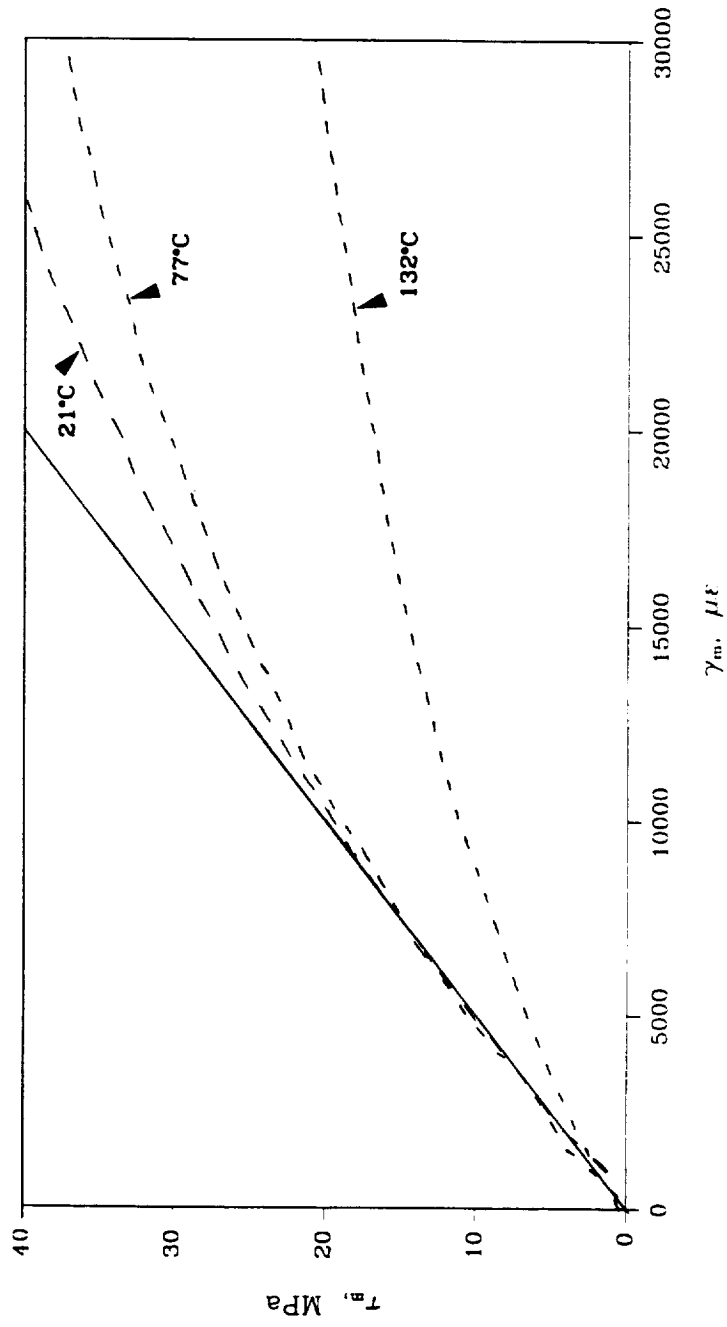
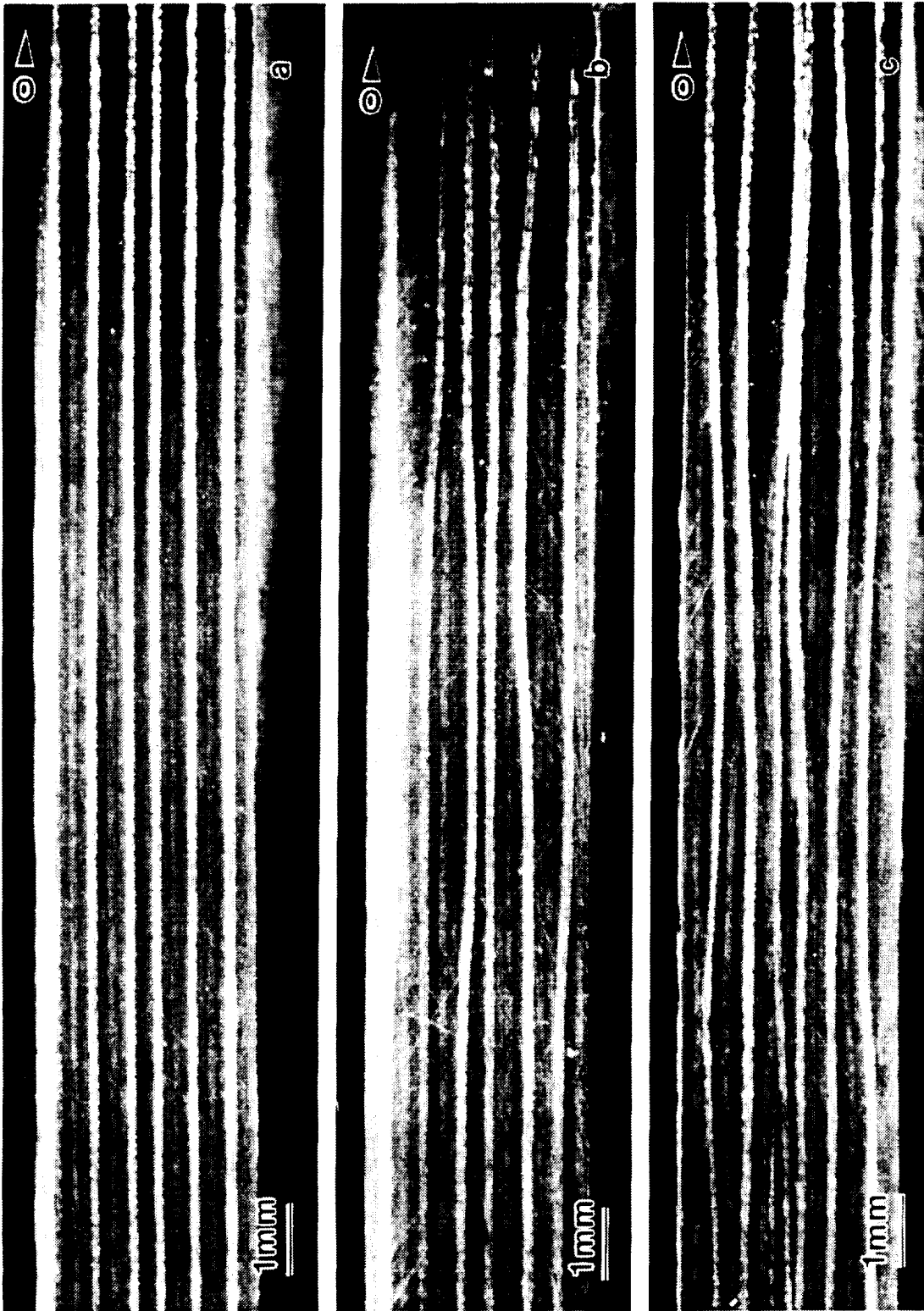


Fig. 40 Shear constitutive behaviors of PEEK resin as a function of temperature.

Fig. 41 Cross-sections of laminates for initial fiber waviness studies.
a) APC-2 tape laminates, $[\pm 45/0/90]_{3s}$.
b) Quadrax 8-harness, $[\pm 45/(0/90)]_{3s}$.
c) Quadrax 1-harness, $[\pm 45/(0/90)]_{3s}$.

ORIGINAL PAGE
BLACK AND WHITE PHOTOGRAPH



measured with a scale accurate to 0.254 mm, is very near zero for the tape laminate and approximately 0.082 and 0.093 for the 8- and 1- harness Quadrax laminates, respectively.

Figure 42 shows the representative in-plane waviness in the $[0_{24}]$ APC-2 composites. The 0° fiber direction is marked with an arrow on this figure. This figure shows that the in-plane fiber waviness ratio is very small, particularly when compared to the out-of-plane ply waviness ratios for the Quadrax laminates (Fig. 42). Two observations discourage the use of the measuring technique in Ref. 152. First, it is very difficult to find continuous fibers with complete wavelengths in Fig. 42 because the fiber waviness ratio is very small. Second, and more important for this investigation, the in-plane fiber waviness of the unidirectional composite is not representative of the actual local fiber waviness in each ply at the notch. In this study, it is expected that the in-plane fiber waviness at the notch has a more significant effect on fiber microbuckling initiation than the representative waviness of the unidirectional laminates. However, at the present, it is not possible to measure the in-plane waviness at the notch and then test the same specimen. Consequently, the in-plane waviness at the notch or in a unidirectional laminate was not actually digitized.

Fiber/Matrix Interfacial Bond Strength

In the initial 10 fibers selected from the multidirectional APC-2 laminate, two fibers gave exceptionally high IFSS values (the highest values reported to date) of 136.9 MPa and 121.1 MPa. Because of the skewed distribution of the IFSS values, an additional series of 10 fibers was tested. The average IFSS value for this second series is reported. Evidently, the surface treatment of the fibers is not uniform.

The ITS interfacial shear strengths for the unidirectional and multidirectional

Fig. 42 Representative in-plane fiber waviness in $[0_{24}]$ APC-2 laminates.



APC-2 and AU4U/PEEK laminates are summarized in Table IX. The average IFSS values measured were 95.87 MPa and 79.86 MPa, respectively, for the APC-2 and AU4U/PEEK unidirectional laminates. For both materials, the $[0_{24}]$ and $[(\pm 45/0_2)_3/\pm 45/0]$, stacking sequences yielded the same (within 4.0%) IFSS values, indicating that the residual cure stresses do not affect the interfacial shear strengths for these particular materials and lay-up. These results indicate that when compared to the commercial APC-2 material, the IFSS for the experimental poor interface material is reduced by 16.7%, regardless of the stacking sequence.

Delamination Fracture Toughness

As an introduction to the fracture results, Fig. 43 contains representative micrographs showing cracks from mode I and mode II delamination fractures for both material systems. The cross-sections in Fig. 43 were cut parallel to the specimen length, near the crack tip, to observe matrix deformation and fiber/matrix adhesion. Figures 43a and 43b are the mode I cracks for the APC-2 and AU4U/PEEK materials, respectively. Figure 43a shows large amounts of matrix deformation, including fibrils and matrix drawing in the opening mode, for the APC-2 laminates. However, for the poor interface AU4U/PEEK material, Fig. 43b shows very little matrix deformation with bare fibers, indicating that the crack grows at the fiber/matrix interface. The mode II cracks for the APC-2 and AU4U/PEEK materials are shown in Figs. 43c and 43d, respectively. The amount of resin deformation and fiber/matrix bonding for the mode II laminates is similar to the results reported for mode I, but as expected, the type of deformation is different. Again, the crack in the APC-2 laminate (Fig. 43c) is in the resin while the crack in the AU4U/PEEK laminate (Fig. 43d) grew at the fiber/matrix boundary. The fibers in Fig. 43d are bare, as with Mode I (Fig. 43b).

Table IX. Interfacial Strength and Fracture Toughness Data.

LID	Stacking Sequence	Material	IFSS, ^a MPa	G_I^b , J/m ²	G_{II}^b , J/m ²
<i>OG</i>	[0] ₂₄	APC-2	95.87	1458 ^d	2500
<i>OP</i>	[0] ₂₄	AU4U/PEEK ^c	79.86	729	1150
<i>OG</i>	[(±45/0 ₂) ₃ /±45/0] _s	APC-2	97.28	—	—
<i>OP</i>	[(±45/0 ₂) ₃ /±45/0] _s	AU4U/PEEK ^c	79.90	—	—

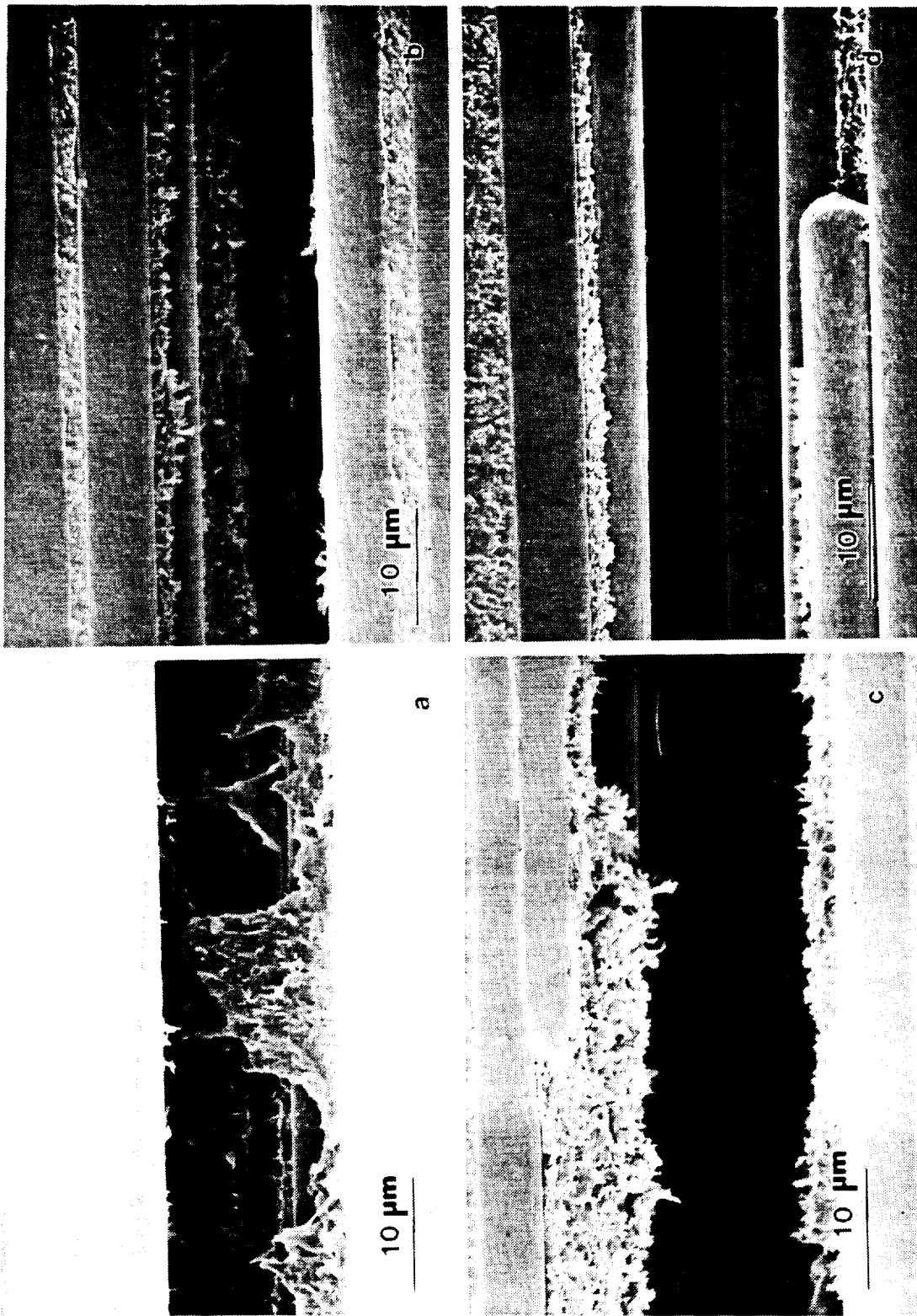
^aITS interfacial shear strength.

^bAverage steady-state values.

^cExperimental poor interface material.

^dSpecimen OG5 (not included in average) had multiple crack surfaces and $G_I = 2130$ J/m².

Fig. 43 Resin deformation near fracture crack tips.
a) Mode I, APC-2.
b) Mode I, AU4U/PEEK.
c) Mode II, APC-2.
d) Mode II, AU4U/PEEK.



Mode I — Typical load-displacement curves for the APC-2 and AU4U/PEEK mode I DCB tests are presented in Fig. 44. These two curves indicate that both the good and poor interface materials behaved linearly-elastic and exhibited stable delamination growth in mode I loading. The curves show that much more energy is absorbed for crack growth in the APC-2 material. It should be noted that frequent popping noises were heard prior to the maximum load, although growth was not observed. Because of the difficulty in detecting the initiation of crack growth, true G_{Ic} values were not determined. The strain energy release rate, G_I , is computed using Eqn. 51 in conjunction with the load and crack length measurements described in the Methods section of Chapter III. This instantaneous or steady-state G_I is plotted as a function of crack length in Fig. 45 for the APC-2 and AU4U/PEEK specimens tested. Initial crack lengths are ≈ 23 – 25 mm for APC-2 and ≈ 17 – 21 mm for AU4U/PEEK. For the commercial APC-2, the average steady-state G_I of specimens OG3 and OG4 is ≈ 1458 J/m². This steady-state value is reported in Table IX. However, the steady-state G_I for specimen OG5 is ≈ 2130 J/m². The critical strain energy release rate, G_{Ic} , for APC-2 is reported as 2680 J/m² in Ref. 149 and 2890 J/m² in Ref. 167. According to Ref. 150, values have been reported between 1500 J/m² and 3000 J/m², depending on processing techniques. For the experimental AU4U/PEEK material, the specimen average is a steady-state G_I of ≈ 729 J/m². The average values are indicated on the graph in Fig. 45. This steady-state G_I value is included in Table IX. During these tests, a small amount of fiber bridging was observed for both material systems.

Micrographs of the representative mode I DCB fracture surfaces are shown in Fig. 46. In this figure, the direction of crack propagation is from the top of the micrographs to the bottom of the micrographs. Figure 46a is an overview of

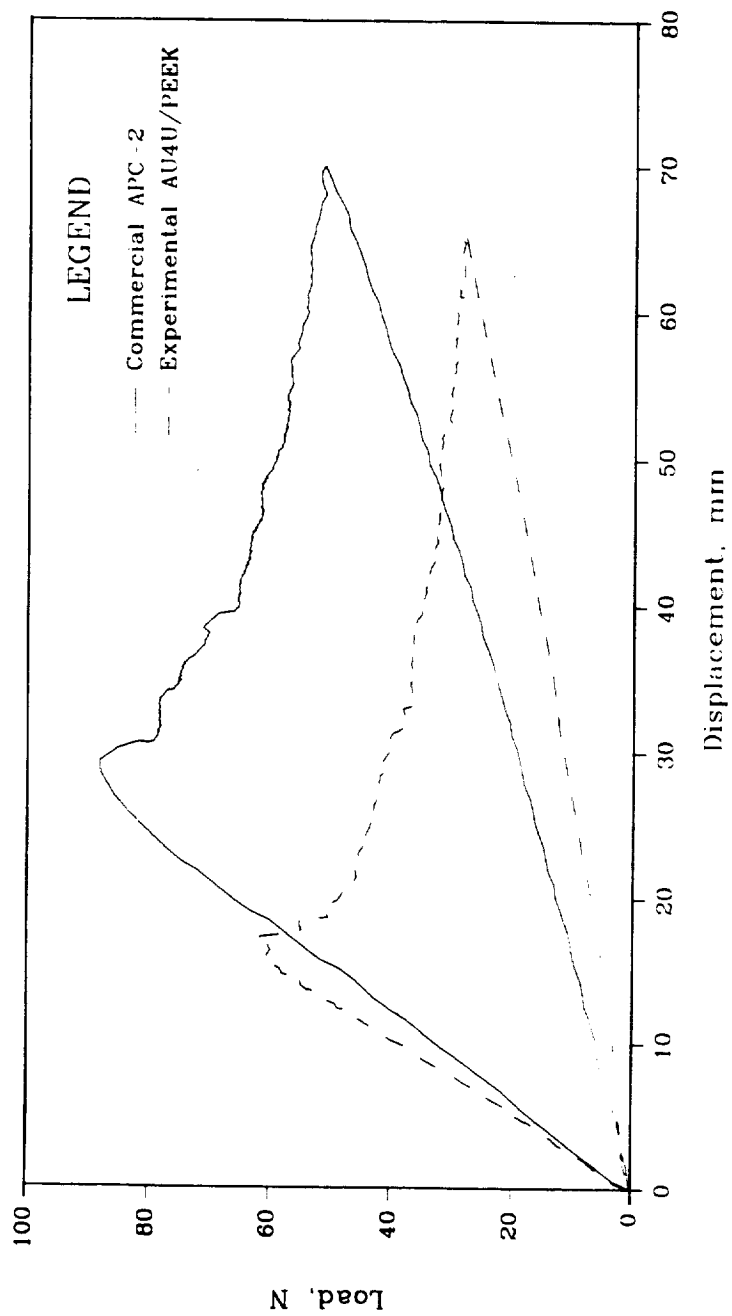


Fig. 44 Mode I load-displacement data for $[0_{24}]$ laminates.

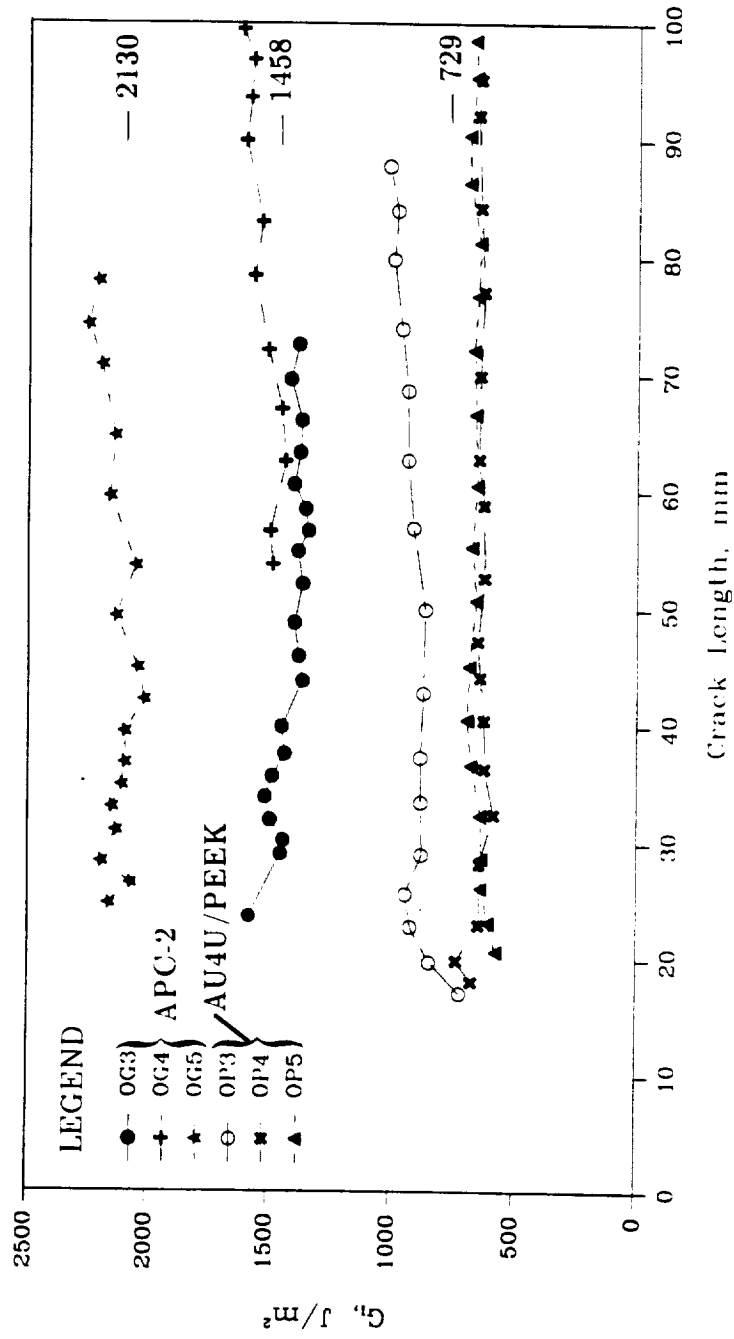
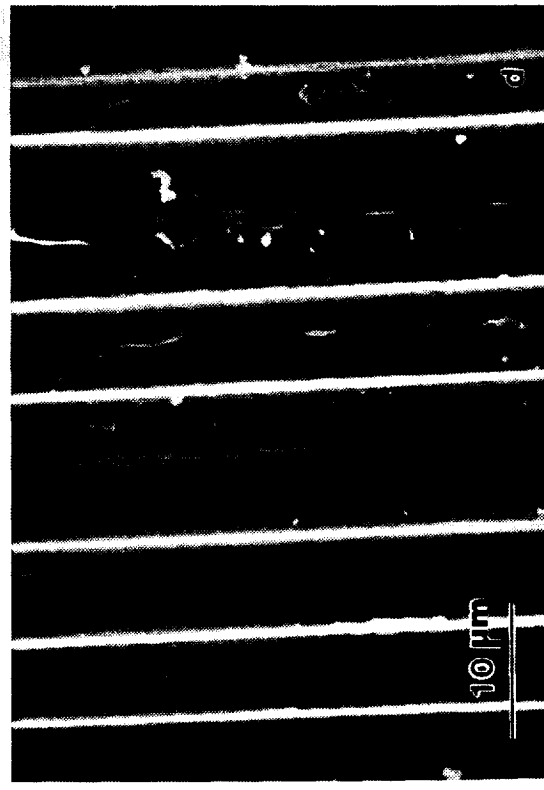
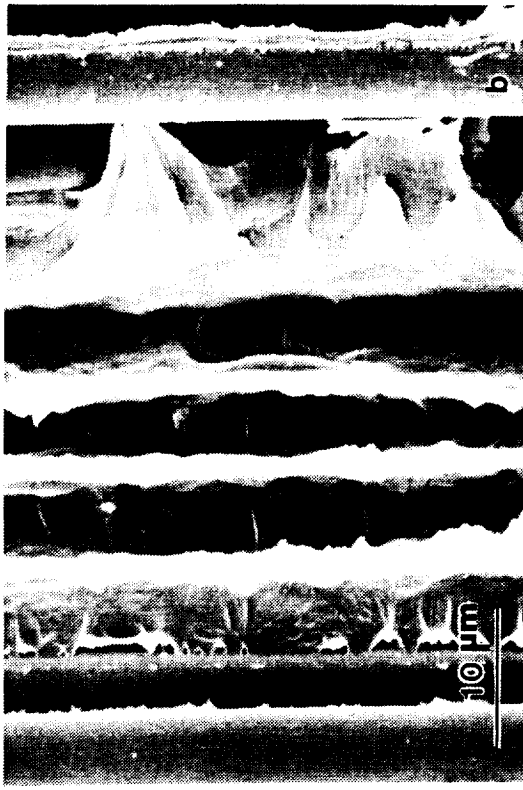


Fig. 45 G_I versus crack length for $[0_{24}]$ DCB specimens.

- Fig. 46** Micrographs of Mode I DCB fracture surfaces.
- a) Overview of APC-2 fracture surface.
 - b) APC-2 fiber/matrix interface.
 - c) Overview of AU4U/PEEK fracture surface.
 - d) AU4U/PEEK fiber/matrix interface.

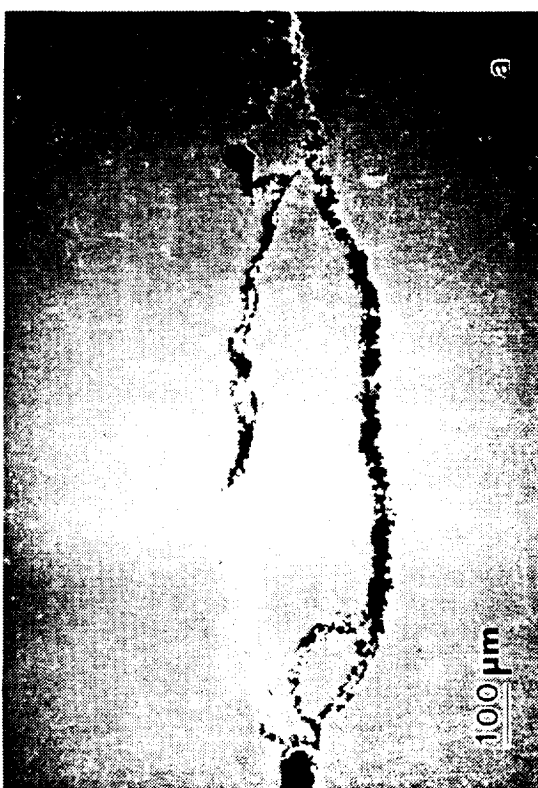
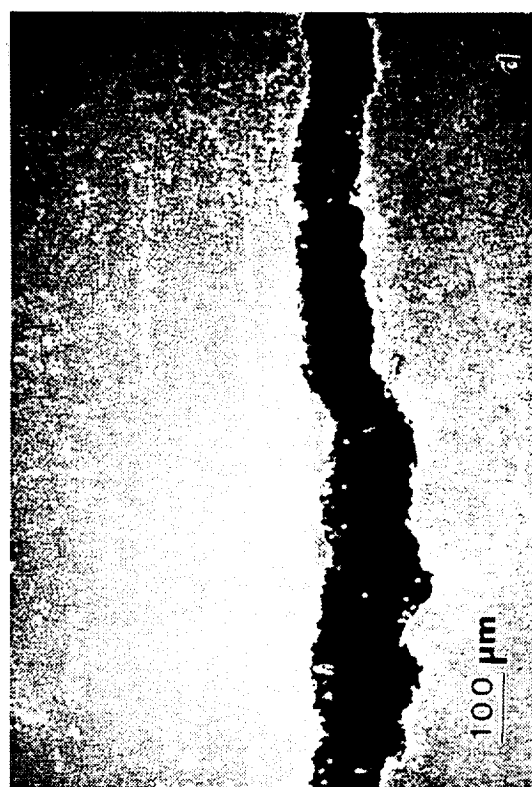
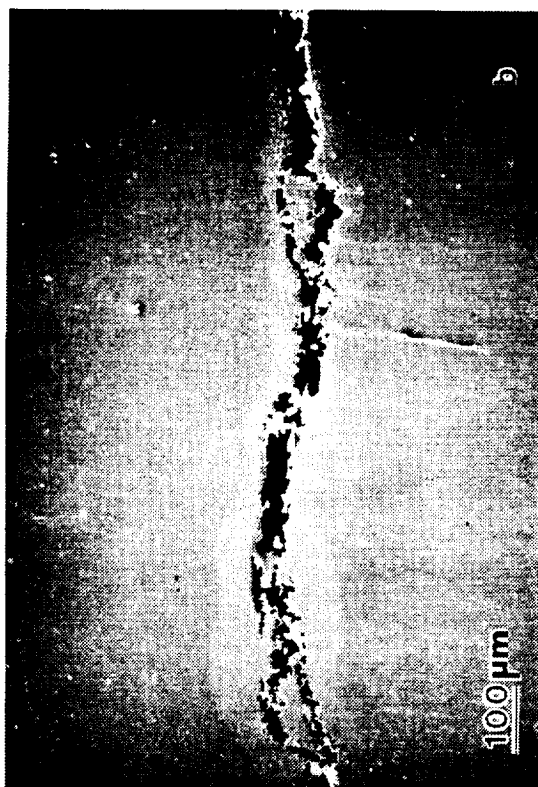


the APC-2 mode I fracture surface showing the severely drawn PEEK matrix well-adhered to the fibers. This result is also confirmed by the higher magnification micrograph in Fig. 46b, a detail from Fig. 46a. Figure 46c is an overview of the AU4U/PEEK mode I fracture surface showing essentially bare fibers with little resin deformation. An additional detail of the bare fibers is shown in Fig. 46d. The bare fibers in Figs. 46c and 46d indicate that the crack is growing at the fiber/matrix interface, rather than in the resin-region between plies. Notice that the fracture surface of the poor interface system (Fig. 46c) contains many loose fibers compared to APC-2 in Fig. 46a. Considering the lack of resin deformation and the crack location at the fiber/matrix interface in this material, loose fibers are not surprising. The loose fibers in this micrograph (Fig. 46c) indicate that more fiber bridging occurred in the AU4U/PEEK system than in the APC-2 system (absence of loose fibers in Fig. 46a).

To explain the difference between the two steady-state G_I values for the APC-2 laminates in Fig. 45, cross-sections were cut perpendicular to the specimen length to observe the fracture path of the crack. Figure 47 shows these fracture paths. Figures 47a and 47b are the fracture paths of specimen OG5 (higher G_I). These micrographs indicate that multiple crack paths exist for this specimen. The consequent increase in fracture surface area causes an increase in G_I . Although it is difficult to distinguish the ply boundaries in this specimen, careful observation indicates that the cracks are growing within the ply (intraply). Typically, intraply cracking occurs at lower fracture energies because of the reduced resin volume fraction within the ply, compared to between the plies. Figure 47c shows one intraply fracture path in specimen OG3 (lower G_I). Considering the micrographs in Fig. 47 and comparing the steady-state G_I values with the critical values reported

Fig. 47 Cross-sections perpendicular to DCB specimen length
to show crack fracture path.

- a) Specimen OG5, APC-2.
- b) Specimen OG5, APC-2.
- c) Specimen OG3, APC-2.
- d) Specimen OP4, AU4U/PEEK.



in the literature, it appears that intraply cracking causes a significant decrease in the fracture energies (specimens OG3 and OG4) of APC-2 laminates. However, the multiple intraply crack paths (specimen OG5) caused an increase in the energy absorbed and thus G_I . The specimens in this study did not realize the maximum toughness of the PEEK resin since the cracks did not grow between the plies (interply). If the cracks had grown interply, it is expected that the steady-state G_I would have been closer to the values in Refs. 149 and 167. Although cracks in the APC-2 laminates grew intraply, observation of the micrographs in Figs. 43a, 46a, and 46b indicate that the failure is of cohesive type in the PEEK matrix. Similar observations were reported in Ref. 149. Figure 47d shows the fracture path of specimen OP4, a representative micrograph from the experimental material. Again, the fracture path is intraply. Because of the poor interfacial bond, the crack grows intraply at the fiber/matrix boundary revealing bare fibers and without deforming the matrix, as seen in Figs. 43b, 46c, and 46d. The poor interface in conjunction with the reduced resin volume fraction in the ply (compared to between the plies) causes a significant decrease in G_I , as shown in Fig. 45.

Mode II — Typical load-displacement curves for the APC-2 and AU4U/PEEK mode II ELS tests are presented in Fig. 48. These two curves indicate that both the good and poor interface materials behaved linearly-elastic and exhibited stable delamination growth in mode II loading. The crack for the APC-2 material grew under the clamp. This portion of the load-displacement curve is indicated with an arrow in Fig. 48. The curves show that much more energy is absorbed for crack growth in the APC-2 material. It should be noted that crack growth was detected prior to reaching the maximum load in these tests, yielding critical initiation strain energy release rates, G_{IIc} , as low as 1250 J/m^2 (APC-2) and



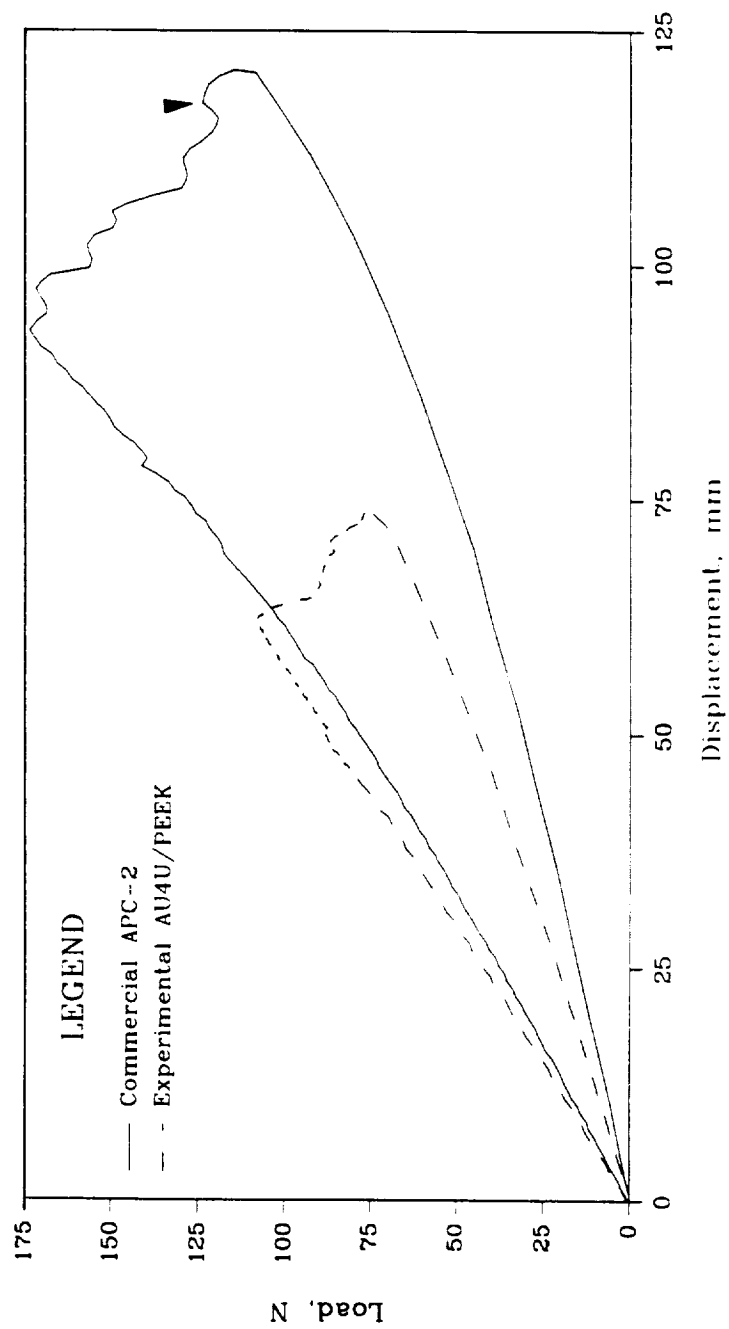


Fig. 48 Mode II load-displacement data for $[0_{24}]$ laminates.

625 J/m² (AU4U/PEEK). However, due to the difficulty in detecting initiation of crack growth, true G_{IIc} values could not be determined. The instantaneous strain energy release rate, G_{II} , is computed using Eqn. 52 in conjunction with the load and crack length measurements described in the Methods section of Chapter III. The instantaneous G_{II} is plotted as a function of the crack length normalized by the 20.32 cm gage length, a/L , in Fig. 49. Crack arrest values are indicated with arrows. For the commercial APC-2, the average of the valid G_{II} measurements for the 3 specimens is a steady-state G_{II} of ≈ 2500 J/m². For the experimental AU4U/PEEK material, the average G_{II} of the 3 specimens is a steady-state G_{II} of ≈ 1150 J/m². The average steady-state G_{II} values are tabulated in Table IX and shown on the graph in Fig. 49.

Micrographs of the representative mode II ELS fracture surfaces are shown in Fig. 50. In this figure, the direction of crack propagation is from the top of the micrographs to the bottom of the micrographs. Figure 50a is an overview of the APC-2 mode II fracture surface showing the severely drawn PEEK matrix well-adhered to the fibers. This result is also confirmed by the detail in Fig. 50b. Figure 50c is an overview of the AU4U/PEEK mode II fracture surface showing bare fibers with a small amount of resin deformation between the fibers. Higher magnifications of the bare fibers are shown in Fig. 50. Fiber striations from processing are also visible in this figure. Figure 50c shows a reduced number of loose fibers, compared to those observed in the mode I micrographs in Fig. 46a. This difference is attributed to the sliding, rather than opening, mechanism in mode II. Although fiber bridging or interlocking cannot be observed during the ELS tests, the loose fibers in Fig. 50c indicate that more fiber bridging occurred in the AU4U/PEEK system than in the APC-2 system (few loose fibers in Fig. 50a).

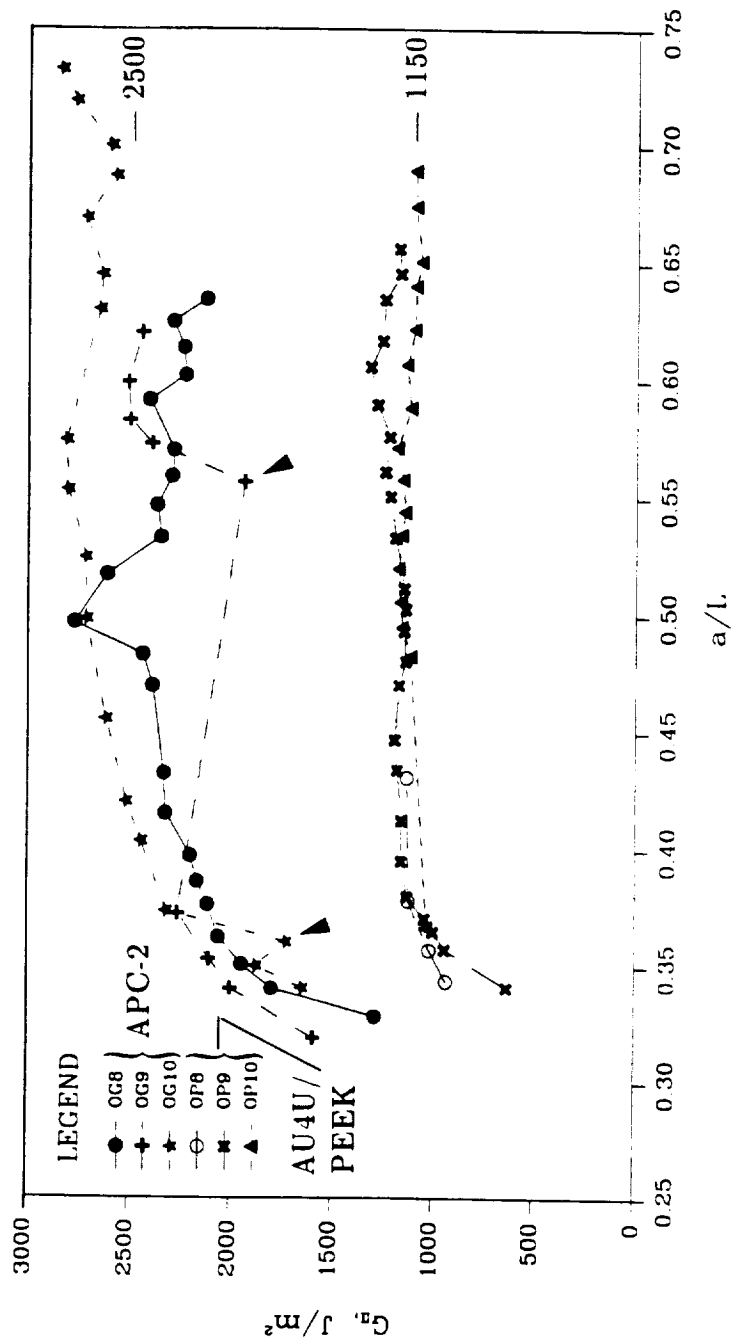
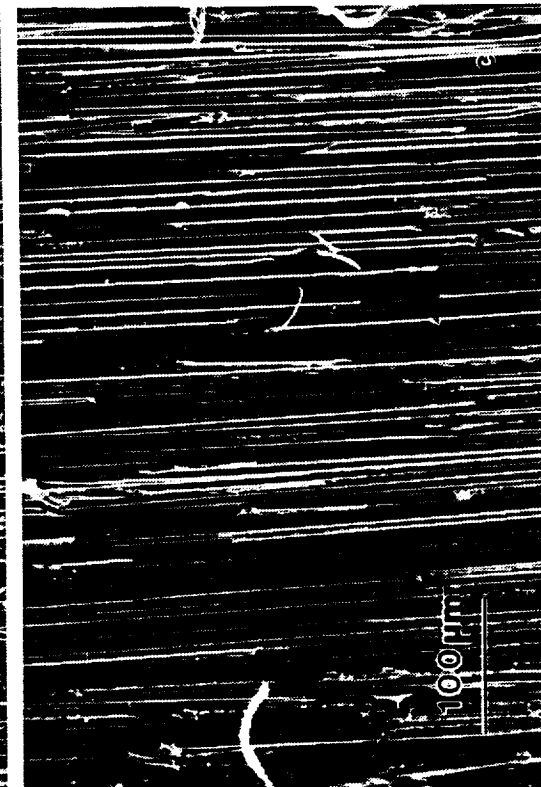
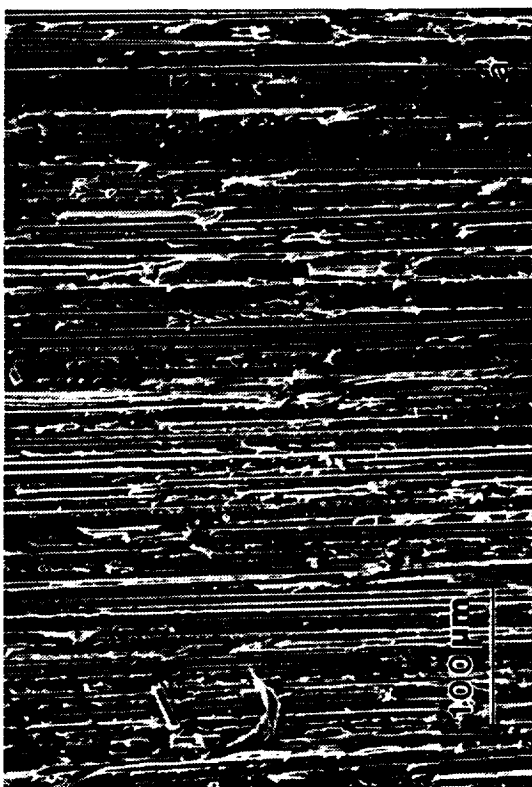
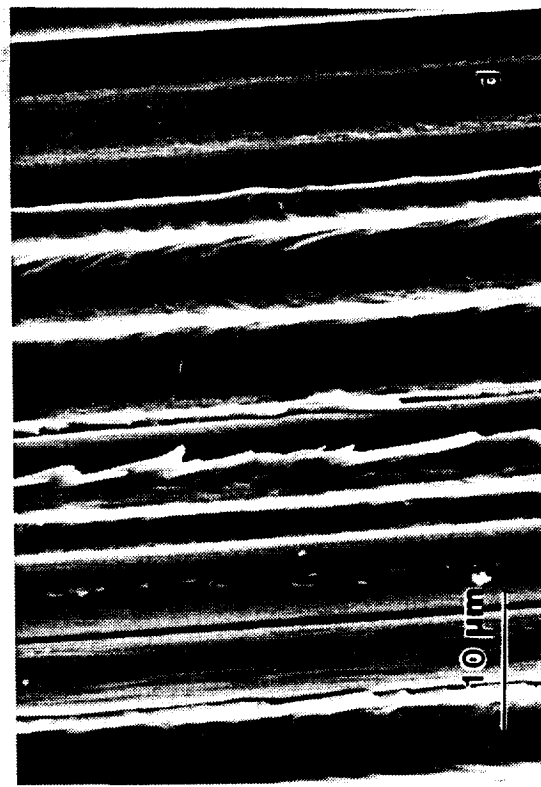


Fig. 49 G_{II} versus normalized crack length for [024] ELS specimens.

- Fig. 50** Micrographs of Mode II ELS fracture surfaces.
- a) Overview of APC-2 fracture surface.
 - b) APC-2 fiber/matrix interface.
 - c) Overview of AU4U/PEEK fracture surface.
 - d) AU4U/PEEK fiber/matrix interface.



Cross-sections were cut perpendicular to the specimen length to observe the fracture paths of the cracks. Figure 51 shows these fracture paths. Figure 51a and 51b are the typical mode II fracture paths for the APC-2 and AU4U/PEEK laminates, respectively. In both cases the fracture paths are intraply, indicating that the maximum mode II resistance to fracture was not achieved for either material. Observation of the APC-2 micrographs in Fig. 43c, 50a, and 50b indicates that although the crack grew intraply, the failure was still cohesive in the PEEK matrix.

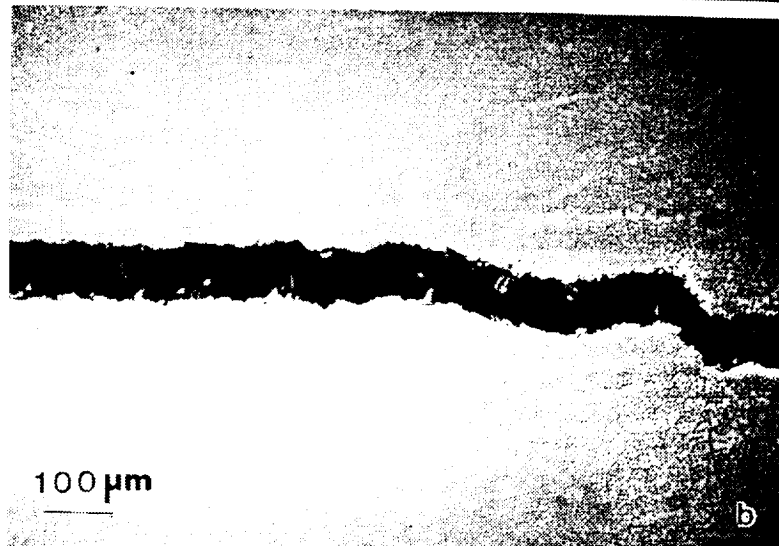
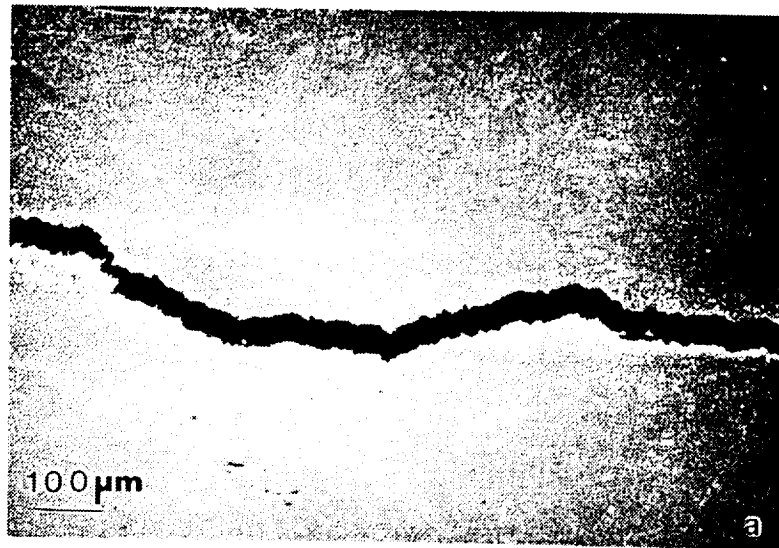
Damage Progression Investigation

In-situ observations of damage progression in the stereomicroscope indicate initial elastic deformation of the composite followed by excessive fiber bending in-plane and subsequent in-plane fiber microbuckling in the 0° plies in the notch region.

Initial elastic deformation of the composite is not obvious through the stereomicroscope due to the slowly applied displacement rates. However, when the specimen is unloaded (faster displacement rate), the release of elastic energy/deformation is clearly obvious through the stereomicroscope. This result was concluded after completion of the first two strain increments. At the higher strain increments ($\approx 60\%$ – 70% of fiber microbuckling initiation strain level, depending on lay-up), the discontinuous 0° fibers in the notch radius translate vertically, relative to the adjacent plies, into the notch as a result of the elastic deformation. Similar damage was also reported in Refs. 104 and 105. It is suspected that these translations are associated with local delaminations between the terminated fibers in the 0° plies and the adjacent plies. With additional applied strain, it is evident from the motion of the observed 0° fibers that the subsurface 0° fibers bend in-plane toward the free surface of the notch. These observations are supported by the micrographs

Fig. 51 Cross-sections perpendicular to ELS specimen length
to show crack fracture path.
a) APC-2.
b) AU4U/PEEK.

ORIGINAL PAGE
BLACK AND WHITE PHOTOGRAPH



in Fig. 52. This figure shows the typical succession of damage progression in the same 0° ply. Figure 52 shows the initial state in a, increment 3, 2.0% local strain in b, and increment 4, 2.5% local strain in c. Fiber microbuckling in this ply led to catastrophic failure of the specimen at increment 5, 2.54% local strain. Figures 52b and 52c show the typical resulting in-plane deformation caused by the subsurface fiber bending. It should be noted that some of the fiber breakage (both bending and shear types) in Fig. 52 is a result of drilling processes.

Fiber microbuckling occurs at one of three locations in the notch radius. These locations are the notch centerline (shown in Fig. 52) and either above or below the notch centerline behind the discontinuous 0° fibers. When the fiber microbuckling is not along the notch centerline, it is indirectly observed by in-plane protruding of the discontinuous fibers into the notch.

The micrographs in Fig. 53 show the damage progression for an initially damaged fiber (fiber breaks indicated with arrows). The figure shows the initial state (a) and increments 1, 2, and 4 in Figs. 53b, 53c, and 53d, respectively. Increment 3 is omitted because the damage was similar to that seen in Fig. 52c. Obviously by increment 4, the fiber has failed in a bending mode. A new fiber break (indicated by arrow) has developed in Fig. 52b. Additionally, a fiber with some in-plane bending in Fig. 53c (indicated with an arrow) is completely broken in Fig. 53d (indicated with an arrow). It should be noted that the orientation of the fracture surface of the fiber may be erroneously interpreted to imply a shear-type failure. These intermittent SEM observations during this incremental study show that the fibers with initial damage have some load-carrying capacity.

It should be noted that absolute determination of damage caused by drilling processes would require a very systematic, academic study documenting the initial

Fig. 52 Damage progression in a 0° ply.
a) Initial state.
b) Increment 3, 2.0% local strain.
c) Increment 4, 2.5% local strain.

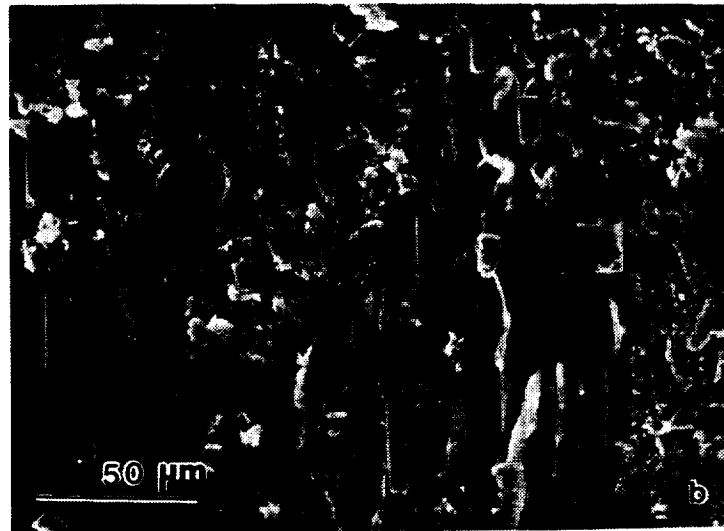
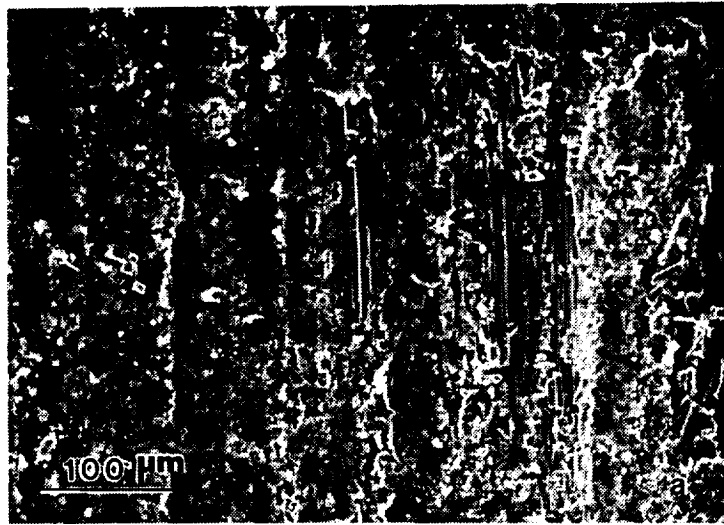


Fig. 53 Damage progression for an initially damaged 0° fiber.

- a) Initial state.
- b) Increment 1, 1.0% local strain.
- c) Increment 2, 1.5% local strain.
- d) Increment 4, 2.5% local strain.

ORIGINAL PAGE
BLACK AND WHITE PHOTOGRAPH



fiber damage and then subsequent damage at each load increment. The process would be very tedious because many fibers would need to be documented at each load increment.

The results presented in this study verify that the stereomicroscope observations of fiber microbuckling correspond with higher magnification observations in the SEM. Consequently, the stereomicroscope observations were determined to be sufficient for repeatable recognition of the initiation of fiber microbuckling.

Effects of Supporting Ply Orientation

The test matrix used to illustrate the effects of supporting ply orientation on the initiation of fiber microbuckling in 0° plies is given in Table II. Data showing these effects are presented in this section.

The effects of supporting ply orientation on in-plane fiber microbuckling are shown in Fig. 54. This bar chart shows the average remote axial strain level for fiber microbuckling, ϵ_I , in specimens with $\theta = \pm 15, \pm 45, \pm 75$, and 90_2 plies as surface plies. Additionally, data is shown for laminate B ($[(0_2/\pm 45)_3/0/\pm 45]_s$). Recall from Table II that the ± 45 and 0_2 plies are interchanged for laminates with 0_2 as surface plies. When the surface ply orientation at 21°C is considered, the nominal strain for fiber microbuckling initiation occurs at $6878 \mu\epsilon$ ($S = 218 \mu\epsilon$) for 0_2 , $4993 \mu\epsilon$ ($S = 203 \mu\epsilon$) for ± 15 , $7919 \mu\epsilon$ ($S = 79 \mu\epsilon$) for ± 45 , $7295 \mu\epsilon$ ($S = 504 \mu\epsilon$) for ± 75 , and $6406 \mu\epsilon$ ($S = 115 \mu\epsilon$) for 90_2 . At 77°C , fiber microbuckling initiation occurs at $5793 \mu\epsilon$ ($S = 1175 \mu\epsilon$) for 0_2 , $4677 \mu\epsilon$ ($S = 592 \mu\epsilon$) for ± 15 , $6448 \mu\epsilon$ ($S = 499 \mu\epsilon$) for ± 45 , $4481 \mu\epsilon$ ($S = 335 \mu\epsilon$) for ± 75 , and $4000 \mu\epsilon$ ($S = 424 \mu\epsilon$) for 90_2 . The global data shows that at both 21°C and 77°C , the ± 45 plies appear to provide the most resistance to fiber microbuckling while the ± 15 plies appear to provide

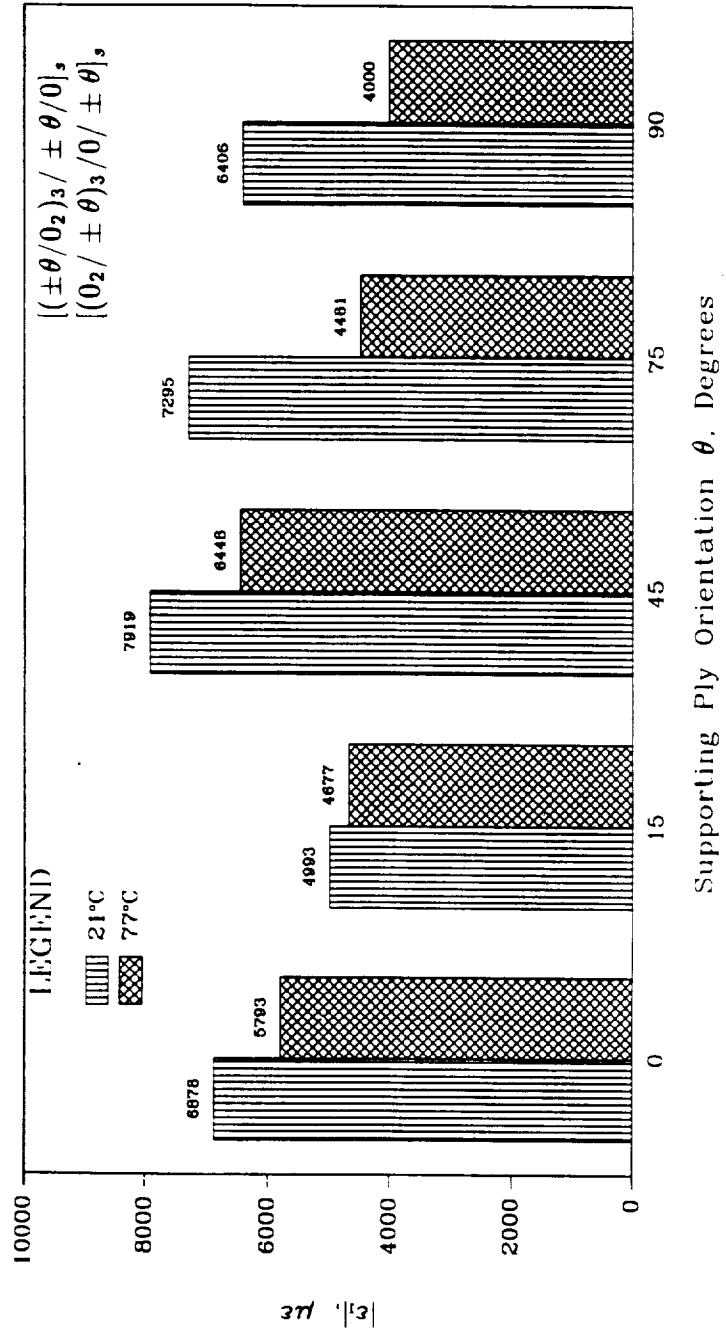


Fig. 54 Bar chart showing the effects of supporting ply orientation on fiber microbuckling initiation strains in laminates A, B, C, D, and E, tested at 21°C and 77°C.

the least resistance. At 77°C, the fiber microbuckling initiation strains are reduced 6–20%, compared to those at 21°C. In particular, ϵ_I at 77°C is significantly reduced ($\approx 38\%$), compared to 21°C, for those laminates with ± 75 and 90_2 as supporting plies.

To include laminate orthotropy, the SCFs were computed using the two-dimensional finite element analysis of an orthotropic plate with two semi-circular edge notches. Due to the availability of elastic properties, the SCFs were computed only for 21°C data. It is assumed that these SCFs are reasonable approximations for the 77°C tests. It is anticipated that the SCFs are reduced at 77°C, compared to those at 21°C, because of matrix softening. Additionally, fringe plots of the stress distributions (not included) were examined to verify that the strain gages were in remote locations, with respect to the notches, on the specimens. The SCFs are listed in Table X for these laminates, and the local fiber microbuckling initiation strain levels are shown as a function of the supporting ply orientation in the bar chart in Fig. 55. The trend in Fig. 55 indicates that when the laminate orthotropy is considered, the fiber microbuckling initiation strain at 21°C is essentially constant, like a material property, regardless of the supporting ply orientation. The range of the local ϵ_I at 21°C is 21321–24880 $\mu\epsilon$. The average local ϵ_I at 21°C, considering all supporting ply orientations, is 23361 $\mu\epsilon$. However the 77°C results, reflecting those in Fig. 54, imply two constants for ϵ_I . The average local ϵ_I values at 77°C are 19935 $\mu\epsilon$ (consider 0_2 , ± 15 , and ± 45 surface ply orientations) and 15031 $\mu\epsilon$ (consider ± 75 and 90_2 as surface ply orientations). Thus, the average local ϵ_I at 77°C is reduced, compared to 21°C, 14.6% for laminates with 0_2 , ± 15 , and ± 45 as supporting plies and 35.7% for laminates with ± 75 and 90_2 as supporting plies.

Observation of the local strain values in Fig. 55 poses another question; namely,

Table X. Strain Concentration Factors (21°C).

LID	Stacking Sequence	SCF
<i>B</i>	$[(0_2/\pm 45)_3/0/\pm 45]_s$	3.28364
<i>C</i>	$[(\pm 15/0_2)_3/\pm 15/0]_s$	4.19298
<i>A, F</i>	$[(\pm 45/0_2)_3/\pm 45/0]_s$	3.28364
<i>D</i>	$[(\pm 75/0_2)_3/\pm 75/0]_s$	3.41052
<i>E</i>	$[(90_2/0_2)_3/90_2/0]_s$	3.69487
<i>G</i>	$[(\pm 45/f/0_2/f)_3/\pm 45/f/0]_s$	3.28206
<i>H</i>	$[(\pm 45/f_3/0_2/f_3)_3/\pm 45/f_3/0]_s$	3.27466
<i>K</i>	$[\pm 45/0/90]_{3s}$	2.89953
<i>KQ8, KQ1</i>	$[\pm 45/\langle 0/90 \rangle]_{3s}$	2.94003

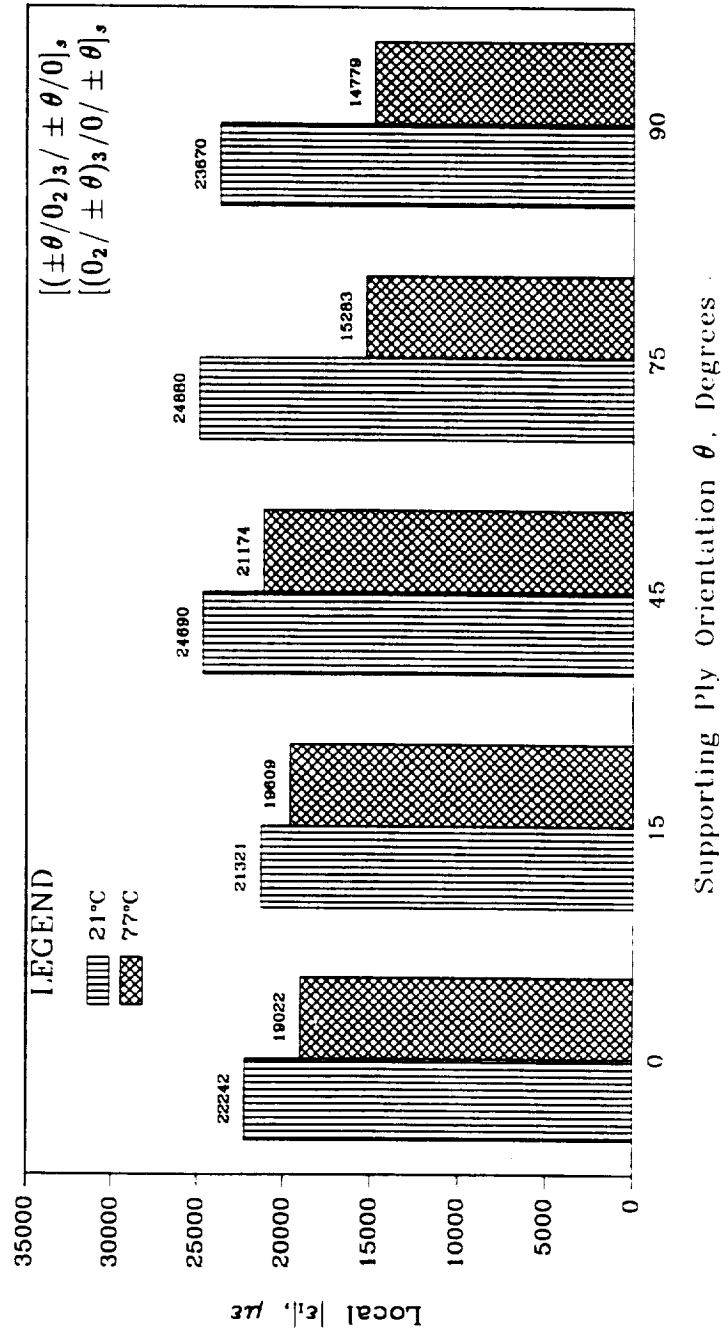


Fig. 55 Bar chart showing the effects of supporting ply orientation on local fiber microbuckling initiation strains in laminates A, B, C, D, and E, tested at 21°C and 77°C.

what about fiber failure? Tensile failure strains for AS4 fibers are reported to be 1.45%.¹⁶⁸ However, DeTeresa¹⁶⁹ has observed fiber shear failure strains of $\approx 3.6\%$ for a single AS4 fiber embedded in matrix and loaded in compression. Thus, the local ϵ_I strains of 1.48%–2.49% reported in Fig. 55 are high, but compatible in magnitude with the fiber failure strains reported by other authors.

Figure 56 is a bar chart showing the average remote axial strain for fiber microbuckling, ϵ_I , for two lay-ups, considering both in- and out-of-plane fiber microbuckling. The two lay-ups are laminates *A* (± 45 plies as surface plies) and *B* (0_2 plies as surface plies). At 21°C, in-plane fiber microbuckling initiated in specimens with ± 45 plies as surface plies at average global strain levels of $\approx 7519 \mu\epsilon$ ($S = 79 \mu\epsilon$) and in specimens with 0_2 plies as surface plies at average global strain levels of $\approx 6878 \mu\epsilon$ ($S = 218 \mu\epsilon$). On the other hand, out-of-plane fiber microbuckling toward the free surface initiated in the specimens with 0_2 plies as surface plies at average remote strain levels of $\approx 6677 \mu\epsilon$ ($S = 186 \mu\epsilon$). Stereomicroscope observations indicate that the out-of-plane fiber microbuckling in laminates with 0_2 as surface plies initiates as in-plane fiber microbuckling into the notch immediately followed by part of the ply buckling out-of-plane toward the free surface. Comparing the average ϵ_I for in- and out-of-plane fiber microbuckling in the *B* laminates with ϵ_I for the *A* laminates indicates a 9.9% reduction in the remote initiation strain level for specimens with 0_2 , rather than ± 45 , as surface plies. Similar reductions (10.1%) were observed at 77°C. However, initiation by out-of-plane fiber microbuckling was not observed in the *B* laminates. This reduction indicates a small free surface effect and is attributed to the reduced lateral constraint. Larger reductions ($\approx 20\%$), computed analytically, were reported in Ref. 96.

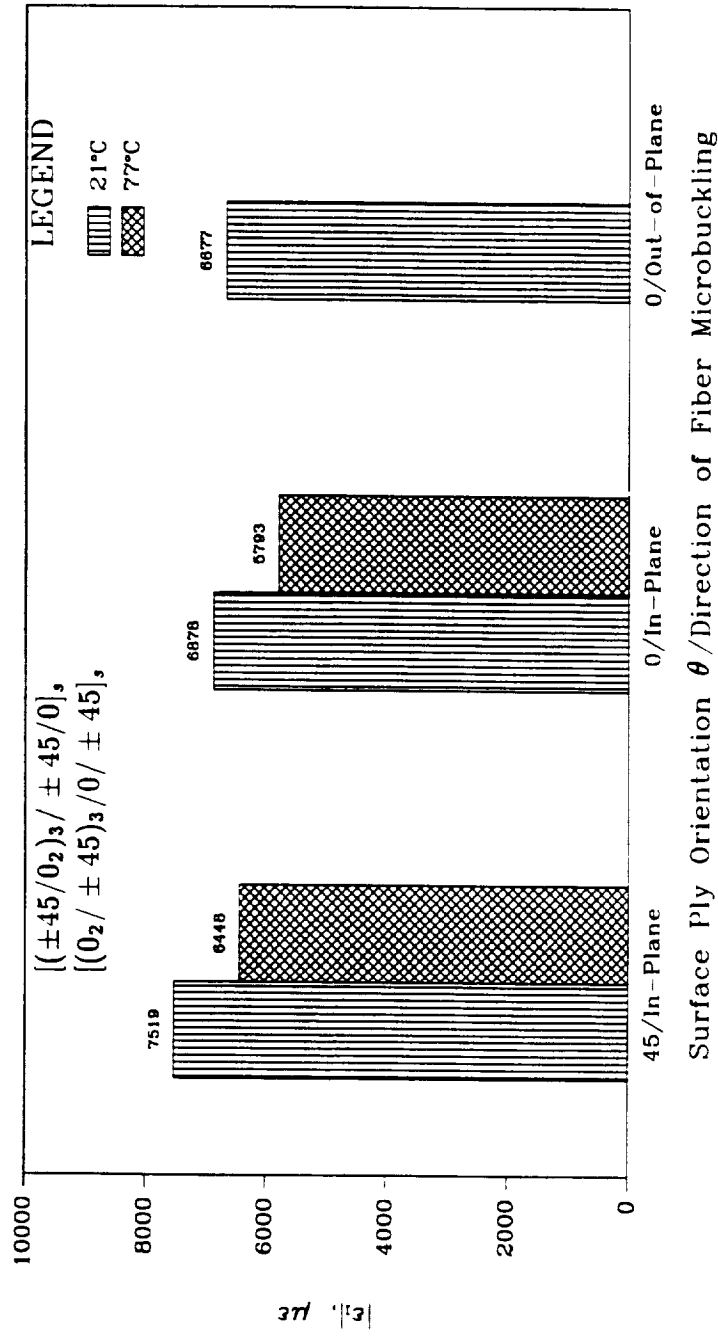


Fig. 56 Bar chart showing the free surface effects on fiber microbuckling initiation strains in laminates A and B, tested at 21°C and 77°C.

Figure 57 contains SEM micrographs of representative in- and out-of-plane fiber microbuckling. Figures 57a, 57b, and 57d are looking into the notch radius, while Fig. 57c is looking at the specimen surface. The representative 21°C in-plane fiber microbuckling is shown in Fig. 57a for interior 0₂ plies and in Fig. 57b for surface 0₂ plies. Figure 57b shows the in-plane fiber microbuckling and subsequent partially out-of-plane fiber microbuckling toward the free surface. SEM observation of laminates *A*, *C*, *D*, and *E* (tested at 21°C and 77°C) showed fiber microbuckling similar to that in Fig. 57a, and thus, for brevity, the micrographs are not included in this dissertation. Figure 57c shows a surface view of a [(0₂/ ± 45)₃/0/ ± 45]_s laminate tested at 21°C. This micrograph shows the in-plane fiber microbuckling into the semi-circular notch and also fiber microbuckling out-of-plane toward the free surface. Figure 57c was one of the micrographs used to measure the column length modelled in the finite element analysis. This view (with surface 0₂) is conducive for observation of matrix deformation attributed to in-plane fiber microbuckling. Since the surface plies are 0₂, sectioning is not required. When sectioning is required, it is difficult to find the correct section that allows observation of the matrix deformation. Figure 57d shows the in-plane fiber microbuckling and subsequent partial ply out-of-plane fiber microbuckling toward the free surface for a *B* laminate tested at 21°C. Ply delamination is indicated with an arrow. Compared to Fig. 57b, more deformation is observed in the adjacent +45° ply.

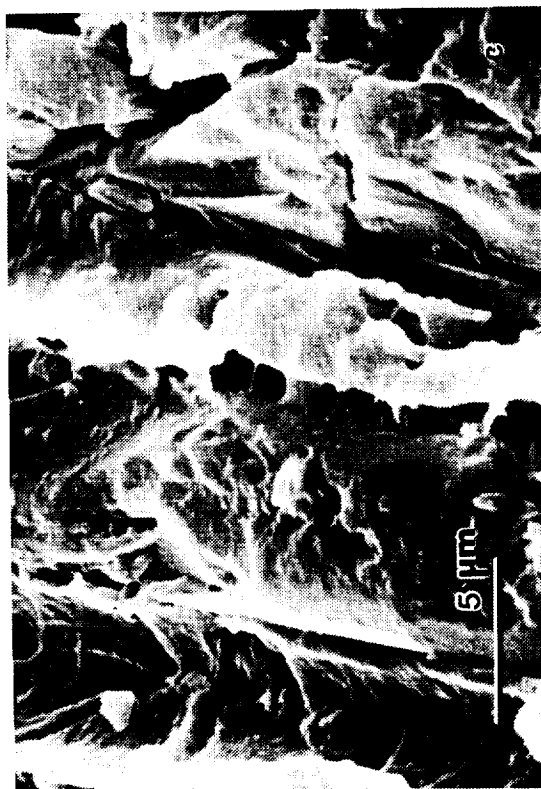
Figure 58 shows matrix deformation in *B* laminates caused by fiber microbuckling at both 21°C and 77°C. Figure 58b is looking into the notch radius and shows representative in-plane fiber microbuckling of interior 0° plies tested at 77°C. Ply delamination at the 0/-45 interface is indicated with an arrow. Notice that from this viewpoint, it is very difficult to observe any matrix deformation.

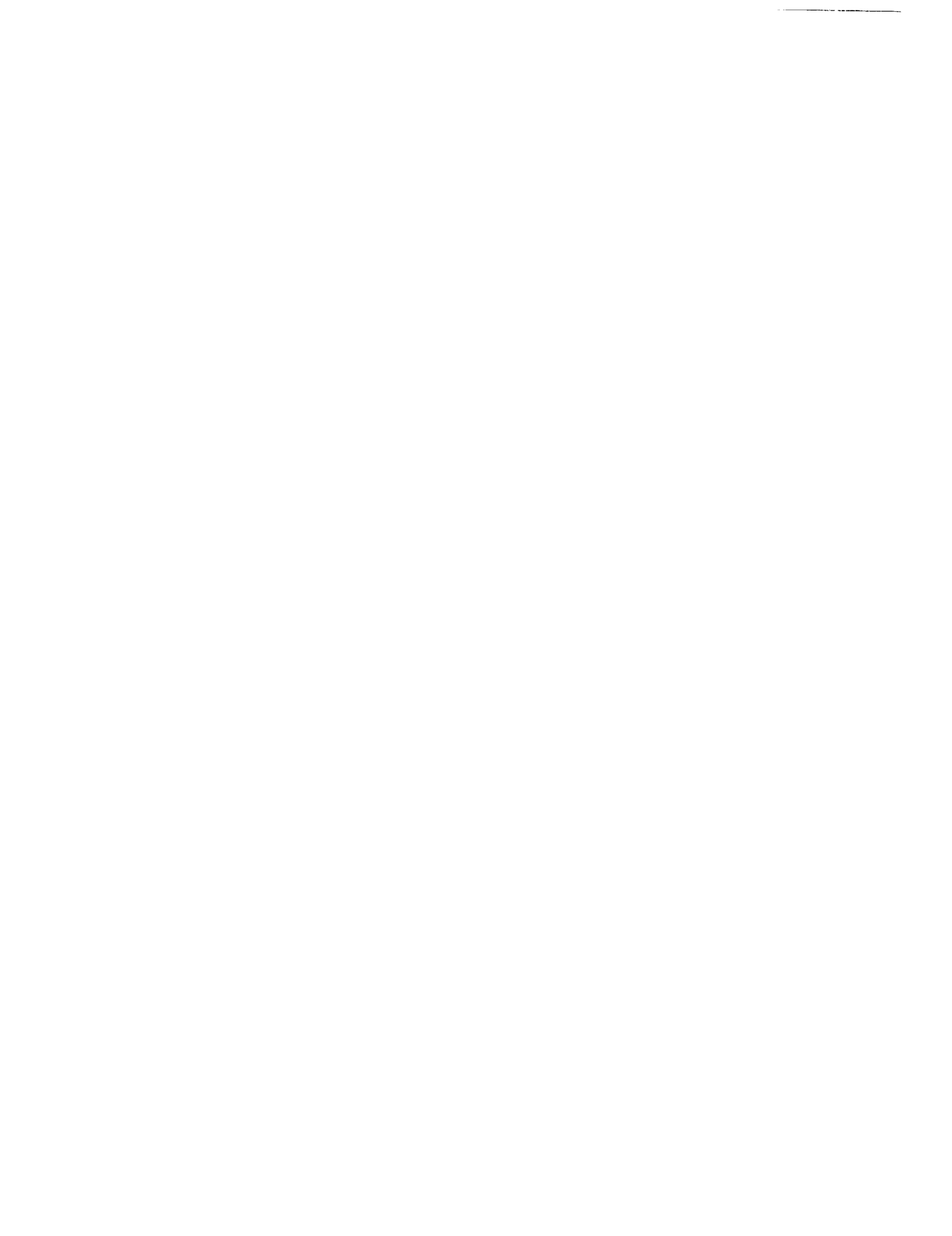
Fig. 57 Representative in- and out-of-plane fiber microbuckling damage in APC-2 laminates.

- a) $[(\pm 45/0_2)_3/\pm 45/0]_s$, 21°C, notch view.
- b) $[(0_2/\pm 45)_3/0/\pm 45]_s$, 21°C, notch view.
- c) $[(0_2/\pm 45)_3/0/\pm 45]_s$, 77°C, surface view.
- d) $[(0_2/\pm 45)_3/0/\pm 45]_s$, 77°C, notch view.



- Fig. 58** Representative in-plane fiber microbuckling damage in APC-2 laminates.
- a) Shearing deformation in matrix, 21°C.
 - b) In-plane fiber microbuckling in interior 0° ply, 77°C.
 - c) Matrix drawing between fibers, 77°C.
 - d) Matrix drawing between fibers, 77°C.





Figures 58a, 58b, and 58d are high magnification surface views (like Fig. 57c) to show the severely deformed matrix at 21°C (a) and 77°C (c and d) caused by in-plane fiber microbuckling. Figures 58c and 58d show more resin drawing at 77°C than observed at 21°C (Fig. 58a). Figure 58a also shows shear deformation of the matrix, probably caused by two fibers sliding relative to each other. Figures 58c and 58d show drawn matrix, indication that the fibers are being pulled away from each other. In Figs. 58a, 58c, and 58d, it is obvious that the fiber/matrix interfacial bond is very strong for these APC-2 composites. Furthermore, comparison of Figs. 58c and 58d (77°C) with Fig. 58a (21°C) indicates that the APC-2 fiber/matrix interfacial bond is not degraded at the higher temperature.

Effects of Initial Fiber Waviness

The laminates used to evaluate the effects of initial fiber waviness on the initiation of fiber microbuckling are given in Table III, and their representative cross-sections are shown in Fig. 41. Data showing these effects are presented in this section.

The effects of initial ply curvature on the initiation of in-plane fiber microbuckling are shown in Fig. 59. This bar chart shows the average remote axial strain level for in-plane fiber microbuckling initiation, ϵ_I , in specimens made with tape, 8-harness Quadrax, and 1-harness Quadrax prepreg. At 21°C, the remote ϵ_I is 6433 $\mu\epsilon$ ($S = 643 \mu\epsilon$), 6607 $\mu\epsilon$ ($S = 11 \mu\epsilon$), and 7191 $\mu\epsilon$ ($S = 351 \mu\epsilon$) for the tape, 8-harness Quadrax, and 1-harness Quadrax laminates, respectively. At 77°C, the remote ϵ_I is 5537 $\mu\epsilon$ ($S = 248 \mu\epsilon$), 6158 $\mu\epsilon$ ($S = 495 \mu\epsilon$), and 6396 $\mu\epsilon$ ($S = 648 \mu\epsilon$) for the tape, 8-harness Quadrax, and 1-harness Quadrax laminates, respectively. At both 21°C and 77°C, the global data indicates a monotonic increase in ϵ_I as the ply

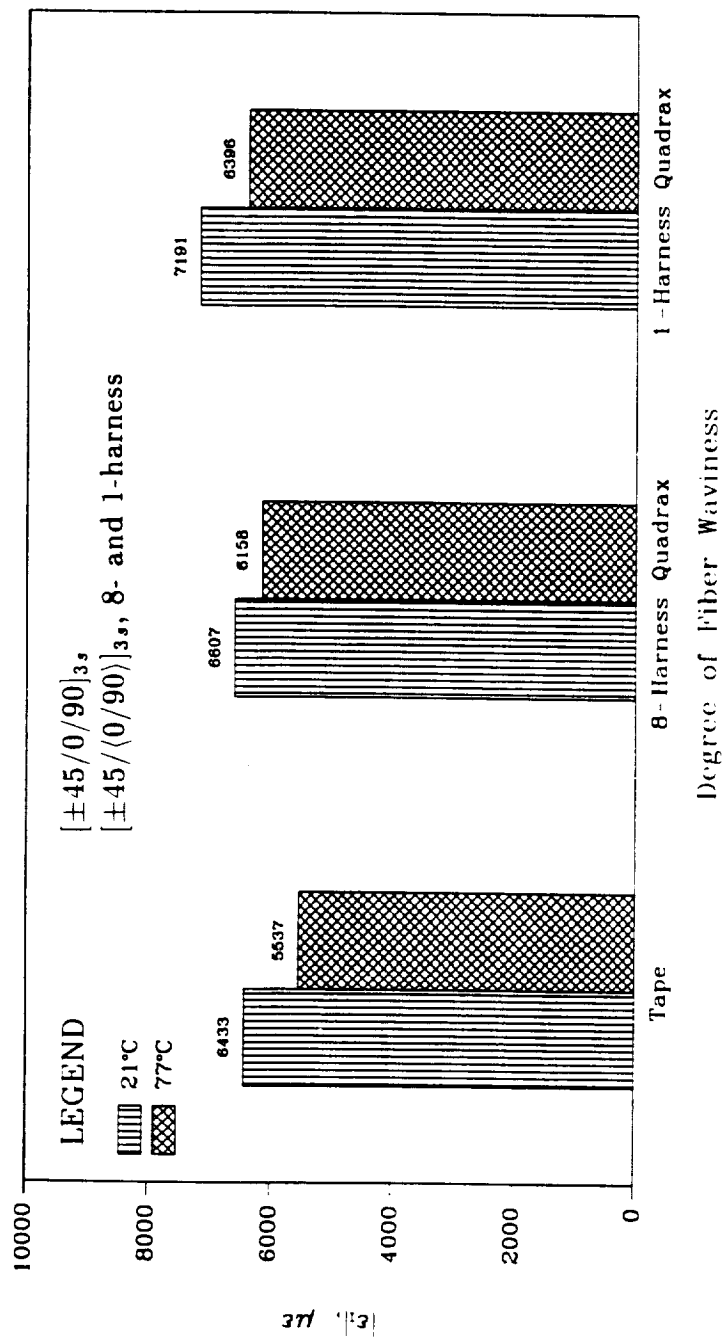


Fig. 59 Bar chart showing the effects of ply waviness on fiber microbuckling initiation strains in laminates K , $KQ8$, and $KQ1$, tested at 21°C and 77°C.

waviness increases from that in the tape laminates (Fig. 41a) to that in 1-harness Quadrax laminates (Fig. 41c). It should be noted that although the ply waviness in these laminates is out-of-plane (Fig. 41), all fiber microbuckling occurred in-plane into the notch. Increasing the temperature from 21°C to 77°C causes ϵ_I to be decreased by 13.9%, 6.8%, and 11.0% for the tape, 8-harness Quadrax, and 1-harness Quadrax, respectively.

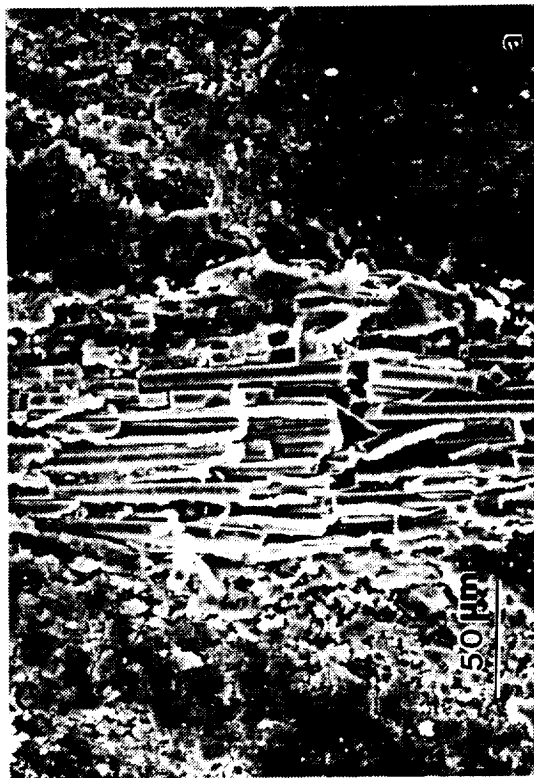
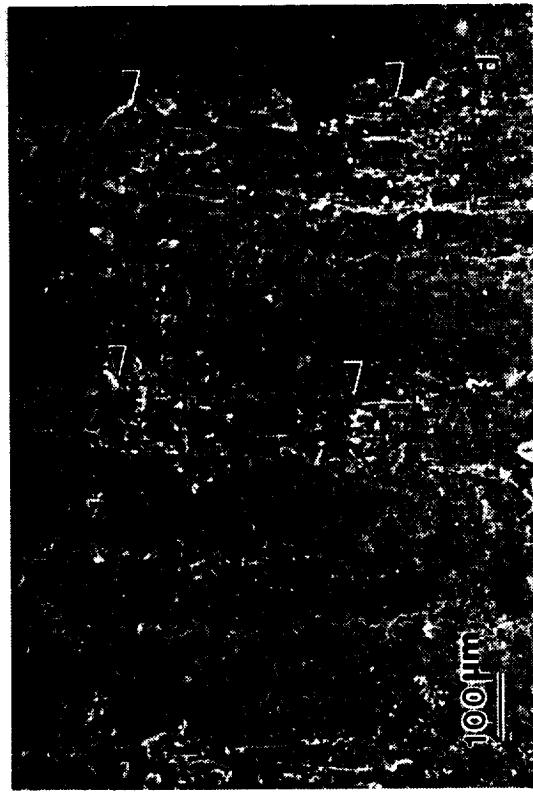
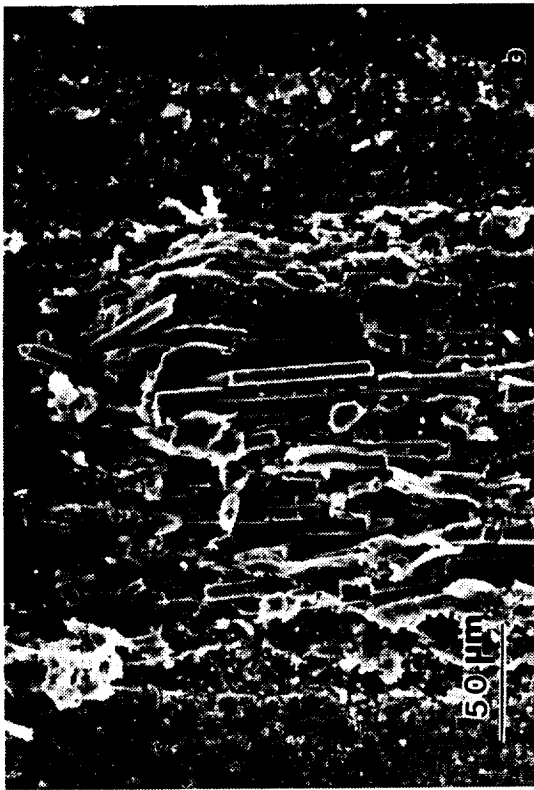
Figure 60 shows representative in-plane fiber microbuckling in this series of laminates tested at 21°C; all views are from the notch center. The in-plane fiber microbuckling damage observed in the tape laminate (*K*) in Fig. 60a is similar to damage presented in Fig. 57a. Figure 57b shows the in-plane fiber microbuckling for the 1-harness Quadrax laminates. It appears that the out-of-plane ply waviness may have caused some out-of-plane motion (indicated by arrow) at the notch. Figures 60c and 60d show an overview of three buckled 0° plies in an 8-harness Quadrax laminate. Figure 60c is just above the center of the buckled region, and transverse cracking in the 0° plies is indicated with arrows. Figure 60d shows the in-plane buckled regions in these plies. Each of these 0° plies have two buckled regions, indicated by arrows, approximately $85 d_f$ apart. It is believed that rather than fiber failure at the column mid-span (as typically observed in the tape laminates), fiber failure occurred at the ends of the unsupported column. High temperature (77°C) specimens were also examined in the SEM, but revealed nothing different than that already reported herein.

Effects of Interfacial Bond Strength

The fracture toughnesses (modes I and II) and fiber/matrix interfacial shear strengths are given in Table IX for the two materials used to investigate the effects

Fig. 60 Representative in-plane fiber microbuckling damage at 21°C, notch view.

- a) APC-2 tape laminate, $[\pm 45/0/90]_{3s}$.
- b) Quadrax laminate, 1-harness, $[\pm 45/(0/90)]_{3s}$.
- c) Quadrax laminate, 8-harness, $[\pm 45/(0/90)]_{3s}$.
- d) Quadrax laminate, 8-harness, $[\pm 45/(0/90)]_{3s}$.



of interfacial bond on the initiation of fiber microbuckling. Data illustrating these effects are presented in this section.

The effects of the interfacial bond strength are shown in Fig. 61. This bar graph shows the average remote axial strain level for fiber microbuckling initiation, ϵ_I , as a function of the material tested at 21°C and 77°C. The IFSS values from Table IX are included on the abscissa of the graph. At 21°C, fiber microbuckling initiation occurred at 7519 $\mu\epsilon$ ($S = 79 \mu\epsilon$) for the APC-2 laminates and 5487 $\mu\epsilon$ ($S = 186 \mu\epsilon$) for the experimental AU4U/PEEK material, indicating a 27% decrease in ϵ_I attributed to the poor fiber/matrix interface. However, at 77°C, fiber microbuckling initiation occurred at a global strain of 6448 $\mu\epsilon$ ($S = 499 \mu\epsilon$) for the APC-2 laminates and 6123 $\mu\epsilon$ ($S = 501 \mu\epsilon$) for the experimental AU4U/PEEK material, indicating a 5% decrease in ϵ_I attributed to the poor fiber/matrix interface. This result indicates that softer resins do not appear to need interfacial bonds as strong as those required by stiffer resins.

Figure 62 shows representative in-plane fiber microbuckling damage for the experimental AU4U/PEEK material at 21°C (a and b) and 77°C (c and d). Figure 62a is a notch view of in-plane fiber microbuckling and protruding of the discontinuous 0° fibers into the notch. Delamination at the +45/-45 and -45/0 interfaces are indicated with arrows. Higher magnification of the fibers in the buckled region (Fig. 62b) shows little resin deformation and many bare fibers. Figure 62c is an overview of the protruding 0₂ plies being pushed into the notch by subsurface fiber microbuckling. In the background, surface 45s (indicated with an arrow) are seen pushed out of the plane of the laminate, again by subsurface damage. Higher magnification of these buckled 45° fibers in Fig. 62d again shows bare fibers with essentially no resin drawing.

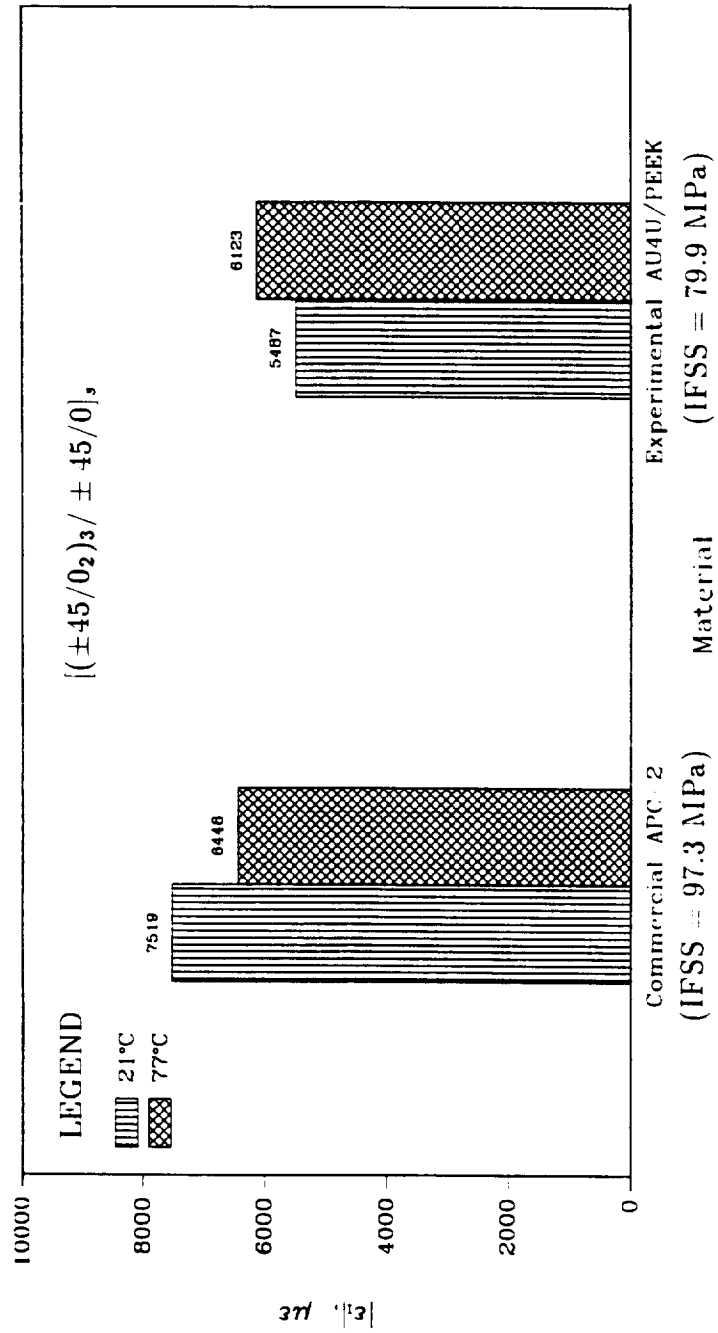
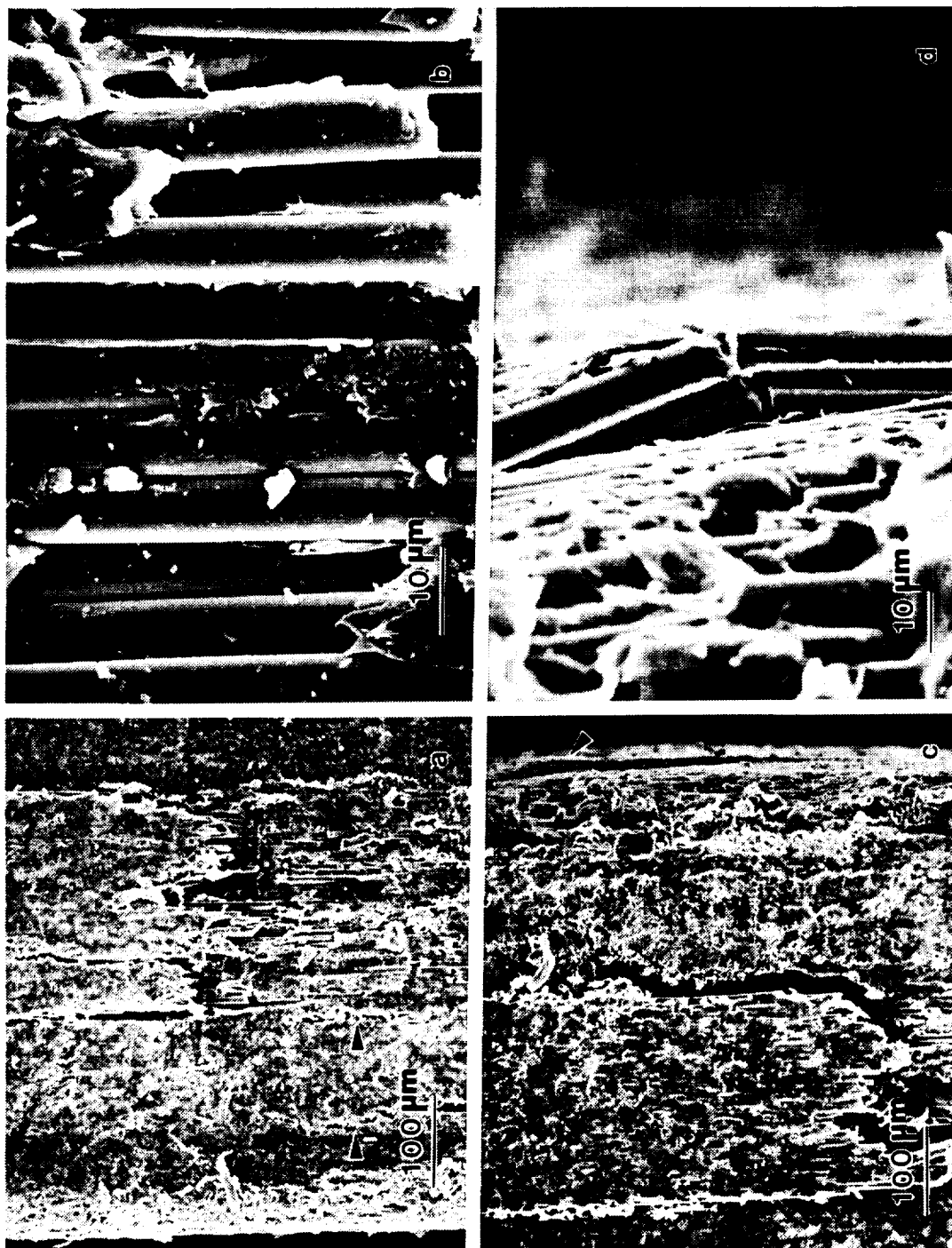


Fig. 61 Bar chart showing the effects of the interfacial bond on fiber microbuckling initiation strains.

Fig. 62 Fiber microbuckling in the experimental AU4U/PEEK material, $[(\pm 45/0_2)_3 / \pm 45/0]_s$. All views are from the notch center.

- a) 21°C.
- b) 21°C.
- c) 77°C.
- d) 77°C.

ORIGINAL FACE
BLACK AND WHITE PHOTOGRAPH



Effects of Resin-Rich Regions Between Plies

The test matrix to study the effects of resin-rich regions between plies was summarized in Table IV. Data illustrating these effects are shown in the bar chart in Fig. 63. In-plane fiber microbuckling initiated at average global strain levels of $7919 \mu\epsilon$ ($S = 79 \mu\epsilon$) for the baseline lay-up (*A*), $6916 \mu\epsilon$ ($S = 280 \mu\epsilon$) for the laminate with one layer of neat resin at the 0/-45 interfaces (*G*), and $6335 \mu\epsilon$ ($S = 88 \mu\epsilon$) for the laminate with three layers of neat resin at the 0/-45 interfaces (*H*) at 21°C . Compared to the baseline lay-up, the introduction of one layer of neat resin at the 0/-45 interfaces through the laminate thickness causes a 12.6% reduction in the strain level for in-plane fiber microbuckling initiation. The addition of three layers of neat resin at 0/-45 interfaces through the laminate thickness causes a 20.0% reduction (compared to the baseline lay-up) in the initiation strain level. These results indicate that the addition of soft resin layers on each side of the 0_2 plies significantly reduces the resistance to in-plane fiber microbuckling at 21°C .

At 77°C , the fiber microbuckling global initiation strains were $6448 \mu\epsilon$ ($S = 193 \mu\epsilon$) for the baseline lay-up, $6715 \mu\epsilon$ ($S = 435 \mu\epsilon$) for laminate *G*, and $6805 \mu\epsilon$ ($S = 588 \mu\epsilon$) for laminate *H*. These 77°C data indicate a slight monotonic increase in ϵ_I as the resin-rich regions are increased. However, because of scatter in the data, definite conclusions about the trend may not be made. The 132°C data is discussed in the next section of this dissertation.

Figure 64 shows typical fiber microbuckling damage in APC-2 laminates with resin-rich regions at each 0/-45 interface. Figure 64a is an overview (laminate *G*, 77°C) showing fiber microbuckling and protruding of the discontinuous 0° fibers in the notch, through the thickness of the laminate. Figure 64b is a high magnification from a, showing the details of fiber microbuckling. Delamination is indicated with an

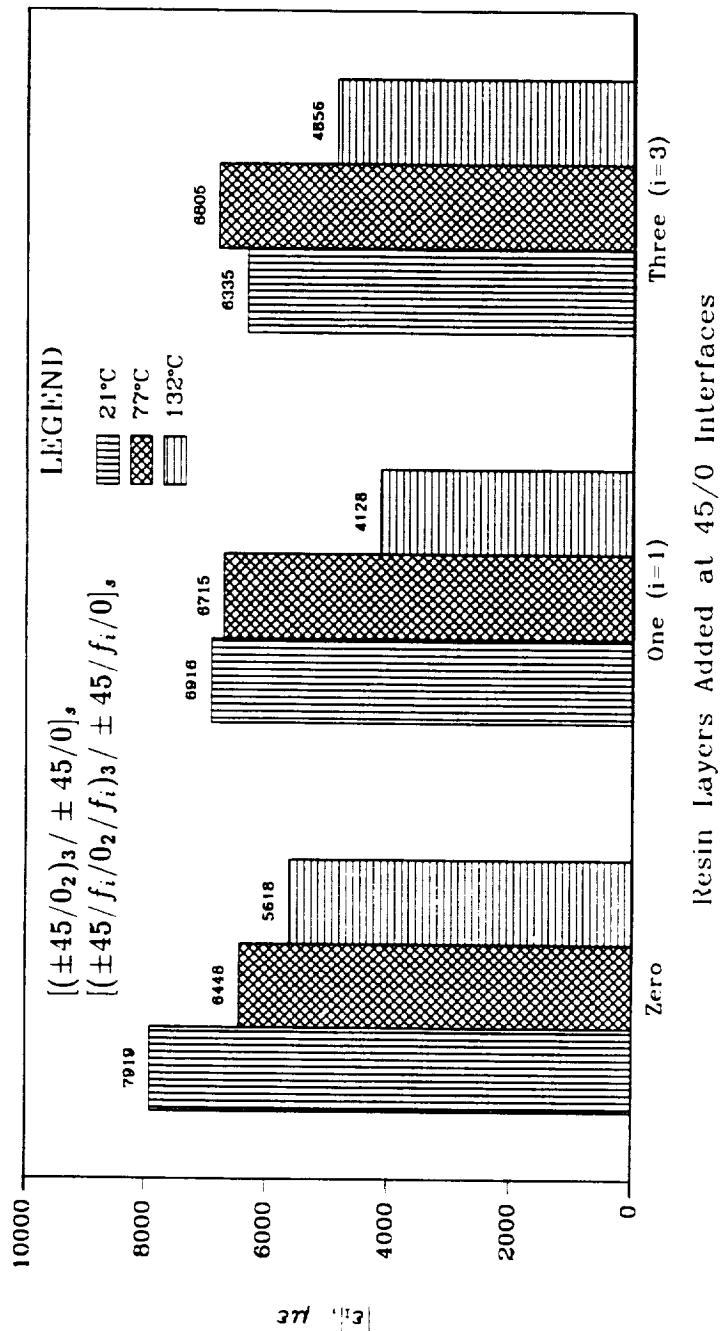


Fig. 63 Bar chart showing the effect of resin-rich regions on fiber microbuckling initiation strains in laminates A, G, and H, tested at 21°C, 77°C, and 132°C.

- Fig. 64** Notch view of in-plane fiber microbuckling in APC-2 laminates with resin-rich regions.
- a) Specimen cross-section, $[(\pm 45/f/0_2/f)_3 / \pm 45/f/0]_s$, 77°C.
 - b) Detail from a.
 - c) Out-of-plane fiber microbuckling into resin-rich region, $[(\pm 45/f_3/0_2/f_3)_3 / \pm 45/f_3/0]_s$, 21°C.

ORIGINAL PAGE
BLACK AND WHITE PHOTOGRAPH



arrow. It appears that after in-plane fiber microbuckling initiation occurs, some 0° fibers push into the adjacent plies. Deformation at the right-hand $0/-45$ interface indicates that some of the 0° fibers pushed into the adjacent resin region. The micrograph in Fig. 64c shows the $0/-45$ interface in a specimen from laminate *H*, tested at 21°C . The deformation and flow lines of the resin (marked with an arrow) indicates that some 0° fibers have pushed into the adjacent resin layers.

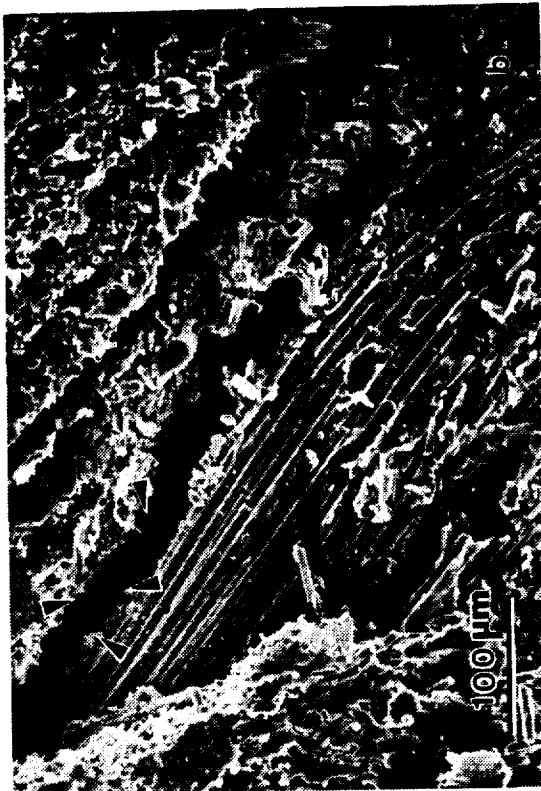
Microbuckling Failures at 132°C

As described in Chapter II of this dissertation, compression tests were to be conducted at 21°C , 77°C , and 132°C . However, because of catastrophic failures, only a few tests were conducted at 132°C . Stereomicroscope observations indicate that fiber microbuckling in these specimens always initiated in the 0° plies nearest the specimen surface with the larger compressive strain. After fiber microbuckling initiation, the specimen stiffness is unsymmetric, and thus, the effects of any bending are pronounced. Additionally, the resin has very little shear stiffness at 132°C (see Fig. 40). The pronounced bending in conjunction with the compliant resin caused the specimens to fail progressively by out-of-plane global ply buckling. In this case, fiber microbuckling initiation and failure are the same. The nominal fiber microbuckling initiation strains for these specimens are included in Fig. 63. Failure initiated at $5618 \mu\epsilon$ (one specimen) for the $[(\pm 45/0_2)_3 / \pm 45/0]_s$ laminate, $4128 \mu\epsilon$ ($S = 814 \mu\epsilon$) for the $[(\pm 45/f/0_2/f)_3 / \pm 45/f/0]_s$ lay-up, and $4856 \mu\epsilon$ ($S = 95 \mu\epsilon$) for the $[(\pm 45/f_3/0_2/f_3)_3 / \pm 45/f_3/0]_s$ lay-up, all at 132°C .

Figure 65a shows a notch overview, through the laminate thickness, of the global ply buckling in a specimen from the baseline stacking sequence tested at 132°C . Ply delamination is present at every $0/-45$ interface. Negligible fiber failure

- Fig. 65** Failures in APC-2 laminates tested at 132°C, $(\pm 45/0_2)_3 / \pm 45/0$._s.
- a) Overview.
 - b) Detail from a.
 - c) Fiber/matrix interfacial bond and matrix deformation.
 - d) Fiber/matrix interfacial bond and matrix deformation.

ORIGINAL PAGE
BLACK AND WHITE PHOTOGRAPH



is observed in Fig. 65a except at the bend points in the 0° plies, as seen at higher magnification in Fig. 65b. Additionally, in Fig. 65b, mode I type drawing (examples indicated by arrows) of the resin can be seen in the opening of the delamination. Figures 65c and 65d show the severe shearing deformation of the matrix between the fibers, and the fibers covered with resin. Sigmoidal-type cracks¹⁷⁰ (indicated by arrows), attributed to shearing forces, have formed in the matrix, as shown in Fig. 65c. However, due to matrix ductility, the cracks did not coalesce to form hackles.

Comments on Fiber Microbuckling Initiation

Finally, two general comments about fiber microbuckling initiation in these notched laminates remain to be stated. First, based on in-situ stereomicroscope observations and the required testing methods, fiber microbuckling initiation of these notched laminates defines the laminate strength and thus controls failure initiation. As mentioned in the test procedures in Chapter III, the laminates were loaded to fiber microbuckling initiation and partially unloaded rapidly by manual control of the MTS. Additional growth of fiber microbuckling damage or initiation in other 0° plies occurred quite often at stress levels less than or equal to the first-ply initiation stress. A few specimens (of different lay-ups) were reloaded beyond the first-ply fiber microbuckling initiation strains in an effort to grow larger fiber microbuckling damage zones for SEM postmortem observations. For these specimens, the ratio of the first-ply fiber microbuckling initiation stress to the composite failure stress ranges from 81–100% (average is $\approx 94\%$) for 21°C and 82–102% (average is $\approx 96\%$) for 77°C . The ratio of 100% is observed because the specimens failed while holding the strain at first-ply fiber microbuckling initiation

constant. The same ratio is always 100% for 132°C because initiation of fiber microbuckling and specimen failure are essentially the same. Note that when the ratio is greater than 100%, growth of additional fiber microbuckling damage (beyond first-ply initiation) occurs at stress levels lower than the first-ply initiation stress. In Ref. 112, the first indication of failure was observed at 85% of the ultimate compressive load for multidirectional graphite/epoxy laminates with center holes. However, this damage was an interfiber matrix failure in the 0° plies (similar to longitudinal splitting in the unidirectional laminates), rather than the initiation of fiber microbuckling.

Second, the in-situ stereomicroscope observations and the testing differences (regarding instability) indicate that fiber microbuckling initiation is a more stable process in the $[\pm 45/0/90]_3$ laminates than in those laminates containing 0₂ plies through the thickness. The initial purpose of the 0₂ plies was to provide easier observation of fiber microbuckling initiation. When the first 0₂ ply buckled in these laminates, the other 0₂ plies buckled simultaneously or immediately after the first-ply buckle. However, for the $[\pm 45/0/90]_3$ laminates, it was easier (more stable) to unload partially and grow additional damage. This difference is attributed to the amount of load redistribution and the reduction in load-carrying capacity when the 0₂ plies, rather one 0° ply, buckle.

CHAPTER VI

FINITE ELEMENT RESULTS

Contained within this chapter are the results of the finite element analysis for both the straight and wavy fiber models. First, the straight fiber results for the five cases, examining the perfect composite and the effects of the free surface, finite width plates, and fiber constitutive properties are presented. Second, the wavy fiber results, demonstrating the effects of matrix nonlinear constitutive behavior, initial fiber curvature, fiber/matrix interfacial bond strength, free surface, and fiber constitutive properties are presented. Refer to Chapter IV and Table VIII for specific model descriptions and constituent properties.

The Straight Fiber Problem

The critical buckling strains for the straight fiber problem are summarized in Table XI.

Case 1S

In these models, the matrix is linear, the fibers are transversely isotropic, and the unidirectional smear regions are orthotropic. The infinite plate buckled at $\epsilon_{cr} = 27700 \mu\epsilon$ while the semi-infinite plate buckled at $\epsilon_{cr} = 24900 \mu\epsilon$. This result indicates that the free surface effect causes a 10% reduction in the critical buckling strain. The finite plate buckled at $\epsilon_{cr} = 15300 \mu\epsilon$, and the infinite array of fibers and matrix buckled at $\epsilon_{cr} = 20000 \mu\epsilon$.

Case 2S

The ten fibers and matrix finite plate with Type A isotropic fibers (properties in Table VIII) and linear matrix buckled at $\epsilon_{cr} = 16400 \mu\epsilon$.

Table XI. Critical Buckling Strains for the Straight Fiber Problem.

Case	Model	$\epsilon_{cr}, \mu\epsilon$
1S	Infinite Plate	27700
1S	Semi-Infinite Plate	24900
1S	Finite Plate	15300
1S	Infinite Series	20000
2S	Finite Plate ^a	16400
3S	Finite Plate ^b	39400

^aType A isotropic fibers.

^bType B isotropic fibers.

Case 3S

The ten fibers and matrix finite plate with Type *B* isotropic fibers (properties in Table VIII) and linear matrix buckled at $\epsilon_{cr} = 39400 \mu\epsilon$.

Case 4S

The semi-infinite plate modelled with linear matrix, Type *B* isotropic fibers, and an isotropic smear region buckled at $\epsilon_{cr} = 99400 \mu\epsilon$. This strain level is a numerical calculation that is unrealistically high. This high ϵ_{cr} is a direct result of the low axial modulus (see Table VIII) of the Type *B* isotropic fibers and the isotropic smear region.

Case 5S

The infinite series with linear matrix and Type *B* isotropic fibers buckled at $\epsilon_{cr} = 94100 \mu\epsilon$. This strain level is a numerical calculation that is unrealistically high. This high ϵ_{cr} is a direct result of the low axial modulus (see Table VIII) of the Type *B* isotropic fibers and the isotropic smear region.

The Wavy Fiber Problem

This section contains the results for the wavy fiber problem. For the x - y plots presented, the absolute values of the shear strains, the global axial strains, and the global axial stresses are plotted. The global axial stress is computed as the sum of the reaction forces divided by the area of the column cross-section. When the local shear strain (implies in a local region, not element coordinates) is the dependent variable, it is plotted in the global coordinates from the local region of maximum shear, elements 29 and 57 in Fig. 33. The location of this region was verified with fringe plots (color contours generated with PATRAN¹⁶⁵) in the convergence studies.

Unless otherwise noted, the global stress-strain curves are plotted to failure (defined as fiber microbuckling). Fiber microbuckling is defined as the point when additional increases in the applied strain do not yield additional increases in the load-carrying capacity of the column. As with the experimental results, the strain level for fiber microbuckling initiation is designated ϵ_I . The fiber microbuckling initiation strains for the wavy fiber problems are summarized in Table XII.

Effects of Matrix Constitutive Behavior

The infinite series model (Fig. 33) is used to show the effects of the matrix constitutive behavior on fiber microbuckling initiation. Figure 66 is a plot of the global axial stress, σ_{xx} , as a function of the applied global axial strain, ϵ_{xx} , for four different matrix constitutive behaviors (Cases 1C-4C). The initial fiber curvature for this comparison is $\frac{a_0}{L} = 0.0050$.

The global stress-strain behavior for the model with the linear matrix continued indefinitely. Failure is not flagged in this model because with an initial waviness, the eigenvalue analysis is not possible and with linear matrix, the system matrix remains positive definite so that the negative eigenvalue warning does not appear. The column does have a linear, global response. At best, failure of this column with the linear matrix is predicted to occur between 94100 $\mu\epsilon$ (eigenvalue analysis of straight fiber) and 21923 $\mu\epsilon$ (21°C nonlinear matrix with the same initial curvature). Fiber microbuckling (indicated with arrows) in the initially wavy series occurs at 21923 $\mu\epsilon$, 18023 $\mu\epsilon$, and 12192 $\mu\epsilon$ when the 21°C, 77°C, and 132°C nonlinear matrix constitutive behaviors (Cases 2C-4C) are assumed respectively. The trend indicates that fiber microbuckling strains for initially wavy models are very sensitive to nonlinear matrix constitutive behavior. The reduction in ϵ_I from 21°C to 77°C is 17.8%. Furthermore, including the matrix nonlinear constitutive

Table XII. Fiber Microbuckling Initiation Strains for the Wavy Fiber Problem.

Case	Model	Fiber	Matrix	a_o/L	$\epsilon_I, \mu\epsilon$
1C	Infinite Series	<i>B</i>	Linear	0.0050	—
2C	Infinite Series	<i>B</i>	21°C	0.0050	21923
3C	Infinite Series	<i>B</i>	77°C	0.0050	18023
4C	Infinite Series	<i>B</i>	132°C	0.0050	12192
1W	Semi-Infinite Plate	<i>B^a</i>	21°C	0.0050	39462
2W	Infinite Series	<i>B</i>	21°C	0.0000	94100
3W	Infinite Series	<i>B</i>	21°C	0.0025	27046
4W = 2C	Infinite Series	<i>B</i>	21°C	0.0050	21923
5W	Infinite Series	<i>B</i>	21°C	0.0075	18369
1D	Infinite Series	<i>B</i>	21°C	0.0050	21961
2D	Infinite Series	<i>B^b</i>	21°C	0.0050	11692
3D	Infinite Series	<i>B^c</i>	21°C	0.0050	6700
4D	Infinite Series	<i>B^d</i>	21°C	0.0050	2108
1F = 4W = 2C	Infinite Series	<i>B</i>	21°C	0.0050	21923
2F	Infinite Series	<i>A</i>	21°C	0.0050	7765

^aIsotropic smear regions.

^bDebond length is 10.7% of total column length.

^cDebond length is 25.0% of total column length.

^dDebond length is 50.0% of total column length.

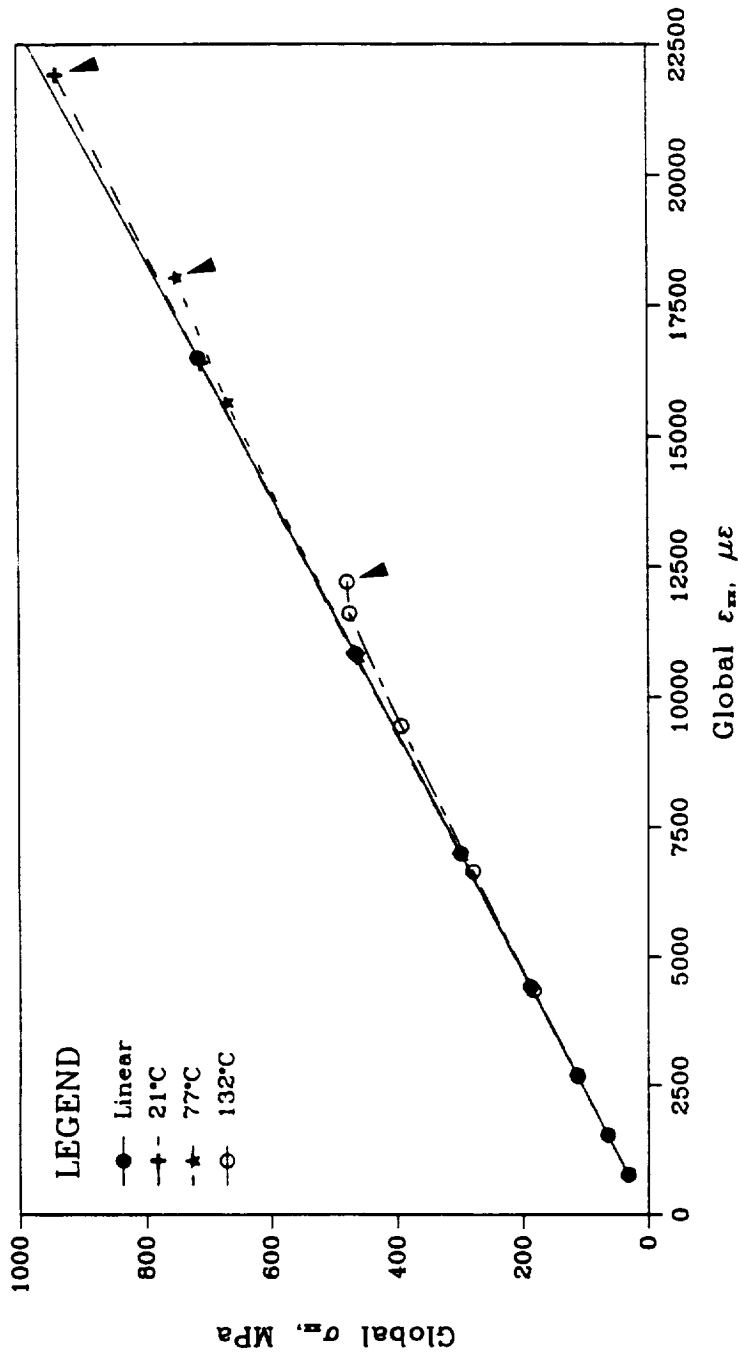


Fig. 66 Global stress-strain response of infinite series for four matrix constitutive behaviors with $\frac{a_e}{L} = 0.0050$.

behavior introduces nonlinearity in the global stress-strain behavior of the composite (Fig. 66). As the shear yield strength of the resin is decreased (Fig. 40), the global behavior of the composite becomes more nonlinear.

Figure 67 is a plot of the local shear strain, γ_{xy} , as a function of the applied global axial strain, ϵ_{xx} , for the same four resin constitutive behaviors and initial waviness (Cases 1C–4C). The initial slope of the linear matrix model (Case 1C) is slightly different from the three nonlinear matrix models (Cases 2C–4C). This difference is observed because the actual modulus, $E_m = 3599$ MPa, from the material data sheets¹³⁷ was used for the linear matrix behavior while the equivalent modulus (derived from composite $[\pm 45]_n$, data), $E_m = 3899$ MPa, is used for the nonlinear matrix behavior. However, $G_m \propto E_m$ in the linear elastic region of the resin constitutive response. Therefore, with the same Poisson's ratio, a lower E_m produces a lower G_m . Consequently, the model with the assumed linear behavior is slightly more compliant in shear and develops higher local shear strains for a given applied axial strain in the initial portion of the curves in Fig. 67. Further observation of the model containing linear matrix (Case 1C) in Fig. 67 indicates that although the matrix constitutive behavior is linear, local γ_{xy} versus global ϵ_{xx} is only initially linear. This result implies that large deformations (nonlinear geometry) and possibly the increased local waviness (due to additional loading) contribute to increasing the local shear strain developed in the matrix. When the curve deviates from linear behavior, large deformation theory becomes important.

When the matrix nonlinearity is included (21°C, 77°C, and 132°C) in the infinite series model, the local shear strain in Fig. 67 increases monotonically and then asymptotically. Notice that the nonlinear matrix curves in Fig. 67 are initially linear and coincide. This collinearity represents the linear portion of the matrix

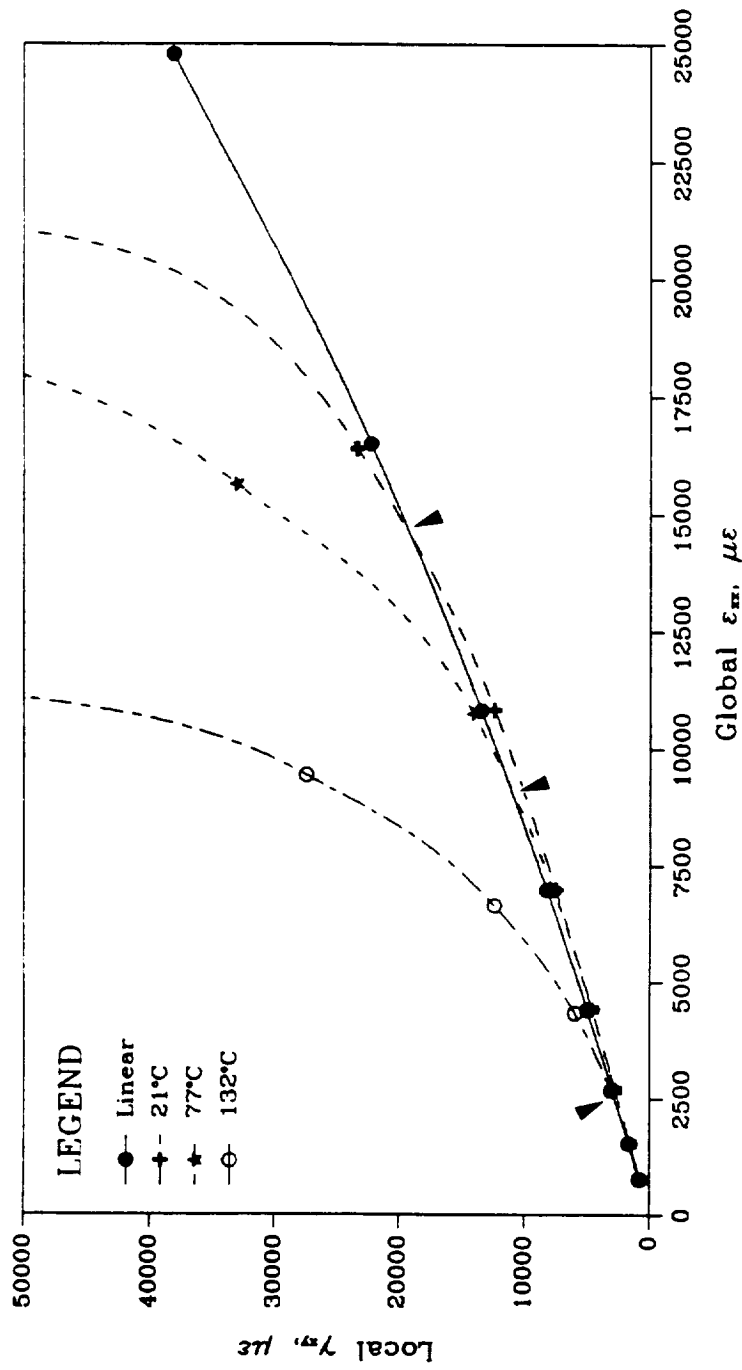


Fig. 67 Local shear strain versus global applied strain of infinite series for four matrix constitutive behaviors with $\frac{a_0}{L} = 0.0050$.

constitutive behavior (Fig. 40) where the axial and shear moduli each coincide for all three cases. Furthermore, as the temperature is increased, the axial strain at which the resin reaches its shear yield strength is decreased. The dramatic increase in the local shear strains in Fig. 67 is associated with the decrease in the matrix shear modulus as the resin approaches the yield point on the $\tau_m-\gamma_m$ curve. The applied strains, ϵ_{xx} , associated with deviation from the linear data in Fig. 67 (indicated with arrows) correlate with the equivalent strains that correspond to the resin yield strain in Fig. 36. Additionally, the axial strains that correspond to the asymptotic behavior in Fig. 67 correlate well with the fiber microbuckling initiation strains in Fig. 66. The axial strains associated with the asymptotic behavior in Fig. 67 are ≈ 1.46 , ≈ 2.00 , and ≈ 4.80 times the resin yield strain (Fig. 36) for the 21°C, 77°C, and 132°C data, respectively. This result indicates that fiber microbuckling initiates after the resin shear strain reaches the yield point on the $\tau_m-\gamma_m$ curve, as assumed in Refs. 68, 69, and 114, for example.

Fringe plots (color contours generated with PATRAN¹⁶⁵) of the distribution of the axial, transverse, and shear strains in the model are shown in Figs. 68–70, respectively. These distributions correspond to the applied global $\epsilon_{xx} = 2692 \mu\epsilon$, increment 3 on Figs. 66 and 67. These contours correspond to the geometry in Fig. 33. For orientation, the color bar is at the symmetry line of the model. The mesh (white lines) is superposed on each of the fringe plots. Also note that the color bar is scaled accordingly for each figure.

The fringe plot in Fig. 68 shows the distribution of axial strain, ϵ_{xx} , throughout the model. The axial strain varies from $-2660 \mu\epsilon$ to $-2790 \mu\epsilon$. The axial strains are approximately the same as the global applied strain. This strain distribution indicates some bending of the fiber.

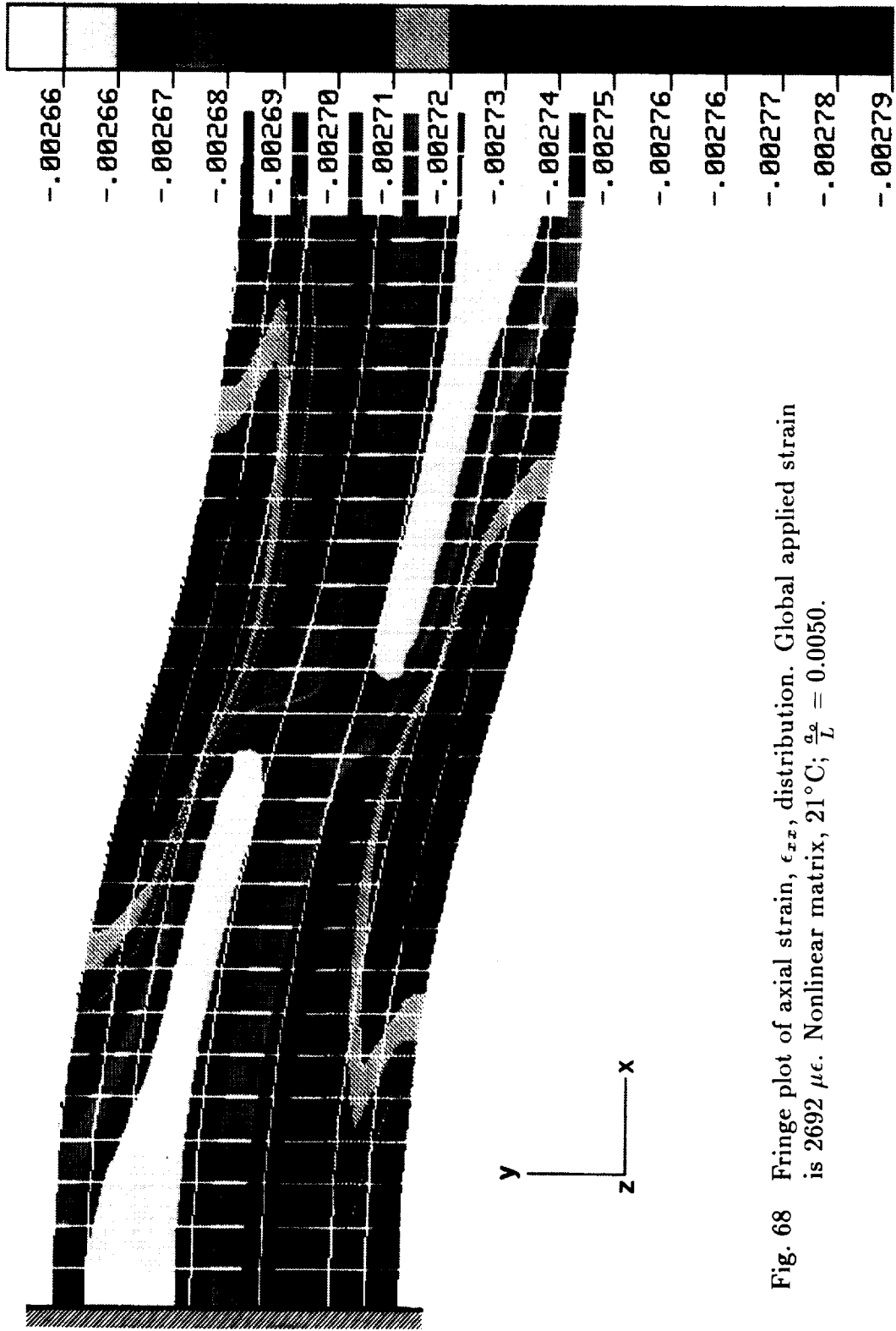


Fig. 68 Fringe plot of axial strain, ϵ_{xx} , distribution. Global applied strain is $2692 \mu\epsilon$. Nonlinear matrix, 21°C ; $\frac{\Delta\sigma}{L} = 0.0050$.



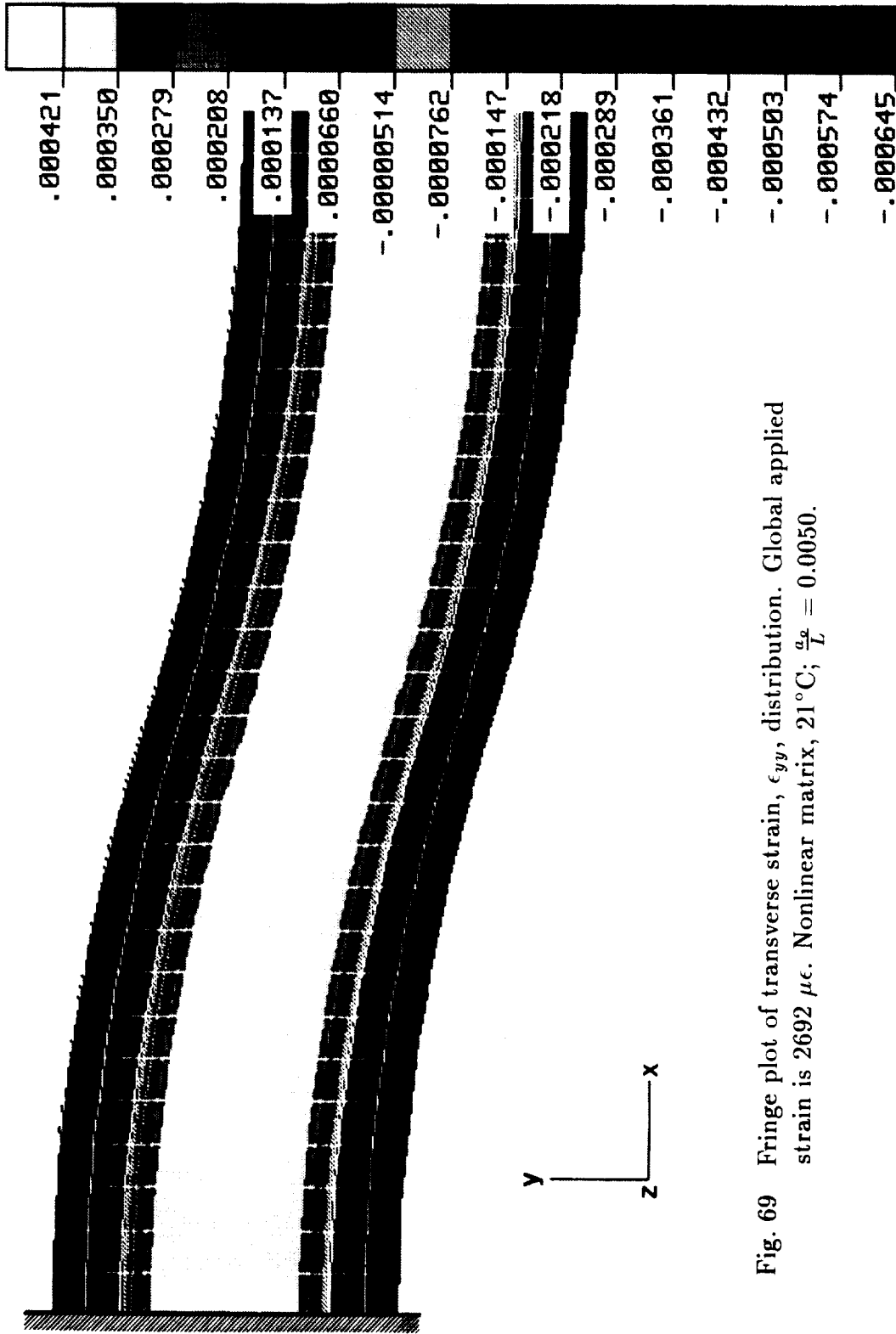


Fig. 69 Fringe plot of transverse strain, ϵ_{yy} , distribution. Global applied strain is 2692 $\mu\epsilon$. Nonlinear matrix, 21°C; $\frac{\alpha}{T} = 0.0050$.

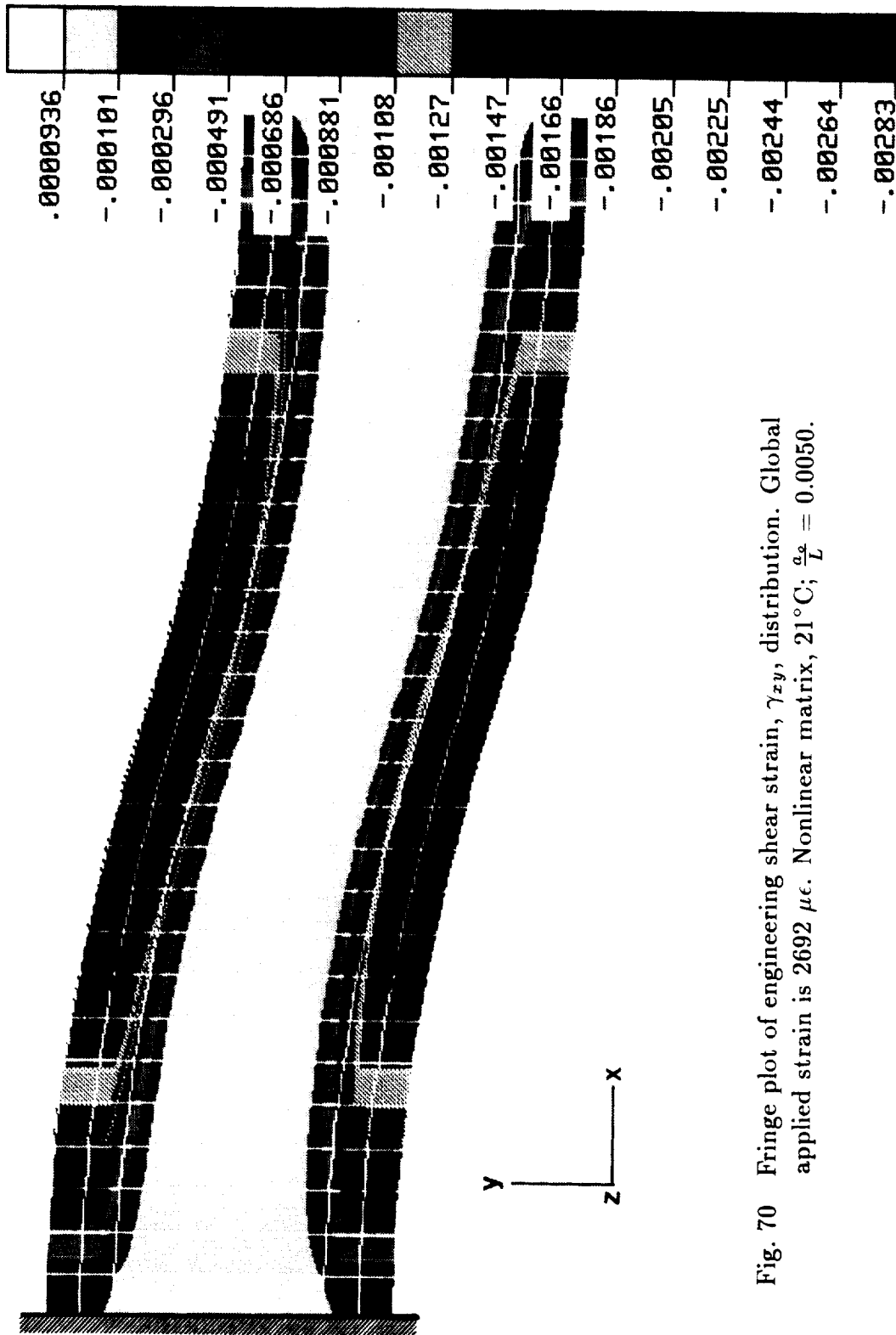


Fig. 70 Fringe plot of engineering shear strain, γ_{xy} , distribution. Global applied strain is 2692 $\mu\epsilon$. Nonlinear matrix, 21°C; $\frac{a}{L} = 0.0050$.

Figure 69 is a fringe plot showing the distribution of the transverse strain, ϵ_{yy} , throughout the model. The transverse strains vary from $+350 \mu\epsilon$ in the fiber to $-645 \mu\epsilon$ in the matrix. These transverse strains are an order of magnitude smaller than the applied strain.

The fringe plot in Fig. 70 shows the distribution of the engineering shear strains, γ_{xy} , throughout the model. The shear strains vary from $-101 \mu\epsilon$ in the fiber to $-2830 \mu\epsilon$ in the maximum region of the matrix. At this particular applied strain level, the magnitude of the maximum shear strain ($2830 \mu\epsilon$) in the matrix is the same order of magnitude as the applied strain ($2692 \mu\epsilon$). Observation of the trends in Fig. 67 indicate that at higher applied strains or with the higher temperature resin behavior, the maximum shear strain would be significantly larger than the applied strain. Additionally, the shear strain distribution in Fig. 70 confirms that the shear is primarily transferred by the matrix rather than the fiber.

Figures 71–73 show a linear approximation of the distribution of strain energy (including geometrix and material nonlinearity) in the fiber and the matrix for the same infinite series model (Fig. 33) with 21°C nonlinear resin constitutive behavior and $\frac{\sigma}{L} = 0.0050$ (Case 1C). The distributions in Figs. 71 and 72 are for an applied strain of $2692 \mu\epsilon$, increment 3 on Figs. 66 and 67. The distribution in Fig. 73 corresponds to an applied axial strain of $16392 \mu\epsilon$, increment 7 on Figs. 66 and 67. Increment 3 is a relatively low applied global stress and strain while increment 7 is just prior to fiber microbuckling. The abscissa, $\frac{x}{L}$, in Figs. 71–73 represents the percent of the total length of the column, extending from zero at the column base to 50 at the symmetry line. The ordinate in Figs. 71–73 represents the percent of total matrix (Figs. 71 and 73) or fiber (Fig. 72) energy in the system.

The data in Fig. 71 indicates that the strain energy in the matrix is primarily

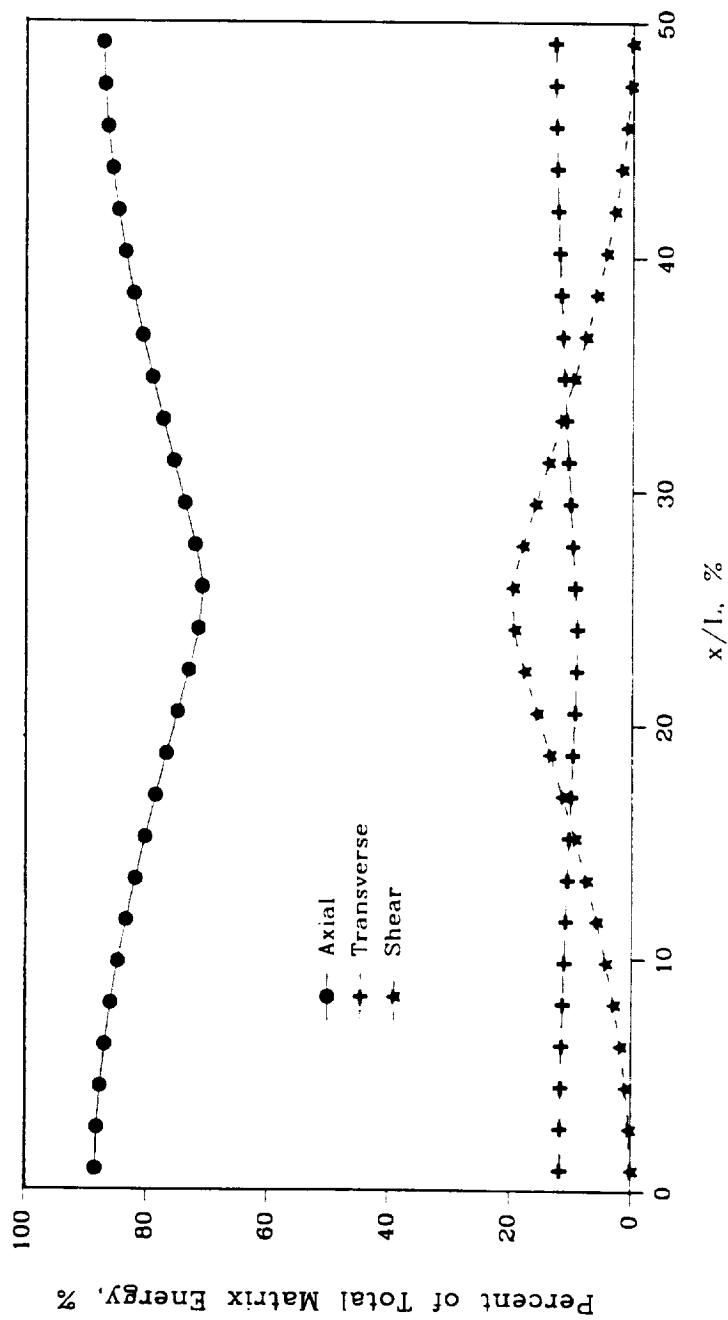


Fig. 71 Distribution of strain energy along the matrix. Global applied strain is $2692 \mu\epsilon$. Nonlinear matrix, 21°C ; $\frac{\sigma}{E} = 0.0050$.

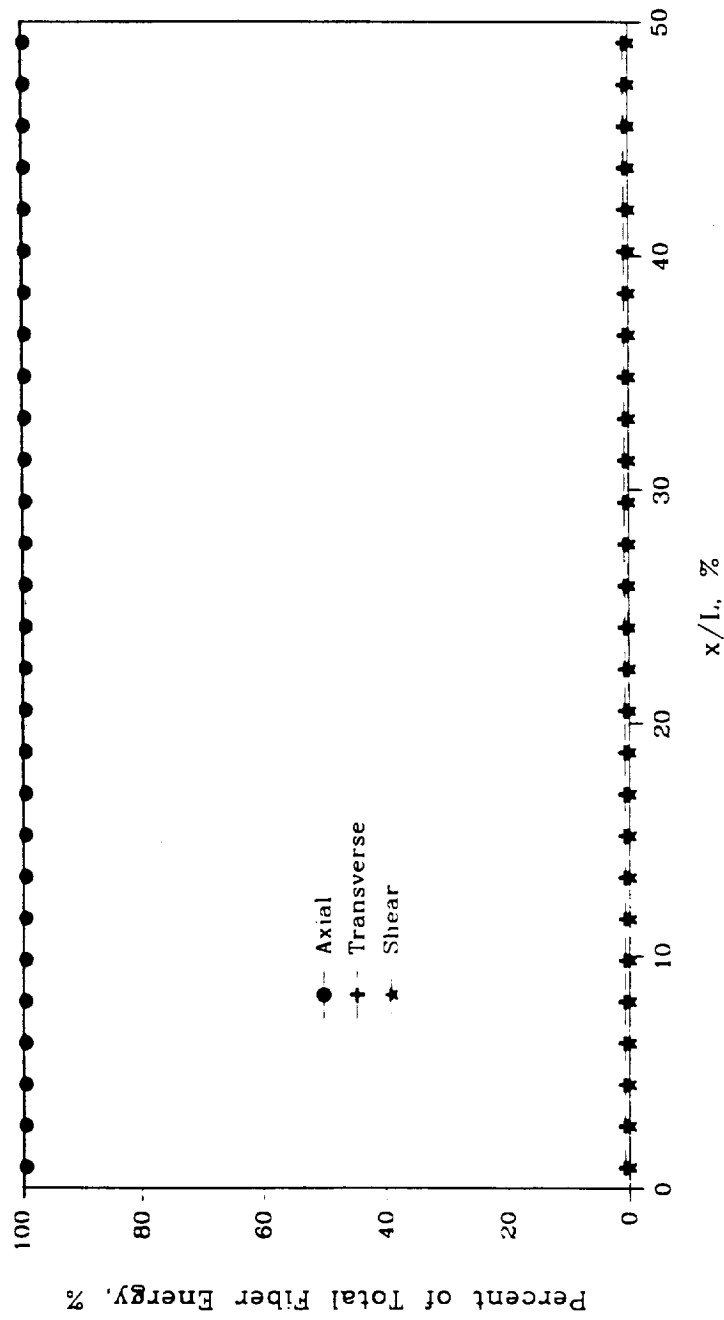


Fig. 72 Distribution of strain energy along the fiber. Same for all levels of applied strain. Nonlinear matrix, 21°C; $\frac{a^2}{L} = 0.0050$.

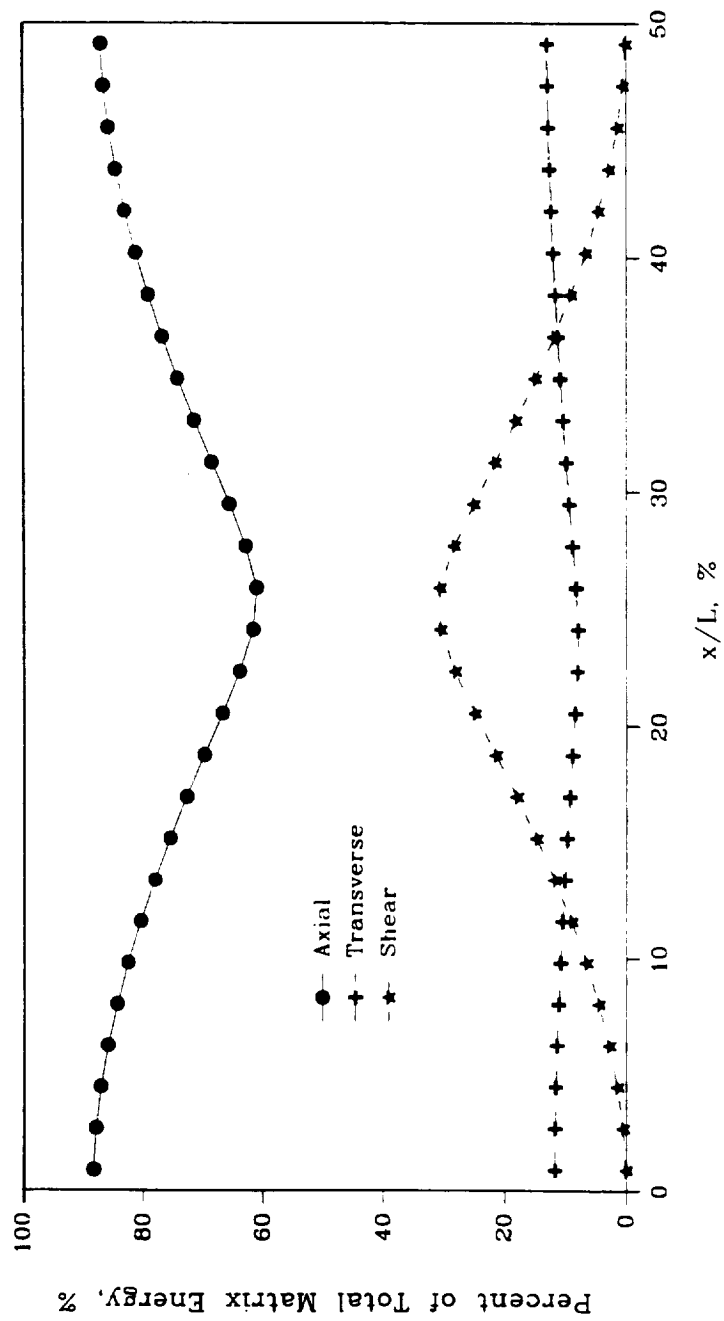


Fig. 73 Distribution of strain energy along the matrix. Global applied strain is $16392 \mu\epsilon$. Nonlinear matrix, 21°C ; $\frac{a}{L} = 0.0050$.

axial. However, in the region of maximum shear ($\frac{z}{L} = 25\%$), the shear contributions to the strain energy are increased, and the axial contributions to the strain energy are decreased. The sum of the axial and shear contributions to the strain energy in the matrix represents $\approx 90\%$ of the total matrix energy at each $\frac{z}{L}$ location.

Although the same trend for the strain energy in the matrix is shown in Fig. 73, the amount of axial and shear strain energy in the matrix along the critical shear region ($\frac{z}{L} = 25\%$) is different. From increment 3 (2692 $\mu\epsilon$) to increment 7 (16392 $\mu\epsilon$), the axial component of the strain energy at $\frac{z}{L} = 25\%$ decreases from 70% to 61% while the shear component increases from 20% to 31%. However, the sum of the axial and shear strain energy components in the matrix still represents 90% of the total matrix energy at each $\frac{z}{L}$ location. The transverse component remains unchanged. The increase in the shear component of energy is attributed to the increase in the instantaneous waviness that occurs with compressive loading.

The data in Fig. 72 show that the strain energy in the fiber is dominated by the contribution from the axial strain; the transverse and shear contributions are negligible. The strain energy distributions for the fiber at increment 7 (16392 $\mu\epsilon$) are identical to those shown in Fig. 72 and are not included. Thus, the strain energy distribution for the fiber is independent of the applied strain level and the $\frac{z}{L}$ position along the model.

Effects of Initial Fiber Curvature

In Case 1W, the semi-infinite geometry (Fig. 32b) is modelled with an initial waviness, $\frac{a_0}{L} = 0.0050$, buckling toward the free surface. The global stress-strain behavior of this model is shown in Fig. 74. Fiber microbuckling initiation (indicated with an arrow), flagged by negative eigenvalues in the system matrix, occurred at 38462 $\mu\epsilon$. With additional increases in the applied strain, up to 42231 $\mu\epsilon$, the entire

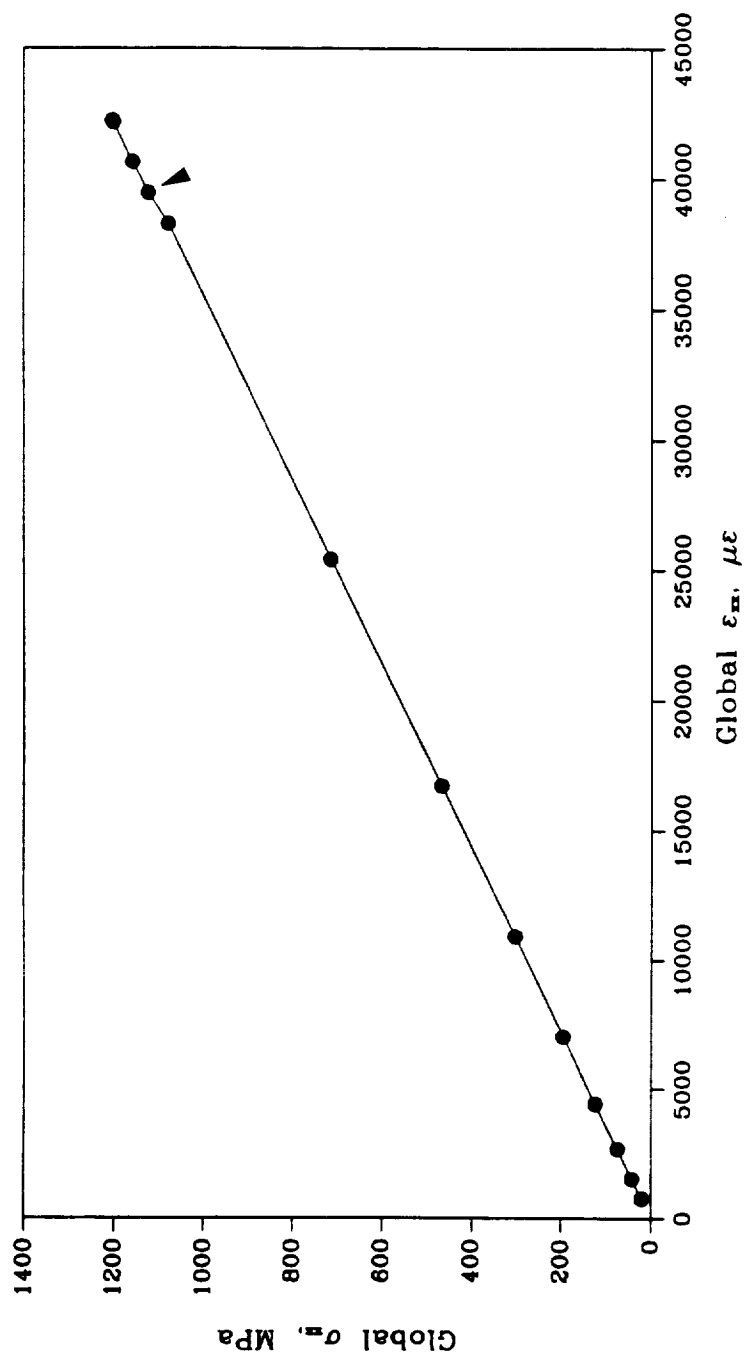


Fig. 74 Global stress-strain response of semi-infinite plate.
Nonlinear matrix, 21°C; $\frac{a}{L} = 0.0050$.

column buckled.

The infinite series model (Fig. 33) is also used to show the effects of initial fiber waviness on fiber microbuckling initiation strains and the development of shear strain in the matrix. The matrix constitutive behavior assumed is the 21°C nonlinear data. Figure 75 is a plot of the global axial stress, σ_{xx} , as a function of the applied global strain, ϵ_{xx} , for four different initial fiber curvatures ($\frac{a_0}{L} = 0.0000$, $\frac{a_0}{L} = 0.0025$, $\frac{a_0}{L} = 0.0050$, and $\frac{a_0}{L} = 0.0075$). The curve for the perfectly straight fiber continues to the numerical critical buckling strain (eigenvalue analysis) of 94100 $\mu\epsilon$. Fiber microbuckling (indicated with arrows) for the initially wavy infinite series model occurred at 27046 $\mu\epsilon$ for $\frac{a_0}{L} = 0.0025$, 21923 $\mu\epsilon$ for $\frac{a_0}{L} = 0.0050$, and 18369 $\mu\epsilon$ for $\frac{a_0}{L} = 0.0075$, Cases 3W-5W respectively. These trends indicate that a small amount of waviness (e.g., 0.25%) causes a significant reduction, compared to those for the perfectly straight fiber, in the initiation strain levels. Additional increases in the initial fiber curvature cause further reduction in the fiber microbuckling initiation strains.

Figure 76 is a plot of the local shear strain, γ_{xy} , as a function of the applied global axial strain, ϵ_{xx} , for the same four models (Cases 2W-4W). This graph illustrates, as previously mentioned, that when the fibers are perfectly straight, zero shear strain is developed in the matrix. However, these results also indicate that as the initial fiber curvature increases, the amount and rate of shear strain development in the resin for a given applied strain increases. Additionally, the applied strains associated with the asymptotic behavior in Fig. 76 are ≈ 1.80 , ≈ 1.46 , and ≈ 1.20 times the resin yield strain (Fig. 36) for the 21°C data. This result indicates that as the initial fiber waviness increases, the axial strain necessary for fiber microbuckling initiation decreases. Additionally, the axial strains that correspond

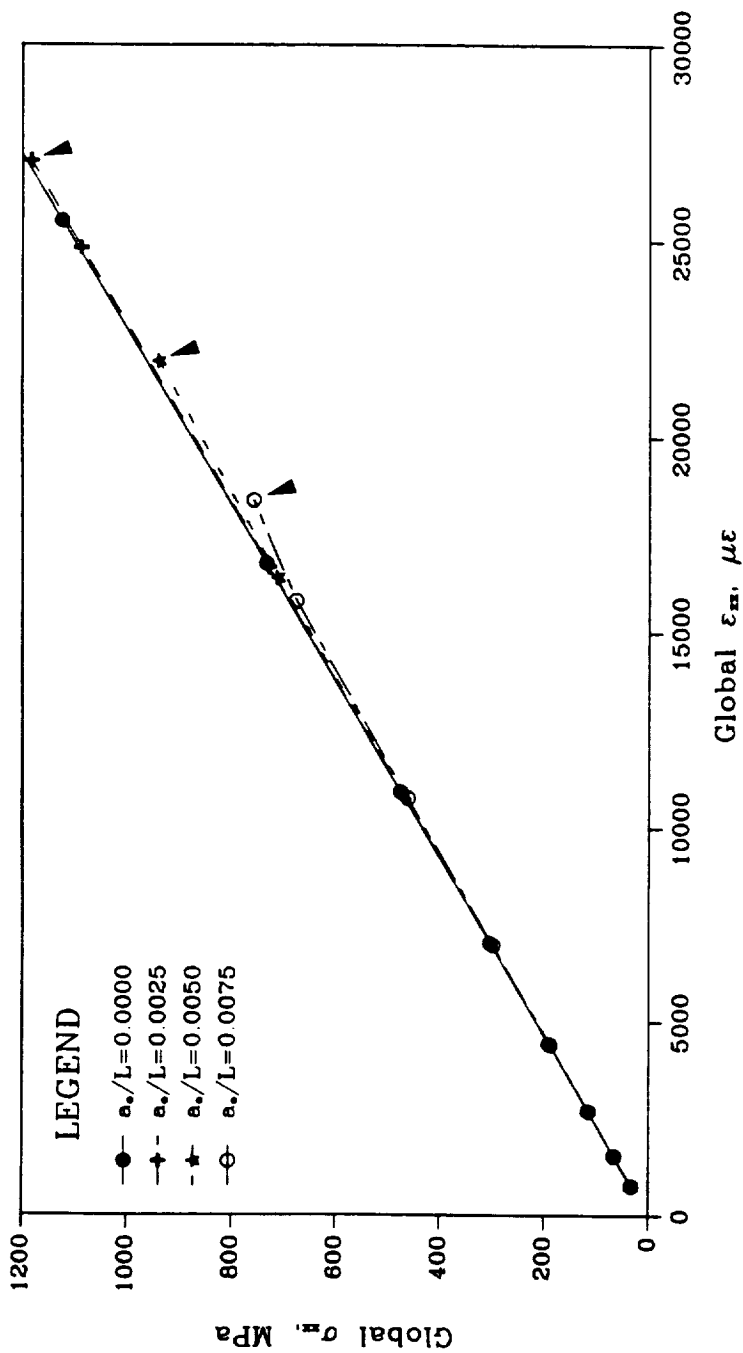


Fig. 75 Global stress-strain response of infinite series for four initial fiber curvatures. Nonlinear matrix, 21°C.

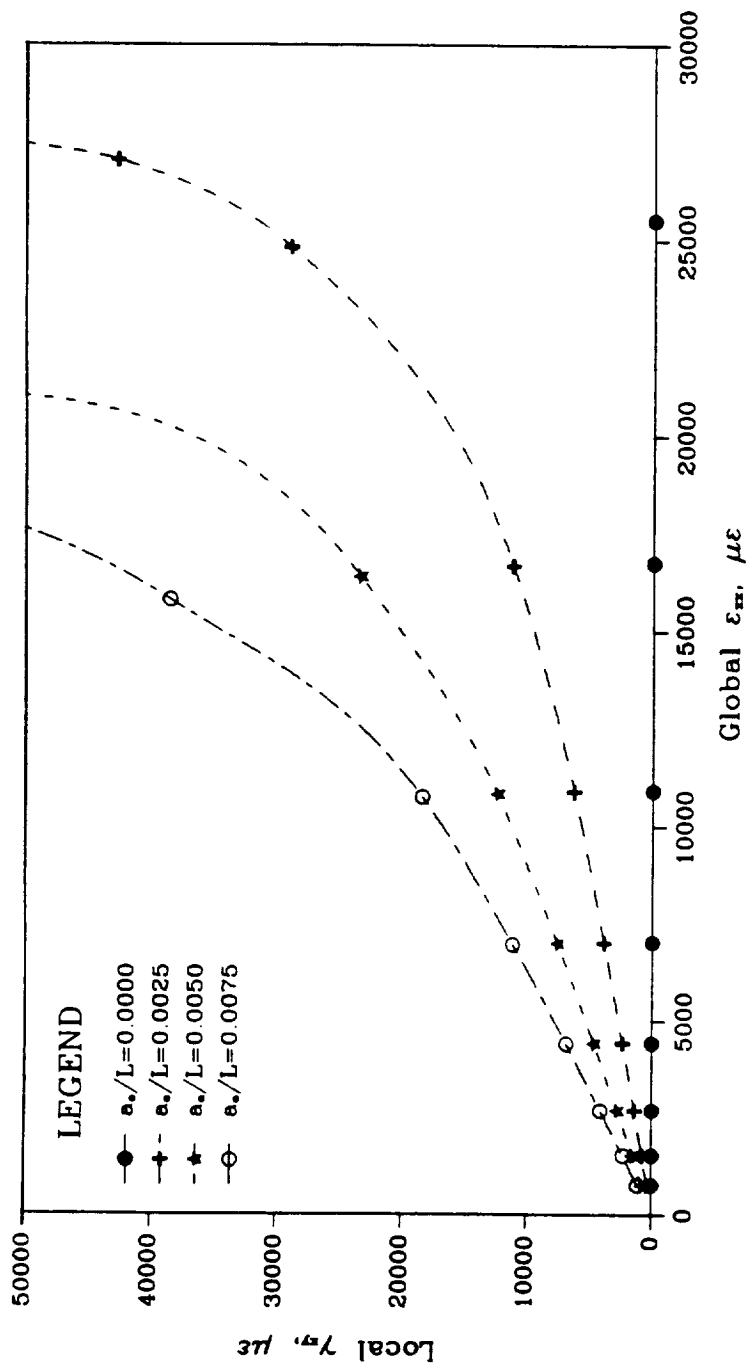


Fig. 76 Local shear strain versus global applied strain of infinite series for four initial fiber curvatures. Nonlinear matrix, 21°C.

to the asymptotic behavior in Fig. 76 correlate well with the fiber microbuckling initiation strains in Fig. 75. This correlation is additional proof that as the tangent modulus of the resin decreases (with increasing applied load), the resistance to fiber microbuckling decreases. Similar trends, although significantly lower fiber microbuckling strains, were observed in a parallel study^{78,79} for an infinite model using a minimum potential energy approach. In Fig. 76, notice that for the smaller initial curvatures, $\gamma_{xy} \propto \epsilon_{xx}$ in the initial region of each curve. As the initial fiber curvature increases, the local shear strain becomes larger than the applied axial strain. This result implies that for larger initial curvatures, the axial component of the strain energy in the matrix becomes negligible.

Effects of Interfacial Bond Strength

The infinite series model in Cases 1D–4D shows the effects of debond location and length on fiber microbuckling. Figure 77 is a plot of the global stress as a function of the global applied strain for a debond extending 10.7% of the fiber length at two different locations along the fiber (Cases 1D and 2D). The debonds are located near the symmetry line in Case 1D and along the regions of maximum shear in Case 2D. The column in Case 1D buckled at 21961 $\mu\epsilon$, and the column in Case 2D buckled at 11692 $\mu\epsilon$. Locating the debond along the critical shear region (Case 2D) caused a 46.8% reduction, compared to Case 1D (no reduction from perfect bond), in the fiber microbuckling strain.

Fringe plots (same orientation as Fig. 33) for both of these debond locations are shown in Figs. 78 (debond at symmetry line, Case 1D, is indicated with an arrow) and 79 (debond along critical shear region, Case 2D, is indicated with an arrow). The applied strains for Figs. 78 and 79 are 2692 $\mu\epsilon$ and 2662 $\mu\epsilon$ respectively. The distribution of shear strain in Fig. 78 is identical to that in Fig. 70 (perfect

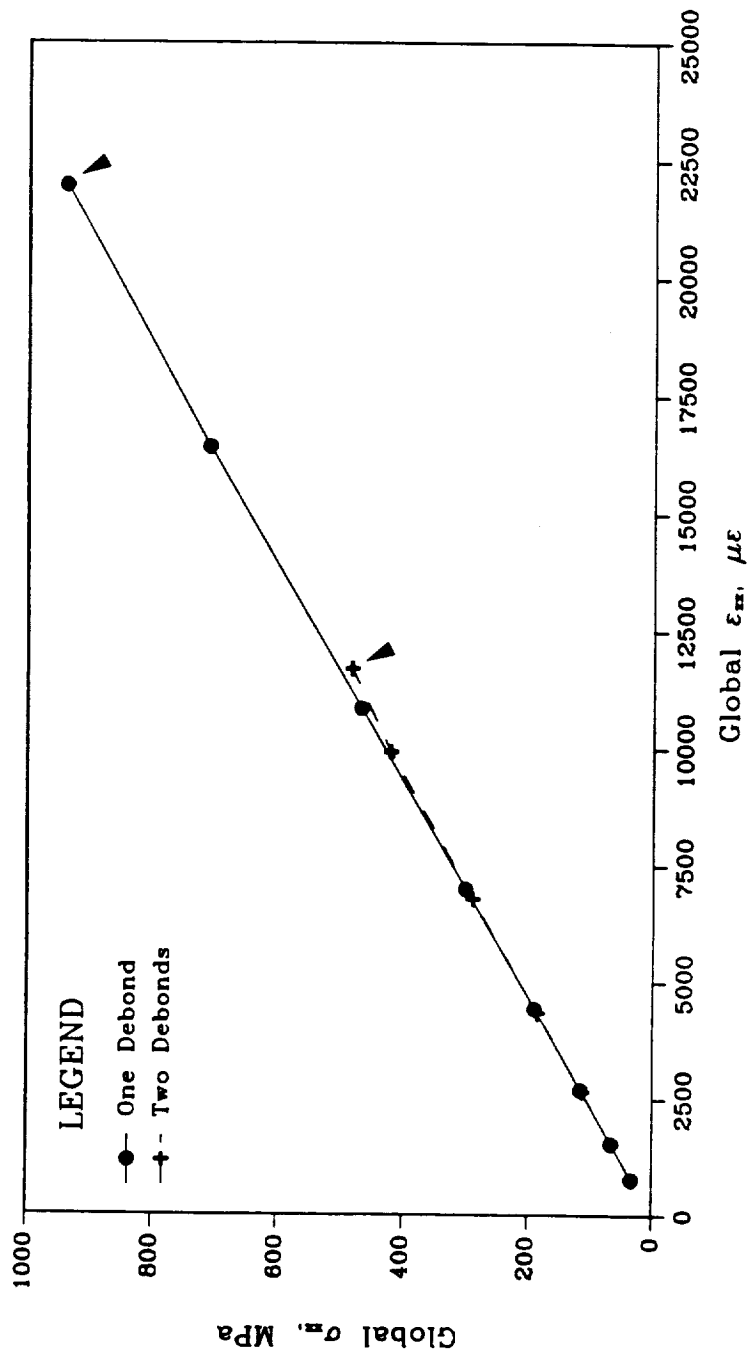


Fig. 77 Global stress-strain response of infinite series for 2 locations debonded 10.7%. Nonlinear matrix, 21°C; $\frac{a_0}{L} = 0.0050$.

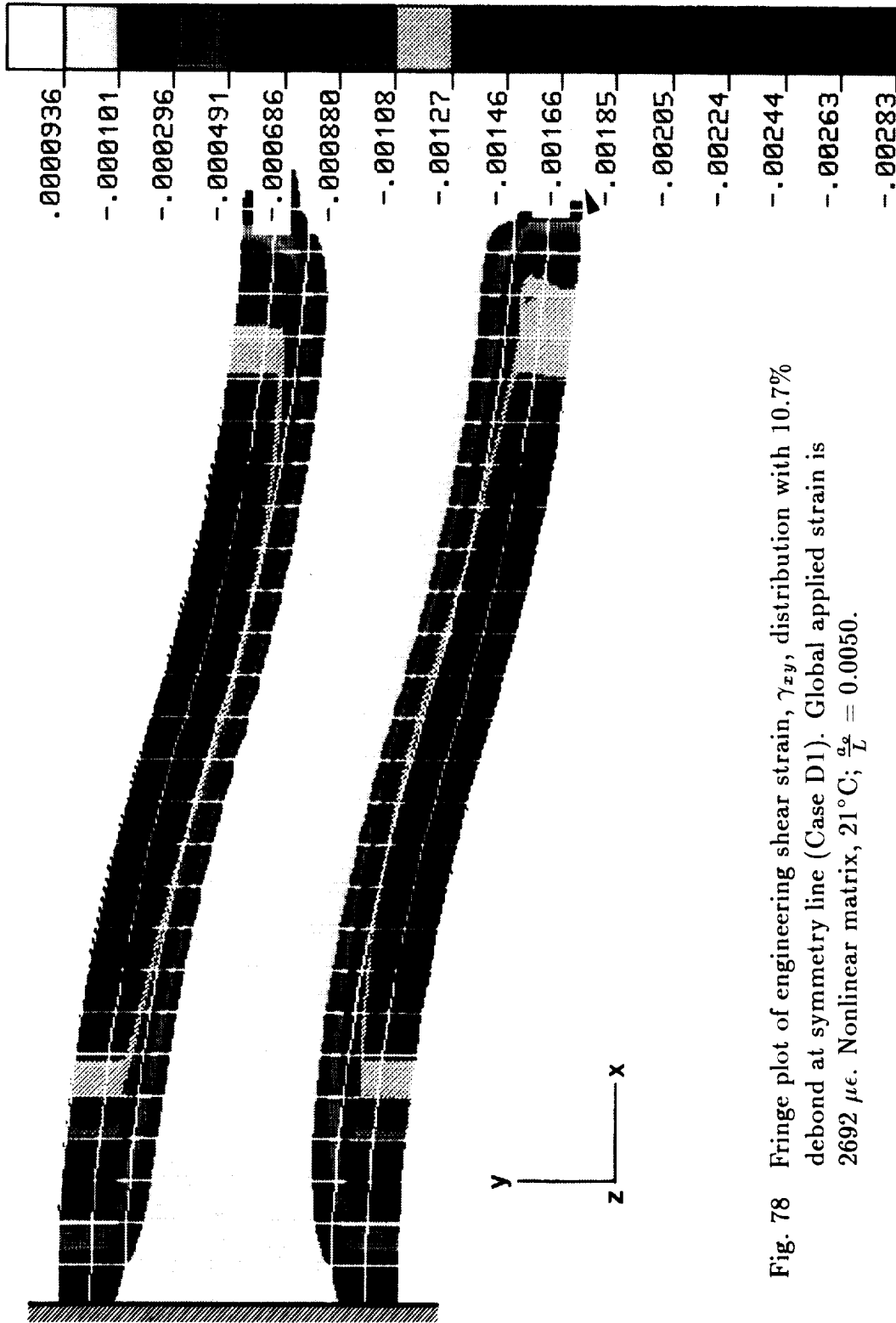


Fig. 78 Fringe plot of engineering shear strain, γ_{xy} , distribution with 10.7% debond at symmetry line (Case D1). Global applied strain is $2692 \mu\epsilon$. Nonlinear matrix, 21°C ; $\frac{\sigma_2}{T} = 0.0050$.

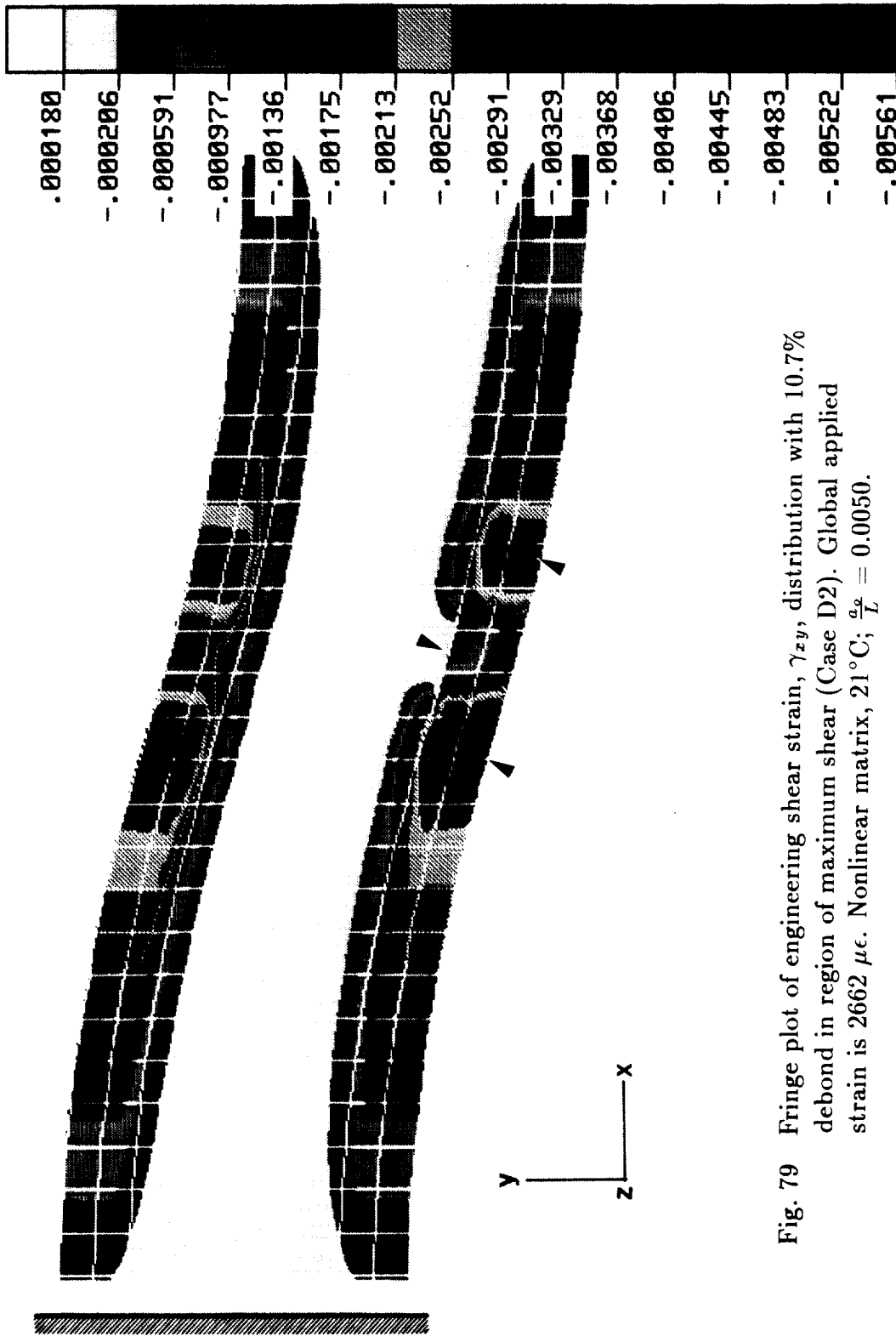


Fig. 79 Fringe plot of engineering shear strain, γ_{zy} , distribution with 10.7% debond in region of maximum shear (Case D2). Global applied strain is 2662 $\mu\epsilon$. Nonlinear matrix, 21 $^\circ$ C; $\frac{\sigma}{E} = 0.0050$.

CF

bond, Case 2C) except that the contour gradient in the matrix between the critical shear region and the debond location is steeper. In fact, the scales on the color bars are identical. However, when the debond location is along the critical shear region (Case 2D), the fringe plot (Fig. 79) is significantly different from that in Fig. 79. Debonds along the maximum shear regions cause a discontinuity at the fiber/matrix interface (preventing shear transfer between fiber and matrix) and cause a shear strain concentration within the matrix (indicated with arrows), both shown in Fig. 79. Furthermore, the maximum shear strain in the matrix is $4450 \mu\epsilon$ (Case 2D), compared to $2830 \mu\epsilon$ in the perfect bond model (Case 2C), for the same applied strain.

Figure 80 is a plot of the global stress-strain behavior for the infinite series model with a perfect bond (Case 2C) and with debonds along 10.7% (Case 1D), 25.0% (Case 3D), and 50.0% (Case 4D) of the column length. Fiber microbuckling is indicated with arrows. The data in Fig. 80 show that the 10.7% debond at the symmetry line (Case 1D) has a negligible effect on the global stress-strain behavior of the column, buckling at $21961 \mu\epsilon$. However, when the debond extends along 25% of the column length (Case 3D), fiber microbuckling occurs at $6700 \mu\epsilon$ and when the debond extends along 50% of the column length (Case 4D), fiber microbuckling occurs at $2108 \mu\epsilon$. The 25% and 50% debonds cause 69.4% and 90.4% reductions, compared to the perfect bond, respectively in the fiber microbuckling strains. Since the longer debonds extend over the critical shear regions, it is difficult to determine what portion of the reduction is caused by debond length and what portion is caused by debond location. The results in Figs. 77–80 indicate that the combination of two factors, debond length and location, cause these large reductions in the fiber microbuckling strains.



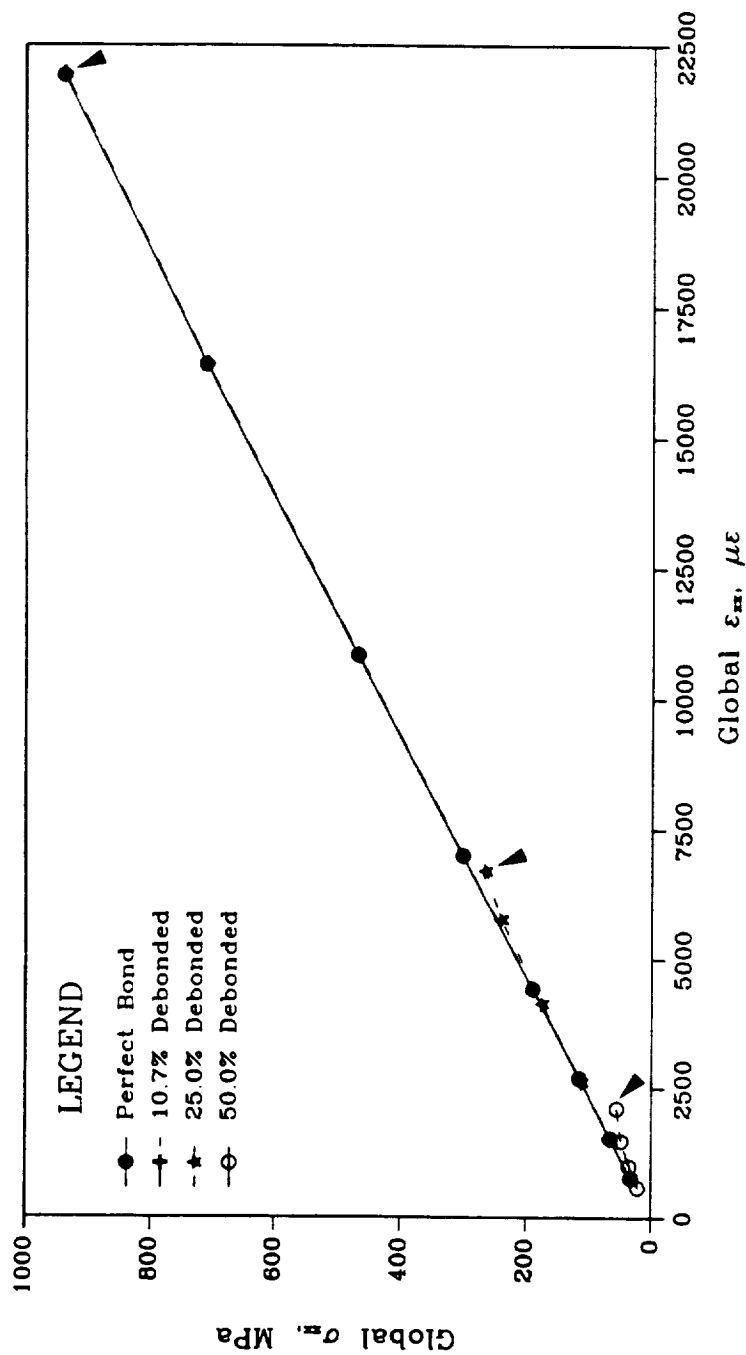


Fig. 80 Global stress-strain response for infinite series for 3 debond lengths along the region of maximum shear. Nonlinear matrix, 21 °C; $\frac{a^2}{l} = 0.0050$.

Effects of Free Surface

Evaluation of the free surface effects are attempted with the results from the semi-infinite plate in Case 1W (Fig. 32b with waviness). The global stress-strain behavior of this model is given in Fig. 74. The maximum local transverse and shear strains were examined in the interior (first whole-width matrix nearest the smear region) and near the free surface (first whole-width matrix nearest the free surface) of the model. These local strains are compared with those for the infinite array (Fig. 33) with the same matrix and initial fiber waviness (Case 2C). The local shear strain is plotted as a function of the global applied strain in Fig. 81 for these two models. For a given applied strain, the magnitude of the interior shear strains in the semi-infinite plate are smaller than those observed in the infinite array. Additionally, the local shear strains near the free surface are even smaller than those in the interior matrix of the semi-infinite plate. Similar trends are observed for the transverse strains (not included). The strains in the interior region of the semi-infinite plate are smaller than those in the infinite array because the shear modulus of the fiber is approximately 5 times that of the smear region. Consequently, less strain is developed in the interior matrix of the semi-infinite plate, compared to the infinite series model. The boundary conditions of the semi-infinite plate require that all of the strains go to zero at the free surface. Therefore, it is not surprising that the local shear strains in the exterior matrix are smaller than those developed in the interior. These results imply that the free surface effect, attributed to localized high shear strains, does not exist. However, the problem is that they simply do not illustrate the free surface effect caused by the reduced support for the fibers.

The effects of the free surface are best demonstrated by the early appearance of the negative eigenvalue warning. Recall that a negative eigenvalue occurs when

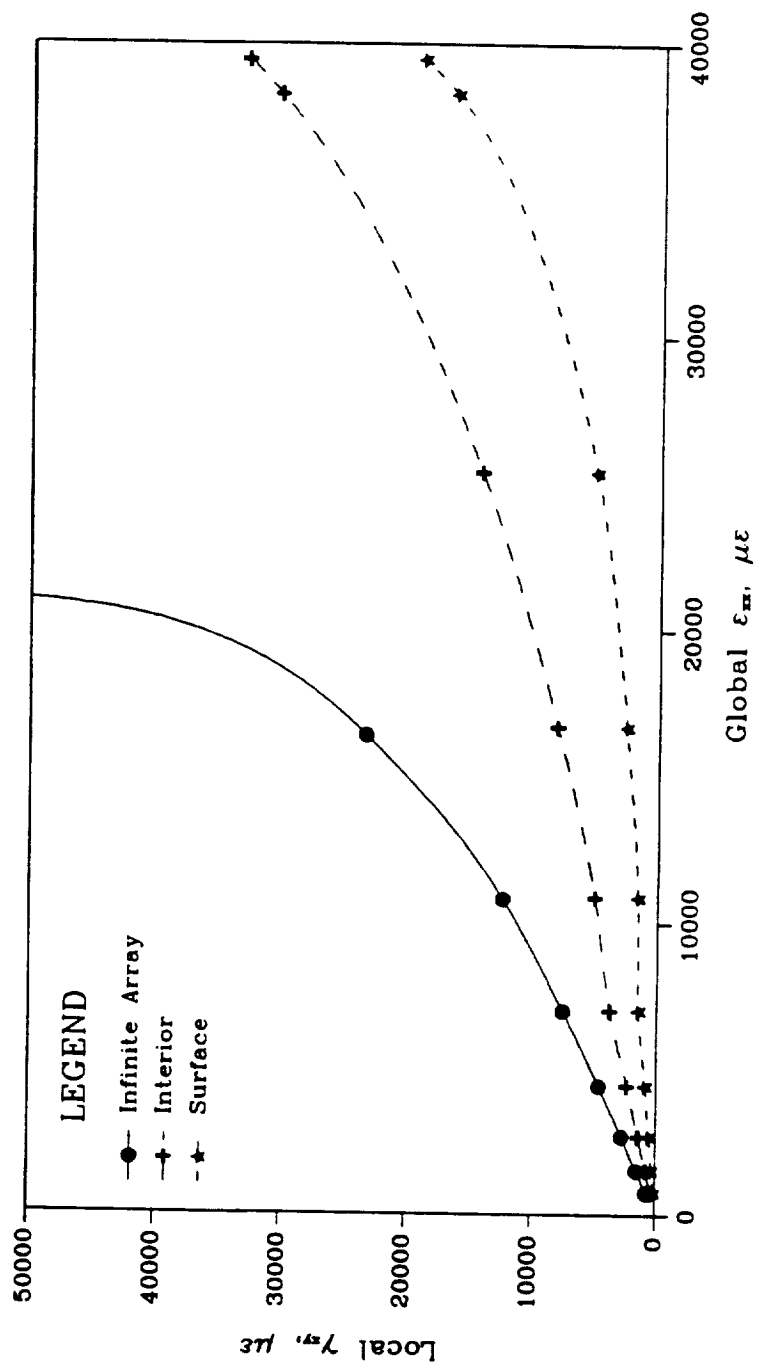


Fig. 81 Local shear strain versus global applied strain for infinite series (Case 2C) and semi-infinite plate. Nonlinear matrix, 21°C; $\frac{a^2}{L} = 0.0050$.

the system matrix is no longer positive definite, and it is typically associated with the point when additional increases in the applied strain do not yield additional increases in the load-carrying capacity of the column. Deformed shapes for the semi-infinite plate (Case 1W) are shown in Figs. 82 and 83. Figure 82 corresponds to increment 7 ($\epsilon_{xx} = 16715 \mu\epsilon$) on Fig. 74, prior to the negative eigenvalue warning. Figure 83 corresponds to increment 10 ($\epsilon_{xx} = 39462 \mu\epsilon$) on Fig. 74, the first increment with the negative eigenvalue warning. Comparison of the deformed shapes in Figs. 82 and 83 indicates that fiber microbuckling initiation has occurred at the free surface (indicated by an arrow in Fig. 83). In Fig. 83, the interior fibers are not buckled (compare with Fig. 82). The localized initiation of fiber microbuckling at $38269 \mu\epsilon$ in Fig. 83 is enough to cause the system matrix to no longer be positive definite. However, the large unbuckled smear area in the interior of the plate prevented complete buckling of the column until $42231 \mu\epsilon$. Comparison of these strains indicates a 9.4% reduction in ϵ_I caused by the lack of support at the free surface.

Effects of Fiber Constitutive Properties

The infinite series model (Fig. 33) in Cases 1F (same as 2C and 4W) and 2F illustrate the effects of fiber constitutive properties on fiber microbuckling. The initial fiber waviness is $\frac{a_0}{L} = 0.0050$ and the matrix constitutive behavior is 21°C nonlinear. Figure 84 is a plot of the global stress-strain behavior of the infinite series model with Type *A* and Type *B* isotropic fibers. See Table VIII for assumed mechanical properties. Fiber microbuckling for the infinite series model with Types *A* and *B* isotropic fibers occurred at $7765 \mu\epsilon$ and $21923 \mu\epsilon$ respectively. Although the strains are dramatically different, the compressive strengths are not so different, 1064 MPa versus 938 MPa. Observation of Fig. 84 shows that the

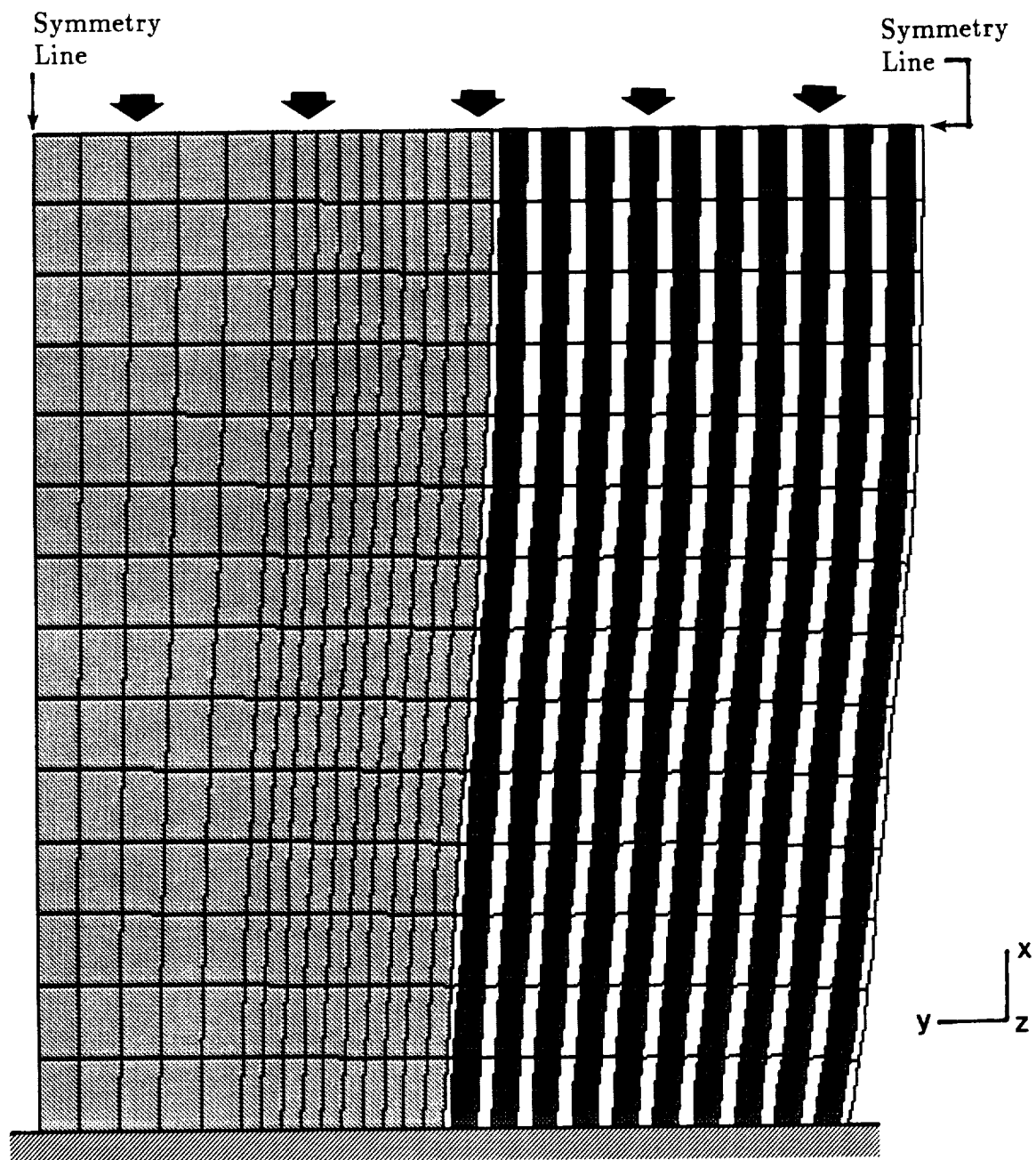


Fig. 82 Deformed shape of semi-infinite model. Applied strain is $16715 \mu\epsilon$, prior to fiber microbuckling initiation. Nonlinear matrix, 21°C ; $\frac{a_0}{L} = 0.0050$.



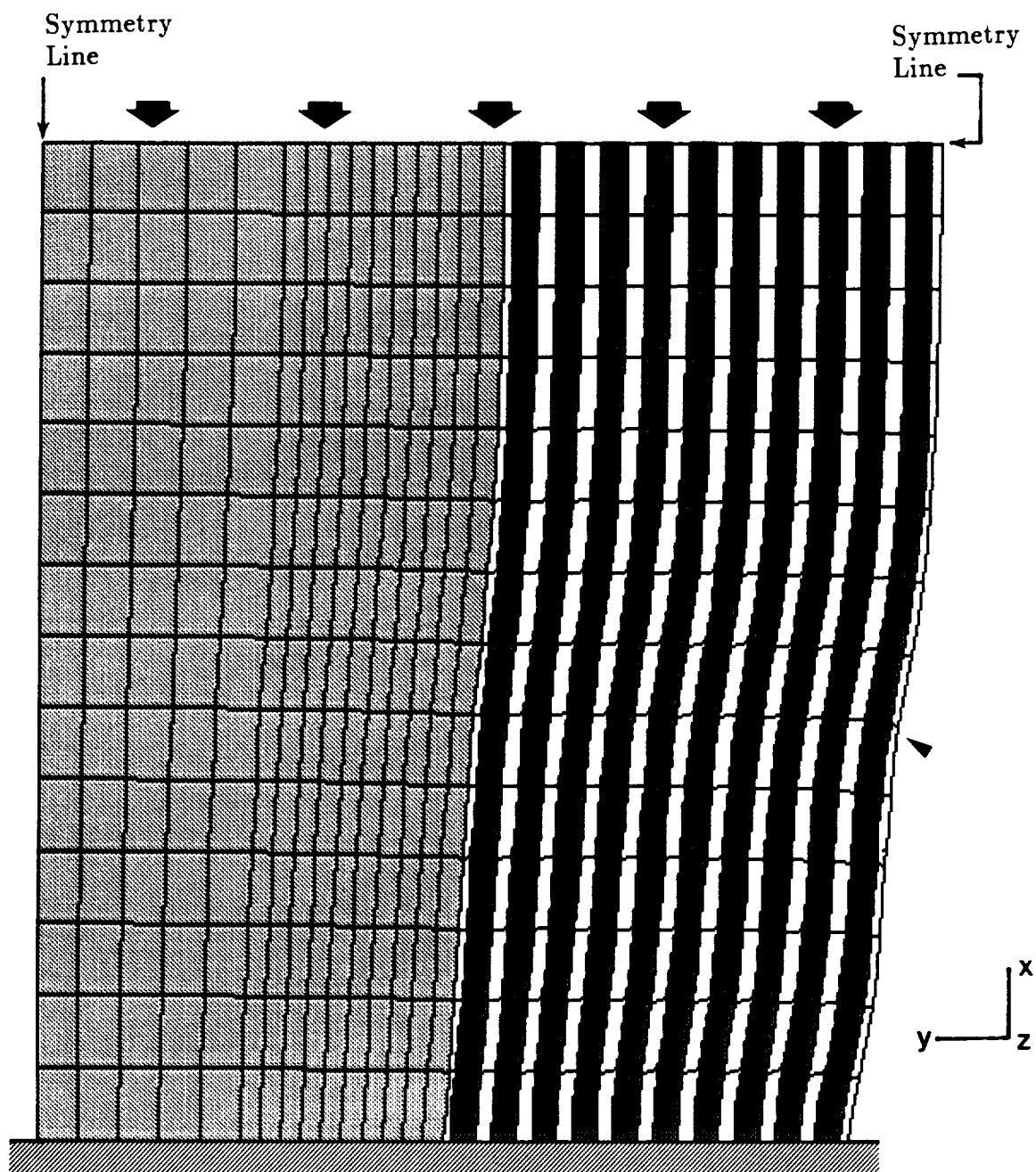


Fig. 83 Deformed shape of semi-infinite model. Applied strain is $39462 \mu\epsilon$, at fiber microbuckling initiation. Nonlinear matrix, 21°C ; $\frac{\alpha_p}{L} = 0.0050$.

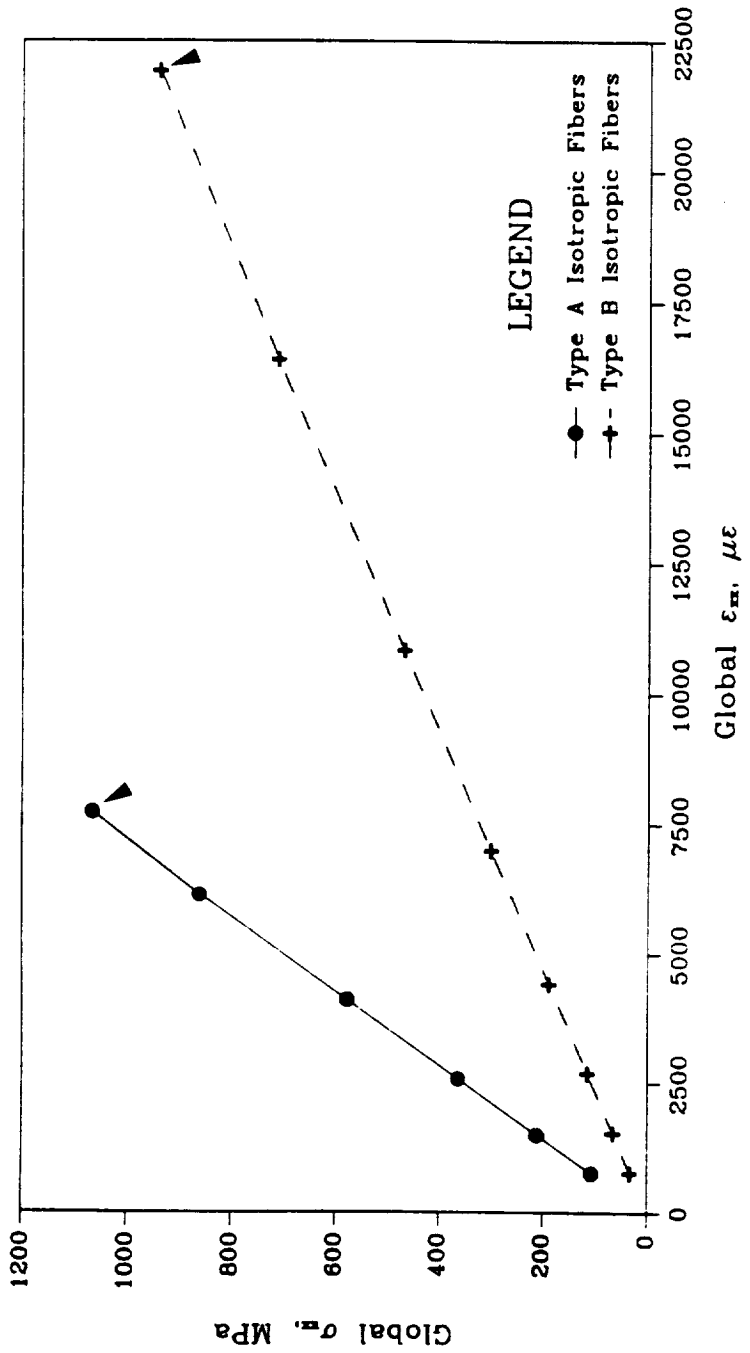


Fig. 84 Global stress-strain response of infinite series for two isotropic fiber constitutive behaviors. Nonlinear matrix, 21 °C; $\frac{\sigma_f}{L} = 0.0050$.

axially stiffer Type *A* isotropic fibers cause a stiffer global response of the model. However, the Type *A* isotropic fibers also have a stiffer shear modulus which provides additional resistance to a microbuckling instability. From this graph it is not possible to determine what portion of the additional resistance to fiber microbuckling is caused by the increased axial modulus and what portion is caused by the increased shear modulus.

Figure 85 is a plot of the local shear strain, γ_{xy} , as a function of the applied global strain, ϵ_{xx} , for Cases 1F and 2F. The stiffer Type *A* isotropic fibers (Case 2F) causes significantly higher local shear strains to develop in the matrix for a given applied axial strain. Furthermore, the asymptote for Type *A* isotropic fibers occurs at a lower axial strain ($\approx 7500 \mu\epsilon$) than the asymptote for the Type *B* isotropic fibers ($\approx 21000 \mu\epsilon$) because the stiffer fibers cause the resin to develop shear strains at a much higher rate, and thus, they reach the yield point on the $\tau_m-\gamma_m$ curve at a lower applied strain. Recall that for the Type *A* fibers, E_f and ν_f are held constant and consequently G_f is increased (see Chapter IV for property descriptions). This G_f increase means that the Type *A* fibers are stiffer in shear than the Type *B* fibers, and thus, the Type *A* fibers cause the shear strain to be primarily in the matrix. The lower shear modulus for the Type *B* fibers allows some shear strain to be transmitted in the fibers. Consequently, the Type *A* fibers behave more rigidly than the Type *B* fibers. The higher rate of development of the shear strains for the stiffer fibers is attributed primarily to the higher fiber axial modulus.

The trends for the data in Figs. 84 and 85 and the strain magnitudes for the Type *A* isotropic fibers both correlate well with those presented in Refs. 78 and 79. This result occurs because the Type *A* isotropic fibers have the same axial modulus as those used in Refs. 78 and 79.

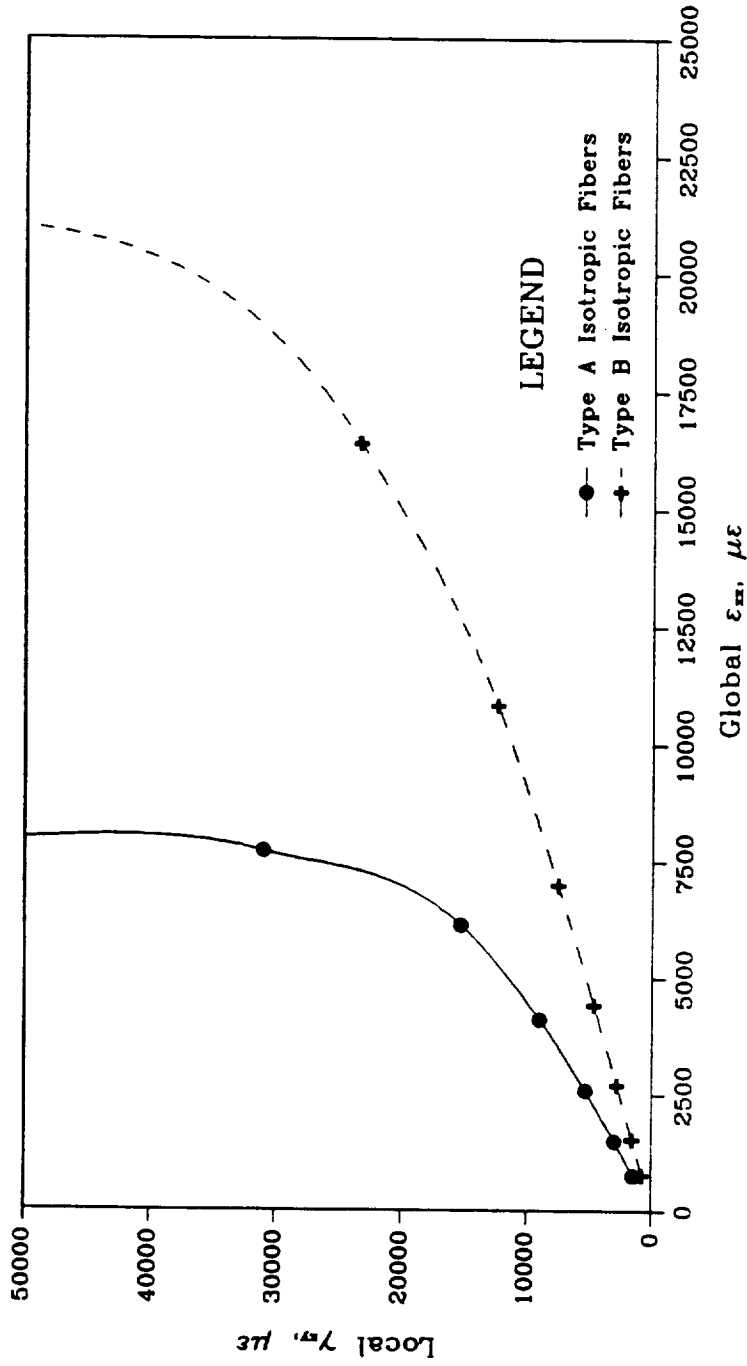


Fig. 85 Local shear strain versus global applied strain of infinite series for two isotropic fiber constitutive behaviors. Nonlinear matrix, 21°C; $\frac{\sigma}{E} = 0.0050$.

CHAPTER VII

DISCUSSION

A discussion of the results obtained in this investigation is presented in this chapter. The discussion of the experimental results is followed by the discussion of the finite element results for both straight and wavy fiber models. Finally, the chapter is concluded with the relevant comparisons between the experimental and finite element results. Again, note that the absolute value of the ϵ_{cr} and ϵ_I strains are used for magnitude comparison throughout this chapter.

Experimental Results

Material Property Characterization

The experimental results presented in Figs. 37–40 show that with increasing temperature, there is a significant reduction in the shear stresses and strains associated with the yield points on the composite τ_{12} – γ_{12} (Fig. 37) and the subsequently derived matrix τ_m – γ_m (Fig. 40) curves. Additionally, it was shown for the composite that tension testing of the $[\pm 45]_n$ specimens yielded matrix cracks (Fig. 38) and a flatter plateau, compared to a similar compression test, on the τ_{12} – γ_{12} (Fig. 37) curve. The flatter plateau is attributed to the matrix cracking.

The introduction of fiber waviness via QuadraX interlacing caused a global ply waviness rather than the desired localized fiber waviness. Compared to the global out-of-plane ply waviness (Fig. 41), the in-plane fiber waviness (Fig. 42) is negligible.

The interfacial shear strength results (Table IX) indicate that when compared to the commercial APC-2 material, the IFSS for the experimental AU4U/PEEK material is reduced by 16.7%, regardless of the stacking sequence. A skewed



distribution of the IFSS values for one series of fibers in the multidirectional APC-2 laminate indicates that the surface treatment of the fibers is nonuniform.

The average steady-state G_I was 1458 J/m^2 and 729 J/m^2 for the APC-2 and AU4U/PEEK laminates, respectively, as shown in Fig. 45 and Table IX. The average steady-state G_{II} was 2500 J/m^2 and 1150 J/m^2 for the APC-2 and AU4U/PEEK laminates, respectively, as shown in Fig. 49 and Table IX. The poor fiber/matrix interface in the experimental material caused 50.0% and 54.0% reductions, compared to the commercial APC-2, in the steady-state G_I and G_{II} , respectively. These reductions are explained by the micrographs in Figs. 43, 46, and 50. For both mode I and mode II loading, the cracks grew at the fiber/matrix interface in the AU4U/PEEK composite. Comparison of the APC-2 fracture surfaces (Figs. 46a, 46b, 50a, 50b) and crack tips (Figs. 43a, 43c) with the AU4U/PEEK fracture surfaces (Figs. 46c, 46d, 50c, 50d) and crack tips (Figs. 43b, 43d) shows severely deformed PEEK matrix well-adhered to the fibers in the APC-2 composites and bare fibers with little resin deformation in the AU4U/PEEK composites. Comparison of the APC-2 mode I (Figs. 46a, 46b) and mode II (Figs. 50a, 50b) fracture surfaces shows that the resin drawing is parallel to the fracture surface in the mode II or shearing mode and perpendicular to the fracture surface in the mode I or opening mode. The micrographs of the crack fracture paths (Figs. 47 and 51) show that all cracks grew intraply (within the ply). Typically, intraply cracking occurs at lower fracture energies because of the reduced resin volume within the ply, compared to between the plies. Thus, it is expected that the G_I and G_{II} values reported herein are lower than would be realized for interlaminar cracking. For the toughness to be fully realized, the crack must grow in an interlaminar manner. Observation of the APC-2 micrographs in Figs. 43a,

43c, 46a, 46b, 50a, and 50b indicates that although the crack grew intraply, the failure was still cohesive in the PEEK matrix.

The trends, presented in Table IX, for G_I , G_{II} , and IFSS are consistent with each other for the commercial APC-2 and experimental AU4U/PEEK materials. Degradation of the fiber/matrix interface causes significant reductions in G_I , G_{II} , and IFSS. It is not surprising that the IFSS reduction caused by the poor interface is only 16.7%, compared to 50% for G_I and 54% for G_{II} . According to Ref. 147, G (both modes I and II) plotted as a function of IFSS is a bell-shaped curve; it is possible for a small reduction (e.g., $\approx 17\%$) in IFSS to cause large reductions (e.g., $\approx 50\%$) in G .

Initiation of Fiber Microbuckling

Results from the incremental damage study in Figs. 52 and 53 verified that the stereomicroscope observations of fiber microbuckling initiation correspond with the higher magnification observations in the SEM, and thus, the stereomicroscope observations are sufficient for repeatable recognition of the initiation of fiber microbuckling.

Although the sample standard deviations for the fiber microbuckling initiation strains presented in Figs. 54–56, 59, 61, and 63 are large in some cases, it is believed that the trends are accurate. The limited experimental data prevents absolute determination of the magnitude of the trends.

The results presented in Fig. 54 indicate that there is an optimum angle for maximum resistance to fiber microbuckling. However, when the laminate orthotropy is considered, Fig. 55, it appears that the initiation strain level for fiber microbuckling is a geometric property. At 21°C, the average local ϵ_I is 23361 $\mu\epsilon$, and at 77°C, the average local ϵ_I is 19935 $\mu\epsilon$ for laminates with 0°, $\pm 15^\circ$, and $\pm 45^\circ$ as

supporting plies and $15031 \mu\epsilon$ for laminates with ± 75 and 90_2 as supporting plies.

Two possible reasons for the reduced local ϵ_I for the $[(\pm 75/0_2)_3/\pm 75/0]$, and $[(90_2/0_2)_3/90_2/0]$, laminates at 77°C are inaccurate SCFs at 77°C and reduced resistance to fiber microbuckling associated with resin yielding. First, it is possible that the 21°C SCFs are not accurate for the 77°C data. However, one would expect the higher temperatures and consequent softer material to reduce the strain concentration around the hole. Then, the SCFs at 77°C would be smaller than those at 21°C . This change would increase the reduction in ϵ_I for the *D* and *E* laminates in Fig. 55. A second and more likely reason for the significant reduction in the local ϵ_I is the combination of the reduced resin shear yield strain (see Fig. 40) and the larger angles (± 75 and 90_2) of supporting ply orientation. With the other adjacent ply orientations, the fibers and fiber/matrix interaction may provide some resistance to fiber microbuckling. At the larger angles of supporting plies, it appears that at 77°C , the resistance to fiber microbuckling is significantly reduced. It is possible that at the lower fiber orientations, some fiber rotation occurs and apparently increases the interlaminar shear strength and the resistance to fiber microbuckling. The larger ply orientation angles appear not to accommodate fiber rotation so that the interlaminar shear strength and resistance to fiber microbuckling is controlled by the resin shear yield strength, which is significantly reduced at 77°C .

The effects of the free surface on fiber microbuckling initiation were shown in Fig. 56. The results indicate that ϵ_I is reduced 9.9–10.1% for specimens with 0_2 , rather than ± 45 , as surface plies. In-situ stereomicroscope observations and SEM micrographs (Figs. 57b and 57d) indicate fiber microbuckling initiates in-plane into the notch followed immediately by partial ply buckling out-of-plane toward the free surface for the $[(0_2/\pm 45)_3/0/\pm 45]$, laminates. It is anticipated that the relatively



high G_I (Table IX) for APC-2 laminates prohibits ply delamination and thus out-of-plane buckling of the entire 0_2 surface plies.

The fiber microbuckling data presented in Fig. 59 indicates a monotonic increase in the remote ϵ_I as the ply waviness increases from that in tape laminates (Fig. 41a) to that in plain weave 1-harness Quadrax laminates (Fig. 41c). Consideration of the local ϵ_I has no effect on the results since the SCFs (Table IX) are within 1.3% of each other. The small monotonic increase in ϵ_I is attributed to interlocking of the interlaced plies. Another factor related to ply waviness that may affect ϵ_I in these notched laminates is the physical condition of the interlacing at the notch free surface. The transverse tensile stresses necessary to cause the transverse cracking in the 0_2 plies in Figs. 60c and 60d are caused by the increase in the out-of-plane ply waviness when the specimens are compressively loaded. Even though the deformation may be elastic, it is large enough to cause the tensile stresses for the transverse cracking. The fiber failures at the column ends, rather than the mid-span, in Fig. 60d may be caused by the geometry (over and under shape) of the weave.

The micrographs in Figs. 58a, 58c, and 58d show that the fiber/matrix interfacial bond is very strong for these APC-2 composites. Furthermore, comparison of Fig. 58a (21°C) with Figs. 58c and 58d (77°C) and Figs. 65c and 65d (132°C) indicates that the interfacial bond is not degraded at either of the elevated temperatures. The matrix drawing or fibrils in Figs. 58c and 58d are similar to those observed in the mode I fracture surfaces in Figs. 43a, 45a, and 46b; the shearing deformation of the matrix in Fig. 58a is similar to that observed on the mode II fracture surfaces in Figs. 50a and 50b.

However, the bare fibers in the micrographs in Figs. 62 indicate poor

fiber/matrix adhesion for the AU4U/PEEK material. These micrographs correlate with the fracture surface results in Figs. 43b, 43d, 46c, 46d, 50c, and 50d. Bare fibers with little resin deformation are characteristic of all of these figures.

The ϵ_I data in Fig. 61 indicates a 27% decrease in ϵ_I at 21°C caused by the poor fiber/matrix interfacial bond. This decrease is smaller than expected. Based on the fractography previously discussed and the 50% and 54% reductions in G_I and G_{II} , respectively, one would expect the fiber microbuckling initiation strains to be reduced more than 27%. At 77°C, ϵ_I is reduced by only $\approx 5\%$. This reduction in ϵ_I is smaller than that at 21°C because of the reduced resin yield strain at 77°C.

Comparison of the previously mentioned SEM micrograph results with the ϵ_I data in Fig. 61 leads to Fig. 86. This figure is a schematic representation of ϵ_I as a function of temperature for fiber microbuckling initiation by either yielding of the matrix or failure of the interfacial bond. The circled curve intersections indicate failures. Figure 86 shows that for the APC-2 material, fiber microbuckling initiation is controlled by the shear yield strain of the matrix. However, fiber microbuckling initiation for the AU4U/PEEK material is controlled by failure at the fiber/matrix interface. Thus, the softer resins do not need fiber/matrix interfacial bond strengths as high as those required for stiffer resins. The reduction in ϵ_I at 77°C is smaller than that at 21°C because resin yielding is easier at 77°C. Bascom and Jensen¹⁷¹ showed with birefringence patterns that materials with poor fiber/matrix interfacial strengths may have interfacial bonds sufficient for elastic deformation of the resin but too low to cause shear yielding of the resin. The higher ϵ_I may be attributed to the accommodation of more elastic deformation of the resin at 77°C than at 21°C. The micrographs in Figs. 58 and 62 (previously described) support this result.

The effects of resin-rich regions adjacent to 0° plies on fiber microbuckling



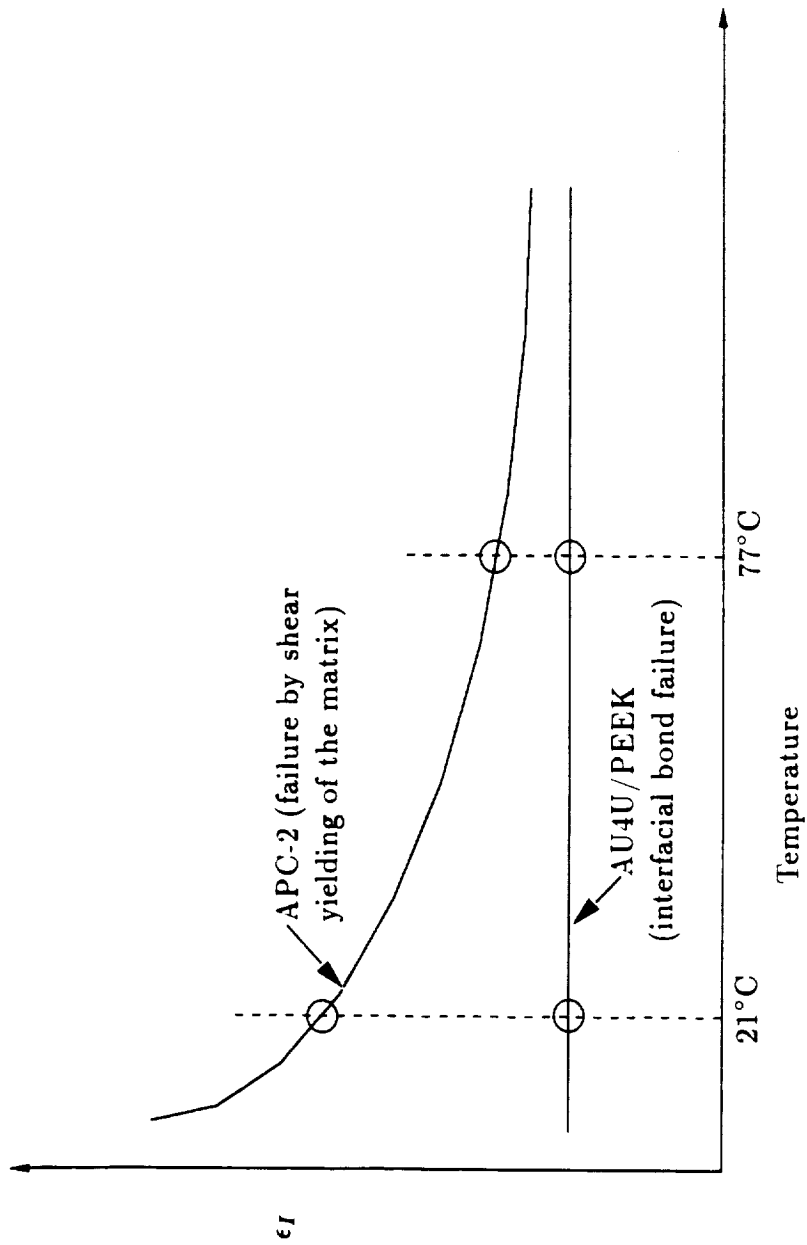


Fig. 86 Schematic of variation in ϵ_l as a function of temperature for failure by exceeding the matrix yield strain or the fiber/matrix interfacial bond strength.

initiation are presented in Figs. 63 and 64. The ϵ_I data in Fig. 63 indicates that at 21°C, the resistance to fiber microbuckling initiation is decreased as the resin volume is increased. However, at 77°C, a slight monotonic increase (within scatter) in ϵ_I is observed as the resin-rich regions are increased. A schematic representation of this trend is shown in Fig. 87. The circled curve intersections represent fiber microbuckling failures. For a given temperature, the resistance to fiber microbuckling decreases as the resin volume is increased. Additionally, for a given resin volume, the resistance to fiber microbuckling initiation decreases as the temperature is increased. However, when both resin volume and temperature change at the same time, the trend may not be determined because of the effects of each variable may not be separated. No conclusions are made about the 77°C data. The micrographs in Fig. 64 show that some 0° fibers near the ply boundary buckle out-of-plane into the adjacent resin layers, although the primary mode of buckling is in-plane into the notch.

Observation of the fiber microbuckling initiation strain, ϵ_I , results in Figs. 54, 55, 56, 59, 61, and 63 indicates that, in general, reducing the resin shear stress and strain associated with the yield point on the $\tau_m-\gamma_m$ curve reduces the resistance to fiber microbuckling. However, two exceptions were the AU4U/PEEK material and the $[(\pm 45/f_3/0_2/f_3)_3/\pm 45/f_3/0]_s$ stacking sequence. It is believed that the weak interface of the AU4U/PEEK material, rather than the reduced yield point on the $\tau_m-\gamma_m$ curve, controlled its failures at both 21°C and 77°C. However, no explanation is offered for the increase in ϵ_I at 77°C for the $[(\pm 45/f_3/0_2/f_3)_3/\pm 45/f_3/0]_s$ laminates.

Although the 21°C local ϵ_I strains, 2.13–2.49%, reported in Fig. 55 seem high, they are comparable in magnitude with fiber failure strains reported in

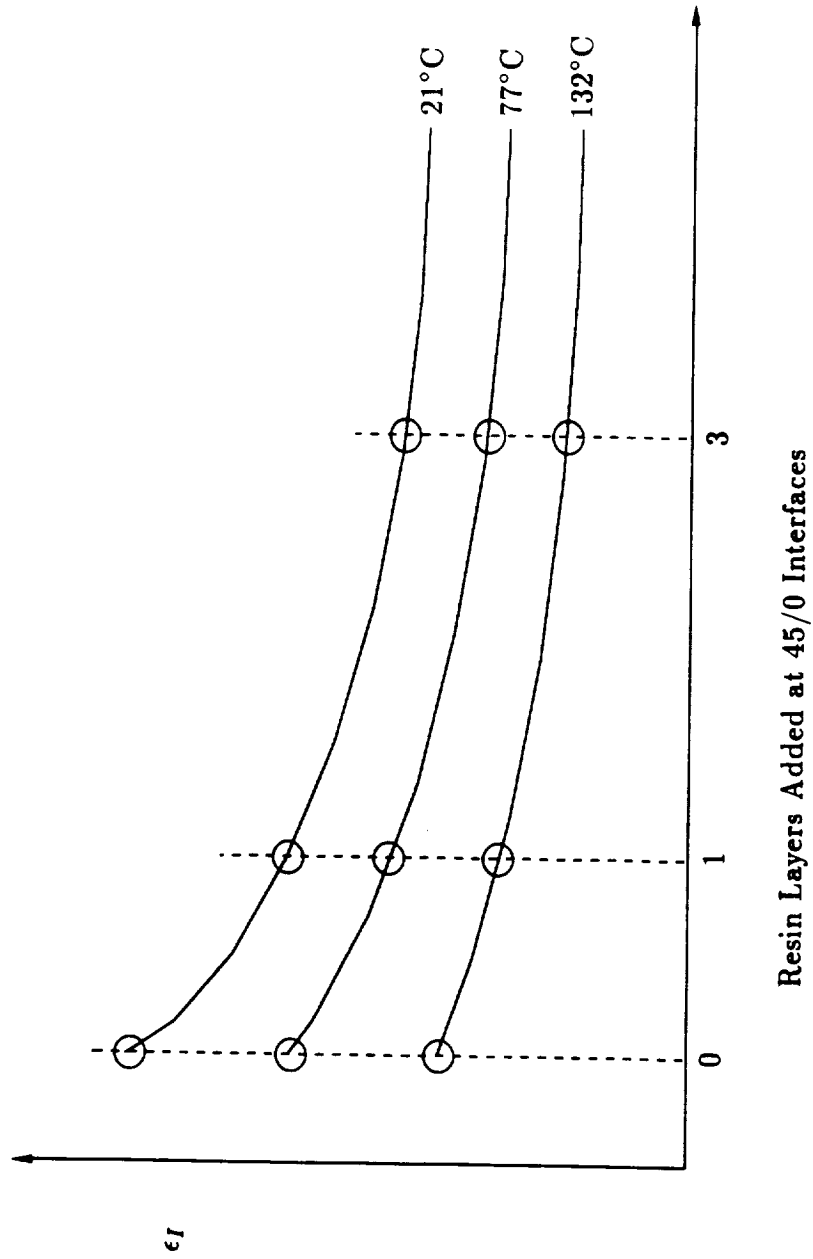


Fig. 87 Schematic of ϵ_I as a function of temperature for laminates with built-in resin-rich regions.



Refs. 168 (1.5% for fiber tensile failure) and 169 (3.6% for fiber shear failure, under compressive load). Observation of the relatively few broken fibers in Fig. 65 indicates that AS4 fibers can withstand relatively large (probably greater than at least 3%) strains when loaded in bending. Figure 88 is a graph of results from Ref. 112. This figure plots failure strain as a function of $\frac{a_o}{w}$ (ratio of hole diameter to specimen width) for T300/5208 laminates. The stacking sequence is $[\pm 45/0_2/\pm 45/0_2/\pm 45/0/90]_{2s}$. Assuming a strain concentration factor of ≈ 3 for this data indicates that for small $\frac{a_o}{w}$ ratios, the failure strain is on the order of 2.5%. One possible reason is posed for these high local strains. It appears that local softening at the notch may allow more deformation of the fibers and matrix (seen in the APC-2 micrographs) leading to higher strains. The large amount of elastic deformation seen through the stereomicroscope (described in Chapter V) supports this theory. However, the finite element analysis for the SCFs is linear elastic. If local softening occurs at the notch, the SCFs are over predicted. The combination of the local softening and the overpredicted SCFs cause the actual local strains at the notch to be overestimated. Additionally, the linear elastic analysis in Ref. 66 shows that a model of an array of 0° fibers and matrix subjected to the stress distribution in the neighborhood of a hole (for a multidirectional laminate) has a fiber microbuckling initiation strength that is 1.79 (lay-up dependent) times its unidirectional strength.

The notch view micrographs presented in Figs. 57, 60, and 64 and observations of numerous buckled 0° plies (not included in this dissertation) indicate that the notch radius dictates the unsupported fiber length at the notch free surface. This length in conjunction with the local fiber waviness along the unsupported notch free surface is believed to be the critical fiber waviness parameter that affects

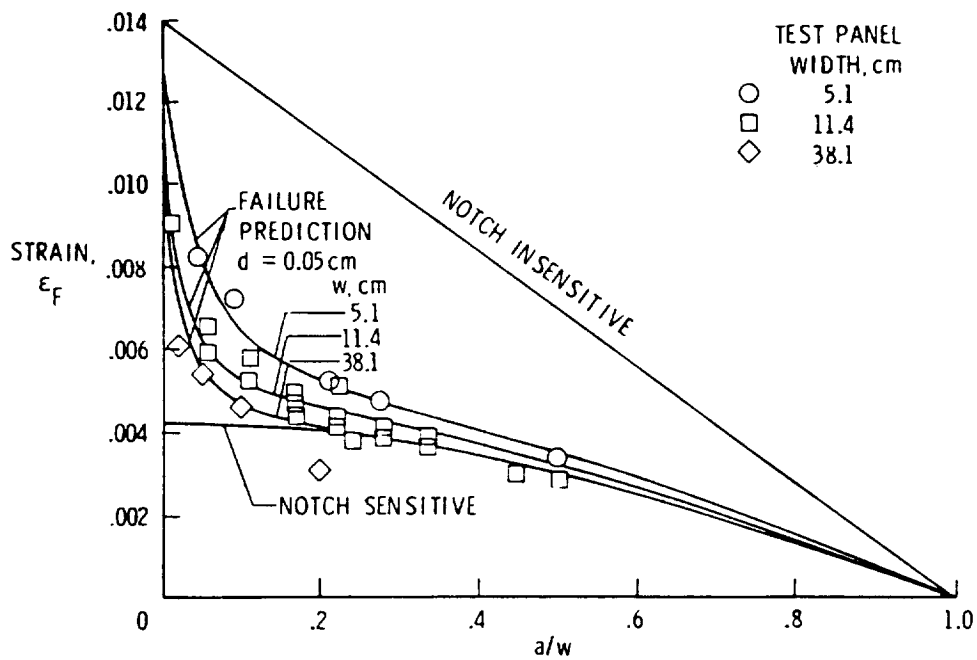


Fig. 88 Failure strain of T300/5208 $[\pm 45/0_2/\pm 45/0_2/\pm 45/0/90]_{2s}$ laminates as a function of hole size. Laminates contain center holes.¹¹²

fiber microbuckling initiation in these notched laminates. It is believed that as the notch radius increases, the consequent decrease in notch curvature increases the unsupported length of the fiber and causes decreases in the fiber microbuckling initiation strains (longer columns buckle with greater ease than shorter columns). In the limit, the unsupported surface of the notch approaches that of a free edge. Initial fiber waviness becomes important when its wavelength is either smaller than the length of the unsupported column in the notch root or perfectly centered along the notch root. The initiations seen slightly above or below the notch root centerline may have been caused by the location of column wavelength. However, data is not conclusive.

Finite Element Results

The Straight Fiber Problem

A comparison of the infinite and semi-infinite models in Case 1S indicates that the free surface effect causes a 10% reduction in the critical buckling strain.

Additionally, within Case 1S, the critical buckling strains for the finite plate (15300 $\mu\epsilon$) and the infinite series (20000 $\mu\epsilon$) indicate that ten fibers embedded in matrix do not imply an infinitely wide plate. However, the critical buckling strains in Case 1S for the infinite and semi-infinite plates are 10%-39% more conservative and thus, more realistic than the infinite series of fibers and matrix.

The finite plate is modelled with transversely isotropic fiber properties (Case 1S) and two types of isotropic fiber properties (Cases 2S and 3S) to illustrate the sensitivity of the critical buckling strains to Young's modulus of the fibers. This ten fiber model is similar to that of Rosen,³³ and thus the results may be compared with Eqn. 2 where $\epsilon_{cr} \propto \frac{\sigma_c}{E_f}$. Since the second term (Euler term for the fiber) of



Eqn. 2 is only geometry dependent, the critical strain depends on the ratio $\frac{G_m}{E_f}$ in the first term of Eqn. 2. As $\frac{G_m}{E_f}$ increases, the critical buckling strain also increases. The ratios of $\frac{G_m}{E_f}$ are 0.0153, 0.0153, and 0.0536 (see Table VIII) for Cases 1S, 2S, and 3S respectively. The trends presented for these cases are consistent with Rosen's equation. The small increase (7.2%) in the critical buckling strain between the Case 1S and Case 2S finite plates ($\frac{G_m}{E_f} = \text{constant}$) is attributed to the higher shear modulus (increased by 250%) for the Type A isotropic fiber.

Similar comparisons for the semi-infinite plate (Cases 1S and 4S) and the infinite series model (Cases 1S and 5S) also indicate that as $\frac{G_m}{E_f}$ is increased, the critical buckling strains increase. In the semi-infinite plate, both $\frac{G_m}{E_c}$ and $\frac{G_m}{E_f}$ are increased, and the critical buckling strain increases by a factor of ≈ 3.0 . In the infinite series, the critical buckling strain increases by a factor of ≈ 3.7 .

The Wavy Fiber Problem

From the results presented in Figs. 66–73, it is obvious that the matrix constitutive behavior significantly affects the fiber microbuckling initiation strain levels in models with an initial fiber curvature. When the matrix is linear, geometric nonlinearity becomes important. With an initial waviness, reducing the shear strain associated with the yield point on the $\tau_m - \gamma_m$ curve (Fig. 40) causes significant reductions in the fiber microbuckling initiation strain levels. The combination of the resin nonlinear constitutive behavior and initial fiber curvature cause a nonlinear global response of the model.

Energy analysis (Figs. 71–73) and fringe plots (Figs. 68–70) show that the axial and shear strains dominate the matrix strain energy (composing 90% of the total matrix strain energy), and the axial strain dominates the fiber strain energy. The transverse strain contribution to the matrix strain energy is small, and the

transverse and shear strain contributions to the fiber strain energy are negligible. However, the axial and shear components of the matrix strain energy are functions of the applied load. This dependence is attributed to additional waviness induced by the additional compressive loading. The transverse component of the matrix strain energy and all components of the fiber strain energy are independent of the applied load. These results indicate that an energy analysis of the problem should consider the axial and shear components of the matrix strain energy and the axial component of the fiber strain energy. Additional accuracy may be obtained by including the contribution of the transverse component of strain energy in the matrix. Furthermore, since the axial and shear components of the matrix strain energy are functions of the applied displacement (and thus, increased waviness), these components must also be functions of the initial fiber curvature. As the initial fiber curvature, $\frac{a_0}{L}$, increases, the shear component of the matrix strain energy increases while the axial contribution decreases. However, the total of these two components consistently makes up 90% of the total matrix energy. With sufficiently large initial curvatures, the shear component would dominate the matrix strain energy, and the axial component would become negligible.

The combination of nonlinear matrix constitutive behavior and initial fiber curvature causes significant reductions in the fiber microbuckling initiation strain levels, particularly when compared to the straight fiber model. These two factors cause nonlinear global stress-strain responses of the models (Figs. 66 and 75). Furthermore, it was shown that, for a given applied axial strain, increasing the initial fiber curvature or decreasing the resin yield strength causes a large increase in the rate and amount of shear strain developed in the matrix (Figs. 67 and 76). The fiber microbuckling initiation strains (Figs. 66 and 75) correlate well with the



applied strains associated with the asymptotic local shear strains in Figs. 67 and 76. It appears that each of these factors, or some combination of them causes the localized shear strains to exceed the resin yield strain leading to premature fiber microbuckling initiation.

Introducing an interfacial debond (Figs. 77-80) causes further reductions (in addition to matrix nonlinearity and fiber waviness) in the strains for fiber microbuckling initiation. Both the length and location of the debond influence the strain reductions, but their individual contributions cannot be distinguished. The most detrimental debond location is along the maximum shear region of the model. This debond reduces the support provided for the fiber, reduces the shear stress transfer between the fiber and matrix, and causes localized shear strain concentrations within the maximum shear region of the matrix. These strain concentrations will also cause the localized shear strains to prematurely exceed the resin yield strain leading to lower fiber microbuckling initiation strains.

Results from the semi-infinite plate (Tables XI, XII and Figs. 74, 81-83) show that the introduction of fiber waviness at the free surface causes $\approx 90\%$ reduction in the fiber microbuckling initiation strain. Because of the geometric conditions, observation of the local shear strain in the matrix does not indicate the presence of a free surface effect. However, the deformed shapes and behavior of the finite element analysis (Fig. 74) indicate that the fibers near the free surface buckled prematurely at $38269 \mu\epsilon$ prior to column buckling at $42231 \mu\epsilon$.

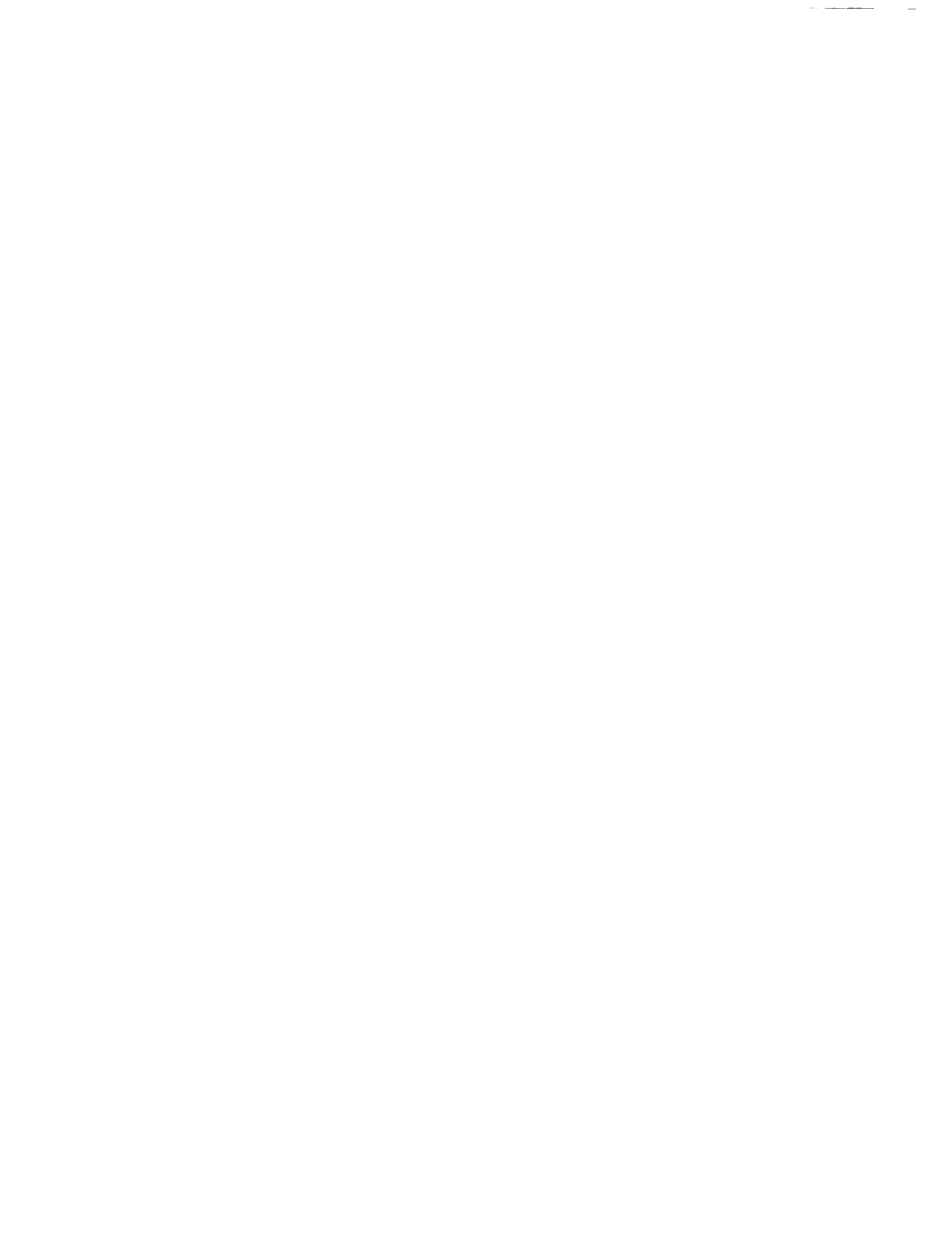
It was established in the literature review in Chapter II that fiber tensile modulus is not a particularly significant variable in the determination of the compressive strength of composite laminates. The fiber tensile modulus appears explicitly in Eqns. 1, 2, 7, 13-17, 24, and 25, which give the compressive strength

for fiber microbuckling failures. The fiber shear modulus is explicit in Eqns. 5, 11, and 12 which also predict the compressive strength for fiber microbuckling failures. However, the contribution of the fiber modulus to the calculated compressive strength in each case is small, unless the fiber shear modulus is the same order of magnitude as the matrix shear modulus and/or the microbuckling wavelength is less than or equal to ten times the fiber diameter.

The shear instability analyses in Refs. 33, 34, 36, 126–128 show that the resistance to fiber microbuckling failure is controlled by shear properties of the foundation. The results of Hayashi³⁴ and Kulkarni et al.,⁴⁸ analyses that neglect $\frac{G_m}{G_f}$, indicate that as G_f is increased, the compressive strength of the composite is increased. In the straight fiber discussion within this chapter it was shown that $\epsilon_{cr} \propto \frac{\sigma_c}{E_f}$ in Rosen's³³ analysis. The finite plate straight fiber model (Fig. 32c and Table XI) is similar to Rosen's model and follows the same trend with E_f . However, the results in Figs. 84 and 85 show that initially wavy models are also sensitive to E_f . It is apparent from the combination of previous analyses and this analysis that the global response and ϵ_f of the composite model are influenced by E_f , although the compressive strength is not influenced. The accuracy of the predictions by this analysis should be significantly improved by including fiber anisotropy in the wavy fiber models, allowing the actual G_f , E_f , and ν_f to be model inputs.

A Comparison of Experimental and Finite Element Results

The finite element models of fiber microbuckling in this investigation are two-dimensional and neglect any additional resistance provided by adjacent supporting plies. Although these models contain the resin constitutive behavior measured experimentally, the initial fiber waviness ratios are assumed arbitrarily. Additionally,



isotropic fibers are assumed. Thus, direct comparisons between the finite element analysis and the experimental results are not possible. However, the experimental and finite element reductions may be compared. In general, the comparisons are very encouraging. It is considered fortuitous that some of the experimental results and finite element predictions coincide.

The experimental results in Figs. 54 and 59 indicate that the fiber microbuckling initiation strain, ϵ_I , is reduced by an average of $\approx 18.6\%$ (range is 6.3–38.6%) as the temperature is increased from 21°C to 77°C. The finite element results in Fig. 66 predict that for an arbitrary fiber waviness of $\frac{a_e}{L} = 0.0050$, ϵ_I is reduced 17.8% as the temperature is increased from 21°C to 77°C.

Comparison of the experimental results in Fig. 42 (in-plane fiber waviness ratio on the order of 0.0050) and the local fiber microbuckling initiation strains in Fig. 55 with the finite element predictions at 21°C and 77°C in Fig. 66, indicates that the two-dimensional finite element predictions for fiber microbuckling initiation are within 10% of the experimentally determined ϵ_I .

The experimental results (Fig. 56) indicate a 10% reduction in ϵ_I caused by the reduced lateral support of the 0₂ plies at the free surface. Finite element analysis of the straight fiber model (Table XI, Figs. 32a and 32b) and the wavy fiber model (Figs. 74, 82, and 83) indicates 10% and 9.4% reductions, respectively, caused by the free surface.

The experimental results in Fig. 61 indicate that ϵ_I for the AU4U/PEEK is reduced 27.0%, compared to APC-2, at 21°C. This reduction is caused by the reduction in the fiber/matrix interfacial bond strength. The 21°C finite element results in Figs. 77 and 78 show that a debond (10.7% of the column length) in the region of maximum lateral deflection causes no reduction in ϵ_I . However, when the

same debond is moved to the region of maximum shear (Fig. 79), ϵ_I is reduced 46.8%. When the original debond, in the region of maximum lateral deflection, is allowed to extend from 10.7% to 25.0% to 50.0% of the column length, ϵ_I is reduced by 69.4% and 90.4%, respectively. These increases are attributed to both debond length and location. The finite element analysis predicts reductions significantly larger than those observed experimentally. However, the finite element analysis consists of a repeating unit cell to make an infinite array of fibers and matrix. Thus, the included debond in the repeating unit implies that every fiber is debonded from the matrix in the critical region. Additionally, the debonded region in the finite element analysis is completely debonded. In reality, when the fiber/matrix interfacial bond strength is reduced, the strength along the fibers is not uniform, and typically, the fibers are not completely debonded from the matrix, at least not every fiber.

CHAPTER VIII

CONCLUSIONS AND RECOMMENDATIONS

The conclusions and subsequent recommendations for future work are summarized in this chapter.

Conclusions

From the observations in the research, a controlling failure mechanism for compression strength of notched composites is postulated as follows. Fiber microbuckling initiation in these notched laminates controls failure and thus, the notched compressive strength. The notch radius dictates the unsupported fiber length (and the associated length to diameter ratio) at the notch. As the notch radius increases, the unsupported fiber length increases, and the fiber microbuckling initiation strains decrease. The notch radius in conjunction with the local fiber waviness at the notch is the critical fiber waviness parameter that affects fiber microbuckling initiation in these notched laminates. In the limit, the notch radius approaches infinity, and the notch root approaches a laminate free edge. In this case, the waviness parameter that affects the resistance to fiber microbuckling initiation is the amount of initial fiber waviness and the critical fiber wavelength along this free edge.

The following conclusions may be drawn from this work.

1. Increasing the test temperature reduces the shear stresses and strains associated with the yield point on the τ - γ curve. This reduction in the resin yield strain causes a reduction in the fiber microbuckling initiation strains. From 21°C to 77°C, average reductions are 18.6% (experimental) and 17.8% (finite element analysis).

2. When laminate orthotropy is considered, the measured local fiber microbuckling initiation strain, ϵ_I , is a constant ($\approx 2.3\%$) at 21°C for this material and geometry. At 77°C , ϵ_I is two constants, $\approx 2.0\%$ and $\approx 1.5\%$, for laminates with supporting ply orientations $\theta \leq 45^\circ$ and $\theta \geq 75^\circ$, respectively.
3. Experimental results and finite element analyses both indicate $\approx 10\%$ reduction in ϵ_I when 0° plies are located at the free surface.
4. Finite element analysis showed that increasing the initial fiber waviness significantly reduces the resistance to fiber microbuckling initiation. Larger amplitudes of the initial fiber wavinesses cause significant increases in the localized matrix shear strains. These increases cause the shear strains to prematurely exceed the resin yield strain and lead to premature fiber microbuckling initiation.
5. Experimental results showed that at 21°C , reducing the quality of the fiber/matrix interfacial bond reduces the resistance to fiber microbuckling initiation. Although the interfacial bond strength controls the resistance to fiber microbuckling initiation at 77°C , the apparent reduction is smaller because of the simultaneous reduction, attributed to the resin nonlinear shear constitutive behavior, in ϵ_I for APC-2. Finite element analysis showed that debonds cause significant increases in the localized matrix shear strains. These increases cause the shear strains to prematurely exceed the resin yield strain and lead to premature fiber microbuckling initiation. The critical debond location was shown to be in the region of maximum shear strain.
6. Experimental results indicate that the addition of resin-rich regions between plies reduces the resistance to fiber microbuckling initiation. These resin-rich regions between adjacent off-axis plies and the 0° plies allow some 0° fibers

near the interfaces to buckle out-of-plane into the adjacent resin-rich regions.

Recommendations for Future Work

Based on the conclusions from this work, the following recommendations for future work are suggested.

Experimental

1. Conduct additional tests at 21°C and 77°C for this series of tests to strengthen the confidence of each of the averages and trends presented.
2. Conduct the same series of tests at 104°C to provide the trends of each variable over three, rather than two, temperatures.
3. Determine the elastic lamina constants at 77°C so that the SCFs at 77°C may be more accurately predicted. Then, use the corrected SCFs to determine the local ϵ_I (consider effects of orthotropy) at 77°C for the laminates used to evaluate the effects of supporting ply orientation on fiber microbuckling initiation.

Finite Element Analysis

1. Include fiber orthotropy (assume transversely isotropic) in the wavy fiber analyses so that the actual fiber properties may be implemented. This improvement allows direct comparison of the straight and wavy fiber models and provides more realistic ϵ_I values and γ_{xy} development.
2. Repeat the comparisons with the correct fiber waviness and orthotropy to improve the accuracy of the results. Finite element analysis and experimental data are now a direct comparison.

3. With the correct fiber waviness and anisotropy, run a series of models with different matrix widths to show the effects of resin-rich regions.
4. Use finite element analysis, including material nonlinearity, to determine the SCFs for the laminates tested. Additionally, determine the strain distribution near the notches.

Future Project

1. Test one multidirectional stacking sequence with varying $\frac{a}{w}$ ratios. Vary both a and w systematically to verify that the notch radius controls the unsupported length (or associated length to diameter ratio) of the fiber microbuckling column and thus, the initiation of fiber microbuckling.
2. Create a finite element model with a finite number of fibers. Apply the strain distribution from the notched (SCF) analysis, rather than a uniform strain distribution, to this model. Model different initial fiber lengths to correspond to the unsupported fiber lengths measured from the different experimental hole diameters.
3. Compare finite element predictions with experimental data.

REFERENCES

- ¹ Guynn, E.G., "Micromechanics of Compressive Failures in Open Hole Composite Laminates," Department of Mechanical Engineering, Texas A&M University, M.S. Thesis, December 1987.
- ² Guynn, E.G., Bradley, W.L., and Elber, W., "Micromechanics of Compression Failures in Open Hole Composite Laminates," in *Second Symposium on Composite Materials: Fatigue and Fracture, ASTM STP 1012*. Philadelphia, PA: American Society for Testing and Materials, 1989, pp. 118-136.
- ³ Guynn, E.G. and Bradley, W.L., "Measurements of the Stress Supported by the Crush Zone in Open Hole Composite Laminates Loaded in Compression," *Journal of Reinforced Plastics and Composites*, Vol. 8, March 1989, pp. 133-149.
- ⁴ Guynn, E.G. and Bradley, W.L., "A Detailed Investigation of the Micromechanisms of Compressive Failure in Open Hole Composite Laminates," *Journal of Composite Materials*, Vol. 23, May 1989, pp. 479-504.
- ⁵ Leonard, L., "Compression Test Results — A Tough Nut to Crack," *Advanced Composites*, July/August 1989, pp. 57-63.
- ⁶ Clark, R.K. and Lisagor, W.B., "Compression Testing of Graphite/Epoxy Composite Materials," in *Test Methods and Design Allowables for Fibrous Composites, ASTM STP 734*. C.C. Chamis, ED., Philadelphia, PA: American Society for Testing and Materials, 1981, pp. 34-53.
- ⁷ Anon., "D695-85 Standard Test Method for Compressive Properties of Rigid Plastics," in *1985 Annual Book of ASTM Standards*. Philadelphia, PA: American Society for Testing and Materials, 1985, pp. 267-274.
- ⁸ Anon., "D3410-75 (Reapproved 1982) Standard Test Method for Compressive Properties of Unidirectional or Crossply Fiber-Resin Composites," in *1982 Annual Book of ASTM Standards*. Philadelphia, PA: American Society for Testing and Materials, 1982, pp. 872-880.
- ⁹ Anon., "C393-62 (Reapproved 1970) Standard Test Method of Flexure Test of Flat Sandwich Constructions," in *1962 Annual Book of ASTM Standards*. Philadelphia, PA: American Society for Testing and Materials, 1962, pp. 313-316.
- ¹⁰ Anon., "D3410-87 Standard Test Method for Compressive Properties of Unidirectional or Crossply Fiber-Resin Composites," in *1987 Annual Book of ASTM Standards*. Philadelphia, PA: American Society for Testing and Materials, 1987, pp. 2573-2585.

- ¹¹ Shuart, M.J., "An Evaluation of the Sandwich Beam Compression Test Method for Composites," in *Test Methods and Design Allowables for Fibrous Composites*, ASTM STP 734. C.C. Chamis, ED., Philadelphia, PA: American Society for Testing and Materials, 1981, pp. 34-53.
- ¹² Hofer, K.E., Jr. and Rao, P.N., "A New Static Compression Fixture for Advanced Composite Materials," *Journal of Testing and Evaluation*, Vol. 5, No. 4, July 1977, pp. 278-283.
- ¹³ Camarda, C.J., "Application of the IITRI Compression Test Fixture at Elevated Temperature," NASA Langley Research Center, Hampton, VA, NASA Conference Publication 2079, March 1979.
- ¹⁴ Woolstencroft, D.H., Curtis A.R., and Haresceugh, R.I., "A Comparison of Test Techniques Used for the Evaluation of the Unidirectional Compressive Strength of Carbon Fibre-Reinforced Plastic," *Composites*, October 1981, pp. 275-280.
- ¹⁵ Gurdal, Z. and Starbuck, J.M., "Compressive Characterization of Unidirectional Composite Materials," in *Analytical and Testing Methodologies for Design with Advanced Materials*. G.C. Sih, J.T. Pindera, and S.V. Hoa, EDS., Elsevier Science Publishers B.V., 1988, pp. 337-347.
- ¹⁶ Adsit, N.R., "Compression Testing of Graphite/Epoxy," in *Compression Testing of Homogeneous Materials and Composites*, ASTM STP 808. R. Chait and R. Papirno, ED., Philadelphia, PA: American Society for Testing and Materials, 1983, pp. 175-186.
- ¹⁷ Ryder, J.T. and Black, E.D., "Compression Testing of Large Gage Composite Coupons," in *Composite Materials: Testing and Design (Fourth Conference)*, ASTM STP 617. Philadelphia, PA: American Society for Testing and Materials, 1977, pp. 170-189.
- ¹⁸ Chan, W., private communications, November 1987.
- ¹⁹ Lamothe, R.M. and Nunes, J., "Evaluation of Fixturing for Compression Testing of Metal Matrix and Polymer/Epoxy Composites," in *Compression Testing of Homogeneous Materials and Composites*, ASTM STP 808. R. Chait and R. Papirno, ED., Philadelphia, PA: American Society for Testing and Materials, 1983, pp. 241-253.
- ²⁰ Chou, T., Stewart, W.B., and Bader, M.G., "On the Compression Strength of Glass-Epoxy Composites," *New Developments and Applications in Composites*, TMS-AIME Publication, 1979, pp. 331-346.
- ²¹ Zhigun, I.G., Polyakov, V.A., and Mikhailov, V.V., "Compression Testing of Composites," Institute of Polymer Mechanics, Academy of Sciences of the Latvian SSR, Riga. Translated from *Mekhanika Kompozitnykh Materialov*, No. 6, pp. 1111-1118, November-December 1979. Original article submitted May 7, 1979.

²² Rehfield, L.W., Armanios, E.A., and Changli, Q., "Analysis of Behavior of Fibrous Composite Compression Specimens," in *Recent Advances in Composites in the United States and Japan*, ASTM STP 864. J.R. Vinson and M. Taya, ED., Philadelphia, PA: American Society for Testing and Materials, 1985, pp. 236-252.

²³ Hahn, H.T. and Williams, J.G., "Compression Failure Mechanisms in Unidirectional Composites," in *Composite Materials: Testing and Design (Seventh Conference, ASTM STP 893)*. J.M. Whitney, ED., Philadelphia, PA: American Society for Testing and Materials, 1986, pp. 115-139.

²⁴ Agarwal, B.D. and Broutman, L.J., *Analysis and Performance of Fiber Composites*, First Edition, New York, NY: John Wiley & Sons, 1980, pp. 48-57.

²⁵ Ewins, P.D. and Ham, A.C., "The Nature of Compressive Failure in Unidirectional Carbon Fibre Reinforced Plastics," *AIAA/ASME/SAE 15th Structures, Structural Dynamics and Materials Conference*, Las Vegas, NE, April 1974.

²⁶ Greszczuk, L.B., "Compressive Strength and Failure Modes of Unidirectional Composites," in *Analysis of the Test Methods for High Modulus Fibers and Composites*, ASTM STP 521. Philadelphia, PA: American Society for Testing and Materials, 1973, pp. 192-217.

²⁷ Tsai, S.W., "Strength Theories of Filamentary Structures," in *Fundamental Aspects of Fiber Reinforced Plastics*. R.T. Schwartz and H.S. Schwartz, EDS., New York, NY: Interscience Publishers (a division of John Wiley & Sons), 1968, pp. 3-11.

²⁸ Shuart, M.J., "Short-Wavelength Buckling and Shear Failures for Compression-Loaded Composite Laminates," NASA Langley Research Center, Hampton, VA, NASA Technical Memorandum 87640, November 1985.

²⁹ Camponeschi, E.T., Jr., "Compression of Composite Materials: A Review," Center for Composite Materials, University of Delaware, CCM 87-40, August 1987.

³⁰ Piggott, M.R., "Compressive Properties of Resins and Composites," in *Developments in Reinforced Plastics*. G. Pritchard, ED., New York, NY: Elsevier Applied Science Publishers, 1985, pp. 131-163.

³¹ Dow, N.F. and Gruntfest, I.J., "Determination of Most Needed Potentially Possible Improvements in Materials for Ballistic and Space Vehicles," General Electric, TIS 60SD389, June 1960.

³² Timoshenko, S.P. and Gere, J.M., *Theory of Elastic Stability*, Second Edition, New York, NY: McGraw-Hill Book Company, 1961.

³³ Rosen, B.W., "Mechanics of Composite Strengthening," Fiber Composite Materials, American Society for Metals Seminar, 1965, pp. 37-75.



³⁴ Hayashi, T., "On the Shear Instability of Structures Caused by Compressive Load," presented at the AIAA/RAES/JSAS Aircraft Design and Technology Meeting, Los Angeles, CA, November 1965, pp. AIAA Paper No. 65-770.

³⁵ Jones, R.M., *Mechanics of Composite Materials*, First Edition, New York, NY: M^cGraw-Hill Book Company, 1975.

³⁶ Schuerch, H., "Prediction of Compressive Strength in Uniaxial Boron Fiber-Metal Matrix Composite Materials," *AIAA Journal*, Vol. 4, January 1966, pp. 102-106.

³⁷ Dow, N.F., Rosen, B.W., and Hashin, Z., "Studies of Mechanics of Filamentary Composites," NASA Langley Research Center, Hampton, VA, NASA Contractor Report 492, June 1966.

³⁸ Foye, R.L., "Compression Strength of Unidirectional Composites," presented at the AIAA 3rd Aerospace Sciences Meeting, New York, NY, November 1966, pp. AIAA Paper No. 66-143.

³⁹ Sadowsky, M.A., Pu, S.L., and Hussain, M.A., "Buckling of Microfibers," *Journal of Applied Mechanics*, December 1967, pp. 1011-1016.

⁴⁰ Lager, J.R. and June, R.R., "Compressive Strength of Boron-Epoxy Composites," *Journal of Composite Materials*, Vol. 3, January 1969, pp. 48-56.

⁴¹ Chung, W.Y. and Testa, R.B., "The Elastic Stability of Fibers in a Composite Plate," *Journal of Composite Materials*, Vol. 3, January 1969, pp. 58-80.

⁴² Biot, M.A., *Mechanics of Incremental Deformation*, First Edition, New York, NY: John Wiley & Sons, 1965, pp. 227-259.

⁴³ Guz, O.M., "Determination of the Theoretical Compression Strength of Reinforced Materials," NASA Technical Translation F-13,443, Translated from "Pro Vyznachennia Teoretichnoi Granitsi Mitsnosti Na Stisk armovanikh Nauk Ukrayns'koy RSR, Servia, Fiziko-Technichni i Matematichni Nauki, Vol. 31, March 1969, pp. 236-238.

⁴⁴ Hayashi, T., "Compressive Strength of Unidirectionally Fiber Reinforced Composite Materials," 7th *International Reinforced Plastics Conference*, British Plastics Federation, Brighton England, Vol. 1970, 11, pp. 1-3.

⁴⁵ Lanir, Y. and Fung, Y.C.B., "Fiber Composite Columns Under Compression," *Journal of Composite Materials*, Vol. 6, July 1972, pp. 387-401.

⁴⁶ Suarez, J.A., Whiteside, J.B., and Hadcock, R.N., "The Influence of Local Failure Modes on the Compressive Strength of Boron/Epoxy Composites," in *Composite Materials: Testing and Design (Second Conference)*, ASTM STP 497. Philadelphia, PA: American Society for Testing and Materials, 1972, pp. 237-256.

- ⁴⁷ Hayashi, I. and Fujikake, M., "Compressive Strength of Unidirectionally Fiber Reinforced Composite Materials," presented at the 18th Japan Congress on Materials Research — Non Metallic Materials, Japan, March 1975, pp. 141-147.
- ⁴⁸ Kulkarni, S.V., Rice, J.S., and Rosen, B.W., "An Investigation of the Compressive Strength of Kevlar 49/Epoxy Composites," *Composites*, Vol. 6, 1975, pp. 217-225.
- ⁴⁹ Greszczuk, L.B., "Interfiber Stresses in Filamentary Composites," *AIAA Journal*, Vol. 9, July 1971, pp. 1274-1280.
- ⁵⁰ Greszczuk, L.B., "Microbuckling of Lamina-Reinforced Composites," in *Composite Materials: Testing and Design (Third Conference)*, ASTM STP 546. Philadelphia, PA: American Society for Testing and Materials, 1974, pp. 5-29.
- ⁵¹ Greszczuk, L.B., "Prediction of Transverse Strength and Scatter in Test Data for Unidirectional Composites," in *Composite Reliability*, ASTM STP 580. Philadelphia, PA: American Society for Testing and Materials, 1975, pp. 311-326.
- ⁵² Greszczuk, L.B., "Microbuckling Failure of Circular Fiber-Reinforced Composites," *AIAA Journal*, Vol. 13, October 1975, pp. 1311-1318.
- ⁵³ Greszczuk, L.B., "On Failure Modes of Unidirectional Composites Under Compressive Loading," in *Proceedings of 2nd USA-USSR Symposium on Fracture of Composite Materials*. G.C. Sih and U.P. Tamuze, EDS., Boston, MA: Martinus Nijhoff Publishers, 1982, pp. 231-244.
- ⁵⁴ Piggott, M.R. and Harris, B., "Compression Strength of Carbon, Glass and Kevlar-49 Fibre Reinforced Polyester Resins," *Journal of Materials Science*, Vol. 15, 1980, pp. 2523-2538.
- ⁵⁵ Piggott, M.R. and Wilde, P., "Compressive Strength of Aligned Steel Reinforced Epoxy Resin," *Journal of Materials Science*, Vol. 15, 1980, pp. 2811-2815.
- ⁵⁶ Piggott, M.R. and Harris, B., "Compression Strength of Hybrid Fibre-Reinforced Plastics," *Journal of Materials Science*, Vol. 16, 1981, pp. 687-693.
- ⁵⁷ Martinez, G.M., Piggott, M.R., Bainbridge, D.M.R., and Harris, B., "The Compression Strength of Composites with Kinked, Misaligned and Poorly Adhering Fibres," *Journal of Materials Science*, Vol. 16, 1981, pp. 2831-2836.
- ⁵⁸ Piggott, M.R., "A Theoretical Framework for the Compressive Properties of Aligned Fibre Composites," *Journal of Materials Science*, Vol. 16, 1981, pp. 2837-2845.

⁵⁹ Guz, A.N., "Mechanics of Composite-Material Failure Under Axial Compression (Brittle Failure)," Institute of Mechanics, Academy of Sciences of the Ukrainian SSR, Kiev. Translated from *Prikladnaya Mekhanika*, Vol. 18, No. 10, October 1982, pp. 3-16.

⁶⁰ Gurdal, Z. and Haftka, R.T., "Compressive Failure Model for Anisotropic Plates with a Cutout," *AIAA Journal*, Vol. 25, November 1987, pp. 1476-1481.

⁶¹ Hanasaki, S. and Hasegawa, Y., "Compressive Strength of Unidirectional Fibrous Composites," *Journal of Composite Materials*, Vol. 8, July 1974, pp. 306-309.

⁶² Maewal, A., "Postbuckling Behavior of a Periodically Laminated Medium in Compression," *International Journal of Solids and Structures*, Vol. 17, 1981, pp. 335-344.

⁶³ Kurashige, M., "Compressive Strength of Fiber-Reinforced Materials," *Acta Mechanica*, Vol. 49, 1983, pp. 49-56.

⁶⁴ DeFerran, E.M. and Harris, B., "Compression Strength of Polyester Resin Reinforced with Steel Wires," *Journal of Composite Materials*, Vol. 4, 1970, pp. 62-72.

⁶⁵ Kurashige, M., "Compressive Strength of a Laminated Fiber-Reinforced Material," *Bulletin of Japanese Society of Mechanical Engineering*, Vol. 27, December 1984, pp. 2694-2697.

⁶⁶ Chang, F.K. and Lessard, L., "Effect of Load Distribution of the Fiber Buckling Strength of Unidirectional Composites," submitted to *Journal of Composite Materials*.

⁶⁷ Davis, J.G., Jr., "Compressive Strength of Fiber-Reinforced Composite Materials," in *Composite Reliability, ASTM STP 580*. Philadelphia, PA: American Society for Testing and Materials, 1975, pp. 364-377.

⁶⁸ Wang, A.S.D., "A Non-Linear Microbuckling Model Predicting the Compressive Strength of Unidirectional Composites," ASME Paper 78-WA/Aero-1, ASME, 1978.

⁶⁹ Wang, A.S.D., "Certification of Composite Aircraft Structures Under Impact, Fatigue and Environmental Conditions, Part III: Environmental Effects on Compression Strength," Naval Air Development Center, Warminster, PA, Report No. NADC-78259-60, January 1978.

⁷⁰ Petit, P.H., "A Simplified Method of Determining the In-Plane Shear Stress-Strain Response of Unidirectional Composites," in *Composite Materials: Testing and Design, ASTM STP 460*. Philadelphia, PA: American Society for Testing and Materials, 1969, pp. 83-93.

⁷¹ Rosen, B.W., "A Simple Procedure for Experimental Determination of the Longitudinal Shear Modulus of Unidirectional Composites," *Journal of Composite Materials*, Vol. 6, October 1972, pp. 552-554.

⁷² Hahn, H.T., "A Note on Determination of the Shear Stress-Strain Response of Unidirectional Composites," *Journal of Composite Materials*, Vol. 7, July 1973, pp. 383-386.

⁷³ Shuart, M.J., "Failure of Compression-Loaded Multi-Directional Composite Laminates," *Proceedings of the AIAA/ASME/ASCE/AHS 29th Structures, Structural Dynamics and Materials Conference*, Williamsburg, VA, April 1988.

⁷⁴ Shuart, M.J. and Williams, J.G., "Compression Behavior of $\pm 45^\circ$ — Dominated Laminates With a Circular Hole or Impact Damage," *AIAA Journal*, Vol. 24, January 1986, pp. 115-122.

⁷⁵ Chang, F.K., Lessard, L., and Tang, J.M., "Compression Response of Laminated Composites Containing an Open Hole," *SAMPE Quarterly*, Vol. 19, July 1988, pp. 46-51.

⁷⁶ Chang, F.K. and Lessard, L., "Damage Tolerance of Laminated Composites Containing an Open Hole and Subjected to Compressive Loadings: Part I — Analysis," submitted to *Journal of Composite Materials*.

⁷⁷ Lessard, L. and Chang, F.K., "Damage Tolerance of Laminated Composites Containing an Open Hole and Subjected to Compressive Loadings: Part II — Experiment," submitted to *Journal of Composite Materials*.

⁷⁸ Davis, J., "The Effects of Fiber Waviness on the Compressive Response of Fiber-Reinforced Composite Materials," Department of Aerospace Engineering, Texas A&M University, M.S. Thesis, December 1989.

⁷⁹ Highsmith, A.L. and Davis, J., "The Effects of Fiber Waviness on the Compressive Response of Fiber-Reinforced Composite Materials," NASA Langley Research Center, Hampton, VA, Annual Progress Report for NASA Research Grant NAG-1-659, January 1990.

⁸⁰ Lee, J.W., "Deformation Analysis of Local Ply Curvature in Laminated Composites," Department of Aerospace Engineering, Texas A&M University, M.S. Thesis, December 1987.

⁸¹ Collings, T.A., "Transverse Compressive Behaviour of Unidirectional Carbon Fibre Reinforced Plastics," *Composites*, May 1974, pp. 108-116.

⁸² Hancox, N.L., "The Compression Strength of Unidirectional Carbon Fibre Reinforced Plastic," *Journal of Materials Science*, Vol. 10, 1975, pp. 234-242.

⁸³ Kim, R.Y., "On the Off-Axis and Angle-Ply Strength of Composites," in *Test Methods and Design Allowables for Fibrous Composites, ASTM STP 734*. C.C. Chamis, ED., Philadelphia, PA: American Society for Testing and Materials, 1981, pp. 91-108.

⁸⁴ Fried, N., "The Compressive Strength of Parallel Filament Reinforced Plastics-The Role of the Resin," *Proceedings of the 18th Annual Meeting of the Reinforced Plastics Division*, Society of the Plastics Industry, Chicago, IL, February 1963.

⁸⁵ Fried, N. and Kaminetsky, J., "The Influence of Material Variables on the Compressive Properties of Parallel Filament Reinforced Plastics," *Proceedings of the 19th Annual Meeting of the Reinforced Plastics Division*, Society of the Plastics Industry, Chicago, IL, February 1964.

⁸⁶ Fried, N., "The Response of Orthogonal Filament Wound Materials to Compressive Stress," *Proceedings of the 20th Annual Meeting of the Reinforced Plastics Division*, Society of the Plastics Industry, Chicago, IL, February 1965.

⁸⁷ Budiansky, B., "Micromechanics," *Computers and Structures*, Vol. 16, 1983, pp. 3-12.

⁸⁸ Chou, T.W. and Kelly, A., "The Effect of Transverse Shear on the Longitudinal Compressive Strength of Fibre Composites," *Journal of Materials Science*, Vol. 15, 1980, pp. 327-331.

⁸⁹ Wilkinson, E., Parry, T.V., and Wronski, A.S., "Compressive Failure in Two Types of Carbon Fibre-Epoxy Laminates," *Composites Science and Technology*, Vol. 26, 1986, pp. 17-29.

⁹⁰ Lee, R.J., "Compression Strength of Aligned Carbon Fibre-Reinforced Thermoplastic Laminates," *Composites*, Vol. 18, January, 1987, pp. 35-39.

⁹¹ Whitney, J.M. and Nuismer, R.J., "Stress Fracture Criteria for Laminated Composites Containing Stress Concentrations," *Journal of Composite Materials*, Vol. 8, July 1974, pp. 253-265.

⁹² Nuismer, R.J. and Whitney, J.M., "Uniaxial Failure of Composite Laminates Containing Stress Concentrations," *Fracture Mechanics of Composites, ASTM STP 593*, 1975, pp. 117-142.

⁹³ Nuismer, R.J. and Labor, J.D., "Applications of the Average Stress Criterion: Part II — Compression," *Journal of Composite Materials*, Vol. 13, January 1979, pp. 49-60.

⁹⁴ Reifsnider, K.L., Stinchcomb, W.W., Bakis, C.R., and Yih, R.Y., "The Mechanics of Micro-Damage in Notched Composite Laminates," in *Composite Materials: Fatigue and Fracture (Second Symposium), ASTM STP 1012*. Philadelphia, PA: American Society for Testing and Materials, 1989, pp. in print.

- ⁹⁵ Renault, M., Valentin, D., and Perez, F., "A Damage Tolerance Study of Notched CFRP Laminates," *Engineering Conference on Fracture: Failure Analysis, Theory and Practice*, Budapest, Hungary, September 1988.
- ⁹⁶ Guz, A.N. and Lapusta, Y.N., "Stability of Fibers Near a Free Cylindrical Surface," Institute of Mechanics, Academy of Sciences of the Ukrainian SSR, Kiev. Translated from *Prikladnaya Mekhanika*, Vol. 24, No. 10, October 1988, pp. 3-9.
- ⁹⁷ Burns, S.W., Herakovich, C.T., and Williams, J.G., "Efficient 3-D Finite Element Failure Analysis of Compression Loaded Angle-Ply Plates with Holes," *Sixth International Conference on Composite Materials — Second Europe Conference on Composite Materials*, London England, Vol. 5, July 1987, pp. 231-240.
- ⁹⁸ Pattnaik, A., Koczak, M.J., and Rogers, H.C., "Compressive Failure Behavior of FP Alumina/Aluminum Composites," in *New Developments and Applications in Composites*. D. Kuhlmann-Wilsdorf and W.C. Harrigan, EDS., AIME Publication, 1979, pp. 261-282.
- ⁹⁹ Chaplin, C.R., "Compressive Fracture in Unidirectional Glass-Reinforced Plastics," *Journal of Materials Science*, Vol. 12, 1977, pp. 347-352.
- ¹⁰⁰ Parry, T.V. and Wronski, A.S., "Kinking and Tensile, Compressive and Interlaminar Shear Failure in Carbon-Fibre-Reinforced Plastic Beams Tested in Flexure," *Journal of Materials Science*, Vol. 16, 1981, pp. 439-450.
- ¹⁰¹ Parry, T.V. and Wronski, A.S., "Kinking and Compressive Failure in Uniaxially Aligned Carbon Fibre Composite Tested Under Superposed Hydrostatic Pressure," *Journal of Materials Science*, Vol. 17, 1982, pp. 893-900.
- ¹⁰² Wronski, A.S. and Parry, T.V., "Compressive Failure and Kinking in Uniaxially Aligned Glass-Resin Composite Under Superposed Hydrostatic Pressure," *Journal of Materials Science*, Vol. 17, 1982, pp. 3656-3662.
- ¹⁰³ Evans, A.G. and Adler, W.F., "Kinking as a Mode of Structural Degradation in Carbon Fiber Composites," *Acta Metallurgica*, Vol. 26, 1978, pp. 725-738.
- ¹⁰⁴ Potter, R.T. and Purslow, D., "The Environmental Degradation of Notched CFRP in Compression," *Composites*, July 1983, pp. 206-225.
- ¹⁰⁵ Purslow, D. and Potter, R.T., "The Effect of Environment on the Compression Strength of Notched CFRP-A Fractographic Investigation," *Composites*, Vol. 15, April 1984, pp. 112-120.
- ¹⁰⁶ Marom, G., Davidovitz, M., Mittelman, A., and Roman, I., "Fracture Mechanisms in Bending of Unidirectional Kevlar-Reinforced Epoxy Composites," *Proceedings of the International Conference on Testing, Evaluation, and Quality Control of Composites*, University of Surrey, Guildford, United Kingdom, September 1983.



¹⁰⁷ Davidovitz, M., Mittelman, A., Roman, I., and Marom, G., "Failure Modes and Fracture Mechanisms in Flexure of Kevlar-Epoxy Composites," *Journal of Materials Science*, Vol. 19, 1984, pp. 377-384.

¹⁰⁸ Rajendran, G., Rogers, H.C., and Koczak, M.J., "The Compressive Failure Modes of Alumina/Aluminum Composites: Dead Weight vs. Machine Loading," *Powder Metallurgy International*, Vol. 18, 1986, pp. 397-400.

¹⁰⁹ Waas, A. and Babcock, C., "Observation of the Initiation and Progression of Damage in Compressively Loaded Composite Plates Containing a Cutout," NASA Langley Research Center, Hampton, VA, NASA Progress Report for Grant NSG-1-483, November 1986.

¹¹⁰ Starnes, J.H. and Williams, J.G., "Failure Characteristics of Graphite/Epoxy Structural Components Loaded in Compression," in *Mechanics of Composite Materials — Recent Advances*. Z. Hashin and C.T. Herakovich, EDS., New York, NY: Pergamon Press, 1982, pp. 283-306.

¹¹¹ Williams J.G., "Effect of Impact Damage and Open Holes on the Compression Strength of Tough Resin/High Strain Fiber Laminates," NASA Langley Research Center, Hampton, VA, NASA Technical Memorandum 85756, February 1984.

¹¹² Rhodes, M.D., Mikulas, M.M., and McGowan, P.E., "Effects of Orthotropy and Width on the Compression Strengths of Graphite/Epoxy Panels with Holes," *AIAA Journal*, Vol. 22, September 1984, pp. 1283-1292.

¹¹³ Sohi, M.M., Hahn, H.T. and Williams, J.G., "The Effect of Resin Toughness and Modulus on Compressive Failure Modes of Quasi-Isotropic Graphite/Epoxy Laminates," in *Toughened Composites, ASTM STP 937*. N.J. Johnston, ED., Philadelphia, PA: American Society for Testing and Materials, 1987, pp. 37-60.

¹¹⁴ Hahn, H.T. and Sohi, M.M., "Buckling of a Fiber Bundle Embedded in Epoxy," *Composites Science and Technology*, Vol. 27, 1986, pp. 25-41.

¹¹⁵ Hahn, H.T., "Compressive Failure of Unidirectional Composites," presented at the 13th International Symposium for Testing and Failure Analysis, Los Angeles, CA, November 1987.

¹¹⁶ DeTeresa, S.J., Allen, S.R., Farris, R.J., and Porter, R.S., "Compressive and Torsional Behaviour of Kevlar 49 Fibre," *Journal of Materials Science*, Vol. 19, 1984, pp. 57-72.

¹¹⁷ Chang, I.Y., "Thermoplastic Matrix Continuous Filament Composites of Kevlar Aramid or Graphite Fiber," *Composites Science and Technology*, Vol. 24, 1985, pp. 61-79.

¹¹⁸ Chang, I.Y., "Static Mechanical Properties of Thermoplastic Matrix Composites," *Proceedings of the International Symposium on Composite Materials and Structures*, Beijing, People's Republic of China, June 1986.

¹¹⁹ Mabson, G.E., Wharram, G.E., Tennyson, R.C., and Hansen, J.S., "On the Compressive Strength of Graphite Composite Laminates Containing Interlaminar Flaws," *Polymer Plastics Technology in Engineering*, Vol. 22, 1984, pp. 99-113.

¹²⁰ Sternstein, S.S., Yurgartis, S.W., and Srinivasan, K., "Deformation, Microdeformation and Toughness in Graphite-Polymeric Matrix Composites," *Proceedings of the Sixth International Conference on Deformation, Yield and Fracture of Polymers*, Cambridge, England, April 1985.

¹²¹ Bishop, S.M., "The Mechanical Performance and Impact Behaviour of Carbon-Fibre Reinforced PEEK," *Composite Structures*, Vol. 3, 1985, pp. 295-318.

¹²² Miyano, Y. and Kanemitsu, M., Kunio, T., and Kuhn, H.A., "Role of Matrix Resin on Fracture Strengths of Unidirectional CFRP," *Journal of Composite Materials*, Vol. 20, November 1986, pp. 520-538.

¹²³ van Dreumel, W.H.M., "A Short Note on the Compressive Behaviour of Aramid Fibre Reinforced Plastics," Drecht University of Technology, Drecht, The Netherlands, Report No. LR-341, January 1982.

¹²⁴ Turner, R.M. and Cogswell, F.N., "The Effect of Fibre Characteristics on the Morphology and Performance of Semi-Crystalline Thermoplastic Composites," *SAMPE Journal*, Vol. 23, January/February 1987, pp. 40-44.

¹²⁵ Vinson, J.R. and Sierakowski, R.L., *The Behavior of Structures Composed of Composite Materials*, First Edition, Boston, MA: Kluwer, 1986, pp. 303.

¹²⁶ DeTeresa, S.J., Porter, R.S., and Farris, R.J., "A Model for the Compressive Buckling of Extended Chain Polymers," *Journal of Materials Science*, Vol. 20, 1985, pp. 1546-1659.

¹²⁷ DeTeresa, S.J., Porter, R.S., and Farris, R.J., "Experimental Verification of a Microbuckling Model for the Axial Compressive Failure of High Performance Polymer Fibres," *Journal of Materials Science*, Vol. 23, 1988, pp. 1886-1894.

¹²⁸ DeTeresa, S.J., Allen, S.R., and Farris, R.J., "The Axial Compressive Strength of High Performance Polymer Fibers," submitted to *Advances in Chemistry Series, Composites: Chemical and Physicochemical Aspects*, T.L. Vigo and V.J. Kinzig, EDS., July 1989.

¹²⁹ Yau, S.S. and Chou, T.W., "Strength of Woven-Fabric Composites with Drilled and Molded Holes," in *Composite Materials: Testing and Design (Eighth Conference)*, ASTM STP 972. J.D. Whitcomb, ED., Philadelphia, PA: American Society for Testing and Materials, 1988, pp. 423-437.

- ¹³⁰ Klein, A.J., "Which Weave," *Advanced Materials and Processes*, March 1986, pp. 40-43.
- ¹³¹ Schapery, R.A., "Mechanical Characterization and Analysis of Inelastic Composite Laminates with Growing Damage," Texas A&M University, College Station, TX, Report No. MM 5742-89-10, April 1989.
- ¹³² Landro, L.D., and Pegoraro, M., "Carbon Fibre-Thermoplastic Matrix Adhesion," *Journal of Materials Science*, Vol. 22, 1987, pp. 1980-1986.
- ¹³³ Ewins, P.D. and Potter, R.T., "Some Observations on the Nature of Fiber Reinforced Plastics and the Implications for Structural Design," *Philosophical Transactions of the Royal Society of London*, Vol. A294, 1980, pp. 507-517.
- ¹³⁴ Malik, B., Palazotto, A., and Whitney, J., "Notch Strength of GR/PEEK Composite Material at Elevated Temperatures," *26th Structures, Structural Dynamics, and Materials Conference*, Orlando, Florida, April 1985.
- ¹³⁵ Ramey, J., Palazotto, A., and Whitney, J., "Comparison of Notch Strength Between Gr/PEEK (APC-1 and APC-2) and Gr/Epoxy Composite Material at Elevated Temperature," *Proceedings (A86-48676 24-35) 1986 SEM Spring Conference on Experimental Mechanics*, Society of Experimental Mechanics, New Orleans, LA, June 1986.
- ¹³⁶ Kar, R.J., Herfert, R.E., and Kessler, R.T., "Fractographic and Microstructural Examination of Compression Failures in Wet Compression Graphite/Epoxy Coupons," in *Composite Materials: Testing and Design (Seventh Conference)*, ASTM STP 893. J.M. Whitney, ED., Philadelphia, PA: American Society for Testing and Materials, 1986, pp. 140-157.
- ¹³⁷ Fiberite Corporation — An ICI (Imperial Chemical Industries) Company, Orange, CA, "APC-2: The Product of High Technology," trade name material data sheets, 1988.
- ¹³⁸ Carlile, D.R., Leach, D.C., Moore, D.R., and Zahlan, N., "Mechanical Properties of the Carbon Fibre/PEEK Composite APC-2/AS4 for Structural Applications," *ASTM Symposium on Advances in Thermoplastic Matrix Composite Materials*, Bal Harbor, FL, October 1987.
- ¹³⁹ Hartness, J.T., "Polyether Matrix Composites," *SAMPE Quarterly*, January 1983, pp. 33-36.
- ¹⁴⁰ Lee, W.I., Talbott, M.F., Springer, G.S., and Berglund, L.A., "Effects of Cooling Rate on the Crystallinity and Mechanical Properties of Thermoplastic Composites," *Journal of Reinforced Plastics and Composites*, Vol. 6, January 1987, pp. 2-12.

¹⁴¹ Iaconis, J.M., "Process Variables Evaluation of PEEK APC-2 Thermoplastic Matrix Composites," 32nd *International SAMPE Symposium and Exhibition*, Anaheim, CA, April 1987.

¹⁴² Blundell, D.J. and Osborn, B.N., "The Morphology of Poly(aryl-ether-ether-ketone)," *Polymer*, Vol. 24, August 1983, pp. 953-958.

¹⁴³ Pagano, N.J. and Pipes, R.B., "The Influence of Laminate Stacking Sequence on Laminate Strength," *Journal of Composite Materials*, Vol. 5, January 1971, pp. 50-57.

¹⁴⁴ Quadrax Corporation, Providence, Rhode Island, "Quadrax Interlaced Unidirectional Tapes," Advertising Brochure, 1988.

¹⁴⁵ Guynn, E.G. and Bradley, W.L., "Micromechanics of Composite Laminate Compression Failures," NASA Langley Research Center, Hampton, VA, Annual Progress Report for NASA Research Grant NAG-1-659, August 1988.

¹⁴⁶ Trademark of The Dow Chemical Company.

¹⁴⁷ Barron, D., private communications, October 1988.

¹⁴⁸ Carlsson, L.A. and Pipes, R.B., *Experimental Characterization of Advanced Composites Materials*, First Edition, Englewood Cliffs, New Jersey: Prentice-Hall, Inc., 1987, pp. 54-65.

¹⁴⁹ Fife, B., Peacock, J.A., and Barlow, C.Y., "The role of Fibre-Matrix Adhesion in Continuous Carbon Fibre Reinforced Thermoplastic Composites: A Microstructural Study," *Sixth International Conference on Composite Materials — Second Europe Conference on Composite Materials*, London England, Vol. 5, July 1987, pp. 439-447.

¹⁵⁰ Leach, D., private communications, June 1990.

¹⁵¹ Whitney, J.M., Daniel, I.M., and Pipes, R.B., *Experimental Mechanics of Fiber Reinforced Composite Materials*, Revised Edition, Englewood Cliffs, New Jersey: Prentice-Hall, Inc., 1984, pp. 185-199.

¹⁵² Highsmith, A.L., Davis, J.J., and Helms, K.L.E., "The Influence of Fiber Waviness on the Compressive Behavior of Continuous fiber Composites," presented at the ASTM Symposium on Composite Materials, San Francisco, CA, April 1990.

¹⁵³ Gray, R.J., "Experimental Techniques for Measuring Fibre/Matrix Interfacial Bond Shear Strength," *Journal of Adhesion and Adhesives*, Vol. 3, No. 4, October 1983, pp. 197-201.

¹⁵⁴ Mandell, J., Grande, D.H., Tsiang, T., and McGarry, F.J., "Modified Microdebonding Test for Direct In-Situ Fiber/Matrix Bond Strength Determination in Fiber Composites," in *Composite Materials: Testing and Design (Seventh Conference)*, ASTM STP 893. J.M. Whitney, ED., Philadelphia, PA: American Society for Testing and Materials, 1986, pp. 87-108.

¹⁵⁵ Caldwell, D.L., "Determination of Interfacial Strength of Composites," *Proceedings of the Advanced Composites Conference*, Detroit, MI, 1987.

¹⁵⁶ Caldwell, D.L. and Cortez, F.M., "A New Method for Determining the Interfacial Strength of Composites," presented at the Society of the Plastics Industry Conference, Cincinnati, OH, February 1988.

¹⁵⁷ Caldwell, D.L. and Jarvie, D.A., "Determination of the Interfacial Strength of Advanced Composites," presented at the 33rd International SAMPE Symposium, Anaheim, CA, March 1988.

¹⁵⁸ Bradley, W.L., Corleto, C.R., and Goetz, D.P., "Studies of Mode I and Mode II Delamination Using a J-Integral Analysis and In-Situ Observations of Fracture in the SEM," Bolling Air Force Base, D.C., Annual Progress Report for AFOSR Research Grant AFOSR-84-0064, July 1990.

¹⁵⁹ Williams, J.G., "Large Displacement and End Block Effects in the DCB interlaminar Test in Modes I and II," *Journal Composite Materials*, Vol. 21, April 1987, pp. 330-147.

¹⁶⁰ Whitney, J.M., Browning, C.E., and Hoogsteden, W., "A Double Cantilevered Beam Test for Characterizing Mode I Delamination of Composite Materials," *Journal of Reinforced Plastics Composites*, Vol. 1, 1982, pp. 297-310.

¹⁶¹ Keary, P.E., Ilcewicz, L.B., Shaar, C., and Trostle, J., "Interlaminar Fracture Toughness of Composites Using Slender Double Cantilever Beam Specimens," *Journal Composite Materials*, Vol. 19, March 1985, pp. 154-175.

¹⁶² Bathe, K.J., *Finite Element Procedures in Engineering Analysis*, First, Englewood Cliffs, NJ: Prentice-Hall, Inc., 1982.

¹⁶³ Zienkiewicz, O.C., *The Finite Element Method (The third, expanded and revised edition of The Finite Element Method in Engineering Science)*, First, London, England: McGraw Hill Book Company (UK) Limited, 1977.

¹⁶⁴ ABAQUS, Hibbitt, Karlsson, and Sorensen, Inc., Providence, Rhode Island, 1987.

¹⁶⁵ PATRAN Plus, PATRAN Division of PDA Engineering, Costa Mesa, California, 1989.

¹⁶⁶ PAT/ABAQUS Interface Guide, PATRAN Division of PDA Engineering, Costa Mesa, California, 1989.



¹⁶⁷ Leach, D.C., Curtis, D.C., and Tamblin, D.R., "Delamination Behavior of Carbon Fiber/Poly(etheretherketone) (PEEK) Composites," in *Toughened Composites*, ASTM STP 937. N.J. Johnston, ED., Philadelphia, PA: American Society for Testing and Materials, 1987, pp. 358-380.

¹⁶⁸ Leeser, D., private communications, June 1989.

¹⁶⁹ DeTeresa, S.J., private communications, December 1989.

¹⁷⁰ Chakachery, E.A., "Deformation Mechanisms in Polymeric Matrices and Carbon Fibre Reinforced Composites," Department of Mechanical Engineering, Texas A&M University, Ph.D. Dissertation, May 1989.

¹⁷¹ Bascom, W.D. and Jensen, R.M., "Stress Transfer in Single Fiber/Resin Tensile Tests," *Journal of Adhesion*, Vol. 19, 1986, pp. 219-239.

VITA

Eunice Gail Guynn was born in Princeton, West Virginia on May 14, 1961, the only child of Everett B. and the late Frances Williamson Guynn. Gail obtained her high school degree from Princeton High School in 1979. She continued her education at Bluefield College, Bluefield, Virginia in a Pre-Engineering Curriculum for one year. In 1980, she transferred to Virginia Polytechnic Institute and State University, Blacksburg, Virginia, where she graduated Cum Laude with a Bachelor of Science in Civil Engineering and a Minor in Engineering Science and Mechanics in June, 1984.

From July, 1984 through January, 1986, Gail worked as a Materials Engineer for PRC Kentron, Inc., Aerospace Technologies Division, Hampton, Virginia. In this position, she served as an in-house contractor providing support to the Mechanics and Materials Branch in the Materials Division of NASA Langley Research Center, Hampton, Virginia. In January of 1986, she entered the graduate program in Mechanical Engineering at Texas A&M University. Gail graduated with a Master of Science degree in Mechanical Engineering in December, 1987 and then began pursuit toward this Doctor of Philosophy degree in Interdisciplinary Engineering. The highlight of Gail's career in graduate school occurred on July 26, 1990, when she married Mr. Joseph P. Fuehne, a fellow graduate student.

Gail's permanent address follows:

1201 Harvey Road, #24

College Station, Texas 77840

The typist for this dissertation was the author, Eunice Gail Guynn.



